Electrochemical Pore Etching in III-V Compounds

Dissertation

zur Erlangung des akademischen Grades
Doktor der Ingenieurwissenschaften
(Dr.-Ing.)
der Technische Fakultaet
der Christian-Albrechts Universitaet zu Kiel

Sergiu Langa

Kiel
2004

1. Gutachter: Prof. Dr. H. Föll
2. Gutachter: Prof. Dr. I.M. Tiginyanu
3. Gutachter: Prof. Dr. U. Gösele
Datum der mündlichen Prüfung: 30.04.2004

Contents

Chapter 1

Introduction

Electrochemistry of metals and semiconductors becomes increasingly important in the development of communication technology, and even microelectronic processes used for integrated circuit (IC) manufacturing are now employing cost-effective electrochemical methods. These microscopic processes require a good understanding of the electrochemical parameters, as well as easy monitoring and control; in addition they should be environmentally friendly. Electrochemistry, as an industrial and scientific field, is aiming to solve all these problems by investigating the mechanisms of etching, deposition, and corrosion.

The best known technological steps and device elements, which make use of electrochemical processes are: copper wiring on IC chips [1, 2], thin-film magnetic heads [3, 4], microelectromechanical systems (MEMS) [5, 6, 7], integral lenses on light-emitting diodes [8], high-aspect-ratio gratings [9, 10], gate grooves in field-effect transistors [11]. These and other technological steps make electrochemical processes unique and at present unavoidable in modern (IC) technology.

It goes without saying that the electrochemical deposition of $sub-\mu m$ copper metallization is partially responsible for the rapid increase in the operating frequency of modern microprocessors. However, the progress achieved still seems not to be enough to process the huge amount of useful information generated nowadays in ordinary situations. In response, the scientific community is permanently considering new possibilities for raising the speed of data processing systems, i.e. ICs.

One of the possibilities for increasing the processing speed and at the same time avoiding some other common difficulties of the standard ICs, is to use light instead of electrons as information carrier. The principal advantage of light over the electrons is quite evident:

�Electrons interact strongly, meaning that circuit designers must provide separate wires for each electronic signal. As chips integrate more functions, the necessary number of interconnecting wires requires more and more space.

▶ Photons, on the other hand, do not interact (strongly), meaning that signals carried by light can cross without affecting each other.

▶ More importantly, large numbers of optical signals can be carried on the same path (connection) without mixing or signal interference. This ability to carry many signals in parallel offers a tremendous advantage for device design.

However, for the moment it is premature to speak about fully optical *ICs* or Photonic Integrated Circuits (*PICs*). Therefore, at least for the next decade, the industry will put a major accent on Optoelectronic Integrated Circuits (*OEIC*). Due to their optical and electrical properties, III-V compounds are the main materials for OEICs production.

Different modern techniques are used for OEICs manufacturing. Among them, electrochemical etching contributed constantly to the development of passive and active optoelectronic/photonic components, *e.g.* Light Emitting Diodes (*LEDs*), Photonic Band Gap structures (*PBG*), Wave Guides (*WG*) etc..

PBG structures are also frequently called photonic crystals (*PC*) [12]. A *PC* is a periodic arrangement of macroscopic dielectric media, exhibiting band gaps for electromagnetic waves similar to electronic states in semiconductors, *i.e.* *PCs* are generalized Bragg reflectors in two (2D) and three (*3D*) dimensions. They can be regarded as an analogue of classical semiconductor crystals for light. Thus, similar to electrons, light can be controlled (molded) and consequently used as information carrier. For more details about *PCs* see Appendix A.

The first attempts to obtain a photonic band gap structure by means of electrochemical etching have been made with Si, which is the primary semiconductor of modern microelectronics. The results were quite successful and promising. Electrochemically etched macroporous Si proved to be adequate for manufacturing 2D photonic crystals with a band gap around one of the wave lengths used for communication ($\lambda = 1.55 \ \mu m$) [13]. Unfortunately, no efficient light sources made from Si have been reported up to now. In addition, Si can not be easily integrated with the already existing light emitting sources, and it is not suitable for PBGs in the visible region of the spectrum, *i.e.* at shorter wavelengths. These difficulties with Si are caused by its small ($E_g = 1.12 \ eV$) and indirect electronic band gap. Thus, the radiative electron-hole recombination is not effective, the light in the visible region is simply absorbed by Si, and no Bragg effects in the visible range can be observed.

Little can be done to avoid these problems with Si, therefore other materials with larger and direct electronic band gaps should be chosen. Ideal candidates for this purpose are porous III-V semiconductor compounds. More than that, the shift from elementary to compound semiconductors entails a major crystallographic modification and offers the possibility to change their chemical composition. This opens the way for new physical properties specific to these polar materials.

At the outset of this investigation little was known about porous III-V semiconductors. Although the number of publications devoted to porous III-V compounds is still much smaller than that devoted to porous Si, some important properties of porous III-V structures have been reported recently. In particular, the following new findings merit attention:

▰ A sharp increase in intensity of the near-band-edge photo luminescence (PL) in anodically etched GaP along with the emergence of blue and ultraviolet luminescence [14, 15, 16].

▰ A strongly enhanced photo response occurring during pore formation in n-GaP electrodes by anodic etching in sulphuric acid solution [17, 18].

▰ Evidence has been found for birefringence in porous InP at wavelengths suitable for optical communication systems [19].

▰ Porosity-induced modification of the phonon spectrum was observed in GaP, GaAs and InP [20, 21, 22].

� A very efficient optical second harmonic generation (*SHG*) was observed in porous GaP membranes [23].

Besides the optical properties enumerated above, the morphologies of the porous structures in III-V compounds was little studied. It will be shown that it is possible to produce a large diversity of pore morphologies in III-V's, which allows to consider porous III-V's as promising materials for different photonic crystal application. The primary challenges in this regard are the improvement of the so-called nucleation stage and the stability of pore growth into the depth of the substrate.

Uniform porous structures in III-Vs are much harder to obtain than in Si and this is mostly due to various difficulties preventing easy homogeneous nucleation, this is also true for lithographically pre-patterned samples. Optimization of the nucleation is thus very important and this may require etching conditions quite different from those needed for stable pore growth. This means that if the conditions for stable pore growth are applied before the nucleation is finished on the entire sample surface, the pores, which are not yet fully nucleated will die out. On the other hand, if the conditions for stable pore growth are applied too late, branching of already nucleated pores can play a significant role in destroying the uniformity of the structure.

Taking into account the lack of morphology investigations in porous III-Vs and the possibility to use the porous structures for applications like photonic crystals, the main goals identified for the present work are:

▸ Achievment of electrochemical pore growth in a wide range of materials.

▸ Improvement of pore nucleation in semiconductors like GaAs, InP and GaP.

▸ Optimization of the stable pore growth phase in these materials.

▸ Investigation of the pore morphologies obtained, in particular with respect to their optical properties.

The notions and principles used to describe the electrochemistry of semiconductors in general, and of III-Vs in particular, will be outlined in Chapters 2 and 3.

The experimental setup is of a great importance during the electrochemical experiments, therefore a detailed description is presented in Chapter 4.

While there are many models for pore formation in Si, none of them can explain the pore formation in III-Vs as well as the current burst model. The main ideas of the current burst model are therefore described in Chapter 3.6.

Entirely new pore morphologies, then unknown in Si, have been observed in III-V compounds. Their particularities and etching conditions are presented in Chapter 5.

As it turned out, self-organization is a very common feature observed during the anodization of semiconductors. Expressions of self-organization like self-induced voltage oscillations in InP and GaP, tetrahedron-like pores, and domains of crystallographically oriented pores in GaAs will be discussed in Chapter 6 and compared to other porous semiconductor materials, like Si.

One of the outstanding results obtained in InP is the self-arranged long-range ordering of pores, presented in Chapter 7.

A separate chapter will be dedicated to some of the optical properties of these structures, in particular cathodoluminescence (CL) will be discussed in Chapter 8.

For comparison reasons, in parallel to porous III-Vs some other materials have been investigated in this work. Am example can be found in Appendix E, where some results about macro pore formation in Germanium are presented.

Conclusions and perspectives will finish the narration.

Chapter 2

The basics of Solids and Solutions

Electrochemistry of III-V compounds has a long tradition. Namely, one of the most well known electrochemical processes used with III-V compounds is the so-called Photo-Electrochemical Etching (*PEC*) [24]. *PEC* etching is a particular case of Electro-Chemical Etching (*ECE*), encompassing light-induced electrochemical reactions at *semiconductor/electrolyte* interfaces.

If the light used to illuminate the *semiconductor/electrolyte* interface has a higher energy than the electronic band gap of the semiconductor, then the incident photons will generate electron-hole pairs. The generated holes and electrons stimulate the local (selective) material etching, or deposition reactions. Selectivity is the major advantage of *PEC* etching. Therefore, electrochemical etching of semiconductors is mainly used to fabricate different anisotropic structures in micro- and optoelectronics. This method is especially effective with III-Vs compounds, due to their high anisotropy and higher solubility of the reaction products.

In few words: *ECE* and *PEC* etching are nothing else but the dissolution of a solid material as a result of charge transfer between the solid and a liquid solution. Pore formation is a particular case of etching, therefore the principles of charge transfer are very important as well. Taking into account that the charge transfer processes are complex and strongly dependent on the charge distribution in the solid and solution, we will start by discussing the models used to describe the charge behavior in these two environments.

2.1   The Solid

The properties of semiconductor and metal electrodes can be understood by examining the electronic structure of these materials. Due to the essentially infinite number of atoms that must be considered, the electronic structure of these solids is typically discussed in terms of energy bands [25]. The band model stems directly from the picture of atomic energy levels. However, the analysis shows that when the atoms are brought close to one another to form a solid, valence electrons interact with one another so that their sharp atomic energy levels are broadened into wider regions called energy bands.

A solid is nothing else than a collection of 10^{22} cm^{-3} interacting atoms. Thus, looking at a crystal as a whole it can be concluded that from each atomic level a number of $2{\cdot}10^{22}$ per cubic centimeter different energy levels (only slightly different from the original atomic level) are generated. Because one atomic orbital can host two electrons, with the same energy but with opposite spins, the number of levels stemming from the same atomic level is doubled as compared
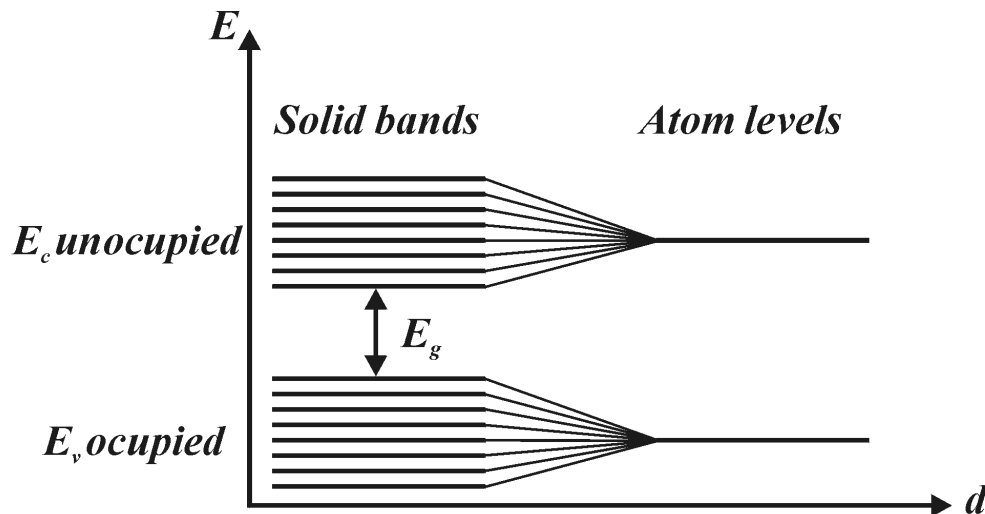
Figure 2.1: *A schematic representation of the splitting of atomic energy levels into bands, and finally into a quasi-continuous energy region, by decreasing the distance between the atoms (d). Last occupied atomic orbitals, i.e. at large distances between the atoms, form the so-called valence band - E_v, i.e. when the atoms are put together to form a crystal. Similarly, first unoccupied atomic level at large distances form the conduction band E_c in a crystal.*

to the number of atoms in the solid and form a so-called energy band. The splitting of levels, when the atoms approach each other, is presented schematically in Figure 2.1.

From the point of view of solid state physics two atomic levels are important: the last one occupied by electrons and the first unoccupied one. In semiconductors these two levels give rise to two different bands. The band resulting from the last occupied level is called the valence band (E_v) and that resulting from the first unoccupied level is called the conductance band (E_c) [26]. The difference between the top of E_v and bottom of E_c is called the electronic band gap (E_g). For a pure semiconductor there are no energy levels for electrons within the electronic bang gap.

The movement of electrons through the material (semiconductor or metal), which is usually referred to as conductivity, requires that the electrons occupy partially filled or free orbitals (states). This is easily done in the conduction band, where a high number of unoccupied states is available. However, this is not the case for a completely filled valence band. For metals, the conduction and valence band overlap, so that the conduction band states can be easily occupied by the electrons in the valence band. Band gaps between the valence and conduction bands are characteristic to semiconductors and insulators but not to metals. For insulators, the band gap is sufficiently large that under normal conditions the electrons can not be transferred from the valence band to the conduction band. On the other hand, in semiconductors the band gap is not as large and the electrons can be transferred into the conduction band, *e.g.* by thermal excitation. The excitation of electrons leaves positively charged vacancies in the valence band, which are referred to as 'holes'.

Therefore, when talking about semiconductors, two types of charge carriers are discussed: electrons and holes [27]. A hole is an empty level in the valence band, or in other words a valence bond with a missing electron. As a result the current in semiconductors is made up of two components:

▸ The mobile electrons in the conduction band;

▸ The mobile holes in the valence band.

The electrons can be excited to the conduction band either electrically, thermally, or optically. However, there is another method for generating charge carriers in semiconductors, referred to as doping. Doping involves the addition of a different chemical element into the semiconductor. The simplest example is the introduction of a group V element (donor, *e.g.*, P) or a group III element (acceptor, *e.g.*, B) into a group IV crystal (host, *e.g.*, Si). The addition of P into Si introduces occupied energy levels into the band gap close to the edge of the conduction band, thereby allowing an easy promotion of electrons from the group V atom into the conduction band of the group IV crystal. On the other hand, *e.g.* the addition of B introduces vacant energy levels into the band gap close to the edge of the valence band which allows facile transfer of electrons from the valence band to group III atoms.

For III-V materials impurity species such as Si, Sn, Te, Se, and S are suitable candidates as donor species. Acceptor impurities include Be, C, Zn, Cd, and Mn. Other metal species such as Cr, Ni, Fe tend to produce mid gap deep level states with high resistivity or semi-insulating characteristics [28].

Undoped semiconductors are known as intrinsic, while doped semiconductors are called extrinsic semiconductors. Doped semiconductors, in which the dominant charge carriers are electrons, are referred to as n-type semiconductors (donor doped), whereas those, in which holes are the majority charge carriers, are referred to as p-type semiconductors (acceptor doped).

Another very important concept used to describe the distribution of charges in solid state materials is the Fermi level [28]. The Fermi level is defined as the energy level where the probability of occupation by an electron is equal to 0.5. For metals at $T = 0$ K the Fermi level represents the energy level separating the occupied from unoccupied levels. In semiconductors, on the other hand, the occupied and unoccupied levels are separated by a band gap and for example, for an intrinsic semiconductor the Fermi level lies at the mid point of the band gap (Figure 2.2a on page 8).

However, the doping changes the distribution of electrons within the semiconductor, and hence changes the Fermi level. For n-type semiconductors the Fermi level lies just below the conduction band (Figure 2.2b on page 8), whereas for p-type semiconductors it lies just above the valence band (Figure 2.2c on page 8).

Depending on the doping level of the semiconductor the Fermi level can be situated within the band gap or within the valence or conduction band. In the former case the semiconductor is said to be non-degenerated, whereas in the latter it is degenerated.

As it will be discussed later in this chapter the Fermi energy is also influenced by the species in the electrolyte when the semiconductor is brought in contact with an electrolyte solution. In addition, the Fermi level of a semiconductor varies also with the applied external potential. For example, moving to more negative potentials will rise the Fermi energy level.

2.2 Electrolyte Solutions

Electrolyte solutions are ionic and not electronic conductors as the usual solids. Nevertheless, when discussing electrolyte solutions in contact with solids it is important to describe the ions in
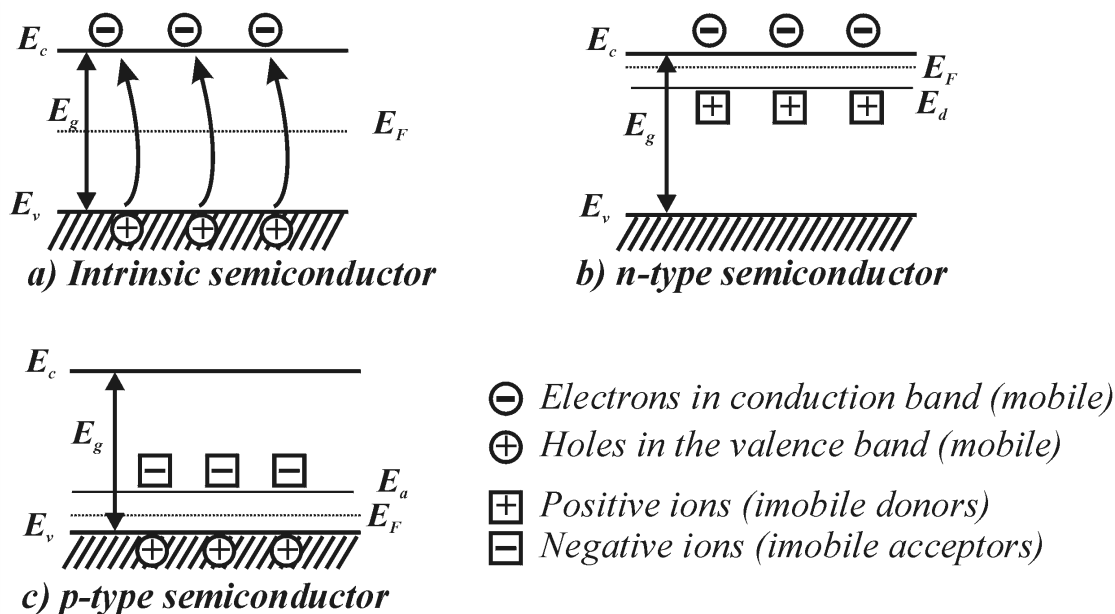
Figure 2.2: *The three types of semiconductors: a) Intrinsic semiconductors. They are perfect semiconductor crystals without any foreign atoms in the crystal lattice. In order for an intrinsic semiconductor to give rise to electrical conduction the electrons should be transferred from the valence band to the conduction band. The Fermi energy in such a semiconductor is in the middle of the electronic band gap; b) n-type semiconductors. These type of semiconductors are not anymore perfect and contain donor atoms (impurities) in their crystal lattice, i.e. the semiconductor is doped. The foreign atoms induce occupied donor levels near the conduction band within the electronic band gap. At room temperature nearly all donor levels are ionized. The Fermi level is near the conduction band; c) p-type semiconductors. Similarly, these type of semiconductors are also not perfect and contain foreign atoms in their crystal lattice but in this case the foreign atoms induce free acceptor levels within the electronic band gap near the valence band. At room temperature nearly all donor levels are occupied by electrons coming from the valence band; The Fermi level is near the valence band.*

solution with the same terms as the solids (semiconductors, metals etc.) are usually described, *i.e.* in terms of energy levels rather that 'chemical potentials' [29]. It should be noted that one of the main differences between the energy levels in electrolyte solutions and solids is that they are localized (on molecular orbitals of ionic species) and delocalized respectively.

The electronic energy levels of an ion or molecule in solution reflect the tendency of that species to release or to accept electrons when the *ion/molecule* approaches an electrode. Usually the species in solution have two or more oxidation states, for example K and K^+ or Fe^{2+} and Fe^{3+}. One of the oxidation states (*e.g.*, K) can donate and the other (*i.e.*, K^+) can accept an electron.

Unfortunately, the energy level model for solutions is by far more complicated as it is usually encountered in semiconductor physics. This is because the polar solvent which is surrounding the ions (for example water) has a great impact on their energy levels, *i.e.* the solvent affects the potential distribution at the location of the ion. More than that, the solvent obeys thermal fluctuations, therefore the potential at the location of the ion is also fluctuating and consequently the energy levels of the ions will fluctuate as well [30]. Although the energy of thermal fluctuations is small ($\approx kT$), the resulting changes in the levels energy are large, typically one electron volt. Thus, in solutions the electron energy levels must be described in terms of a probability

Figure 2.3: *Fluctuating energy levels in a polar solution. The ions in the solution which more easily can donate an electron than accept one are called reducing species. And vice versa, the ions which can accept an electron more easily than donate one are called oxidizing species. E_{red} is the energy level in solution associated with an electron that can be donated by a reducing ion; E_{ox} is the energy level in solution associated with a missing electron on an oxidizing ion where an external electron can be accepted. Due to polarization of the solvent the levels E_{red} and E_{ox} are not constant but fluctuate in time. $W(E)$ is the probability that the states E_{ox} and E_{red} have been moved to a certain energy E in solution. Similarly to solids, an effective Fermi level E_{redox}^o can be defined for solutions as well.*
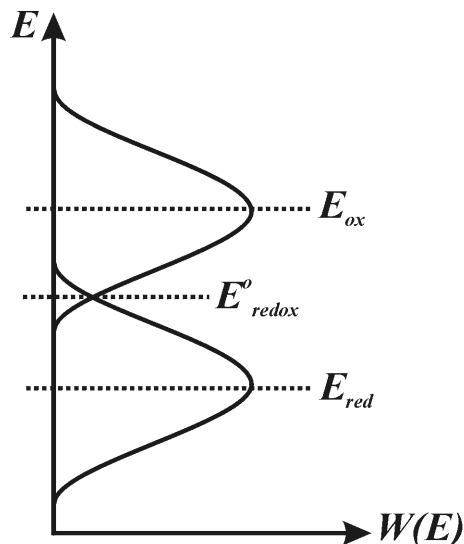
distribution.

The oxidation states of the ions in solution can be represented schematically as strongly fluctuating energy levels. In Figure 2.3 two oxidation states are shown. The species which prefer to donate an electron are called *reducing species* (E_{red}), those which prefer to accept an electron are called oxidizing species (E_{ox}). Pairs of reducing and oxidizing species are called redox couples. In Figure 2.3 gaussian functions centered at E_{ox} and E_{red} are sketched, which represent the probability distribution of the fluctuating energy levels in the electrolyte solution.

As it can be observed from Figure 2.3 the energy of the oxidizing and reducing species in solution are different. The electron transfer is subjected to the Frank-Condon principle. This means that the solvent molecules remain frozen during the transfer, however, after the electron was transferred *e.g.* from vacuum to Fe^{3+}, the resulted ion Fe^{2+} has a lower positive charge and the *ion-solvent* interaction is correspondingly weaker. The solvation shell will therefore relax to a new equilibrium distribution. Thus, the polarization energy arising from the interaction with the solvent effectively splits the electron energy levels of the oxidized and reduced species.

For a solution containing one dominant redox couple it is convenient to define an effective Fermi level E_{redox}, which is defined in such a way that at equilibrium the following relation is satisfied:

$$E_{redox}(solution) = E_F(solid) \tag{2.1}$$

where E_F is the Fermi energy of the electrode.

Thus E_{redox} is a property of solution and in order to find its actual value it is necessary to measure the influence of the solution on the electrode, *e.g.*, on E_F of the solid.

Of particular interest is the redox energy level of a redox couple when there are equal numbers of reducing and oxidizing species in the solution. In this case we will write the redox level as E_{redox}^o. The two redox levels, at different and equal concentrations of oxidizing and reducing species, are related by the following formula

$$E_{redox} = E_{redox}^o - kT \cdot \ln\left(\frac{[E_{ox}]}{[E_{red}]}\right) \tag{2.2}$$
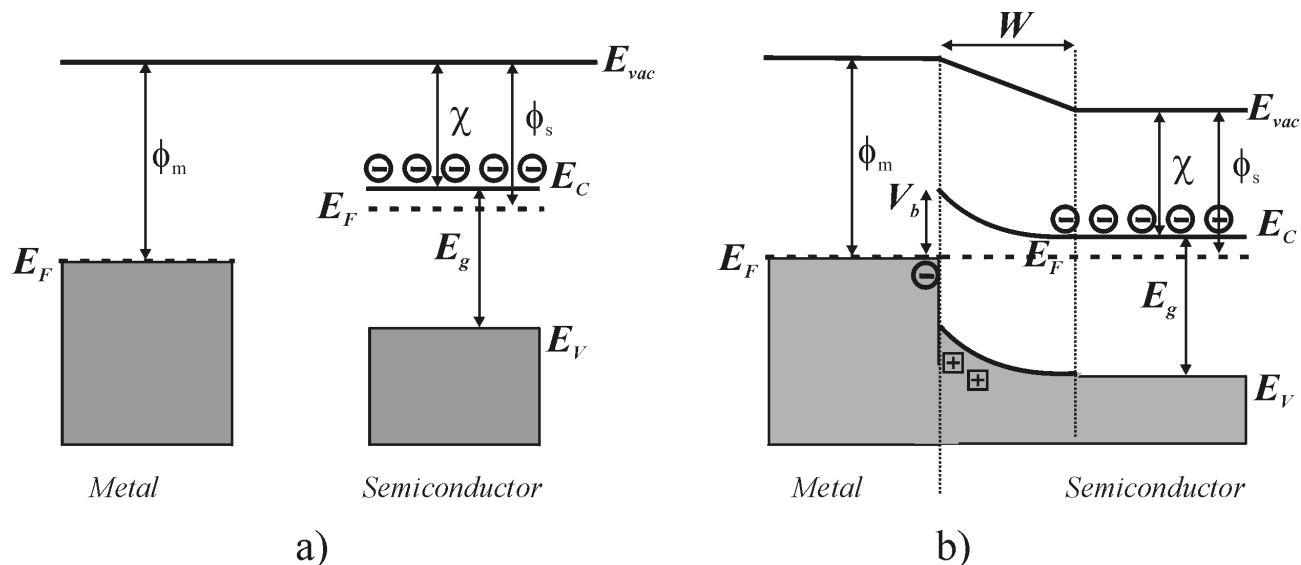
Figure 2.4: *a) A schematic representation of energy bands in a metal and a n-type semiconductor not in contact with each other. Note the different Fermi levels which will cause electrons to flow into the metal; b) A Schottky barrier formed at a metal-semiconductor junction. A region of uncompensated charged donors results in the semiconductor. This 'space charge' causes a voltage drop at the interface. Where χ is the electron affinity in the semiconductor; ϕ_m and ϕ_s are the work functions of the metal and semiconductor respectively;*

where $[E_{ox}]$ and $[E_{red}]$ are the concentrations (activities) of the oxidizing and reducing species respectively. Equation 2.2 is also known as *Nernst* equation. More than that, it is possible to demonstrate [31] that

$$E^o_{redox} = \frac{1}{2} \cdot (E_{ox} + E_{red}) \tag{2.3}$$

The Equation 2.3 is the fundamental definition of E^o_{redox} and is always valid, whereas the Equation 2.1 is valid only at equilibrium. Thus, for a single redox system with equal concentrations of oxidizing and reducing species, the redox energy level E^o_{redox} in solution is at half-way between the energy level of the oxidizing agent and the energy level of the reducing agent.

2.3 The Schottky Barrier

A Schottky barrier is one of the best known barriers in solid state physics. Due to its similarity to the *semiconductor/electrolyte* interface we will give some general notes about it.

A Schottky barrier is created by the intimate contact of a metal and a semiconductor. Figure 2.4 shows the situation of a Schottky barrier of a metal and a n-type semiconductor.

At equilibrium, in the absence of externally applied voltages, the Fermi level must be constant throughout the sample, since otherwise a current would flow. As it was already mentioned, in metals the Fermi level is the top of the electron sea, while in semiconductors, far from the interface, the Fermi level is determined ('pinned') by the doping levels. Before equilibrium, the Fermi level is higher in the semiconductor, *i.e.* the work function of the semiconductor, ϕ_s, is smaller than that of the metal ϕ_m), therefore, electrons will flow from the semiconductor into the metal. This causes the build up of charges on both sides of the interface, resulting in an electric field and

therefore a potential gradient according to Poisson's equation

$$\frac{\partial^2 V}{\partial x^2} = \frac{\rho(x)}{\varepsilon \varepsilon_0} \tag{2.4}$$

This potential leads to band bending. In this region, the electric field causes the electrons in the semiconductor to stay away from the semiconductor-metal interface. As a result in this region of width W there is a surplus of positive charge caused by uncompensated and fixed charged donor ions. This is called the 'space charge region' or 'depletion region', since there is an absence of majority carriers, *e.g.* electrons in n-type semiconductors.

The parameters that describe the Schottky barrier are:

- � V_b - Schottky barrier height. The barrier as seen by electrons coming from the metal. The typical values are between 0.4 - 0.8 eV depending on the metal and doping type of the semiconductor.

- ▛ W - depletion width. The width of the area depleted of majority carriers. The depletion width can be calculated from the doping profile.

For a Schottky barrier in forward bias a negative voltage is applied to the (n-type) semiconductor and a positive voltage to the metal. This will compensate for the band bending and thus diminish the Schottky barrier height.

The formation of the space charge region as well as the transfer of electrons over the interface in the case of a *semiconductor-electrolyte* junction is more or less similar to the case of the Schottky junction. In what follows we will describe in more detail the *semiconductor-electrolyte* junction.

2.4 Semiconductor-Electrolyte Junction

2.4.1 Space Charge Layer in Semiconductors of the SEJ

Without a "junction", *i.e.* transition region between two solids, modern microelectronics simply can not exist. The *semiconductor/semiconductor* or *semiconductor/metal* junctions are the active areas of diodes, transistors, lasers etc. Nevertheless the definition of a junction is wider and is not restricted only to solids. In the following we will have a look in more detail on the *semiconductor-electrolyte junction (SEJ)*, or otherwise saying *semiconductor-electrolyte interface (SEI)*, which is of paramount importance for all electrochemical processes.

Similarly to the case of a Schottky barrier described above, we now discuss the contact between a non-degenerated n-type semiconductor and an electrolyte (instead of metal), thus obtaining a *SEJ*. Assuming that the redox level E_{redox} of the electrolyte solution is lower than the Fermi energy E_F in the semiconductor, *e.g.*, the electrolyte contains strong oxidizing species, the electrons will pass the *SEJ* from the semiconductor into solution until the equilibrium is reached ($E_F = E_{redox}$). The electron transfer from the semiconductor into solution will cause the bands (valence and conduction) to move relatively to the Fermi level, *e.g.*, to bend upwards. This situation is presented in Figure 2.5. As it can be observed, the Fermi level will still remain within the band gap of the semiconductor.
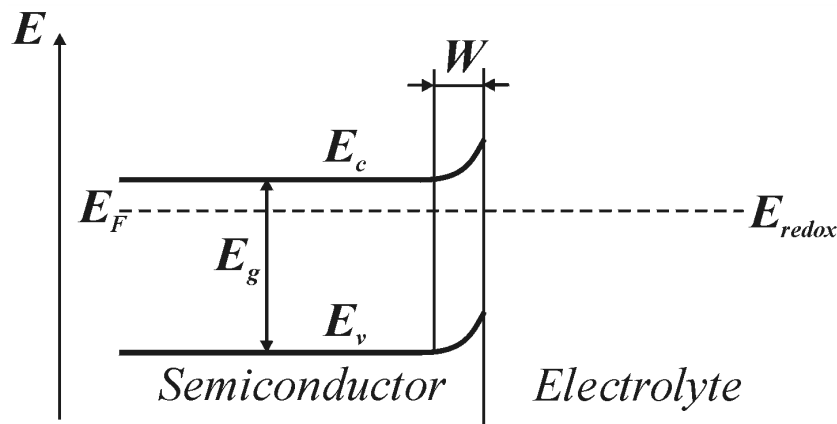
Figure 2.5: *A schematic representation of the energy diagram of the semiconductor-electrolyte junction. When a semiconductor is brought into contact with an electrolyte solution, a net charge transfer between them occurs until the equilibrium is reached. In the presented case it is more favorable for the electrons to move into the electrolyte. Therefore, an electron depleted region with the width W is formed in the semiconductor, which consequently leads to an upward bending of the valence and conduction band. The Fermi level in the semiconductor and E_{redox} in the solution are equal at equilibrium. Please note that in the electrolyte is shown only E_{redox}. E_{ox} and E_{red} levels are not shown for simplicity reasons.*

The region of the semiconductor in the immediate proximity of the *SEJ* where the bands are bend upwards contains less electrons than the bulk of the semiconductor. This depleted region similarly to Schottky barrier and p-n junction is again a 'space charge region' (*SCR*).

Generally, a *SCR* can consist of charged immobile donors or acceptors, or by mobile electrons or holes from the conduction and valence bands respectively (Debye layer). Accordingly, three main forms of a *SCR* layers for a n-type semiconductor can be formed:

▼ Depletion layer - made up of immobile dopant ions.

▼ Accumulation layer - made up of mobile electrons.

▼ Inversion layer - made up of mobile holes.

These three kinds of space charge layers are equivalent to the well known layers from the physics of semiconductor devices and are presented in Figure 2.6. From the electrochemical point of view they are important when an external voltage is applied to the *semiconductor-electrolyte* interface. They determine if the voltage will drop entirely on the semiconductor side, on the electrolyte side, or on both.

The main parameters of a *SCR* layer are the following:

▼ The distribution of the electric field E inside *SCR*. The so-called breakdown mechanism responsible for the hole generation during the electrochemical etching of III-V semiconductors is mainly determined by the electric field E in the *SCR*.

▼ The width W of the *SCR*. During pore formation $2 \cdot W$ is supposed to be the minimum width of the pore walls;
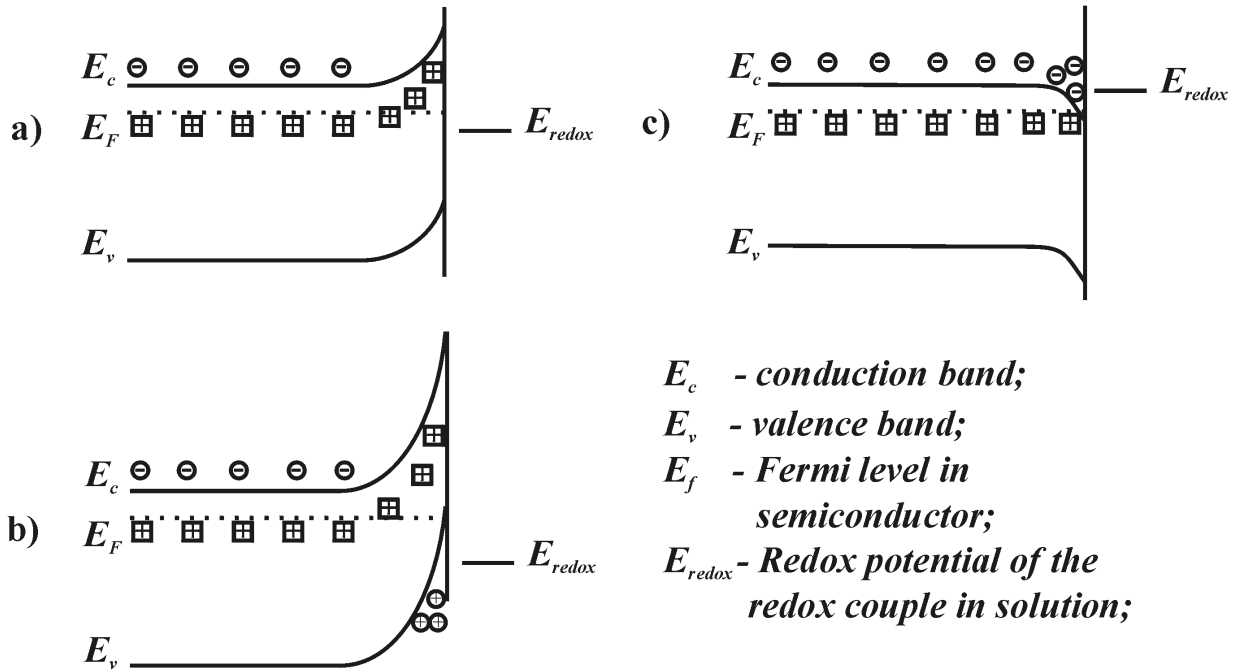
Figure 2.6: *Types of charged layers in n-type semiconductors. a) Depletion layer. Depending on the position of the valence and conduction bands relative to E_{red} and E_{ox} the electrons can move from or into the semiconductor. This figure presents the case when the electrons move easier into the solution than into the semiconductor. As a result a depletion layer in the semiconductor is formed. The charge of the depletion layer consists of immobile donor ions; b) Inversion layer. In the case when the transfer of electrons from the semiconductor to the solution is so strong that the number of electrons in a small region of the depletion layer near the interface is not anymore prevailing over the number of holes, an inversion layer can be formed. In other words, in such cases there is a region where the semiconductor is not n-type anymore but p-type, i.e. the Fermi level is near the valence band; c) Accumulation layer. This case is opposite to the case shown in a. The electrons move easier into the semiconductor than into the solution. As a result an accumulation layer is formed. The charge of the accumulation layer consists of mobile electrons.*

Both these parameters are decisive during pore formation in semiconductors.

If a depletion region is considered, then the charge density in the *SCR* layer is equal to $q \cdot N_D$, where N_D is the dopant concentration in the semiconductor. Therefore, the electric field inside this region is determined from the Gauss equation

$$\bigtriangledown E = \frac{q \cdot N_D}{\varepsilon} \tag{2.5}$$

where ε is the dielectric primitivity of the semiconductor, E is the electric field, and q is the magnitude of the elementary charge.

The width of the space-charge region (W) is related to the potential drop φ according to the following formula:

$$W = \sqrt{\frac{2 \cdot \varphi \cdot \varepsilon}{q \cdot N_D}} \tag{2.6}$$

As it can be observed, by decreasing the donor concentration the width of the SCR will increase. Anticipating the results, we can say that this is why the distance between pores in low

Figure 2.7: *The three double layers at the semiconductor-electrolyte interface on the example of aqueous solution of NaCl; Space charge region of a semiconductor dipped into a solution is a function of the doping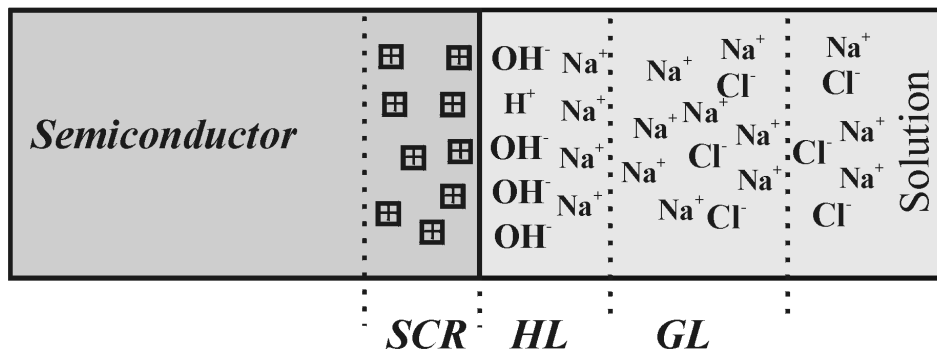 level of the semiconductor and surface states. The number of surface states, and thus the SCR, will be affected by their interaction with the ions in solution. An additional influence on the SCR will have the external voltage applied on the SEI. The width of the SCR can be in the range of 1000 Å, and consequently has a relatively small capacity; The Helmholtz double layer (HL) is considered to be formed by two planar sheets of charges. One is due to the ions in solution adsorbed at the surface of the solid (OH^- in our case), the other is due to the ions of opposite sign (Na^+) attracted by adsorbed ions. The HL can be in the range of 3-5 Å. Therefore its capacity is higher as compared with the capacity of the SCR; Gouy layer (GL) describes a region in the solution near the electrode within which there is a space charge due to an excess of free ions of one sign. The ions attracted to the outer HL do not suffice to compensate all the charges from the electrode surface, and the residual electric field directed normal to the surface results in a charged Gouy layer.*

doped samples is bigger than in high doped ones. Equation 2.6 is similar to the width of the space charge region for an one-side abrupt *semiconductor-semiconductor* p-n junction.

2.4.2   Helmholtz and Gouy Layers in Electrolyte Solutions

Besides the space charge region in the semiconductor, additional charged layers in the electrolyte solution are present when a semiconductor is brought into contact with an electrolyte solution.

Two different charged double layers in the electrolyte are distinguished at the *SEI*. They are the Helmholtz and the Gouy layers. In Figure 2.7 all three charged layers are present, including the *SCR* layer in the semiconductor.

The Helmholtz layer is in general composed of ions adsorbed at the surface of the semiconductor and ions of opposite signs attracted to the surface by the adsorbed ones. The adsorbed ions form the so-called inner Helmholtz layer, while the attracted ions form the so-called outer Helmholtz layer. Therefore, the Helmholtz layer is usually called also a double layer and can be regarded as a planar capacitor. The double Helmholtz layer at a *SEJ* has up to $N_A = 10^{15}$ ions per square centimeter which is decisive for its capacity. This is a very high value as compared with the immobile *donor/acceptor* ions in the space charge region ($N_D = 10^{12} \ cm^{-2}$).

Between the adsorbed (inner) and attracted (outer) layers there is a voltage drop V_H which is called the Helmholtz double layer voltage (Figure 2.8 on page 15). In aqueous solutions the adsorbed ions are usually H^+ and OH^-, with one of these dominating, depending on the pH value of the solution. When the number of adsorbed H^+ and OH^- species is equal, then the effective charge on the surface is zero. In this case the voltage drop across the Helmholtz layer V_H will be zero as well.
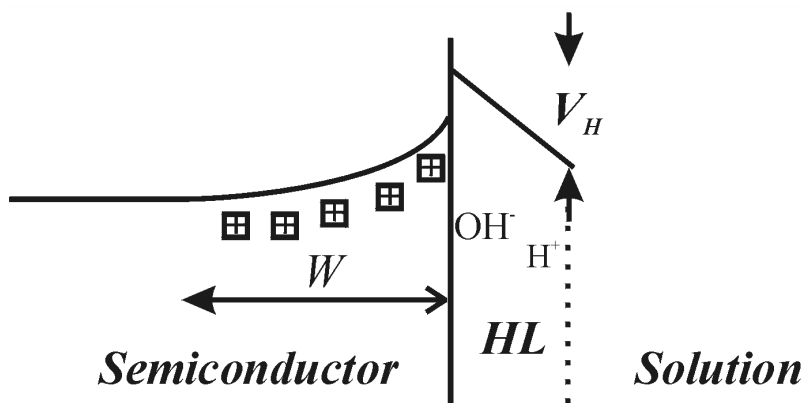
Figure 2.8: *A schematic energy band diagram of a solution in contact with a semiconductor where the most important layers at the semiconductor-electrolyte interface are shown: the Helmholtz layer and the space charge layer. It indicates how the electron energy could vary partly in the band bending region in the semiconductor, partly over the Helmholtz double layer. The positively charged donors are indicated by + and V_H is the Helmholtz double layer voltage.*

It is important to mention that the Helmholtz potential can depend on the applied external potential. However, the dependence is negligible when the *SCR* capacity is much smaller than the capacity of the Helmholtz double layer. This is true when the *SCR* is a depletion layer ($N_{adsorbed} \gg N_D$). For n-type semiconductors this is true at moderate positive external voltages applied to the semiconductor. In this case nearly all externally applied potential will drop in the *SCR* , and will not influence the Helmholtz potential.

On the other hand, V_H will not be independent of the externally applied potential when the capacity of the *SCR* will be of comparable values with the Helmholtz capacity. This is true when an accumulation or inverted space charge layer in the semiconductor is formed, *e.g.*, at negative or very high positive external voltages. In this case the semiconductor behaves like a metal and nearly all externally applied potential drops across the *HL*.

Usually the adsorbed charge on the surface of the semiconductor (*e.g.*, OH^- in Figure 2.7 on page 14) can not be compensated by the attracted ions (*e.g.*, Na^+), therefore a region with Na^+ as majority is formed outside the HL layer. This region is called the Gouy layer. The Gouy layer is usually not important unless very low concentrated electrolyte is used. Thus, the applied potential is considered to be distributed between the SCR and HL, depending on what kind of *SCR* is formed in the semiconductor.

2.5 Influence of Redox Couples on the Fermi Energy of the Electrode

As it was already mentioned the Fermi energy is a very important parameter for semiconductors as well as for electrolyte solutions. Namely the Fermi level is an 'indicator' showing how the energy levels are occupied by electrons. Due to charge exchange at the *SEI*, it is expected that the solution will influence the Fermi level of the semiconductor. We will consider this influence in what follows.

For two phases to be in equilibrium their electrochemical potentials must be the same. The electrochemical potential of a redox couple in solution is determined by E_{redox}, while the electrochemical potential of the electrons in the semiconductor is determined by the Fermi level E_F.

If the redox potential of the solution and the Fermi level are not at the same energy, a charge redistribution between semiconductor and solution is required in order to equilibrate the two phases. In order to find how the Fermi level of the electrode depends on the ions in solution we will define in a more rigorous way the chemical and electrochemical potentials.

For an ideal solution, the chemical potential of an ion i is described by:

$$\mu_i = \mu_i^o + RT \cdot \ln(c_i) \tag{2.7}$$

where c_i is the molarity of the solute.

For a real solution where *ion-ion* interactions are present the Equation 2.7 does not describe the chemical potential adequately, therefore a correction parameter to the molarity has been defined, and Equation 2.7 can be transformed into

$$\mu_i = \mu_i^o + RT \cdot \ln(\gamma_i \cdot c_i) = \mu_i^o + RT \cdot \ln(a_i) \tag{2.8}$$

where γ_i is the correction parameter to the molarity, $a_i = \gamma_i \cdot c_i$ is called the activity of the ion i.

It is important to note that the correction parameter is mainly determined by electrostatic, because in the case of a real solution the activity of ions, *e.g.*, the tendency of ions to react, is affected by the electrostatic forces due to the neighboring atoms.

The electrochemical potential of species is defined by means of the chemical potential as follows:

$$\bar{\mu}_i = \mu_i + Z_i \cdot F \cdot \phi \tag{2.9}$$

where $F = 96489 \, C/mole$ is the Faraday constant, Z_i is the charge of the ion and ϕ is the potential in volts. In what follows we will use the chemical and electrochemical potential to develop the expression for the Fermi energy of the electrode.

The general definition of the electrochemical potential is:

$$\bar{\mu}_i \equiv \left(\frac{\partial G}{\partial n_i} \right)_{T,p,n_{j \neq i}} \tag{2.10}$$

where G is the Gibbs free energy and n_i is the concentration of the i species. Equation 2.10 supposes that the temperature, pressure and concentrations of other species than i are kept constant.

As it was already mentioned above, a very useful feature of the electrochemical potential is that it stays constant at equilibrium in all contacting phases:

$$\bar{\mu}_i = const. \tag{2.11}$$

In addition, for a reaction in equilibrium like the following one

$$a_1 B_1 + a_2 B_2 = a_3 B_3 + a_4 B_4 \tag{2.12}$$

where B's are the species in reaction and a's are integers, the rate of reaction in both directions must be equal. It can be shown that at equilibrium the electrochemical potentials of the reactants and products are related by:

$$a_1 \bar{\mu}_1 + a_2 \bar{\mu}_2 - a_3 \bar{\mu}_3 - a_4 \bar{\mu}_4 = 0 = \triangledown G_{equilibrium} \tag{2.13}$$

Now lets consider a reaction where an electron is exchanged between an electrode and a redox couple B_1/B_2.

$$a_1 B_1 = a_2 B_2 + ne^- \tag{2.14}$$

We can write according to Equation 2.13

$$a_1 \bar{\mu}_1 = a_2 \bar{\mu}_2 + n\bar{\mu}_e \tag{2.15}$$

where $\bar{\mu}_e$ is the electrochemical potential of the electrons in the electrode, which is nothing else but the Fermi energy of the electrode.

Thus using Equation 2.15 we get for the Fermi level in the solid

$$\bar{\mu}_e = \frac{1}{n} (a_1\mu_1 - a_2\mu_2) - F\phi_{sol} = F \cdot E'_B - \frac{RT}{n} \ln\left(\frac{a_{B2}^{a2}}{a_{B1}^{a1}}\right) - F\phi_{sol} \tag{2.16}$$

where

$$n = a_2 Z_{B2} - a_1 Z_{B1}, \tag{2.17}$$

$$E'_B = \frac{1}{F \cdot n} (a_1\mu_{B1}^o - a_2\mu_{B2}^o), \tag{2.18}$$

and ϕ_{sol} is the potential in solution. In order to obtain the Equation 2.16 we substituted the Equations 2.8 and 2.9 in the Equation 2.15.

Taking into account that the electrochemical potential is measured in *joule/mole* and the Fermi energy in *volts/electron* we can write

$$E_F = \frac{q\bar{\mu}_e}{F} = qE'_B - \frac{kT}{n} \ln\left(\frac{[B_2]^{a2}}{[B_1]^{a1}}\right) - q\phi_{sol}. \tag{2.19}$$

In the Equation 2.19 the activities have been substituted by concentrations of the corresponding species. E'_B is a property of the redox couple B_1/B_2 and reflects the tendency to inject or extract electrons from the electrode.

Thus, the Fermi level in the electrode is determined

� First by the properties of the redox couple (E'_B);

▶ Second, by the relative concentration of the reducing and oxidizing agents in solution;

▶ Finally, by the potential applied to the solution reflecting our choice of the zero potential.

From Equation 2.19 it is easy to observe that E'_B is difficult to estimate, because μ_i^o is not so easy to determine (see the Equation 2.18). What is relatively easy to measure is the difference of Fermi levels of two electrodes, one in contact with one redox couple A_1/A_2 and the second electrode in contact with another redox couple B_1/B_2, and where ϕ_{sol} is constant through the solution. According to Equation 2.19 the measured voltage difference between these two electrodes will be

$$-qV_m = E_{F1} - E_{F2} = qE'_A - \frac{kT}{n_A} \ln\left(\frac{[A_2]^{a_{A2}}}{[A_1]^{a_{A1}}}\right) - qE'_B + \frac{kT}{n_B} \ln\left(\frac{[B_2]^{a_{B2}}}{[B_1]^{a_{B1}}}\right). \tag{2.20}$$

In order for the Equation 2.20 to have a practical use, one redox couple is taken to be standard and is defined as a reference redox couple. Thus, V_m of other redox couples are measured relative to

this reference redox couple. Namely, the hydrogen couple (H^+/H_2) is usually chosen as reference redox couple, and its corresponding E_{redox} energy level is chosen as the arbitrary zero.

Therefore, if an arbitrary couple is tending to inject electrons into an electrode stronger than the hydrogen couple, this redox couple will have a negative redox potential, and *vice versa* if the hydrogen redox couple is tending to inject electrons into an electrode stronger than an arbitrary redox couple, then the redox potential of this redox couple will be positive.

Thus, if in Equation 2.18 the couple B_1/B_2 will be considered to be the H^+/H_2 and the concentrations of hydrogen species are equal $[H^+] = [H_2]$ or in other words, the activities of the hydrogen species are considered to be a unity, then Equation 2.20 becomes

$$-qV_m = E_{F1} - E_{F2} = q \cdot (E'_A - E'_{ref}) - \frac{kT}{n_A} \ln \left(\frac{[A_2]^{a_{A2}}}{[A_1]^{a_{A1}}} \right). \tag{2.21}$$

Now if we consider the Fermi energy of the electrode in contact with H^+/H_2 to be our zero reference and consequently we set $E_{ref} = E_{F2} = 0$ then we obtain

$$E_{F1} = qE^o - \frac{kT}{n_A} \ln \left(\frac{[A_2]^{a_{A2}}}{[A_1]^{a_{A1}}} \right). \tag{2.22}$$

Equation 2.22 gives the value of the Fermi energy of an electrode, which is in direct contact to a redox couple A_1/A_2, relative to the hydrogen reference electrode. In the Equation 2.22 was introduced the parameter $E^o = E'_A - E'_{ref}$ which is called 'the standard redox potential' of the redox couple A_1/A_2 and is tabulated in handbooks. As a definition for the standard redox potential of a redox couple A_1/A_2 can be taken the following formulation:

> ◤ The standard redox potential of a redox couple A_1/A_2 is the potential measured relative to the hydrogen reference electrode when the redox couple A_1/A_2 is present is solution at unit activity (*i.e.* in Equation 2.22 the logarithm is zero).

The measurement setup that is mainly used to determine the standard redox potential of a redox couple (see Figure 2.9 on page 19) consists of an electrochemical cell with two compartments. In one compartment are H^+/H_2 species in contact with a metal, which is the reference redox couple at standard conditions. The second compartment contains the redox couple for which the standard redox potential shall be measured, for example Cl_2/Cl^- at unit activities, also in contact with a metal. In order to have a constant potential throughout the solution a salt bridge is used, which is blocking the passage of active species, but passes current by the flow of inert ions, which has negligible effect on the potential. Having these requirements satisfied the voltmeter is measuring the voltage with respect to the reference redox couple which can be considered as the "ground". The voltage measured by the voltmeter is the standard electrode potential of the Cl_2/Cl^- redox couple.

Thus, the standard redox potential of a redox couple is showing the tendency of this couple to inject or to extract electrons from a solid. If the couple is tending to inject electrons into the solid then the standard redox potential will be negative, if the couple is tending to extract electrons then it will be positive.

However, it should be noted that the physicists when dealing with *solid/gas* interfaces usually take as an energy reference the energy of an electron at infinity (E^e). The chemists or better saying electro-chemists take as an energy reference the Fermi energy of the hydrogen electrode under
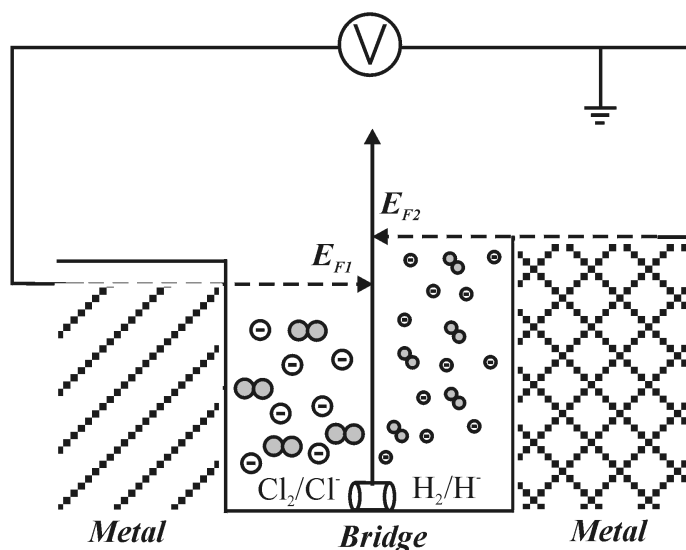
Figure 2.9: *A schematic illustration of the principle for measuring the standard redox potential. In our case the redox couple is Cl_2/Cl^-. The installation contains a double room cell, where in one of the rooms a metal in contact with the solution of interest at unit activity is present, whereas in the second one we have a metal in contact with a hydrogen containing solution at standard conditions. The two rooms communicate electrically by means of a salt bridge. The voltmeter is measuring the difference in potential on these two metals. The measured value is actually the standard electrode potential of the redox couple. Thus, the zero of energy is the Fermi level of the metal in contact with hydrogen under standard conditions.*

standard conditions as described above. In order to have a clear picture of the solids immersed in solutions it is required to have a relation between these two reference energies. Several derivations of the relation between the two zeros of the energy have been proposed up to now. The results show that the hydrogen reference electrode is below E^e by around 4.5 eV [32, 33, 34].

Taking into account that the energies on the hydrogen scale are measurable quantities and are available in handbooks, it is advisable to use this scale.

2.6 Metals and Semiconductors from the Electrochemical Point of View

From the electrochemical point of view, semiconductor electrodes in contact with electrolyte solutions behave very different in comparison to metal ones [31]. The semiconductors can be considered unique for the electrochemistry not only for their capabilities of practical use but also for providing rapid improvement in the basic understanding of the main subject of electrochemistry, *i.e.* the charge transfer through the *electrode-electrolyte* interface. This is based on some characteristic properties of semiconductors when they come in contact with electrolytes.

The first feature is that the energies of conduction and valence band at the interface are fixed, *i.e.* they move only slightly relative to the energy levels of the ions in the electrolyte, since most of the applied potential drops on the semiconductor. This means that if the band edges are favorable for electron transfer to or from a redox couple, the transfer will occur independently of the applied voltage. Certainly this is true only if the surface is clean and no oxides which can hinder the charge

transfer are present.

The second special feature of semiconductor electrodes in redox reactions is the ability to control the band (valence or conduction) in which the reacting carrier will be transfered. These unique properties of semiconductor electrodes allow to measure the characteristics of ions in solutions and to define the steps of an electrochemical reaction with facilities not atainable with metal electrodes.

Thus, semiconductors can allow for a better understanding and control of the processes that play a major role in modern *IC* technology [35, 36] and also allow the prediction of new features which may be used for fabrication of novel semiconductor structures.

2.7   Summary and Conclusions to Chapter 2

Solids and solutions conduct electricity in quite different ways - via *electrons/holes* and ions respectively. In order to investigate the *solid-solution* contacts, a mutual conduction model is required. Thus, the energy level model successfully applied for solids is extended also for electrolyte solutions. One of the major differences is that the energy levels in electrolyte solutions are localized on molecular orbitals of ionic species whereas in solids the energy levels are delocalized. Similarly to the solids, also for solutions a so called Fermi energy level can be defined. The Fermi energy level in solutions is situated in the middle of the so-called oxidized and reduced energy states. As in the case of a *solid-solid* contact, at equilibrium the Fermi energy in the solution is equal to that in the solid.

At a *semiconductor-solution* interface three double layers are distinguished: the space charge region in the semiconductor, the Helmholtz and the Gouy layers in solution. At moderate external voltages (positive or negative depending on the type of semiconductor), applied on the *semiconductor-solution* interface, the whole voltage drop occurs on the space charge layer in the semiconductor. This is the main difference between *metal-solution* and *semiconductor-solution* interfaces. In the case of metals, the external voltage drop occurs on the Helmholtz layer. However, in special cases it is possible to reach conditions where the *semiconductor-solution* interface is behaving like a *metal-solution* one.

From the electrochemical point of view the redox couples are characterized by the so-called standard electrode potential. If the redox couple injects electrons into the solid more efficiently than the hydrogen redox couple, then this redox couple is said to have a negative standard redox potential. If the opposite is true then the redox couple is said to have a positive redox potential.

All these notions are very important in order to predict the behavior of a semiconductor immersed into an electrolyte and we will take them into account for pore formation in III-V semiconductors.

Chapter 3

Chemical and Electrochemical Etching of III-V Semiconductors

3.1 Anisotropy of III-V Compounds

Anisotropic etching is of great importance for semiconductor structuring and is mainly caused by the differences in etching rates of low indexed crystal surfaces. The reasons for this behavior are not yet completely understood.

For the anisotropic etching the geometrical properties of the crystal lattice play an important role. In a nutshell, the crystal structure of III-V compounds is the following:

� They crystallize in the cubic zinc blend lattice (with the exception of nitrides).

▰ The crystal consists of two cubic, surface-centered sublattices being shifted relative to each other by the translational vector $\left[\frac{1}{4}\frac{1}{4}\frac{1}{4}\right]$.

▰ Each sublattice is occupied by one kind of atoms, *i.e.* from III-rd or V-th group (see Figure 3.1a).

The usually investigated low indexed crystal surfaces are {111}, {110} and {100}. Each set of planes has its distinct dissolution behavior. One of the reasons for the dissolution differences of different crystallographic planes could be the density of atoms in these crystallographic planes (high density = low dissolution rate).

However, this is not the only factor determining the anisotropy. In III-V compounds an additional factor contributing to the anisotropy is related to different chemical properties of the atoms from the third and the fifth groups of the periodic table of elements.

For example, along ⟨111⟩ directions, atomic planes are occupied alternatively by atoms from the third and fifth groups forming double layers, *i.e.* alternately short and long distances exist between {111} planes (Figure 3.1b). Each atom has 3 bonds within the same double layer and one bond outside the double layer. The surfaces terminated by Ga or In atoms are called {111}A (or {111A}), whereas those terminated by As or P atoms are called {111}B (or {111B}). It is important to note that in nearly all oxidizing electrolytes {111}A facets show the slowest rate of dissolution [37]. This can be explained assuming that the three bonds (within the same double layer) are much more difficult to brake from the A side than from the B side, due to the fact that the electronic cloud of one bond is polarized towards the B atom (more electronegative).
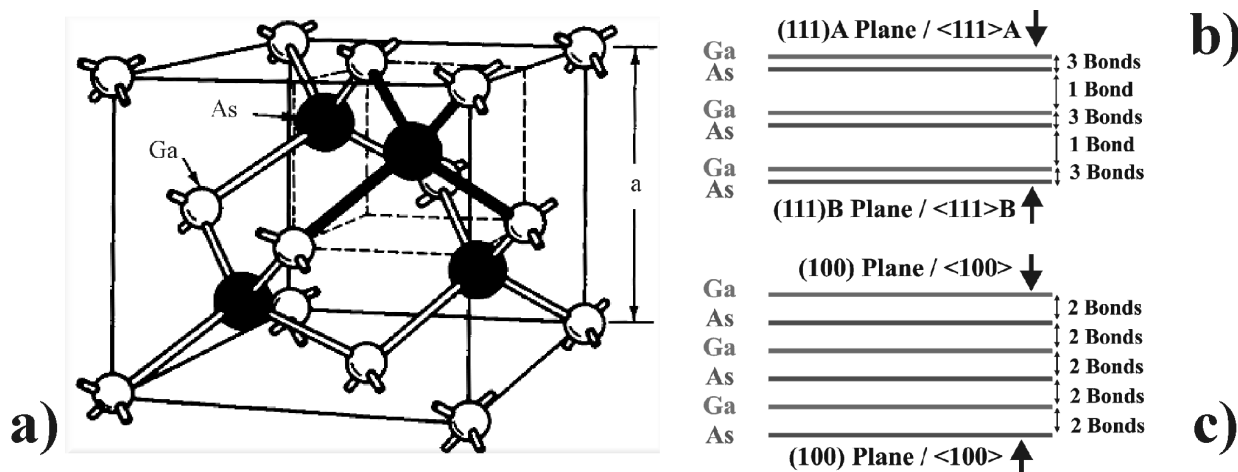
Figure 3.1: *a) GaAs cubic zinc blende crystal structure. The crystal consists of two cubic, surface-centered sublattices shifted relatively to each other by the translational vector (see text). This structure is characteristic also for other III-V semiconductors like InP, GaP, InAs etc., but not for nitrides like GaN which have a wurtzite structure; b) The double layer structure along* ⟨111⟩ *B directions; c) The equidistant layers along* ⟨100⟩ *directions.*

Let's assume that in order to brake a bond from the B side it is needed an average time t_1, whereas from the A side the time $t_2 \gg t_1$. Thus, in order to remove a double layer from the B side we have to spend the time $3t_1 + t_2$, whereas from the A side the total time $3t_2 + t_1$. It is easy to realize that $3t_2 + t_1 \gg 3t_1 + t_2$. As a consequence, it is much faster to etch from the B side (along ⟨111⟩B directions) than from the A side (along (⟨111⟩A directions).

On the other hand, along ⟨100⟩ directions the atomic planes are also occupied alternatively by atoms from the third and fifth groups. However, the planes are equidistant and each atom is symmetrically bonded with neighboring layers (2 and 2 bonds). Thus, the time needed to etch two layers from the A side is $2t_2 + 2t_1$, whereas from the B side $2t_1 + 2t_2$. As a consequence, in this case there is no difference from what surface the etching will take place, because the average time is equal (Figure 3.1c) .

3.2   Chemical Etching of III-V Semiconductors

Chemical etching is basically a process used to remove selectively controlled amounts of material from the substrate. The etch depth can be designed to be just tens of angstroms or up to a few hundred of micrometers. Concerning the fabrication of microelectronic devices, the etching process is one of the most important stages. Errors at this stage will severely impair the performance of devices. More than that, due to the present disadvantages of dry etching, among which is the need for specialized and expensive equipment, wet chemical and electrochemical etching will still be unavoidable for some time [38].

Non-oxidative chemical etching is a potential-independent dissolution and does not involve exchange of free charge carriers between the solid and solution. This concept was introduced for III-V compounds by Gerischer *et al* [39, 40]. They suggested that during a purely chemical etching process a synchronous bond-exchange occurs. As a results the bonds between the atoms in the solid broke and new bonds are formed with reactive molecules in the electrolyte. Such a process
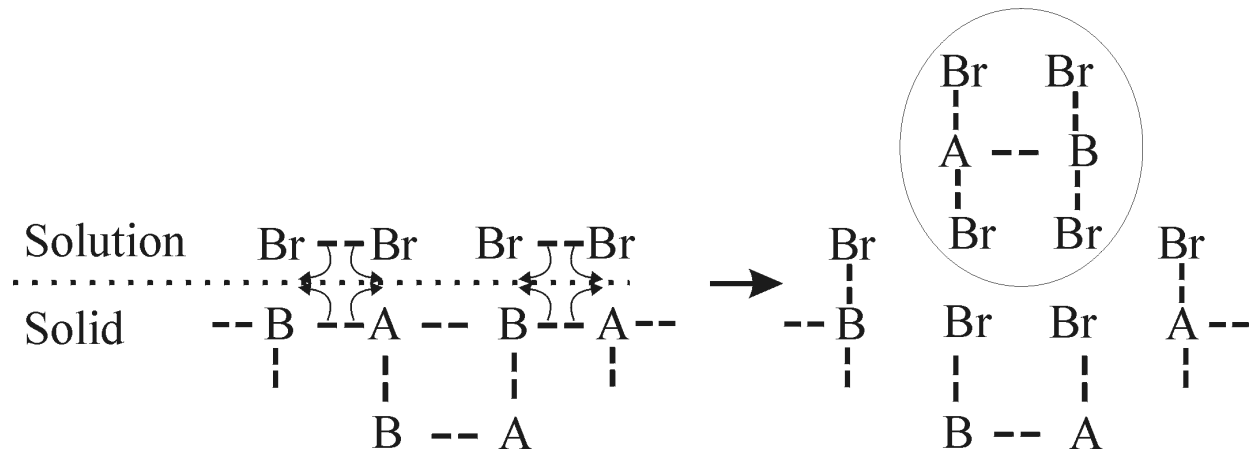
Figure 3.2: *A schematic representation of the model proposed by Gerischer et al for chemical etching of III-V compounds. No free charge carriers are involved in the process. According to this model the chemical decomposition of the semiconductor proceeds via synchronous bond-exchange steps. This mechanism holds for some non-oxidizing chemical enchants such as undissociated HBr, HCl, Br_2 molecules, whereas the oxidative chemical etching is more complex.*

is shown schematically in Figure 3.2.

In order to etch chemically a III-V compound according to the Gerischer model it is necessary to have a non-oxidizing chemical enchant such as undissociated *HCl, HBr, Br_2 etc.* molecules [39]. These molecules should be capable to brake the III-V bonds and consequently to saturate the resulting dangling bonds. Therefore, the chemical etching rate depends strongly on the concentration of undissociated molecules. It is well known that the number of undissociated acid molecules (*HCl, HBr*) increases in aqueous solutions by increasing the concentration of the acid. On the other hand, the number of undissociated molecules can be also increased by using a solvent like acetic acid instead of water. Consequently, in such cases the chemical etch rate is also strongly increased.

A chemical (dissolution) reaction is usually divided in some slow and quick reaction steps. The slowest step in the whole process is the rate determining one. For example, during the chemical reaction of $GaAs$ in H_2O_2 solutions, the braking of a $Ga - As$ bond, which is followed by the formation of $GaOH$ and $AsOH$ bonds, is the rate-determining step. The subsequent steps are much faster than the first one, therefore they do not contribute much to the overall rate of a chemical (dissolution) reaction.

For pore formation purposes, chemical etching can be used as a pre-anodization treatment, *e.g.* for the generation of randomly or uniformly distributed defects at the surface of the sample, in order to improve the nucleation stage of the pore formation process. Pyramid-like pits on Si formed by means of lithography and chemical etching in KOH solutions are a good example for a controlled generation of surface defects.

It is important to note that chemical etching can also significantly influence the electrochemical etching (see the next subchapter) of III-V semiconductors [41]. This should be taken into account when choosing the concentration of the electrolyte for electrochemical etching. By increasing the concentration of acid in solution, the number of undissociated acid molecules increases as well, and thus the chemical etch reaction can proceed parallelly with the electrochemical, which is normally

not desired during a pore formation process.

3.3   Electrochemical Etching

Electrochemical etching can be divided in two different processes:

    � Electroless etching.

    ▸ Anodic etching.

In contrast to the Gerischer model for pure chemical etching, in both cases of electrochemical etching, charge exchange is required at the interface of the semiconductor with the electrolyte.

3.3.1   Electroless Etching

Electroless etching is usually also-called the electrochemical oxidation without an external potential. In order to perform such kind of etching, strong oxidizing species are required which are able to *inject/extract holes/electrons into/from* the valence band of the semiconductor. Thus, redox couples with a high positive standard electrode potential are required and for effective etching the electronic energy distribution function of the oxidizing species must overlap with the valence band of the solid.

An illustration of this process is presented in Figure 3.3. The redox couple Ce^{4+}/Ce^{3+} can be strong oxidizing for GaP, GaAs as well as for InP. Fe^{3+}/Fe^{2+} is strong oxidizing only for GaAs, whereas all the other considered redox couples can not be used in electroless processes for any of the presented III-V compounds.

The mechanism of electrochemical oxidation is usually divided in two partial reactions:

    ▸ Injection of holes into the valence band (extraction of electrons). The holes will be trapped at *SEI* and bond braking will take place.

    ▸ Consequently, the broken bonds will be attacked by nucleophilic species like OH^- resulting in material dissolution.

The two steps involved in electroless etching (injection-dissolution) are separated from each other in time. Due to this separation it is possible to suppress the first step and thus the second one (dissolution) will be stopped as well.

Here is a relevant example. In spite of the fact that Ce^{4+}/Ce^{3+} is a strong oxidizing agent for InP, electroless etching of InP in Ce^{4+}/Ce^{3+} containing solutions does not occur. This can be explained taking into account that the surface of InP is always covered with a native oxide. The native oxide is mainly formed by In_2O_3, which is a wide band gap semiconductor ($E_g(In_2O_3) = 3.5\ eV$). The concentration of phosphorus compounds is reduced in the native oxide due to its high vapor pressure. Assuming that the conduction band of InP crystal and the conduction band of the In_2O_3 oxide are nearly on the same level, the valence band of In_2O_3 is nearly 2 eV lower that the valence band of InP. Consequently, the Ce^{4+}/Ce^{3+} is not a strong oxidizing agent for In_2O_3 (no holes can be injected) as it is for InP itself. Thus, the native oxide acts as a protective layer for the bulk InP against electroless etching and hinders the hole injection process (first step) into the valence band of InP.
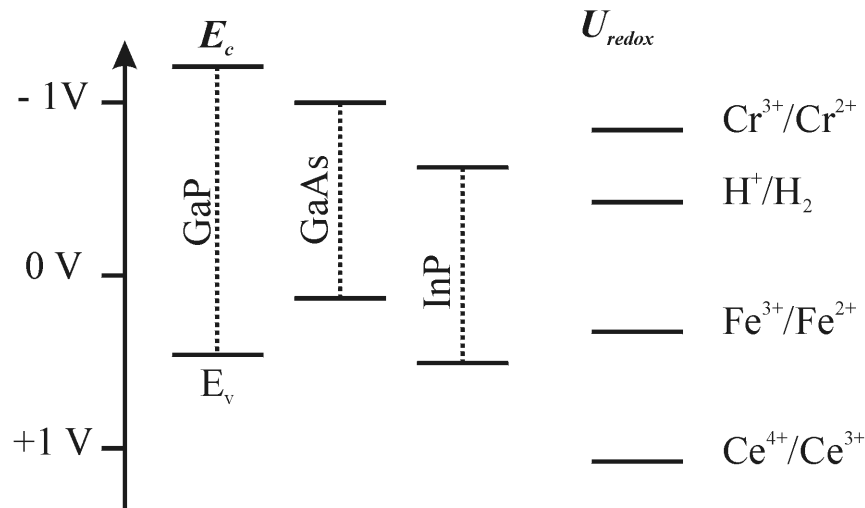
Figure 3.3: *Position of the energy bands of GaP, GaAs and InP with respect to standard redox potentials of some redox couples, measured relative to a standard calomel electrode in acid solution, pH=0 [42]. A change in the pH value has no effect on the redox potential but has a marked effect on the potential difference across the Helmholtz layer, resulting in a shift of the flatband potential. The flat band potential decreases by about 60 mV per pH unit. This means that at pH of 14 the bandedge potentials of semiconductors are shifted to more negative potentials by about 0.84 V as compared to pH = 0. This fact can transfer redox couples, not suitable for electroless etching in acid solution, to suitable oxidizing species in alcaline electrolytes.*

3.3.2 Anodic Etching

When applying a bias which forces the electrons to go from the solution into the electrode the process is called anodic (the holes go towards the interface). On the other hand, if they move from the electrode into the solution the process is called cathodic (the holes go away from the interface).

Anodic etching, similarly to the electroless etching, requires holes in order to take place. A high number of holes at the surface will induce dangling bonds. Similarly to electroless etching, the dangling bonds will react with nucleophilic molecules (such as OH^-) in the electrolyte. If all the bonds of an atom from the solid will be replaced by bonds with nucleophilic molecules, a new compound will form (atom of the solid + nucleophilic molecules). The new compound has no or less direct chemical connection to the solid. If this compound is soluble in the etching medium, then it can dissolve purely chemically and thus the surface of the sample will be free and ready for the next interaction with nucleophilic species in solution. This way, anodic etching of the electrode occurs [24].

Otherwise, i.e. if the newly formed compound is not soluble in the solution medium, a thin oxide layer will form on the surface of the electrode, which will hinder the electrochemical attack to proceed. For this reason the electrolytes supposed to be suitable for electrochemical etching should contain two main components:

� Nucleophilic (*i.e.* reducing) species.

▰ Oxide-dissolving species.

In general, for n-type semiconductors the holes necessary for anodic etching can be generated by avalanche breakdown mechanism, *i.e.* applying a sufficiently high positive potential to the electrode. Or alternatively by illuminating the semiconductor with photons having energies larger than the semiconductor electronic band gap. In the next two subchapters front and back side illumination processes, as well as breakdown mechanism will be explained shortly.

3.3.3   Front and Back Side Illumination

Two arrangements for hole generation via illumination exist:

▸ Front side illumination (*FSI*).

▸ Back side illumination (*BSI*).

With front side illumination, the *SEI* is illuminated directly by a light source and holes are generated closely to where they are consumed, *i.e.* at the illuminated surface. Uniform illumination leads to a uniform hole generation, which usually results in a uniform dissolution of the semiconductor (the so-called electropolishing process). Therefore, *FSI* is typically used only during the nucleation process of pores, whereas during the pore growth process illumination is switched off. However sometimes, pronounced pores may be formed also using front side illumination during the pore growth process [43, 44, 45].

When the so-called 'backside illumination' is used [46], the back side of the wafer, *i.e.* relative to the side where anodization takes place, is illuminated. Consequently the holes are generated far away from the region where the chemical reaction takes place, *i.e.* at the front side surface. Therefore, the holes have to diffuse from the back to the front side of the wafer in order to participate in the reaction. In this case, pore formation will be favored because the holes coming from the back side will be focused mainly at the tips of the pores. For the back side illumination process to be effective, the diffusion length of the holes must be high enough to allow at least some of the back side generated holes to reach the *SEI*. Back side illumination is extensively used for pore formation processes in n-type Si, which has diffusion lengths for holes in the range of some hundreds of micrometers.

Unfortunately, back side illumination is not applicable for III-V compounds. Simply because III-V compounds have small diffusion lengths for holes and electrons, *i.e.* in the range of some tens of nanometers, which is much too small for typical wafers with thicknesses between $500-600 \ \mu m$.

3.3.4   Breakdown Mechanism

As it was already mentioned, applying a positive potential to a semiconductor wafer will cause the positive charge carriers to drift towards the *SEI*. Using n-type samples in the dark (no back or front side illumination), the number of holes (anodic current) reaching the *SEI* will be small due to the fact that holes in n-type semiconductors are minority carriers. However, the anodic current remains low only for a small range of electrode potentials. At higher potentials a steep current increase is usually observed. This high anodic current passing through the *semiconductor-electrolyte* interface is supposed to be related to avalanche processes in the space charge region.

Avalanche breakdown is initiated by a small number of electrons (Figure 3.4, process 1) tunneling from the valence to the conduction band. If the field strength (inside the *SCR*) is high enough,
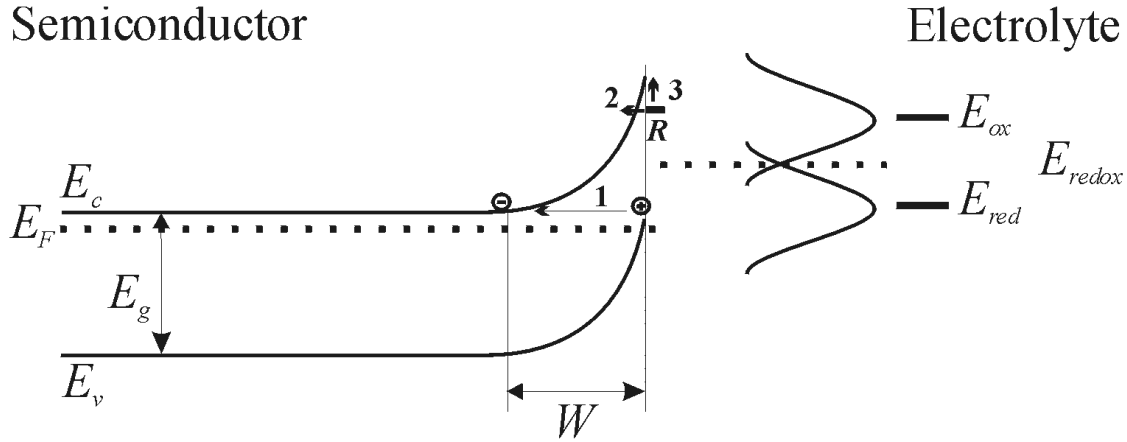
Figure 3.4: *The band diagram of the semiconductor-electrolyte interface explaining the breakdown mechanism when a positive voltage is applied to the sample. There are three possibilities to generate holes necessary for dissolution: 1) direct electron tunneling from the valence to the conduction band. As a result of the direct valence-conduction band tunneling incomplete bonds with energy levels within the band gap can form. These incomplete bonds can be further oxidized in two modes; 2) by tunneling of the second electron again into the conduction band or 3) by exiting the electron into the conduction band as a result of thermal fluctuations. All the electrons which reach the conduction band by these mechanisms are then accelerated by the electric field within the space charge region. If the electric field is high enough they can generate more electron-hole pairs. This multiplication of holes is called the avalanche mechanism.*

the tunneled electrons can gain such a high energy that on their path from the *SEI* towards the bulk they will generate new electron-hole pairs by means of the avalanche mechanism.

It should be noted, that the oxidation intermediates (R in Figure 3.4) produced by the initial tunneling process (process 1, Figure 3.4) can be regarded as surface states with an energy level above the valence band edge, *i.e.* within the band gap. These intermediates are highly reactive and can be oxidized by injection of an electron into the conduction band by thermal excitations (process 3, Figure 3.4) or again by tunneling (process 2, Figure 3.4).

Usually, a localized avalanche mechanism is assumed to start at surface defects, dislocations *etc.* New electron-hole pairs are generated as soon as breakdown starts and thus etching around the defect will occur. The etching process induces new surface defects, *e.g.* pits, and the avalanche breakdown can occur at lower externally applied potentials as before [47]. Thus the presence of defects determines the avalanche breakdown and consequently the anodic current.

The holes generated by the avalanche mechanism will drift towards the *SEI* and as explained earlier, the semiconductor will dissolve. It is generally accepted that in order to dissolve a III-V couple, for example one unit of Ga-As, six holes are necessary according to the following formula:

$$GaAs + 6h^+ \rightarrow Ga^{3+} + As^{3+} \tag{3.1}$$

The holes will generate six incomplete bonds which can be saturated by E_{red} from the electrolyte (Figure 3.4). However, if it is assumed that the GaAs substrate will not dissolve in pairs but atom by atom, then eight holes will be required to dissolve a Ga-As unit. This fact was observed experimentally [48] as well. Thus, depending on the etching conditions six or eight holes are needed for dissolving a Ga-As pair of atoms.

It is important to note that avalanche breakdown in III-Vs is not so evident for electrolytes with neutral pH values. In this case any initial avalanche event localized at one of the defects (*process ON*), is immediately followed by oxide formation. The local resistance then is increased and etching at the defect stops (*process OFF*). More than that, the local avalanche breakdown can also stop after a short period of time in any kind of electrolytes, not only in neutral pH solutions. The electrolyte and/or the semiconductor will quench the avalanche breakthrough due to diffusion losses or nonlinear ohmic effects. As we will see in the following chapters, the current burst model developed for explanation of pore formation in semiconductors is based on such a *ON-OFF* mechanism.

3.4   The Field Strength of a Curved Surface

From what was said above it is clear that dissolution will start at defects, where as a result a crater will be formed. Because the whole surface of the crater is full of surface defects it can be expected that the dissolution velocity will be equal along all directions oriented perpendicularly to the surface of the crater (see Figure 3.5). However, this is not always the case and dissolution usually will take place only at the bottom of the crater. Two reasons for this behavior can be identified.

� Crystallographic features of the substrate,

▼ The enhanced electric field at a curved surface;

Crystallographic features will be discussed in the next chapter. In what follows we will discuss how the curvature of the surface influences the electric field within the space charge region, namely by increasing the local electric field. An increased electric field leads to an increased number of generated holes, and thus to higher rates of dissolution at curved surfaces, assuming that enough reducing species are present in the electrolyte and the reaction products are easily dissolved and transported away.

For an interface with a spherical shape (Figure 3.5) the Poisson equation can be written in the following form:

$$\frac{1}{r^2}\frac{d}{dr}\left[r^2\xi(r)\right] = \frac{\rho(r)}{4\pi\epsilon_0\epsilon} \tag{3.2}$$

where ϵ_0 is the permittivity of vacuum, ϵ is the dielectric constant of the substrate, $\xi(r)$ is the electric field, $\rho(r)$ is the charge density in the space charge layer, equal to $-qN_D$ for $r_0 < r < r_d$, N_D is the ionized donor density, q is the elementary electric charge, r_0 is the radius of the curvature of the interface, $r_d - r_0$ is the width of the space charge layer. Using the boundary conditions and the depletion approximation [49], the relation between the potential, the electric field, the width of the space charge layer, and the radius of curvature can be obtained as follows [50]:

$$V(x + r_0) = \frac{qN_D}{24\pi\epsilon_0\epsilon}\left[(x + r_0)^2 + \frac{2(x_d + r_0)^3}{x + r_0} - 3(x_d + r_0)^2\right] \tag{3.3}$$

and

$$\xi(x + r_0) = \frac{qN_D}{12\pi\epsilon_0\epsilon}\left[-(x + r_0)^2 + \frac{2(x_d + r_0)^3}{(x + r_0)^2}\right] \tag{3.4}$$
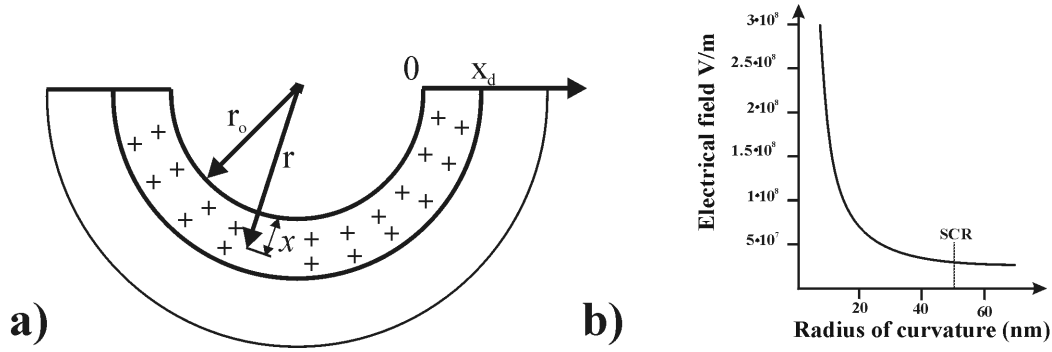
Figure 3.5: *a) A schematic SEI of spherical shape with r_0 representing the radius of curvature and x_d the width of the space charge region [49]; b) Dependence of the electrical field strength on the radius of curvature. The plot was done for $x = 0$, a doping level of $N = 10^{18}$ cm^{-3}, a SCR width of 50 nm and an $\epsilon = 12$. For example the breakdown field for InP is in the range of $5 \cdot 10^7$ V/m. Thus, for a radius of curvature of 60 nm the electric filed is too small for breakdown. On the other hand, for a radius of curvature smaller than 30 nm the the electrical field approaches the critical breakdown voltage.*

assuming $r = x + r_0$. The plot of the electrical field strength, as a function of the radius of curvature, according to Equation 3.4, is presented in Figure 3.5b. As it can be observed, the field strength of a curved surface increases considerably when the radius of the curvature is close to, or smaller than the width of the space charge layer of a flat surface. This means that the field at the pore bottom must be strongly increased due to this effect as compared to the pore walls where the radius of curvature is nearly infinite.

The radius of curvature has also an important effect on the energy band diagram. The potential drops more sharply from the surface to the bulk for a small radius of curvature. The width of the space charge layer is considerably reduced and the field in the space charge layer is strongly increased. The steep band bending due to decreasing the radius of curvature increases also the number of energy levels for electron tunneling. In this way the number of generated holes will be also increased and thus the dissolution process will be favored to take place at pore tips rather than at pore walls.

3.5 Current Voltage Characteristics

Current (I) voltage (V) characteristic, *i.e.* the IV curve, provide a simple method to find the basic properties of a junction. The IV curves of solid state devices reflect purely electronic properties of the junctions. IV measurements of the *semiconductor/electrolyte* junction, while still containing information about the electronic state of the semiconductor, in addition reflect the chemical reactions which determine the kinetic of the anodic dissolution. This makes the IV characteristics of *semiconductor-electrolyte* junctions far more difficult to interpret. However, due to the fact that the main features of the IV-curves are related to pore formation it is necessary to mention their main features here.

Under anodic conditions p- and n-type III-V materials behave quite differently. They show a diode behavior. The forward current direction needs positive (anodic) bias in the case of p-type doping, and negative (cathodic) bias in the case of n-type doping. For instance, in the case of p-
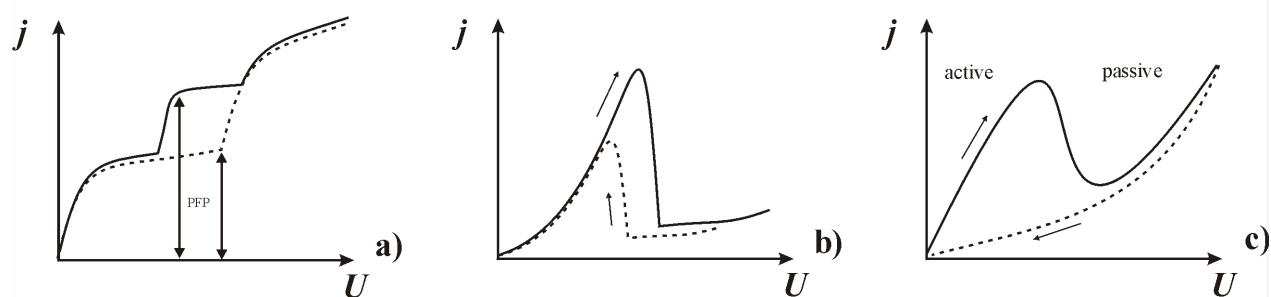
Figure 3.6: *A schematic representation of the IV curves for a) GaAs (in H_2SO_4 solutions), b) GaP (in H_2SO_4 solutions) and c) InP (in HCl solutions).*

GaAs substrates in acidic solutions, the current in the anodic direction rises rapidly to very high values (in excess of 100 mA/cm^2 at 1V) causing electropolishing of the material. In the cathodic regime the current remains relatively low [51]. In what follows we restrict ourselves to anodically biased n-type III-V's.[1]

The reverse current in n-type III-V compounds increases steeply when increasing the voltage, and pits are formed on the surface as soon as a critical potential, the so-called pore formation potential (PFP), is reached (see Figure 3.6a). The pore formation potential is also-called the breakdown potential. It occurs usually at 2-3 V for moderately doped samples. Schmuki *et al* measured the current-voltage curves of samples with intact and diamond-scribe scratched surfaces. The scratched samples showed a PFP significantly lower than the PFP of the intact sample. These results demonstrated that the PFP depends on the number of defects on the surface of the sample, namely it decreases as the number of defects increases. The PFP thus can be viewed as the defect-triggered onset of some kind of junction breakdown in areas of locally large electrical field strengths as discussed in subchapter 3.3.4.

In contrast to n- GaAs, Tjerkstra *et al.* [52] reported for n- GaP (in H_2SO_4 aqueous electrolytes) that the current does not increase strongly after the PFP has been reached, but goes through a maximum at a more positive potential. After that the current decreases rapidly to a lower value, which shows only a week potential dependence. Such peaks are usually related to oxide formation making current flow difficult. Since the formed oxide has to be dissolved before current can flow again, the peak voltage depends on the voltage scan rate and the IV curves show a hysteresis, see Figure 3.6b. The region on the IV-curves before and after the peak are usually called active and passive anodization regions respectively. Similar results, *i.e.* the hysteresis and an evident peak in the IV-curve, have been reported by Kaneshiro *et al.* for InP in HCl electrolytes (Figure 3.6b), which were also attributed to oxide formation.

As we will see later, oxide formation plays a very important role in the formation of the so-called current-line oriented pores. Thus, such kind of pores can be intuitively considered to be obtained in the regime of passive anodization. On the other hand, the so-called crystallographically oriented pores show very strong crystallographic features and according to the current burst model

---

[1]A word of warning is necessary: The current through cathodically biased III-V compounds does not always produce just H_2 (as in the case of Si) - in the case of InP, for example, extremely poisonous PH_3 might be generated. If an electrochemical double cell is used, the sample backside is necessarily in the cathodic regime and extreme care is necessary in conducting experiments.

direct dissolution should be dominant (see section 3.6 on page 31). Thus, the crystallographically oriented pores can be considered to be obtained in the active anodization region.

3.6 Current Burst Model and III-V Compounds

The most fundamental questions about pore formation is why and how do pores grow? Different models (most of them developed for Si) have been proposed, trying to answer these and other questions. The current burst model (*CBM*) is one of them. In contrast to other models, *CBM* assumes that the processes which take place at nanometer scale during the dissolution, *i.e.* at nearly atomic level, are similar for all semiconductors, whereas the macroscopic behavior of different electrodes is determined by the interaction (in space and time) of these nanometer events. This allows the current burst model to have a high prediction power for different semiconductors.

The first phenomenon explained by the *CBM* were the *current/voltage* oscillations observed during the electropolishing of Si [53, 54, 55]. The *CBM* predicted oscillations also for the pore formation regime. Indeed, recently oscillations in the pore formation regime have been observed experimentally, first in III-Vs [56] and later in Si [57].

The general assumptions of the *CBM* are the following:

▸ A mechanism for a local oscillator is required. These local oscillators are called 'current bursts'.

▸ A synchronization mechanism (between current bursts) must exist in order to see macroscopic electrode oscillations.

▸ A desynchronization mechanism is required as well, otherwise electrodes would either oscillate strongly or not at all.

A current burst is assumed to be composed of four main steps: direct dissolution, oxide formation, oxide dissolution and surface passivation (see Figure 3.7). The repetition of these steps in time will result in a local *ON/OFF* oscillatory behavior of the current. These implies that charges are mainly flowing through a current burst during direct dissolution and oxide formation (*ON*), whereas no or little charge is flowing (*OFF*) during oxide dissolution and passivation.

The synchronization between the current burst is due to oxide overlapping of neighboring current bursts, *i.e.* the surrounding current bursts will contribute with their oxide bumps to the oxide bump of a newly nucleated current burst. This way its stopping point is already much closer to the stopping point of the surrounding current bursts, because it has to produce less oxide as if it would have been alone without neighbors.

A desynchronization mechanism is also needed for a realistic model. Once a current burst starts, the current density is locally increased, leading to increased ohmic and diffusion losses, which locally reduces the potential across the oxide layer. This reduces the electric field strength in the neighborhood of an active current burst, and therefore reduces also the probability for nucleation of a new current burst next to an active current burst [53].

Due to the fact that the nucleation of current burst is a stochastic process, it can happen that the oxide of an old current burst is completely dissolved but no new current bursts nucleated meanwhile in its place. In such a case the surface will start passivating. The nucleation probability will depend on how strongly the new surface was passivated by different species from the solution,
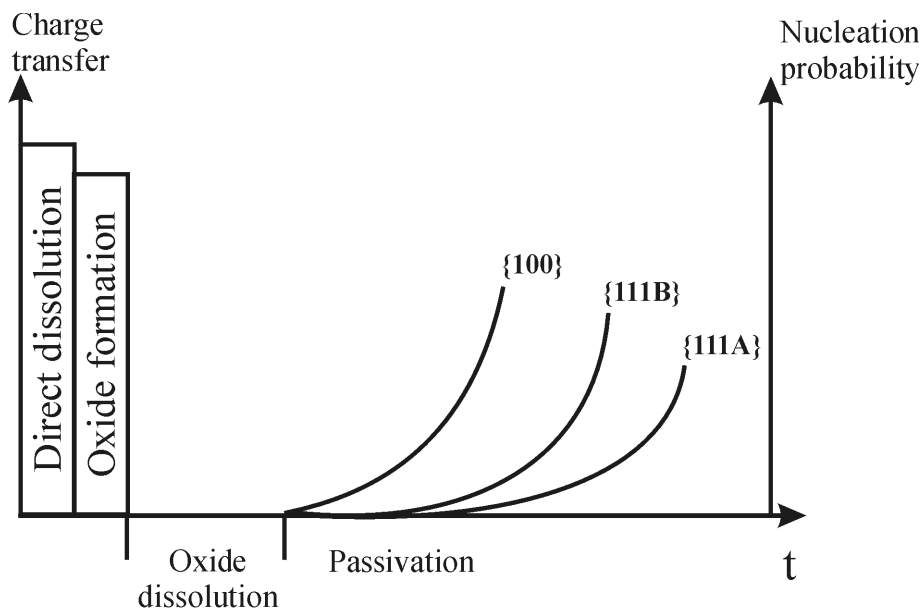
Figure 3.7: *Sequence of events in a current burst: Charge transfer for direct dissolution is followed by oxidation; these are fast processes. The dissolution of the oxide is slow for Si and quick for III-Vs and so is the (hkl dependent) H- passivation and OH- passivation respectively. Sometime and somewhere - depending on the external system parameters and the microscopic conditions - a new current burst nucleates.*

i.e. the higher the passivation the lower the probability that a current burst will nucleate on this surface. The passivation of the surface in time is called "aging".

Since the nucleation probability is larger for smaller degrees of passivation, and passivation in turn is minimal just after the oxide is removed, there is an intrinsic coupling of new current bursts to old ones. This will result in clusters of current bursts, which as one possible consequence, will lead to pore formation.

Passivation in this context means the removal of mid-gap states. In III-V compounds the dissolution process is divided in several reaction steps. After the first reaction step a high density of mid-gap states is generated [39]. If these mid-gap states are easily passivated by the species in solution then the next reaction steps can not occur and dissolution will stop. In other words, the probability for current burst nucleation will decrease if passivation will be increased.

In most cases in Si and III-V compounds {111} surfaces passivate faster that {100} surfaces and thus are more difficult to dissolve [58, 59]. However, in III-V compounds there is a difference in passivation even within the {111} set. Namely {111}A (Ga or In terminated surfaces) are passivated easier (more rapidly) than {111}B (As or P terminated surfaces). This particularity has a great influence on the porous morphologies obtained in these materials (see the nucleation mechanism described in section 5.1). Thus there is a strong tendency to nucleate new current bursts on {100} rather than on {111} Si, and on {100} or {111}B rather than on {111}A in III-V's (see Figure 3.7). The surface is passivated by hydrogen in the case of Si, and by OH^- or Cl^- in the case of III-V compounds [60].

Each of the processes, *i.e.* direct dissolution, oxide formation, oxide dissolution and passivation, are consuming charges and time. For Si, the ratio between the oxide-dissolution-time (*large*) and

charge-transfer-time (*small*) is much higher than for III-V compounds. This is mainly caused by the small dissolution time (low quality) of III-V oxides. Mathematically this can be described as:

$$\frac{t_{ox.-diss.}}{t_{ch.-tr.}}(Si) \gg \frac{t_{ox.-diss.}}{t_{ch.-tr.}}(III - V's) \qquad (3.5)$$

The very long time constant for oxide dissolution in Si is the decisive factor for the large scale difference of macropores in Si ($1-5~\mu m$) and III-Vs ($100-200~nm$). Thus, the size (and morphology) of pores is given by the dominating length scales of a particular system.

Combining all charge and time consuming processes, it is possible to write an average current density for one current burst i_{CB}:

$$i_{CB} = \frac{Q_{dir.-diss.} + Q_{ox.-form.}}{t_{ch.-tr.} + t_{ox.-diss.} + t_{pass.}} \qquad (3.6)$$

where $Q_{dir.-diss.}$ is the charge consumed during the direct dissolution process; $Q_{ox.-form.}$ - charge consumed for oxide formation; $t_{ch.-tr.}$ - time required for charge transfer (both $Q_{dir.-diss.}$ and $Q_{ox.-form.}$); $t_{ox.-diss.}$ - time required for oxide dissolution; $t_{pass.}$ - time left for passivation before a new current burst starts on the same place;

The shape and growth velocity of the pores depend on the processes that will dominate the current of a current burst: direct dissolution or dissolution via oxide formation.

The direct dissolution part of a current burst has the following properties:

� The valence of dissolution is higher as compared with dissolution via oxide formation.

▮ Strong preference for nucleation on {100} and {111}B surfaces.

▮ Preferred reaction at high field strength (including carrier generation by avalanche effects, always true for III-V's).

▮ Depends on passivation kinetic.

▮ If dominant, produces 'dendritic pores' (or 'break-through pores', 'fractal pores', octahedron pores, tetrahedron pores, etc.).

On the other hand, the oxidation part of a current burst has the following properties:

▮ It is a rather isotropic process.

▮ Driven by electrochemistry, *i.e.* potential at interface.

▮ Preferred reaction at high potentials and surplus of holes if sufficient O^- is available.

▮ If strong compared to direct dissolution, it produces 'macropores' with not very pronounced directionality.

Macropores are formed if the direct dissolution part and the oxidizing part of a current burst are balanced within some limits depending on the system. If the system looses this balance, *e.g.* the supply of holes (or reactants) decreases, a critical point may be reached where the pore morphology changes suddenly. A relevant example is the switch from crystallographically oriented to current-line oriented pores in InP and GaP (see Chapter 5).

So far, pores were discussed as a consequence of current bursts correlated (or synchronized) in space. It was implicitly assumed that there is no correlation in time between the pores. The correlation in time was assumed only between the current bursts. There is no particular reason why a correlation in time between the pores should not exist.

Relevant examples for time correlation between pores are the macroscopic oscillations observed in InP, GaP, and Si (see Chapter 6.2 and 6.5). As it was explained above, the synchronization mechanism responsible for the correlation in time between current bursts is the overlapping of the oxide bumps. For pore correlation in time, the synchronization mechanism is provided by the overlapping of the space charge regions of the pores.

3.7   Summary and Conclusions to Chapter 3

The anisotropy of III-V compounds is influenced by the different chemical properties of the atoms from the third and the fifth groups of the periodic table of elements.

The etching of semiconductors can be divided into two main types: chemical and electrochemical. According to Gerischer *et al.*, chemical dissolution does not involve charge exchange between the semiconductor and the electrolyte, but simultaneous bond exchange between the atoms of the solid and those in solution takes place.

On the other hand, electrochemical etching involves charge exchange between the solid and the solution. Electrochemical etching is also divided in two categories: electroless and anodic etching. In contrast to anodic etching, electroless etching does not require external voltages, but strong oxidizing species in the solution are needed. Often no differences are made between chemical and electroless dissolution, nevertheless it is important to distinguish between these two types of etching.

Anodic etching is mainly responsible for pore formation and requires holes. The usual supply of holes in n-type Si is provided by back side illumination. Backside illumination is not applicable to III-V compounds due to the short diffusion lengths of holes in these materials. The only way for generating necessary holes (in the dark) for pore formation in III-V's is the break down mechanism.

The IV-curves of the III-V/electrolyte junctions show a diode behavior and strongly depend on the density of defects on the surface of the sample.

The "current burst" is a general model and can be successfully applied to other semiconductors like III-Vs and Ge and not only to Si as was initially developed. The main assumption of the current burst model is that the current on the surface of the electrode is changing in time and space. The competition between direct dissolution and dissolution via oxide formation is the primary factor determining the pore morphology and the time constants of the system.

Chapter 4

Experimental Setup

4.1 Electrochemical Cells

The most simple experimental setup for performing electrochemical experiments has the following elements:

▌ Three electrodes immersed into an electrolyte.

▌ A battery.

▌ A voltmeter.

▌ An amperemeter.

The electrode, which has to be studied, is called the working electrode (*WE*). The second electrode, which is closing the circuit, is called the counter electrode (*CE*). The third one, used to measure the voltage between the electrolyte and the *WE*, is called the reference electrode (*RE*). A schematic representation of such a simple experimental set up is presented in Figure 4.1a on page 36.

As we have already discussed, when a current is flowing thought a *solid-electrolyte* interface, chemical reactions occur at the interface. Electrons leaving the solid will reduce species in solution, whereas electrons moving into the solid lead to the oxidation of species in the solution. Due to chemical reactions at the interface the composition of the electrolyte near the surface of the solid will change and thus the distribution of the voltage across the double layers at the *semiconductor-electrolyte* interface will vary as well. This is especially true for high current densities. For this reason, in order to maintain a constant composition of the solution near the sample, *i.e.* the working electrode, continuous pumping of the electrolyte is necessary.

In such a simple system there are two important junctions: *WE/electrolyte* and *CE/electrolyte*. Therefore, assuming that the voltage losses in the bulk of the solid and electrolyte are negligible the potential controlled by the battery and applied to the system will be distributed as follows:

$$U = U_{WE} + U_{CE} \tag{4.1}$$

where U_{WE} and U_{CE} are the voltage drops on *WE/electrolyte* and *CE/electrolyte* junctions respectively.
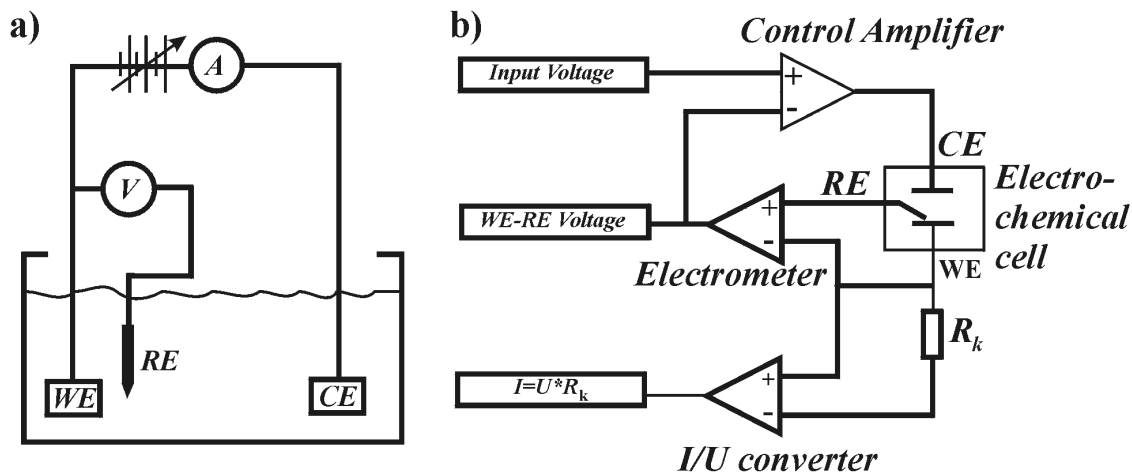
Figure 4.1: *a) The simplest experimental set up for performing electrochemical experiments. The set up contains a working electrode (WE), a counter electrode (CE) and a reference electrode (RE) immersed into electrolyte solution. WE and CE are connected to a battery. An amperemeter is measuring the current of the cell, whereas a voltmeter is measuring the U_{WE} voltage. The only controlled voltage in the system is that supplied by the battery and it is not possible to control directly the WE-RE voltage. To accomplish this a feedback device like a potentiostat is used instead of the battery; b) A schematic representation of a three electrode potentiostat. Generally the main difference between a battery and a potentiostat is that the potentiostat has an intern feedback and can keep the WE-RE potential constant.*

In practice, however, the setup presented in Figure 4.1a is not always satisfactory. In many cases we wish to fix, *i.e.* to control, the voltage (U_{WE}) between the sample and solution, and consequently to measure the resulting current change. Taking into account that the current will stimulate electrochemical reactions also at the *CE/electrolyte* interface, it can be expected that the state of the counter electrode, *i.e.* U_{CE}, will vary in time. Consequently, the instability of U_{CE} will influence the value of U_{WE} due to the fact that their sum should be equal to the voltage supplied by the battery. Thus, controlling the voltage U supplied by the battery, *e.g.* setting it constant as indicated in Figure 4.1, does not assure that the voltage of interest, *i.e.* measured between the sample and the reference electrode (U_{WE}), will stay constant as well.

The first thing to do in order to avoid this problem is to decrease somehow the value of U_{CE} in such a way that $U_{CE} \ll U_{WE}$. The logic behind is that a negligible value of U_{CE} will have a negligible influence on U_{WE}. This can be done by choosing a counter electrode with a relatively high area $A_{CE} \gg A_{WE}$. In this case the resistance of *CE* will be much smaller than the resistance of *WE* and consequently the condition $U_{CE} \ll U_{WE}$ can be satisfied. In this case it is possible to neglect in Equation 4.1 the value of U_{CE} and the result will be

$$U = U_{WE} \tag{4.2}$$

Thus, Equation 4.2 states that the potential applied by the battery will drop entirely on the WE/electrolyte junction. This is actually what is needed to control U_{WE} by controlling the value of U. Nevertheless, choosing a *CE* with a large area is not always a good solution. The influence of U_{CE} on U_{WE} will again be significant when appreciable current densities will flow though the system. As we will see later, for pore formation in III-V compounds very high current densities
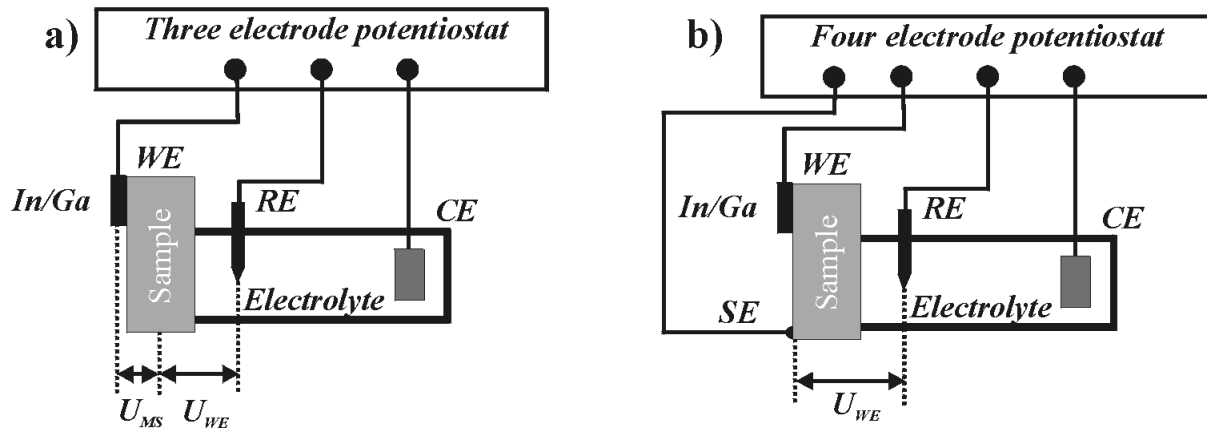
Figure 4.2: *a) A schematic representation of a setup with a three electrode potentiostat. The configuration of the setup is similar to that presented in Figure 4.1 on page 36. The battery is replaced by a potentiostat. The potentiostat, by means of a feedback mechanism, has the possibility to measure and control directly the voltage of interest, namely U_{WE}. In spite of the fact that it has also some disadvantages, it is a much better tool for electrochemical experiments than a simple battery. b) A schematic representation of a set up with a four electrode potentiostat. The voltage desired by the user is measured between SE and RE. Now the contact SE/sample is not critical because no current is flowing through it. Such a four electrode configuration was used in all experiments presented in this work.*

are usually required. Therefore some additional improvements of the set up are required.

The solution to all these problems is the potentiostat, which allows to control the voltage between the working electrode and the reference electrode directly. The working principle of a potentiostat is shown in Figure 4.1b. A potentiostat is a three or a four electrode device (see Figure 4.2). The desired voltage shown between the reference electrode and the sample is provided as the input voltage. The actual WE-RE voltage is measured by a differential amplifier (Electrometer in Figure 4.1b) and is compared with the input voltage by a second differential amplifier (Control Amplifier). In case there is a difference between the input voltage and the WE-RE voltage the control amplifier will increase/decrease the voltage to the cell until the actual and the input voltage are equal. The I/U converter measures the cell current and forces it to flow through a current measurement resistor, R_k. The voltage drop across R_k is a measure of the cell current. The cell current in an anodization experiment can often vary by several orders of magnitude. It is impossible to measure current over such a wide current range using a single resistor. Therefore, a number of different R_k resistors can be used. The potentiostat used in our experiments has 9 resistors (5K, 2K, 1K, 500, 200, 100, 50, 20, 10 Ohms). This allows measurements of widely varying currents (from 0.01 mA to nearly 1A), where each current range is measured using an appropriate resistor. Measurement of small currents requires large R_k values and vice versa. However, the problems do not stop here. A three electrode potentiostat solves the problem as long as the contact between the sample and the working electrode is good enough.

However, if the ohmic resistance between the *WE* and the sample is not insignificantly small, *e.g.* when using *In/Ga* alloy, a four electrode potentiostat must be used (Figure 4.2b). The fourth electrode is called the sense electrode (*SE*) and is connected to the sample. Now, the potentiostat can be regarded as being composed of two 'independent' subsystems. One containing the *WE*

and *CE* electrodes through which the current flows and the second containing the *SE* and *RE* electrodes which measures the potential. A feedback interaction between these two subsystems results in an ideal tool for controlling electrochemical processes. In this configuration the contact between the sense electrode and the sample is not critical because no current is flowing through it. Now the desired potential will be exactly applied on the *sample/electrolyte* junction.

However, during the pore formation process the quality of the contact between the sample and the working electrode is still very important. It determines how uniform the current is distributed across the whole surface of the sample. If the contact is not uniform the distribution of the current, and consequently the porous layer, will not be uniform.

A significant improvement of the uniformity of the backside contact can be achieved by a liquid contact, *i.e.* the sample has two electrolyte junctions. The first junction (the front side) will be the one of interest and where the pores will grow. The second junction will play the role of an uniform backside contact. On both junctions electrochemical reactions will take place. If at the front junction an anodic reaction takes place, then at the back contact a cathodic reaction will occur.

The experiments in the present work have been carried out in a Teflon electrochemical double cell presented in Figure 4.3 on page 40 using a four electrode configuration:

� A Pt reference electrode in the electrolyte.

▸ A Pt sense electrode on the sample.

▸ A Pt counter electrode in the electrolyte (in the front side room of the cell).

▸ A Pt effective working electrode in the electrolyte (in the back side room of the cell).

The Teflon rooms of the double cell are mounted on four metallic rods along which they can easily slide. The sample is mounted between the two rooms and by means of four clamping bolts a 'sandwich' *room-sample-room* is safely fixed. Two *O-rings* on both sides of the sample are used in order to obtain a good adhesion of the sample with the Teflon rooms and thus to prevent the leakage of the electrolyte.

It is well known that the technology of crystal growth of III-V compounds is much more expensive as compared to Si. Therefore, the wafers of GaAs, InP or GaP are quite expensive as well. Taking this fact into account the area of the sample exposed to the electrolyte was chosen to be relatively small, namely $A_s = 0.2 \ cm^2$. The exterior and interior diameters of the O-rings were 7 and 5 mm respectively.

Three holes with small diameters (two in the front - Cell 1; and one in the back - Cell 2) have been drilled into the walls of the cells through which the *Pt* electrodes (*WE, RE,* and *CE*) were inserted. The sense electrode *SE* is on the sample, therefore no separate hole is required for it. After the *Pt* wires for electrodes have been inserted into the cells the holes were glued. In exterior, easy to use sockets have been attached to the wires of the electrodes. Also, each cell has one window that allows the illumination of the sample if needed. See Figure 4.3 for a schematic representation of the double cell.

For each cell the electrolyte is pumped from a container into the cell using a peristaltic pump. The two containers are not connected in order to avoid an electrical short cut. Each container has two rooms (non communicating with each other). One of the rooms is in the center and contains the electrolyte, whereas the second room surrounds the first one and is filled with oil (or water).

The oil in the second room is *heated/cooled* by a *Julabo F25* thermostat (working range of the thermostat is between 0 and 40 ^oC). The temperature of the electrolyte inside the containers is measured by a *Pt-100* thermocouple.

The electrodes were connected to a specially manufactured *potentiostat/galvanostat* which can deliver a maximum of 1 A and ± 80 V. As will be seen later, high *current/voltage* values are very important in order to obtain self ordered 2D porous structures in InP. The temperature is controlled by a special circuit which receives the data from the thermocouple. These data are processed by the computer and corresponding commands for heating or cooling are send to the thermostat. In this way the thermostat receives a feedback concerning the actual temperature of the electrolyte which is normally different from the temperature of the oil.

The potentiostat and the thermostat are computer controlled by a $Windows^{(c)}$ multi-thread program. *SiPor*, the actual name of the program, allows to work in potentiostatic ($U = const.$) and galvanostatic ($I = const.$) regimes. The user can specify how U or I should behave during the experiment. The program allows U and I to vary as sinus, saw, linear or a combination of these functions.

A complete overview of the experimental set up is shown in Figure 4.4 on page 41.

4.2   Summary and Conclusions to Chapter 4

One of the most important parameters in electrochemical experiments is the voltage drop across the *semiconductor/electrolyte* junction. An experimental set up which is based only on a simply battery is not satisfactory for electrochemical experiments due to the fact that it can not control directly the voltage drop on the *SEI*. Instead a so called *potentiostat/galvanostat* device must be used. The *potentioistat/galvanostat* has an incorporated feedback mechanism that allows to control exactly the voltage which drops across the *semiconductor/electrolyte* interface.

In our experiments we used a double electrochemical cell and a four electrode potentiostat. The most important feature of the potentiostat is its ability to deliver high voltage and high currents. The double cell is built from Teflon in order to be resistant to all kinds of electrolytes. The temperature of the electrolyte as well as the *voltage/current* delivered by the potentiostat are computer controlled.
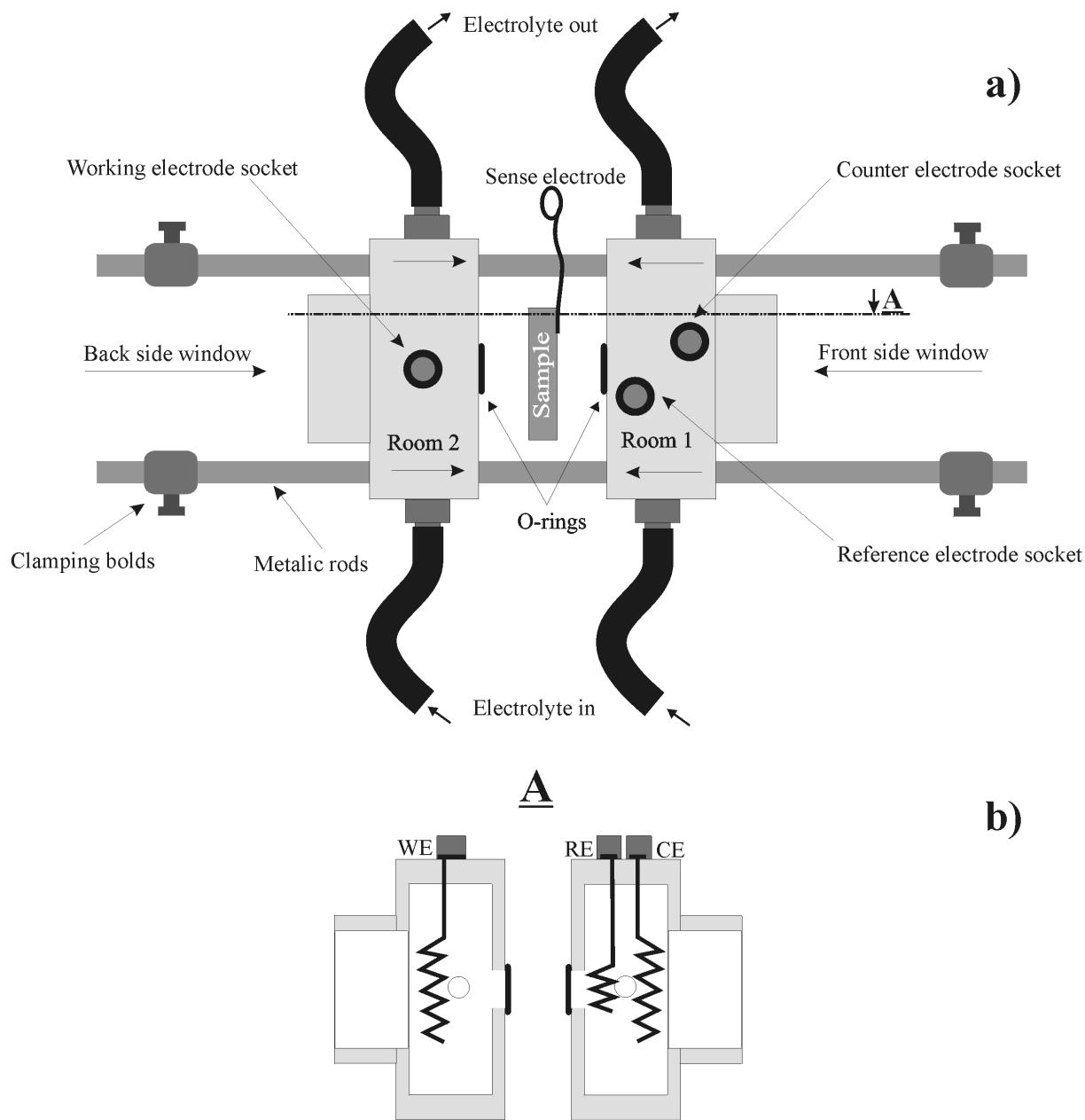
Figure 4.3: *Schematic representation of the electrochemical double cell used for anodization of III-V compounds. a) The cell consists of two Teflon rooms (Cell 1 and Cell 2) which are nearly identical. The only difference between them is that Cell 1 contains two Pt electrodes (CE and RE) whereas Cell 2 only one electrode (WE). Two windows in the cells provide the possibility for front and back side illumination. The cells slide easily on four horizontal metallic rods and can be fixed face to face by eight clamping bolts. The sample is placed between the cells and a mild mechanical contact with the Teflon cells is supplied by two rubber O-rings. The internal and external diameters of the O-rings are 7 and 5 mm respectively. On the sample, additionally, the fourth electrode is placed (sense electrode (SE)). The electrolyte can flow in and out of the cells through four rubber tubes. The tubes also connect the chambers to two different electrolyte containers; b) The cross section of the double cell along the cutting plane A (see a). It shows the inside of the cell and how the Pt electrodes are arranged. The electrodes are designed to provide a short distance between the sample and the reference electrode. Each Pt electrode is quite long and has an external socket for connection to the potentiostat.*
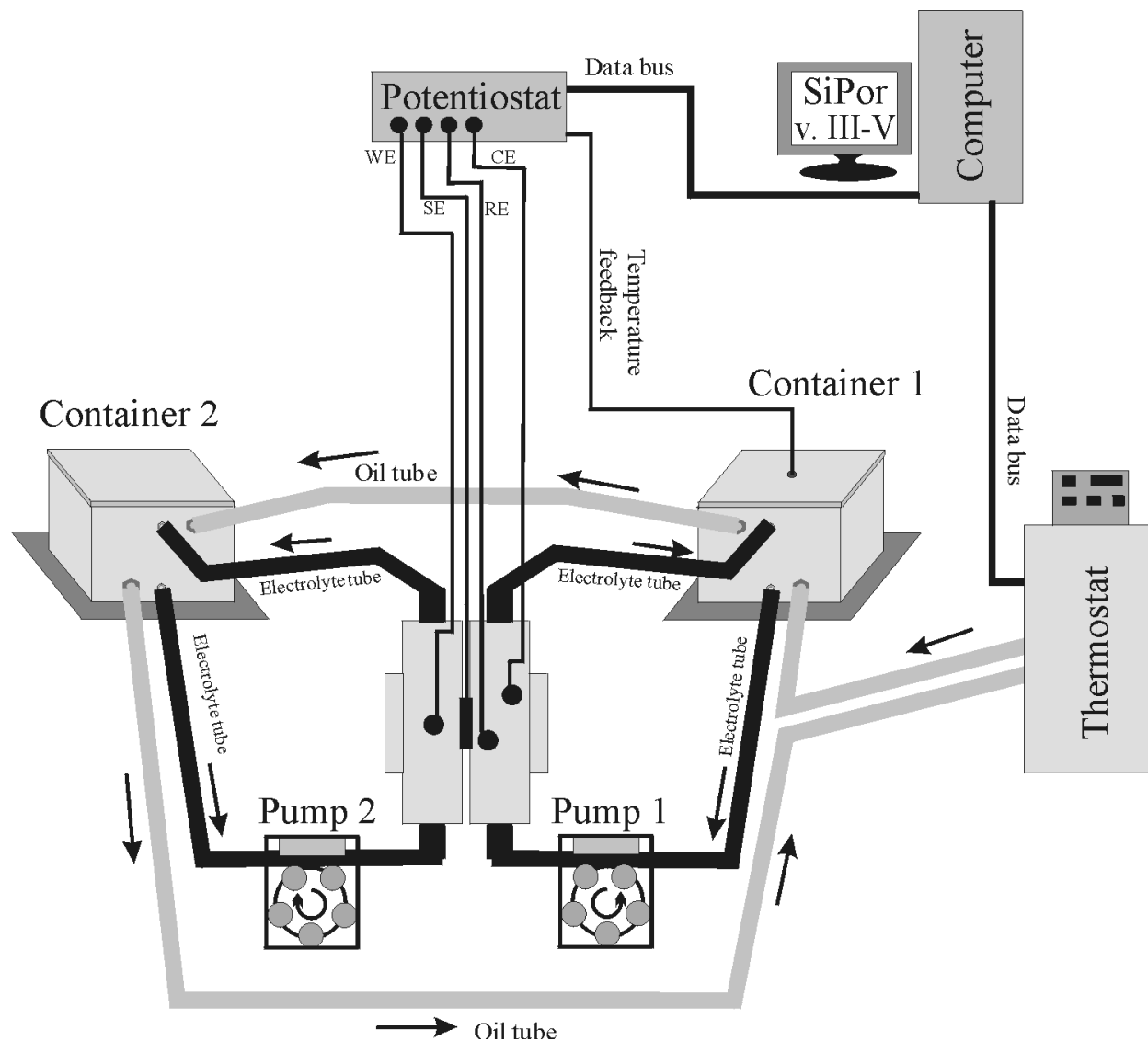
Figure 4.4: *The overview of the experimental set up used for anodization of III-V compounds in this work. The set up has six important components: the electrochemical double cell, the electrolyte containers, the peristaltic pumps, the potentiostat, the thermostat and the computer. The containers and the cells are made of Teflon in order to withstand all kinds of electrolytes. The electrolyte from Container 1 is pumped by Pump 1 through the front cell, whereas the electrolyte from Container 2 is pumped by Pump 2 through the back cell. The thermostat is pumping the oil through both electrolyte containers. The temperature is measured only in Container 1, which supplies the front cell with electrolyte. The potentiostat has a four electrode configuration: Working electrode (WE), Counter electrode (CE), Reference electrode (RE), Sense electrode (SE). Additionally, the potentiostat is collecting the information from the thermocouple, which is transmitted to the computer. The computer controls the thermostat and the potentiostat. The rotation velocity of the peristaltic pumps is fixed manually at the beginning of each experiment (normally 100 rotations per minute).*

Chapter 5

Porous Morphologies of III-V Compounds

The morphology of porous layers obtained during the anodization of semiconductors is one of the main characteristics which must be investigated in detail before any other properties should be considered, *e.g.* electrical, optical or mechanical properties.

By morphology of porous structures is meant the form of pores as individual units and the structure of porous layers as a whole. The form of pores is characterized by the shape, size and the direction of pore growth. The morphology determines the main properties of the resulting porous structure. Most evident in this context are the mechanical properties, however optical, electrical, and thermal properties can be influenced by the morphology as well.

The morphologies obtained during anodization of semiconductors depend strongly on the material and are mainly determined by particular characteristics of the *semiconductor-electrolyte* junctions and the bulk properties of the semiconductor itself. The most direct methods for investigation of porous morphologies are the modern optical and electron microscope techniques.

5.1 Crystallographically Oriented Pores

5.1.1 Experimental Conditions

(100) and (111) n-type GaAs ($n = 10^{17}\ cm^{-3}$), InP ($n = 10^{17}\ cm^{-3}$), and GaP ($n = 10^{17}\ cm^{-3}$) samples have been anodized at low constant current densities (galvanostatic conditions). Please note that in this work current densities up to 10 mA/cm^2 will be considered "low". InP and GaAs have been anodized in 5% HCl, whereas GaP in 5% H_2SO_4 aqueous solutions. The anodization time was from several seconds up to 120 min. The pumps had a constant velocity of 100 rotations per minute. The anodized samples were rinsed in acetone and deionized water and consequently investigated in cross section and plane view by a Philips XL series Scanning Electron Microscope working at an acceleration voltage of 10 kV. The cross section planes were (011)/(01$\bar{1}$).

5.1.2 Results and Discussions

Even using advanced electron microscopes it is not easy to determine the exact 3D structure of porous layers. There are two possibilities to investigate the porous samples, *i.e.* from the top and
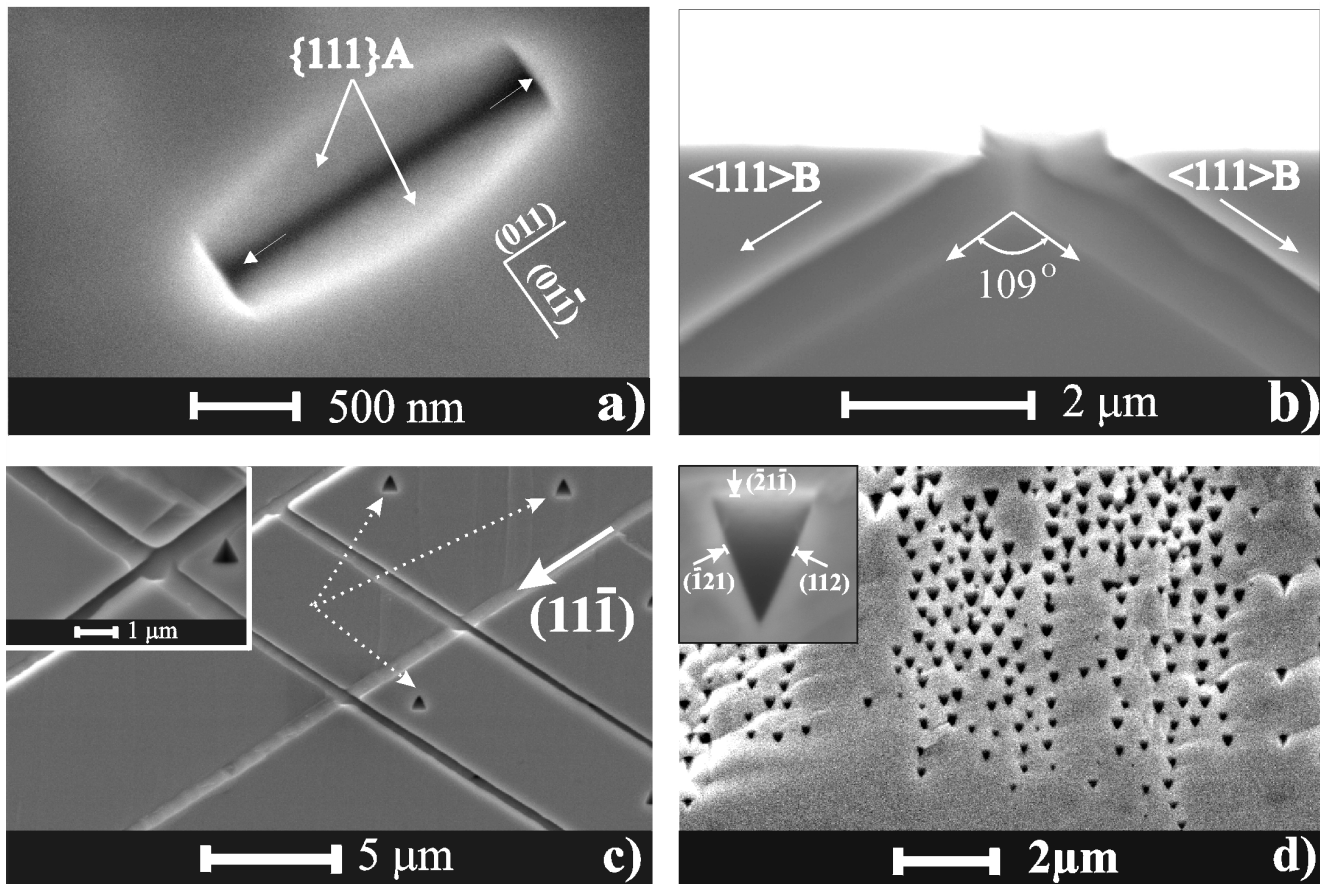
Figure 5.1: *Nucleation and growth of crystallographically oriented pores on (100)-oriented GaAs, (n = 10^{17} cm^{-3}), anodized at j = 4 mA/cm^2 in 5 % HCl; a) Plane view. The stretching of the pyramid-like cavity takes place until {111}A planes have been reached. The high aspect ration of the cavity (length/width) is confirming the difference in dissolution rates of {111}B and {111}A planes. After that the pores begin to grow along $\langle 111B \rangle$ directions. b,c) (011) cross section view; d) (01$\bar{1}$) cross section view; The difference between the two cross sections is evident: one, i.e. (011), is mainly exposing the channels of the pores, whereas (01$\bar{1}$) is exposing the triangular shape of the pores.*

in cross section. The top views provide approximately 20 % of the information required to find the exact morphology. The rest of 80 % is obtained from cross section views.

Unfortunately, it is very difficult to investigate all kinds of cross section planes. Usually we are limited only to cross sections made along the cleavage planes, *i.e.* easy to break planes. Due to the persisting danger to destroy the porous layer or to introduce artifacts in the morphology, mechanical polishing is not suited to obtain different cross section planes.

Typical top and cross section views of pores in (100) n- GaAs are presented in Figure 5.1. As it can be observed, these macropores are totally different from the usual macropores known from Si. The typical macropores obtained in (100) n- Si are round and grow perpendicular to the surface of the sample, *i.e.* along (100) direction.

It is evident that the difference to Si is a result of the anisotropy of III-V compounds as discussed in section 3.1. Namely, the difference in the dissolution rate between {111A} and {111B} facets strongly influences the shape and the direction of pore growth. The experiments

done for very short anodization times (1-2 seconds) and high current densities (20-50 mA/cm^2) show that the first step of pore nucleation leads to the formation of pyramid-like pits exposing four planes, which in analogy with Si are catalogued to be {111} planes. However, in III-Vs, from four {111} planes of the pyramid, two are {111}A and another two {111}B (see a schematic view in Figure 5.2).

Such a pyramid is not as stable, from the dissolution point of view, as it would be in the case if it would expose only {111}A planes. Therefore, as the etching process goes on the pyramid will change its shape exploiting the difference in the dissolution rate of the two types of {111} planes. Thus, the initial pyramid begins to stretch along the directions marked with X in Figure 5.2b. Simultaneously the B-planes rotate around the Z axis (Figure 5.2b) until an A-type plane is reached, which is more stable. The resulted cavity (or pit) exposes only A-type planes and has two sharp tips oriented along $\langle 111 \rangle B$ directions (Figure 5.2c). The $\langle 111 \rangle B$ directions point from B to A planes along the shortest distance between them, *i.e.* from the most unstable (B = As or P) to most stable (A = Ga or In) planes (see Figure 3.1) [1].

Due to the small radius of curvature (see section 3.4) during the anodization it is expected that at the tips of the pits the electrical field strength is much higher as compared to flat surfaces. Thus, electron-hole pairs are more easily generated at the two tips and consequently the dissolution will be favored as well. This way, the tips of the pits will start to move (due to dissolution) along the $\langle 111 \rangle B$ directions and as a result, pores will be generated.

The pores formed according to this mechanism will have a triangular shape. The crystallographic planes defining the triangular shape of the pores and simultaneously being the walls of the pores can be calculated relatively easily. Let's take the $[11\bar{1}]$ direction as an example, *i.e.* a B-type direction. The pores growing along this direction will expose at their tips the following crystallographic planes: $(1\bar{1}1)$, $(1\bar{1}\bar{1})$ and $(\bar{1}\bar{1}\bar{1})$. The intersection of each of these planes with the plane perpendicular to the growth direction of the pore, *i.e.* $(11\bar{1})$, will result in a triangle having its sides on the pore walls. The sides of the triangle can be found by taking the cross product between the normal vectors to the planes participating in intersection. Thus, we have to calculate the following cross products $\vec{a}(1,1,-1) \times \vec{b_1}(1,-1,-1)$, $\vec{a}(1,1,-1) \times \vec{b_2}(1,-1,1)$ and $\vec{a}(1,1,-1) \times \vec{b_3}(-1,-1,-1)$. The results are the following:

$$\vec{c_1} = \vec{a} \times \vec{b_1} = (1,1,-1) \times (1,-1,-1) = (-2,0,-2) \tag{5.1}$$

$$\vec{c_2} = \vec{a} \times \vec{b_2} = (1,1,-1) \times (1,-1,1) = (0,-2,-2) \tag{5.2}$$

$$\vec{c_3} = \vec{a} \times \vec{b_3} = (1,1,-1) \times (-1,-1,1) = (-2,2,0) \tag{5.3}$$

Now we know the vectors defining the sites of the triangle and we additionally know that the triangle will form the pore walls if it is moved along the $[11\bar{1}]$ direction. By taking the cross product between each side of the triangle and the direction of movement we will obtain the normal vector to the planes of the pore walls.

$$\vec{n_1} = \vec{a} \times \vec{c_1} = (1,1,-1) \times (-2,0,-2) = (-2,4,2) \tag{5.4}$$

---

[1] It should be noted, however, that in the literature a second definition can be found. In this case the $\langle 111 \rangle B$ directions point from B to A planes along the longest (not shortest) distance between these planes. The author believes that the first definition is more appropriate to describe the dissolution process.
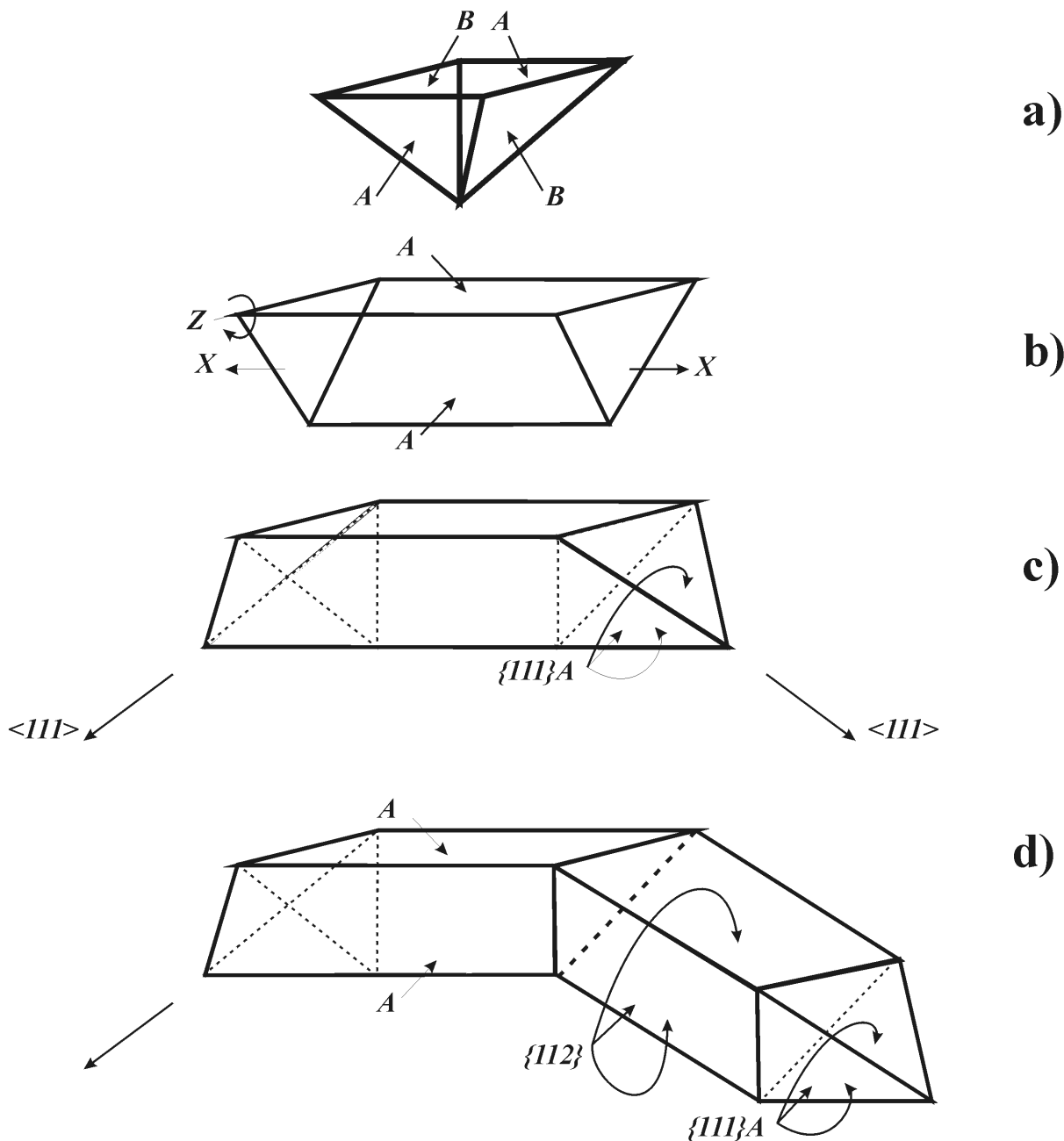
Figure 5.2: *A schematic representation of the nucleation of crystallographically oriented pores in III-V compounds. The dissolution process starts at defects and proceeds until stable (against dissolution) crystallographic planes are reached, i.e. {111}A. As in the case of Si, in III-V compounds {111} planes are the most stable against chemical attacks. a) A pyramid-like pit is formed at the beginning of the etching process, exposing four {111} planes. However, in III-V compounds the four exposed {111} planes are not equivalent from the chemical/electrochemical point of view. The so-called {111}A planes are more stable against dissolution as compared to the so-called {111}B planes; b) The dissolution process continues only along the directions perpendicular to the {111}B planes. This process will continue until all four planes of the cavity will be equally stable, i.e. {111}A. c) This cavity exposes only {111}A planes. The pores start to grow into the substrates along ⟨111⟩ B directions. d) The resulted pore walls are {112} and not {111}A planes.*

$$\vec{n_2} = \vec{a} \times \vec{c_2} = (1,1,-1) \times (0,-2,-2) = (-4,2,-2) \tag{5.5}$$

$$\vec{n_3} = \vec{a} \times \vec{c_3} = (1,1,-1) \times (-2,2,0) = (2,2,4) \tag{5.6}$$

We are interested only in the direction of the normal vectors, therefore we can write that $\vec{n_1}$, $\vec{n_2}$, $\vec{n_3}$ have the following coordinates $(-1,2,1)$, $(-2,1,-1)$, $(1,1,2)$ respectively.

Thus we obtained that the pore walls of the pore oriented along $(11\bar{1})$ direction are defined by three planes from the $\{112\}$ set of planes. In a similar way the planes of the pore walls for the $(1\bar{1}1)$ pores can be obtained. SEM pictures showing the triangular shapes of the pores and the corresponding pore walls taken from (100) n-GaAs are presented in Figure 5.1c and d.

The formation of triangular pores introduces a second anisotropy of the electrochemical etching, besides the preferred directions of pore growth along $\langle 111 \rangle B$ directions, and establishes $\{112\}$ planes as particularly stable against dissolution. In the framework of the current burst model, these anisotropy features can be explained assuming that:

� Direct dissolution (see Chapter 3.6) is dominant over the dissolution via oxide formation. This is understandable if we take into account that the experiments were done at low current density, *i.e.* the rate of oxide formation is very low. Additionally, the oxides of III-Vs are very unstable in acidic solutions.

▧ The passivation has a very high selectivity between different crystallographic planes, *i.e.* $\{111\}$ and $\{112\}$) planes are easier passivated as compared to $\{100\}$ or $\{110\}$) planes.

As discussed in section 3.6 by passivation we mean the neutralization of the surface states. With many surface states, the Fermi energy of the semiconductor is "pinned" and the bands can not move up or down. Therefore, the major potential drop then occurs over the Helmholtz layer of the electrolyte, thus favoring the electrochemical dissolution reaction. On the other hand, with neutralized surface states the space charge region in the semiconductor 'consumes' most of the applied potential and thus the rate of the electrochemical dissolution reaction decreases significantly. This means that a good passivated surface will be more stable against dissolution than a less passivated one.

The angle between the two $\{111\}$B directions can be calculated using elemental geometry. In this case we take the scalar product of the vectors determining the two $\{111\}$B directions. In strict crystallographic notations the two directions are $[11\bar{1}]$ and $[1\bar{1}1]$. As a result the angle is:

$$\cos(\alpha) = \frac{1 \cdot 1 + 1 \cdot (-1) + (-1)(1)}{\sqrt{(1)^2 + (1)^2 + (-1)^2}\sqrt{(1)^2 + (-1)^2 + (1)^2}} = -\frac{1}{3} \tag{5.7}$$

$$\alpha = \arccos\left(-\frac{1}{3}\right) = 109^o, 47'' \tag{5.8}$$

The nucleation cavity discussed above and the pores growing from it are easily recognizable also on the SEM pictures presented in Figure 5.2a and b. The experimentally measured angle between the two pores in Figure 5.2b is 109°. These results confirm the nucleation model presented in Figure 5.2.

However, the nucleation model described above makes an additional restriction, namely that the pores can grow only along $\langle 111 \rangle$B directions and not along $\langle 111 \rangle$A. This means that for a (100)
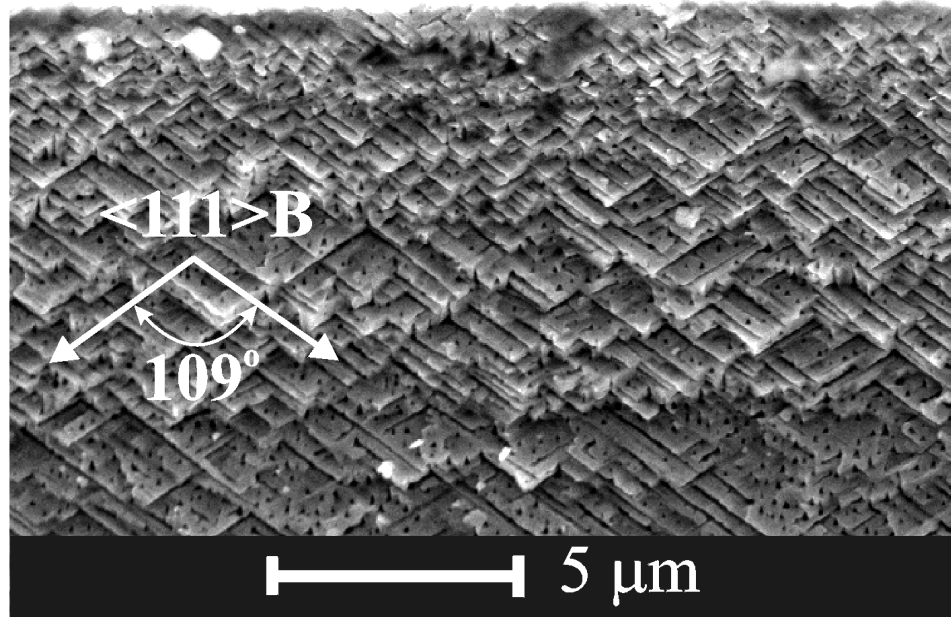
Figure 5.3: *(011) cross-section SEM picture taken from a (100) oriented n- InP sample, $n = 10^{17}$ cm^{-3}, anodized at $j = 4$ mA/cm^2 in 5 % HCl. The triangular voids growing perpendicular to the cleavage plane are more numerous as in the case of GaAs. Thus, the branching of downward growing pores is easier than in GaAs.*
.

oriented sample we will have only two different directions along which the pores could grow, *i.e.* $(11\bar{1})$ and $(1\bar{1}1)$. Therefore, all the pores should grow within $\{011\}$ planes which are perpendicular to the $\{01\bar{1}\}$ planes.

Nevertheless, the careful analysis of the SEM micrographs (see *e.g.* Figure 5.1c) shows a number of triangular voids within the $\{011\}$ planes (see the dashed arrows). Thus, the experiment shows that pores can grow also within $\{01\bar{1}\}$ and perpendicular to $\{011\}$, not only vice versa as the model predicts.

In addition, it is important to note that the same behavior for the pores was observed also in (100) n- InP. The pores obtained in InP are shown in Figure 5.3. In this case the number of triangles observed on the (011) cleavage plane is even higher as compared to GaAs. Thus, the low density of triangles observed in GaAs was not accidental but is a common characteristic of GaAs and InP.

Two assumptions can explain the experimental results for pores growing within $\{01\bar{1}\}$ planes:

�▌ These pores grow downwards, *i.e.* into the substrate, along $\langle 111 \rangle$A directions, however with a lower probability, therefore the number of such triangles is relatively small.

▌ The pores grow upwards, *i.e.* along $\langle 111 \rangle$B direction. Therefore these pores have to start as branches of $\langle 111 \rangle$B pore which grow into the depth.

Up to now no experimental results exist which could unambiguously prove that $\langle 111 \rangle$A pores can grow. However, there are clear evidences, obtained with (111) oriented samples, in the favor of the second assumption. (111) oriented samples have an important particularity. One side of

the sample is terminated with Ga atoms, whereas the other side is terminated with As atoms. Therefore, the two sides are called (111)A and (111)B respectively. We anodized the (111) oriented samples from both sides. The results for (111) oriented samples anodized on both sides, *i.e.* A and B, in n- GaAs and n- InP are presented in Figure 5.4.

From the micrographs it is evident that the pores starting from the (111)B side grow perpendicularly to the surface of the samples (see Figure 5.4a and c for GaAs and Figure 5.4b for InP). On the other hand, from the (111)A surfaces the pores are inclined at an angle of 70.5^o relative to the normal of the anodized surface (Figure 5.4e). This is actually the angle between an A-type surface and a B-type direction.

Thus, there is no doubt that on both (100) and (111)-oriented substrates the pores at low current densities grow only along $\langle 111 \rangle B$ directions. More than that, pores growing towards the surface of the sample can be observed on both (100) and (111)B oriented samples. Upward growing pores are usually observed near the O-ring of the electrochemical cell, or within regions with a bad pore nucleation (see Figure 5.4c). The $[1\bar{1}1]$ direction is pointing downwards the substrate (perpendicular), whereas the $[11\bar{1}]$ direction is pointing upwards. This means that as in the case of (100) oriented samples the upward growing pores nucleate somewhere in the substrate (as branches of the main pores) and grow upward until the surface of the sample is reached. In section 5.3 will be shown that such upward pore growth leads to the formation of the so-called domains of crystallographically oriented pores in n- GaAs and n- InP.

Another very important feature of the pores growing along $\langle 111 \rangle B$, reported for the first time, is their intersection. The reason for the importance of intersection is due to the fact that the $\langle 111 \rangle B$ oriented pores nucleated from a (100)-oriented surface can form a 3D structure. Figure 5.1a illustrates an example of the intersection of two pores oriented along $[1\bar{1}1]$ and $[11\bar{1}]$ directions (see also the inset). Somewhat surprisingly, the intersection has no influence on the pore shape, the size, and the direction of subsequent propagation.

However, the crossing of pores is somewhat unexpected because according to some existing models [17, 50], the formation of pores in n-type semiconductors is a self-adjusted process controlled by the distribution of the electric field at the *semiconductor-electrolyte* interface. The pores may branch and form porous domains but both individual pores and domains should be separated by walls with characteristic dimensions of twice the thickness of the surface depletion layer and can *NOT* intersect [61].

The inability of the pores to grow after they meet was explained by Erne *et al* assuming that when the pore wall between the two pores becomes too thin, *i.e.* smaller than twice the space charge region, it can no longer support a field perpendicular to the surface which is sufficiently high for anodic hole generation (avalanche mechanism), thus the pore etching must stop [17].

However, as the experiments show, this is not true for crystallographically oriented pores (see Ref. [56]). The crysto pores will always intersect if the pores will meet each other with their tips (see Figure 5.5, case A), and will not intersect if a tip of a pore will try to penetrate another pore far away from the tip. This is caused by the fact that the pore tips are very bad passivated and consequently the space charge region at the tips is very small. This fact favors the intersection.

On the other hand, if a tip of a pore is running in a pore wall of another pore (Figure 5.5, case B), the intersection will not succeed. A pore wall is very well passivated and has a much larger space charge region which is more difficult to penetrate. As we will see in section 7.4, the situation is different for the current-line oriented pores. The current-line oriented pores can not intersect even if they will meet each other with their tips. This hints to the fact that the passivation of the
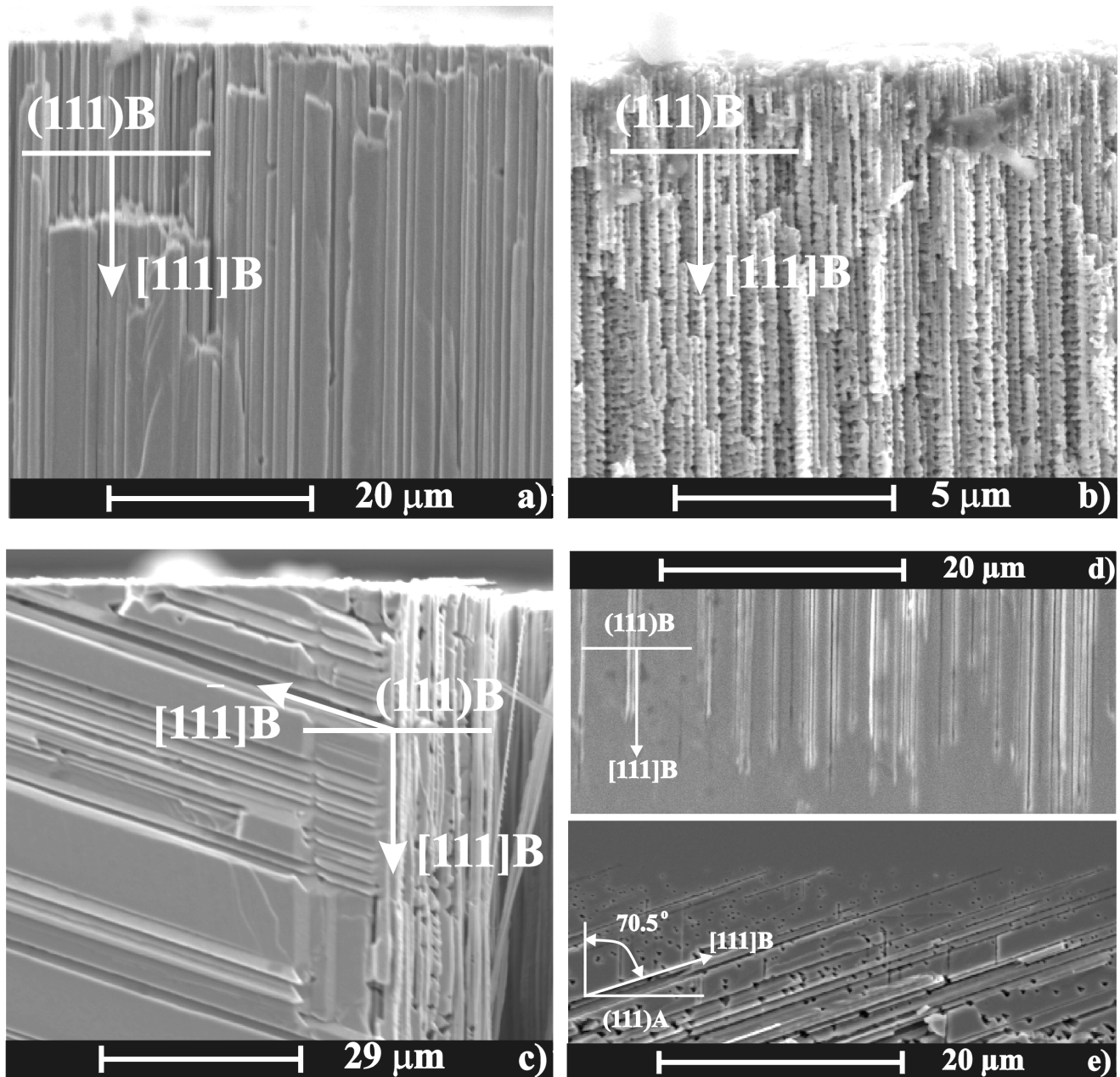
Figure 5.4: *(111)-oriented samples anodized at low current densities $j = 4\ mA/cm^2$ in 5% HCl aqueous electrolyte solution; a) n- GaAs, $n = 10^{17}\ cm^{-3}$. The pores grow perpendicular to the (111)B surface; b) (111)B, n- InP, $n = 10^{18}\ cm^{-3}$ anodized at the same conditions as (111)B-oriented n- GaAs in figure* a)*. The pores on (111)B-oriented n- InP also grow perpendicularly to the surface of the sample. However, the pores in InP have a lot of branches as compared to GaAs. In InP, the nucleation of pores in HCl solutions is much easier, therefore the branches can also nucleate more easily. c) Beside the pores growing perpendicularly to the surface, e.g.* [$1\bar{1}1$], *they also grow along* [$11\bar{1}$] *direction, pointing towards the surface of the sample. d,e) A direct comparison between (111)B and (111)A anodized samples. In the first case the pores grow perpendicular to the surface, whereas in the second case they form an angle of* 70.5^o *with the normal to the surface. This is an evident demonstration that the pores do not grow along* $\langle 111 \rangle$ *A directions.*
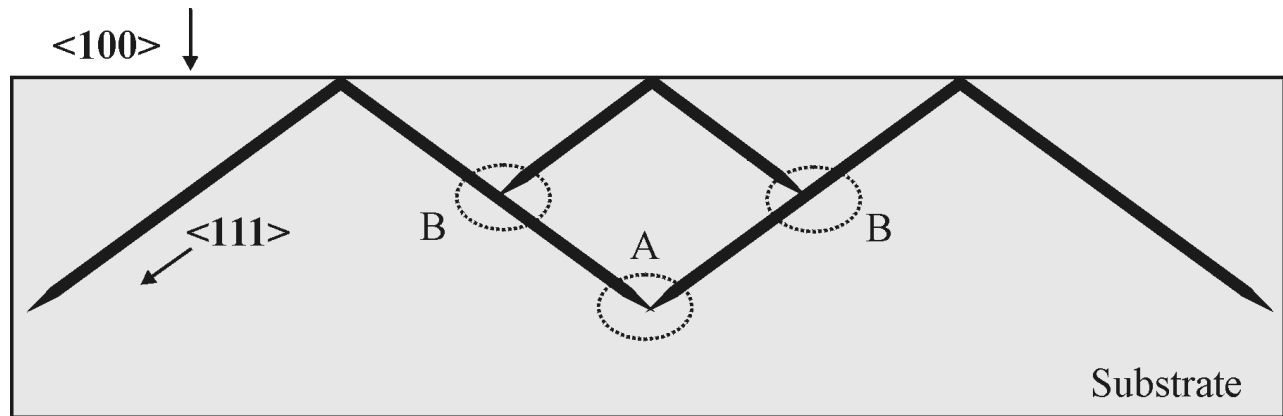
Figure 5.5: *Schematic representation for intersection of crystallographically oriented pores. The pores started at the same moment can intersect, whereas the pores started at different moments can not.*

Figure 5.6: *(100)-oriented n- GaP, n = 10^{17} cm^{-3}, anodized at j = 4 mA/cm^2 in 5% H_2SO_4 aqueous electrolyte solution; The angle between the pores is also 109°. Thus, the pores, as in the case of n- InP and n- GaAs, are crystallographically oriented along $\langle 111 \rangle$ B directions.*
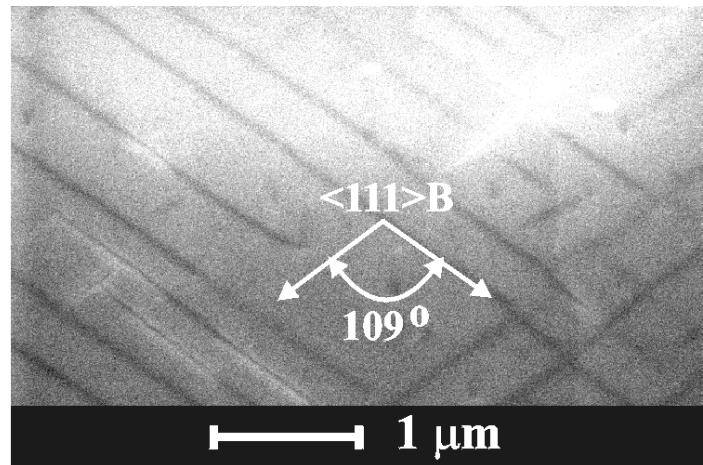
pore tips in the case of current-line oriented pores (see section 5.2) is more effective, *i.e.* have a larger SCR, than in the case of crystallographically oriented pores.

The intersection of crysto pores demonstrates that this may be a suitable tool for production of 3D micro- and nanostructured III-V compounds, *e.g.* for photonic crystals applications. Nevertheless, in addition to pore interconnection, a three-dimensional photonic pore crystal requires a very high level of uniformity [62]. Since the dissolution is stimulated by defects [63, 64] and/or illumination [65], it is expected, that a predefined nucleation and thus a controlled intersection of the pores can be provided by conventional lithography followed by a conventional chemical treatment to generate small pits (defects), or by proper front side illumination of the sample at the beginning of the anodization. This topic will be discussed in Chapter 7.

In order to see if the $\langle 111 \rangle$ B oriented pores are characteristic to other III-V compounds or if they are restricted only to n- GaAs and n- InP, similar experiments have been performed on (100)-oriented n- GaP samples. The results are presented in Figure 5.6 on page 51. As it can be observed the angle between the pores is also 109°, which is a confirmation of the fact that also in the case of (100)-oriented n- GaP the pores are oriented along $\langle 111 \rangle$ B directions.

The main differences in n- GaP is that no triangles within the (011) cleavage plane are observed. This is related to the branching probability of downward growing pores. Comparing the three

materials in this regard, it can be concluded that in GaP the branching is practically non existent, in GaAs is high and in InP is very high.

Another evident difference is the pore size. In GaP the pores are smaller than in n- InP and n- GaAs at the same doping level and etching conditions. At a doping level of $n = 10^{17}$ cm^{-3}, at low anodic current densities, the size of $\langle 111 \rangle B$ oriented pores in GaAs is in the range of 1 μm, in InP it is in the range of 300 - 500 nm, whereas in GaP the pores are in the range of 100-200 nm.

In order to distinguish the pores described in this section from other types of pores which we are going to discuss in what follows, the pores which follow a definite crystallographic direction in their growth will be called crystallographically oriented pores (CO) or simply crysto pores.

5.2   Current-line Oriented Pores

5.2.1   Experimental Conditions

n-type InP ($n = 10^{17}$ cm^{-3}) and GaP ($n = 10^{17}$ cm^{-3}) samples have been anodized at high constant current/voltage values, *i.e.* at galvanostatic and potentiostatic conditions. The actual current density was higher than $j = 10$ mA/cm^2. Note that in this work the values higher than 10 mA/cm^2 will be considered "high" current density. InP was anodized in 5% HCl aqueous solutions, whereas GaP in 5% H_2SO_4 aqueous solutions and in 5% H_2SO_4 + HCl. The orientation of the samples was (100) and (111). As usual after the anodization the samples have been rinsed in acetone and deionized water and consequently investigated by a Philips XL series SEM at an acceleration voltage of 10 kV.

5.2.2   Results and Discussions

In the last subchapter was shown that the pores obtained during the anodization of n-type InP, GaAs, and GaP at low current densities have definite crystallographic directions of growth, namely $\langle 111 \rangle B$ directions. This section describes the pore formation for the same etching conditions, *i.e.* electrolyte concentration, doping, temperature etc., but just increasing the current density.

Figure 5.7a presents the cross section micrograph of a (100)-oriented n- InP sample anodized at U = 10 V (the resulted current was > 10 mA/cm^2). Pores obtained at these conditions obviously have no specific crystallographic orientation, but simply follow some curved lines. In the middle of the anodized sample such kind of pores are mainly oriented perpendicularly to the surface showing only small disturbances in their direction of growth. On the other hand, near the O-ring of the electrochemical cell, or near defects in the substrate, the pores are far more unstable.

The lack of preferential crystallographic direction of growth for these pores hints that they will look similarly even if the anodization will be performed on other than (100)-oriented n- InP substrates, *e.g.* on (111)-oriented samples.

Therefore, the same experiments have been repeated on (111)-oriented n- InP samples. An example is presented in Figure 5.7b. As was expected, also in this case, at high current densities the pores are mainly oriented perpendicularly to the surface and show important inflections while they are growing. Similarly, the most pronounced inflections are near the O-ring of the electrochemical cell. For the same current density there is no difference between the pores grown from a (111)A or (111)B surface. Please note that at low current densities it is not possible to obtain pores growing
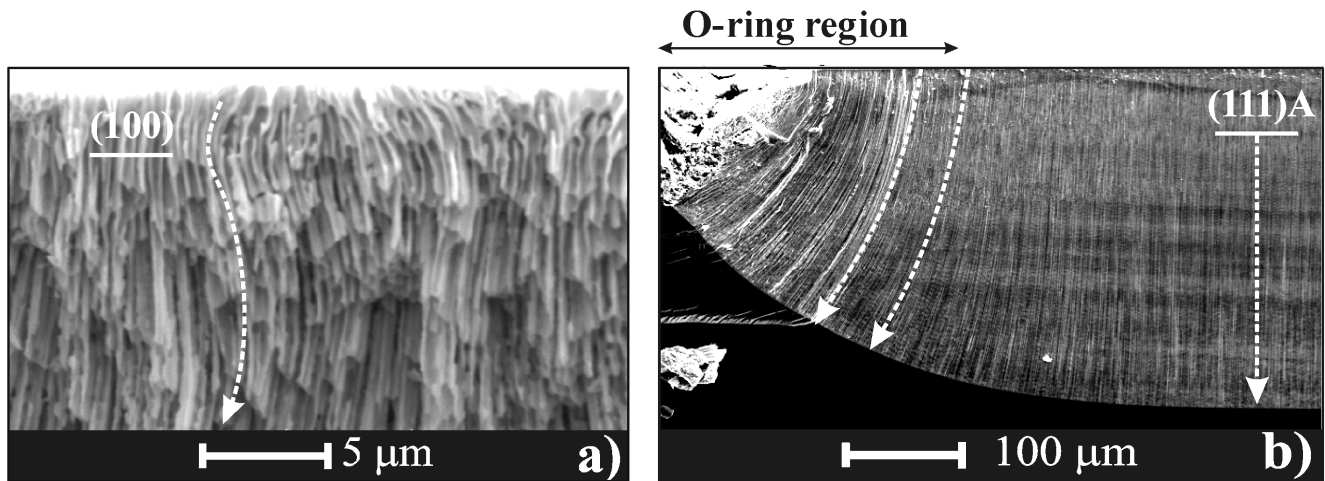
Figure 5.7: *a) (100)-oriented n- InP, $n = 10^{17}$ cm^{-3}, anodized at U = 10 V (j > 10 mA/cm^2), 5% HCl aqueous electrolyte solution. The pores prove to be unstable and are trying to grow perpendicularly to the surface of the sample forming the so-called current-line oriented pores. b) (111)A oriented n- InP, $n = 10^{18}$ cm^{-3}, anodized at U = 7 V (j > 10 mA/cm^2), 5% HCl aqueous electrolyte solution; The pores as in the case of (100)-oriented samples grow perpendicularly to the surface. The pores are curved near the O-ring of the electrochemical cell;*

perpendicularly to a (111)A surface. This suggests that the difference between A and B planes is not anymore important at high current densities.

From all these observations it is evident that the system is trying to minimize the ohmic losses by minimizing the path for the current [66] and thus growing perpendicularly to the surface of the sample. Therefore, such kind of pores, *i.e.* which grow perpendicularly to the equipotential lines of the electric field in the substrate, will be called 'current-line oriented' pores or simply *curro* pores. The curro pores have been reported for the first time by our research group [67].

As it was shown above, under nearly identical conditions, except for a lower anodic current density of more than one order of magnitude, a totally different morphology was obtained for (100) and (111)-oriented n- InP samples (Figure 5.3 on page 48). In this case the pores prove to be strictly oriented along specific crystallographic directions. One can conclude that a change of the current density from low to high values leads to a switch in the pore growth mechanism from being crystallographically oriented to current-line oriented. This conclusion is supported by the images presented in Figure 5.8 on page 54 [67].

The same (100) n-InP sample was subjected to anodization first at high, and then at low current densities. As can be seen in the cross section of the sample, a switch from current-line oriented to crystallographically oriented pores occurs. The upper part of the porous layer has a current-line oriented morphology and corresponds to high current density (Figure 5.8a), while the lower part of the layer contains crystallographically oriented pores. The same procedure was applied to a (111)B oriented sample (Figure 5.8b). However, the switch between the curro and crysto pores is not so evident due to the fact that the curro as well as the crysto pores in this case grow perpendicularly to the surface of the sample.

Earlier in this chapter we concluded that the dissolution during the formation of the crystallographically oriented pores is dominated by the direct dissolution and therefore they expose very strong anisotropic features. On the other hand, the anisotropy features are lost (partially or
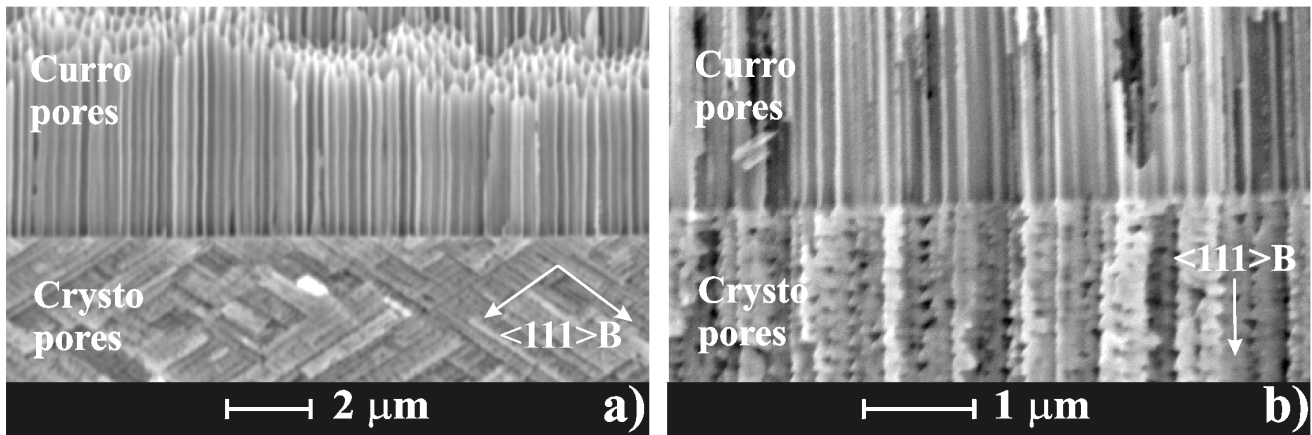
Figure 5.8: *Cross section micrographs of n- InP samples anodized in turn at high and low voltages (7 and [1] V respectively): a) (100) Oriented sample; b) (111) oriented pores; In both cases the upper part of the porous layer shows curro pores, whereas the lower part shows crysto pores; Taking into account that porosity of the layer with crystallographically oriented pore is lower than for the layer with current-line oriented pores, it can be suggested that successive layers with different porosities can be formed by alternating the voltage from high to low values. This subject will be discussed later in Chapter 7.*

totally) if the dissolution via oxide formation is dominating the whole dissolution process. Thus, looking at the main characteristic of the curro pores, *i.e.* NO preferential crystallographic direction for dissolution, it can be concluded that in this case the main dissolution mechanism is the dissolution via oxide formation. This allows the dissolution at the pore tips to be isotropic (the anodic oxides are normally amorphous), *i.e.* there is no difference (from the electrochemical point of view) between different crystallographic planes.

As concluded in the last section, crystallographically oriented pores growing along $\langle 111 \rangle B$ directions are common to all n-type III-V compounds studied in this work: n-type GaAs, InP, and GaP. Thus, it is interesting to investigate whether the current-line oriented pores are also characteristic to GaP and GaAs, or if they are unique for n- InP only.

Figure 5.9 on page 55 presents the results obtained at high current density anodization of (100)-oriented n- GaP samples, $n = 10^{17}$ $cm^{-3}, j = 60$ mA/cm^2. As in the case of n- InP the pores do not show any preferential crystallographic directions of growth and simply grow perpendicularly to the initial surface of the sample. Thus, the pores obtained in n- GaP at high current densities can be also catalogued as current-line oriented. Nevertheless, there are some major differences between the current-line oriented pores in n- InP and n-GaP showed in Figure 5.9.

First of all the current-line oriented pores in n- GaP grow much more unstable (Figure 5.9b). Secondly, the pore diameters are much bigger, they are in the range of 3-4 μm, whereas for the same doping level the current-line oriented pores in n- InP are in the submicrometer range. Thirdly, the ratio pore-diameter/pore-wall-width in GaP is much bigger than in InP. Within the current burst model (at high current densities) this can be explained by a stronger passivation efficiency for the pore walls and probably also weaker oxidation (and less qualitative oxide) in InP as compared to GaP. According to the current burst model less oxidation in InP directly means smaller pores. Additionally, in order to break the more effective passivation and consequently to dissolve InP, a stronger electric field at the pore tips is necessary, *i.e.* a smaller radius of curvature, which is
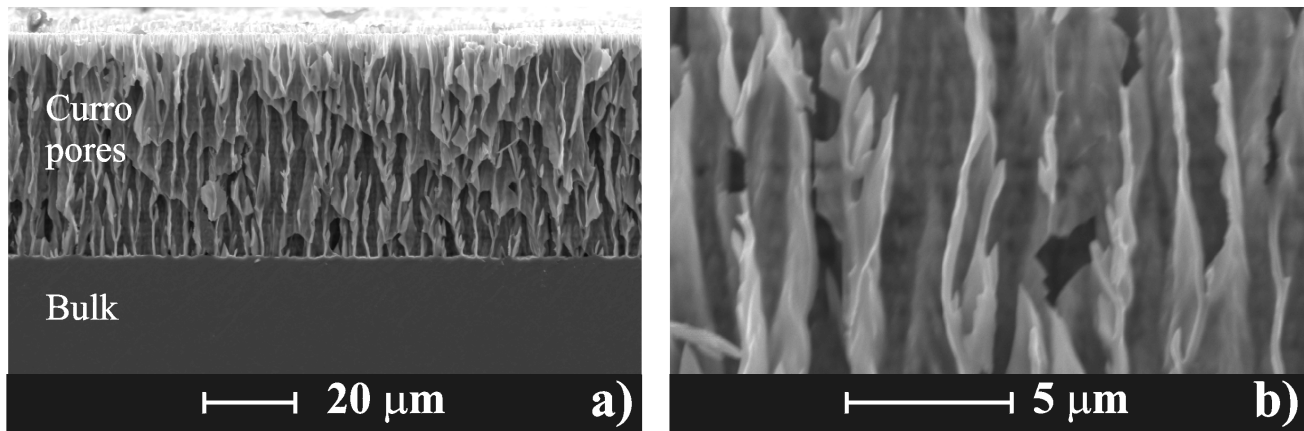
Figure 5.9: *(100)-oriented n- GaP, $n = 10^{17}$ cm^{-3}, anodized at $j = 60$ mA/cm^2, 5% H_2SO_4 electrolyte solution; a) Overview of the porous layer (cross section); b) A higher magnification of the pores; At such high current densities also in GaP the pores do not grow anymore along $\langle 111 \rangle B$ crystallographic directions, but start to grow perpendicularly to the surface resulting in a current-line oriented porous layer. The current-line pores in GaP prove to be much more unstable, i.e. showing branching characteristics, and their diameters are much bigger as compared with those obtained in n- InP. The observations of current-line oriented pores in GaP underlines once again the similarities from the electrochemical point of view between InP and GaP, in spite of the fact that one is an indirect (GaP) and another is a direct (InP) semiconductor ;*

directly related to a smaller pore diameter (see subchapter 3.4). For GaP the passivation at high current densities is not so efficient therefore the electric field inside the space charge region can be lower, *i.e.* the radius of curvature can be bigger and consequently the pore diameter is bigger. More than that, low wall passivation leads to a small space charge region in the semiconductor and consequently thinner pore walls.

In order to increase the passivation of the pore walls in GaP a small amount of HCl was added (5 ml of 35% HCl was added to 200 ml of 5% H_2SO_4) to the aqueous H_2SO_4 solution. The pores obtained with this mixture are presented in Figure 5.10. It is evident that the curro pores in this experiment look more similar to those in InP, *i.e.* the pores grow much more stable and the pore diameters are smaller. Thus, it can be concluded that HCl is a better passivation and oxidation agent for GaP as compared to H_2SO_4. It is interesting to note that in aqueous HCl electrolytes we did not succeed to obtain curro pores in GaP due to the fact that the potential required to pass a high current through the sample was higher than 80 V - the maximum value delivered by our potentiostat.

An important characteristic of both materials (GaP and InP) while anodizing them at high current densities are the external macroscopic voltage oscillations. These oscillations will be discussed in a later chapter (see section 6.2). They provide important information about the pore formation mechanism. In addition, they have been also observed in Si and represent a direct prediction of the current burst model.

So far, current-line oriented pores have been observed only in n-type InP and GaP, but not in GaAs. In GaAs at high current densities the so-called tetrahedron-like pores and domains of crystallographically oriented pores tend to form. This type of pores in GaAs will be discussed in the following two section.
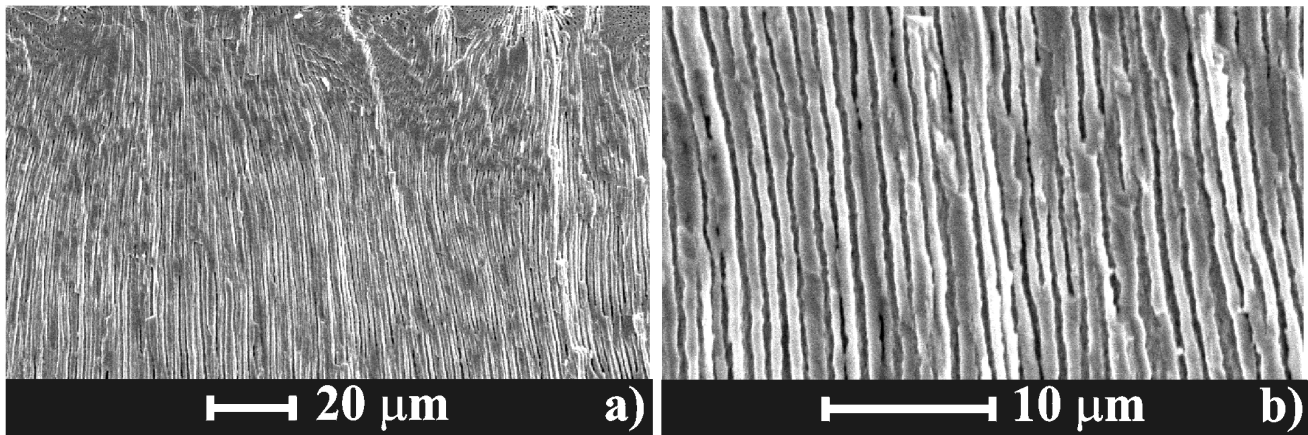
Figure 5.10: *(100)-oriented n- GaP, $n = 10^{17}$ cm^{-3}, anodized at $j = 60$ mA/cm^2, 5% H_2SO_4 + HCl electrolyte solution. a) Overview of the porous layer. b) A higher magnification of the pores. This kind of pores are much more similar to the curro pores observed in InP;*

5.3   Domains of Crystallographically Oriented Pores in GaAs

5.3.1   Experimental Conditions

N-type GaAs ($n = 10^{17}$ cm^{-3}) samples have been anodized at high constant current densities, higher than 10 mA/cm^2. The anodization was performed in aqueous HCl solutions. The orientation of the samples was (100). After the anodization the samples have been rinsed in acetone and deionized water and investigated by a Philips XL series Scanning Electron Microscope working at 10 kV.

5.3.2   Results and Discussions

As it was already demonstrated for n- InP and n- GaP, by gradually increasing the anodization current density, a switch from crystallographically oriented pores to current-line oriented pores will take place. However, in n-GaAs something similar to current-line oriented pores was not observed up to now, at least for all experimental conditions which were tried within this work. Instead, characteristic to n- GaAs at high external current densities are domains of crystallographically oriented pores and the so-called tetrahedron like pores, both of them reported for the first time.

An overview of an anodized sample containing domains of crystallographically oriented pores obtained on (100)-oriented n- GaAs is presented in Figure 5.11a. The domains are rectangular and a peculiar correlation between rows of individual pores, inside the domains, can be observed. The rectangular shape of the domain can be divided into four quadrants shown in Figure 5.11b. The quadrants I and II have a higher degree of porosity as compared with the quadrants III and IV. The difference in porosity between the quadrants is more easily distinguished in Figure 5.11c.

By investigating the samples subjected to anodization at very high current densities for small periods of time, around 1-5 seconds, it was observed that each domain starts to grow from a central point. The size of the domain depends on the anodization time and on the anodization
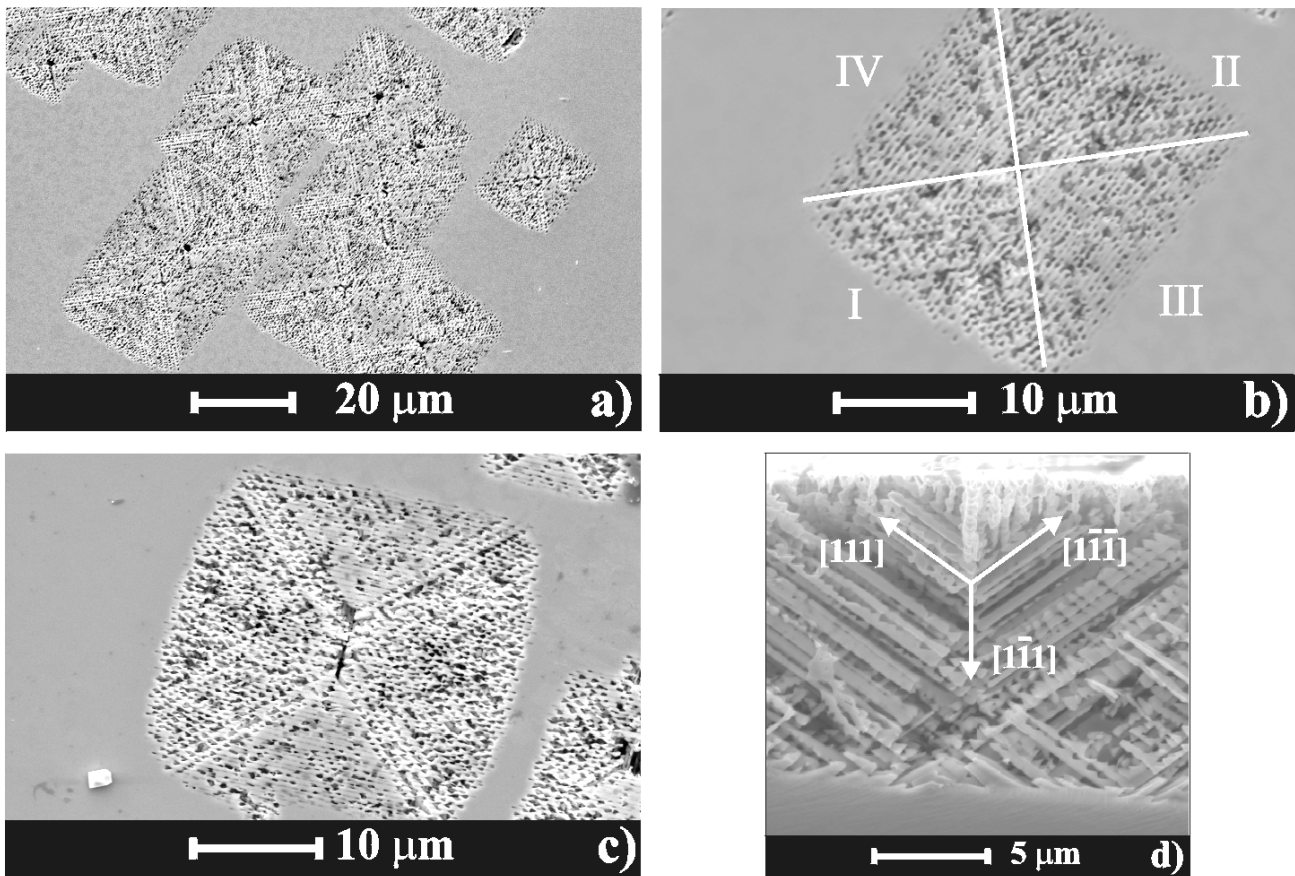
Figure 5.11: *Domains of crystallographically oriented pores in (100) n-GaAs anodized at $j = 80$ mA/cm^2 in 5% HCl solutions for 1 minute; a) Overview of the domains. The domains have a squared shape and are formed by crystallographically oriented pores; b, c) Each domain can be divided in four quadrants. Two of them (I and II) have a high porosity, while the other two (III and IV) have a lower porosity; d) the structure of a domain in cross section. In this micrograph three direction of pores growth can be seen - one pointing into the substrate (not perpendicular, the arrow presents only the projection of the growth direction) and the other two pointing towards the surface (see the schematic view 'Cross section A2' presented in Figure 5.12 on page 59.);*

external current density. The cross-section of domains (Figure 5.11d) reveals a quite complicated 3D structure, where pores growing downwards into the substrate as well as upwards towards the surface of the sample are observed. A schematic description explaining the principle of the domain formation is shown in Figure 5.12.

The heart of a domain is its starting point, shown in Figure 5.12 as a gray disk, where the dissolution probably starts due to a defect in the substrate. From this central point normally two pores begin to grow along two $\langle 111 \rangle B$ directions pointing into the substrate. During the first few seconds of the experiment the whole (huge) amount of the externally applied current succeeds to be consumed by the two pores (in each domain), imprinting them correspondingly a huge velocity of growth. However, soon enough the electrochemical reaction at the pore tips starts to miss species (reducing and oxide dissolving) from the electrolyte and the amount of current consumed by the two pores decreases exponentially.

Nevertheless, the system has to find a way how to carry continuously the constant amount of

current imposed from exterior (note the galvanostatic experiment). The easiest way to go along with this is to nucleate new pores or more specifically - new pore tips. This way, increasing the diffusion 'freedom' of the electrolyte species and reaction products inside the porous structure.

There are two possibilities for nucleating new pores:

� On the surface of the sample,

▶ Under the surface, *e.g.* as branches of the two initial nucleated main pores.

Taking into the account that the surface of the sample can be strongly passivated by the electrolyte species, *e.g.* Cl^- or OH^-- passivation, then it can be assumed that new pore nucleation on the surface is less probable than branching of pores under the surface. Actually, the probability of branching is higher also due to the defects which are created on pore tips during the dissolution and which require time in order to be passivated by the electrolyte species and thus can be suitable candidates as nucleation points for new branches.

Pore branching along $\langle 111 \rangle B$ directions has a lot of freedom if we take into account that there are four $\langle 111 \rangle B$ directions: two pointing downwards into the substrate, whereas the other to pointing upwards, *i.e.* towards the initial surface of the sample. In Figure 5.12 the lines illustrating the $\langle 111 \rangle B$ directions pointing upwards or downwards have corresponding arrows, showing the exact direction.

Similar to the two initial pores stemming from the central point of the domain, the branches, at their turn, will also tend to branch along $\langle 111 \rangle B$ directions. Thus, the formation of a domain is a fractal like branching of pores. Branching increases exponentially the number of pore tips and thus making easier the current flow. This exponential increase of the number of pore tips decreases the current density at each pore tip. The decrease of the current density at pore tips will cause a gradual retardation of pore branching. It is believed that first the upward branching will quench and after that, when the current density will be small enough, the downwards branching will tend to stop as well. Thus, after some time the number of pore tips will be nearly constant in time. What happens after that will be discussed in the next subchapter.

Due to the anisotropic features exposed by the pores forming the domains, it can be assumed, as in the case of 'normal' crystallographically oriented pores, that dissolution is dominated by direct dissolution of the material and not via oxide formation. The reason why in GaAs no curro pores have been observed can be attributed to the fact that GaAs oxides in strong acidic solutions are much more unstable as compared with those of InP or GaP. In this way even at very high current densities chemical dissolution of the oxide is faster than the oxide formation itself. As a result, in GaAs isotropic (amorphous) oxide dissolution at pore tips, responsible for the formation of the current-line oriented pores, can not be achieved even at high current densities. Please, note that similar domains have been observed also in InP and will be discussed in Chapter 7.

5.4   Tetrahedron-like Pores in (100)-oriented GaAs

5.4.1   Experimental Conditions

The experimental conditions are nearly identical to the ones presented in section 5.3. (100) oriented, n-type GaAs ($n = 10^{17}$ cm^{-3}) samples have been anodized at high constant current densities for a longer time. The anodization was performed in aqueous 5-10% HCl solutions.
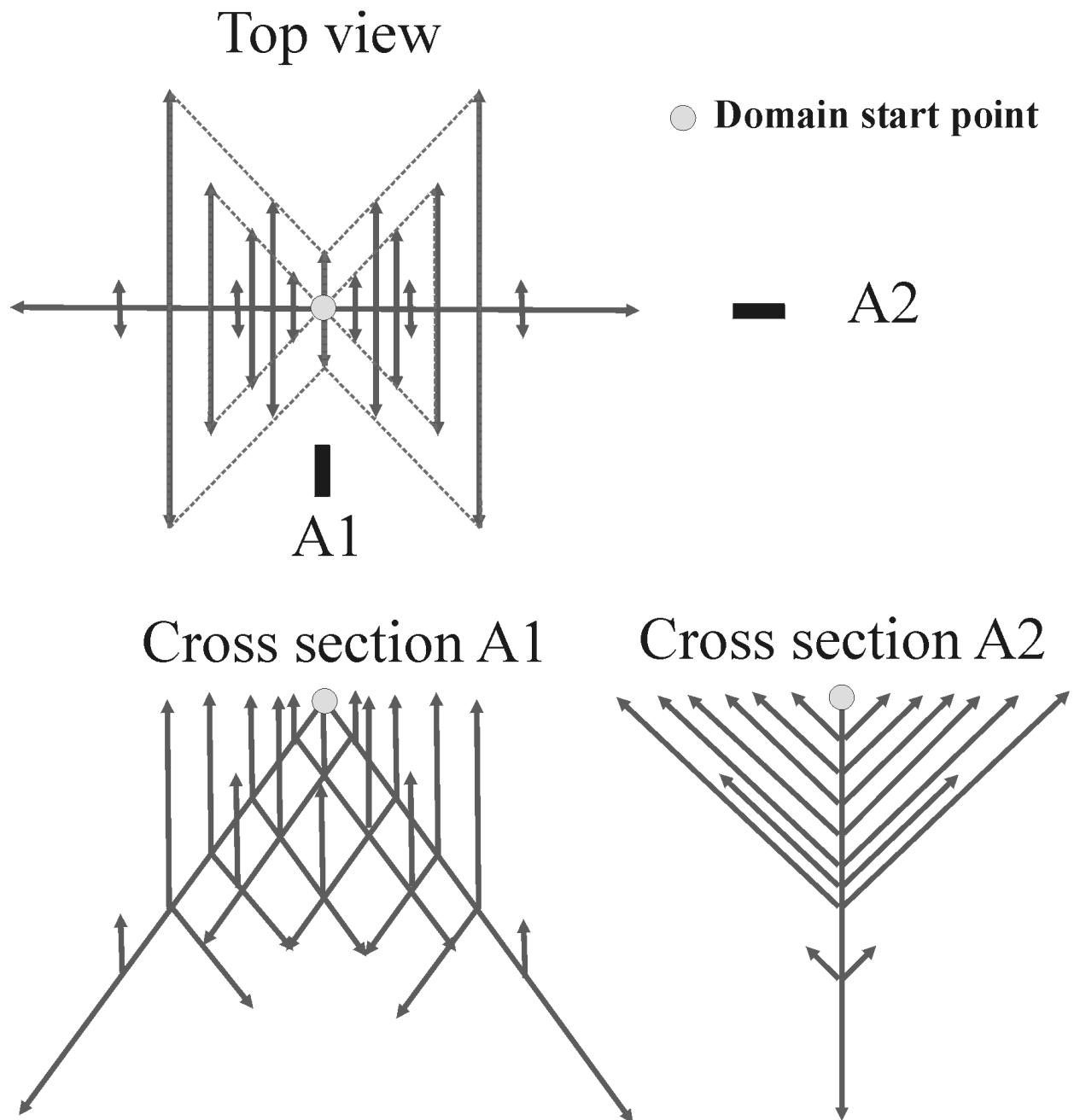
Figure 5.12: *Schematic representation of domain formation in (100) n- GaAs obtained at high externally applied current densities; The plot shows three views of one and the same domain: one from the top, and two reciprocally perpendicular cross sections. The arrows at the end of the lines designate the directions of growth (upwards or downwards) along the ⟨111⟩ B directions. The crystallographic planes (i.e. {011} planes), within which the two different directions (upwards or downwards) are growing, are reciprocally perpendicular;*

The orientation of the samples was (100). After the anodization the samples have been rinsed in acetone and deionized water and investigated by a Philips XL series Scanning Electron Microscope working at 10 kV.

5.4.2   Results and Discussions

Up to now we discussed three types of porous morphologies observed in III-V compounds:

▌ Crystallographically oriented pores or crysto pores.

▌ Current-line oriented pores or curro pores.

▌ Domains of crystallographically oriented pores.

All these types of pores have their particularities. One of the most evident particularities of the crystallographically oriented pores is that they grow along definite crystallographic directions and expose stable and smooth pore walls that also represent a definite set of crystallographic planes. In all experimental descriptions presented above, only the anodization current, the electrolyte concentration, temperature and the etching time was specified and nothing has been said about the measured voltage across the *semiconductor-electrolyte* interface. As it was already mentioned in Chapter 2, the voltage drop across the *semiconductor-electrolyte* junction is a very important parameter which provides information about what is going on at the interface.

In Figure 5.1 on page 44 a cross section was presented taken from a porous layer fabricated at a current density of 4 mA/cm^2. In that case, with the exception of the phase of pore nucleation (up to 5 min), the monitored voltage (under galvanostatic control) between the *RE* and *SE* electrodes has a relatively constant value during the whole experiment. As discussed, the pores are oriented along $\langle 111 \rangle B$ directions and possess a well developed triangular prism-like shape with $\{112\}$ planes as facets [56, 67].

However, the time dependence of the *RE-SE* voltage shows some particular changes when the external current density is sufficiently increased. After an initial interval of nearly constant voltage at the beginning of the etching process (during which the domains of crystallographically oriented pores develop) a sharp increase in the monitored voltage occurs. At the current density $j = 85 \ mA/cm^2$, for instance, a sharp voltage jump can be observed after approximately 75 min of etching in 5% HCl electrolyte solution (see Figure 5.13). As proved by SEM investigations, this sudden change in the voltage across the *semiconductor-electrolyte* junction is a sign of a new phase of pore growth.

Figure 5.14 shows in cross section the pores after the voltage jump, taken from a sample anodized at a current density of 85 mA/cm^2. They still form an angle of 54.5^o with the normal to the surface, *i.e.* they continue to grow along $\langle 111 \rangle B$ crystallographic directions, as they did before the voltage jump. However, the pore walls are not smooth anymore as those presented in Figures 5.1 on page 44, but show evident diameter modulations. The modulations look like chains of interconnected tetrahedral voids. Three of the four facets of the tetrahedron can be easily observed in Figure 5.14b. Taking into account that no influence from the exterior has been applied to the system during the etching process, this clearly indicates that a self-induced diameter oscillation of individual pores takes place at this stage of pore growth.

It is noteworthy to mention that a similar morphology has been observed earlier in Si [68], but instead of tetrahedron-like voids, an octahedron-like structure develops in Si because the 'stopping
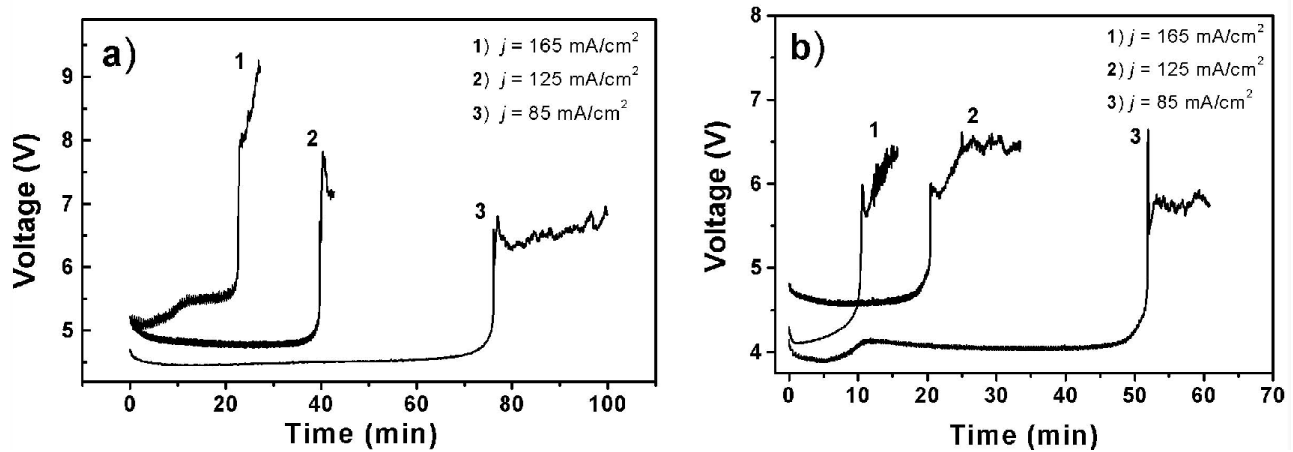
Figure 5.13: *Time dependence of the measured voltage during the anodization process at different high external current densities: a) HCl 5%; b) HCl 10%. The moment when the voltage jump occurs depends on the current density and electrolyte concentration. The increase in the external current density as well as the increase in the electrolyte concentration leads to the decrease in the time required to reach the conditions which cause the external voltage jump.*

planes' are different from those in GaAs (see Figure 5.15 for comparison). In Si the growth of octahedron pores starts with a pyramid like cavity exposing four stable {111} planes. The tip of the pyramid is oriented along one of the ⟨100⟩ directions. In most cases this pyramid is simply sliding continuously along ⟨100⟩ directions forming the pores with smooth walls. However, there are situations determined by the etching conditions when the pyramids will not slide continuously along the ⟨100⟩ directions, but will move in 'steps' resulting in a octahedron like pores.

In the case of GaAs the situation is slightly different. Due to the difference in dissolution rate between {111}A and B planes, the pores will grow along ⟨111⟩B direction and expose {111}A planes forming a tetrahedron-like tip. A continuous sliding of the tetrahedron-like tip will generate smooth crystallographically oriented pores (see also section 5.1). However, the step like movement of the tip will generate the tetrahedron-like pores. A schematic mechanism comparing and SEM pictures of tetrahedron- and octahedron-like pores in GaAs and Si are presented in Figure 5.15a and b [68].

The observation of self-induced diameter oscillation, *i.e.* tetrahedron and octahedron pores, in quite different semiconductors like Si and GaAs (see Figure 5.15c and d), indicates, that the general mechanism governing pore formation in these materials is similar. In Si the observation of the octahedron-like pores was explained using the aging concept introduced by the current burst model (see section 3.6). Thus, we will try to use the 'aging' concept as well, to explain the formation of tetrahedron-like pores observed in GaAs.

Aging in this case describes the passivation of pore tips as a function of time and current density. It is well known that H- passivation hinders the oxidation of Si and is strongly dependent on crystallographic planes. For example, {111} planes are most easy to passivate and as a consequence are the most stable against dissolution. This explains also why in porous Si the observed octahedron-like pores expose {111} planes as most stable, the so-called 'stopping planes'. However, in GaAs it is the Cl- passivation rather than a H- passivation which impedes oxidation and thus the process of local dissolution [60].
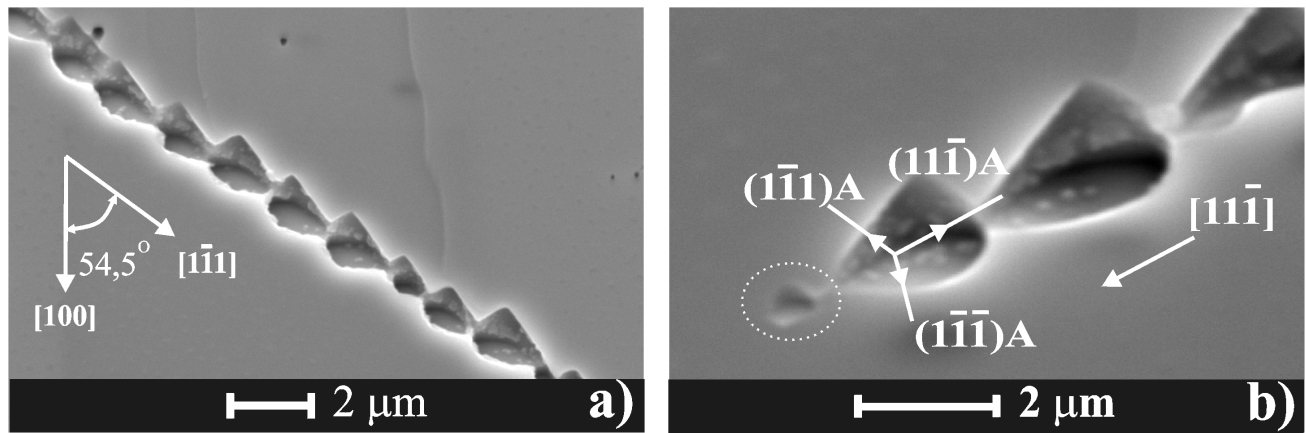
Figure 5.14: *Examples of tetrahedron-like pores in GaAs; a) Tetrahedron-like pores obtained on (100)-oriented GaAs ($n = 10^{17}$ cm^{-3}) at high current densities $j = 85$ mA/cm^2 in 5% HCl aqueous electrolytes after 75 minutes of anodization. They grow along $\langle 111 \rangle B$ directions similar with the usual crystallographically oriented pores; b) The tetrahedron-like pores expose the $\{111\}A$ planes;*

A detailed description of the process assumed to be responsible for the formation of tetrahedron-like pores in GaAs is presented in Figure 5.16. Consider the situation when the current density at a pore tip (j_{tip}) has reached a critical low value j_{min}, where nearly the whole surface of the pore tip (A_{tip}) is passivated ($t < t_1$ in Figure 5.16). The mechanism how the system reaches the critical current density will be explained later. Bearing in mind that the experiments were performed in a galvanostatic regime, the same current must flow through the sample all the time and in all conditions. Thus, it can happen that in order to maintain a constant high current through the whole sample, the system will be forced to 'abandon' a significant part of the strongly passivated surface of the tip and to concentrate the current flow only through a small area at the tip of the pore in order to increase the current density, which in turn decreases significantly the passivation ($t = t_1$ in Figure 5.16). Therefore on the diagram in Figure 5.16 at $t = t_1$ sharp steps for S_{tip} (down) and j_{tip} (up) are sketched.

The reason why the system chooses the small area end of the tip is that here the electric field strength is much higher due to the curvature of the pore tip (see section 3.4) and as a consequence it is easier to break the passivation. Immediately after t_1 a small spherical cavity at the tip of the pore is formed (see the dash circle in Figure 5.14b). At this stage the cavity does not expose any crystallographic planes, no preferential passivation is present and the reaction on the surface of the cavity can be considered to be kinetically controlled. This means that due to dissolution the surface of the sphere will increase with time in a quadratic manner (sphere), while the current density at the tip remains constant ($t_1 < t < t_2$ in Figure 5.16).

Consequently, during this period of time the value of the current (not to mix up with current *density*) $I = j_{tip} \cdot S_{tip}$ will increase as the surface does. Nevertheless, taking into account that the tetrahedron-like pores begin to grow far below the surface, the current I will increase only up to a certain maximum value (I_{max}), which in fact is defined (limited) by the diffusion of the species (reducing, oxide dissolving and reaction products) to and from the pore tips. Because I_{max} is the maximum current value the system can transport through one pore, it will try to keep $I = I_{max}$ constant for a while ($t_2 < t < t_3$). Since the surface of the sphere will continue to grow
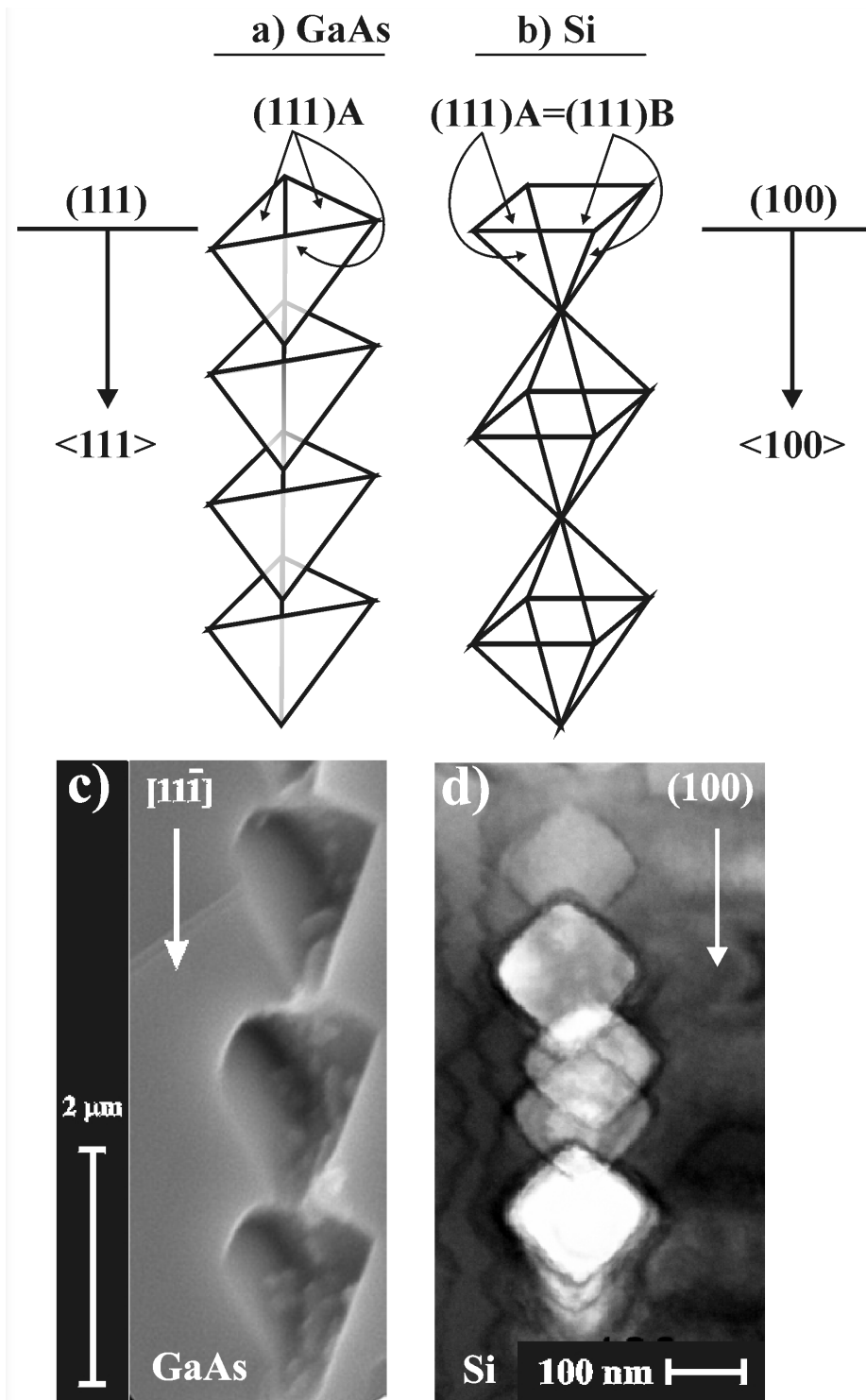
Figure 5.15: *Tetrahedron and octahedron-like pores in GaAs and Si. a) In GaAs four {111}A planes form a tetrahedron cavity which at high current density, after a certain period of time, will start to move in steps along ⟨111⟩B directions. b) In Si, on the other hand, eight {111} planes form an octahedron cavity which moves in steps along the ⟨100⟩ direction. c,d) SEM pictures showing a direct comparison between the observed in GaAs and the similar octahedron-like pores observed in Si. This step-like moving is explained in the framework of the current burst model by means of the aging concept. The picture taken from octahedron-like pores in Si is reproduced with the kind permission of Dr. C. Jäger and Prof. Dr. W. Jäger, University of Kiel.*
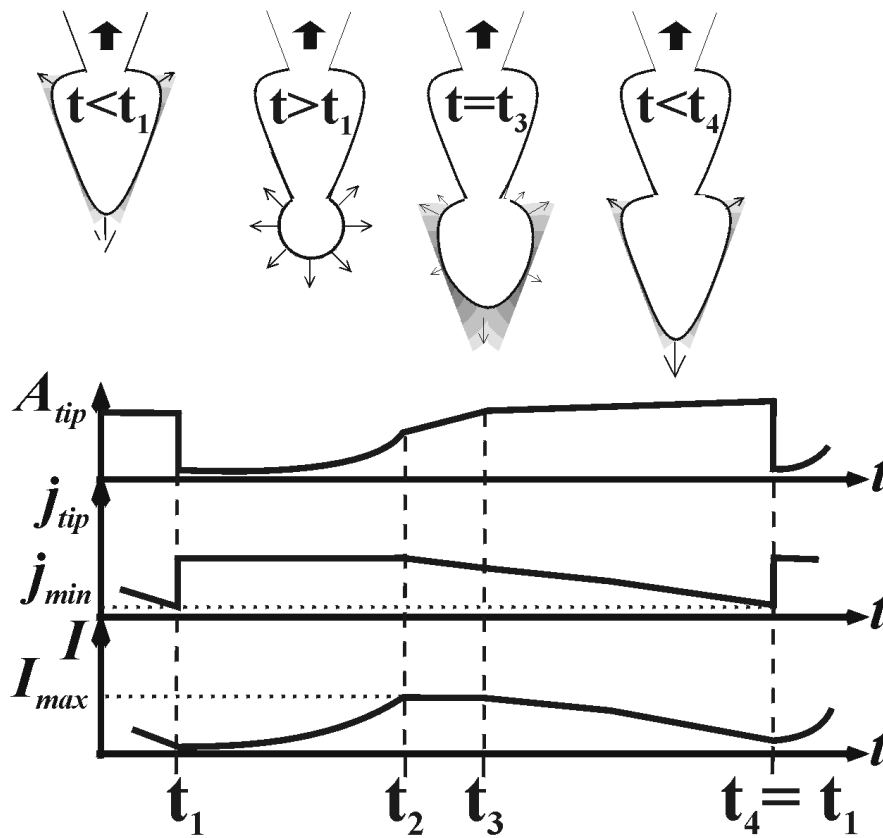
Figure 5.16: *A schematic representation of the process explaining the tetrahedron-like pore formation according to the 'aging' concept. Time t_1 - nearly the whole surface of the pore tip is passivated and a new tetrahedron starts to grow at the very tip of the pore (j_{tip} jumps from the minimum to the maximum value). The new tetrahedron starts to grow as a small spherical cavity whose walls are not passivated at all. The current density is considered to be constant during this period. Time t_2 -The surface of the sphere (A_{tip}) and the current $I = j \cdot A_{tip}$, which is flowing through it, will increase up to the maximum value - I_{max} (diffusion determined), which can be carried through one pore. Due to the fact that the sphere at some moment will begin to expose small areas of $\langle 111 \rangle$ A planes (which can be easily passivated) the current density will start to decrease until the surface will again be totally passivated and a new cycle will start.*

(dissolution takes place) the current density for this cavity starts to decrease and according to the 'current-burst' model the surface passivation will increase. Certainly the $\{111\}A$ planes will be passivated more easily. Thus, after the diffusion limited current I_{max} is reached and the current density at the pore tip begins to decrease again, the spherical cavity will begin to expose these planes ($t > t_2$) transforming itself into a tetrahedron-like cavity. The current density j_{tip} will continue to decrease until it reaches again the critical value and consequently a new step in A_{tip} and j_{tip} will occur ($t = t_4$), *i.e.* a new tetrahedron begins to grow.

As it can be observed from Figure 5.16 on page 64, the current at pore tips I varies in time, following the phase of the growth of the tetrahedrons. Note that within the framework of the 'current-burst' model one of the general assumptions is that the current at the pore tip also oscillates, but due to random phases of the oscillations at different pore tips, a constant macroscopic current across the sample is normally observed.

This model allows to explain two additional observations:

a) The tetrahedron-like pores are observed only after a definite interval of time from the beginning of the experiment.

▷ At the beginning of the experiment the current density at pore tips is much higher than the critical value j_{min}, therefore the system needs some time before reaching it by successive branching of the original pores (domain formation).

b) The system can reach the critical current density at pore tips only at high externally applied currents;

▷ As discussed in section 5.3 at high current densities the pores initially nucleated at the surface of the sample are branching and form domains. If a constant external current is applied to the sample, the current density at pore tips depends on the number of pore tips (pores) into the substrate. Thus, due to branching, the number of pore tips in the substrate increases in time, which means that the current density at the pore tips is not constant but decreases in time. Eventually, the decrease of j_{tip} with time allows the system to reach the critical current density j_{min} at the pore tips, which leads to the formation of linked tetrahedrons as explained above. On the other hand, at low values of the external current the branching effect is practically absent or strongly reduced, therefore the number of pore tips is constant in time and so is the current density at the tips, *i.e.* it can not decrease to the critical value where the tetrahedron pores begin to grow. Also, the diffusion limited current I_{max} (extremely important for the model of tetrahedron formation) at low external current densities can not be achieved because the amount of dissolved material is small as compared with the case of high external current densities.

In order to test experimentally the above explanations, the influence of the electrolyte concentration and current density on the time interval from the beginning of the experiment until tetrahedron-like pores begin to grow was investigated. Figure 5.13 shows the time dependence of the voltage at different current densities for two electrolyte concentrations, 5 % HCl (Figure 5.13a) and 10 % HCl (Figure 5.13b). The time needed for the system to reach the tetrahedron regime of pore growth shortens both by increasing the external current density and the electrolyte concentration.

These observations can be explained by a higher passivation rate for a higher concentration of Cl^- ions in the electrolyte. During the anodization, comparable passivation states (equal number of passivated bonds on surface unit) for two different concentrations of the electrolyte $c_1 < c_2$, are obtained if the current densities that must flow through pore tips satisfy the relation $j_1 < j_2$. Consequently, the critical value j_{min} will be higher in more concentrated solutions ($j_{min1} < j_{min2}$). As was explained above, the actual current density at pore tips decreases in time (due to branching) from the initial value j_{init} at the surface of the sample until j_{min} is reached and the system enters a new state indicated by the voltage jump. So, the time needed to reach j_{min2} is shorter than that required to reach j_{min1} because $j_{init} - j_{min2} < j_{init} - j_{min1}$. This is in good agreement with the results presented in Figure 5.13a and b.

The decrease of the time necessary for the system to reach the tetrahedron-like pore regime when increasing the externally applied current density can be explained if taking into account that branching of pores occurs more frequently at high externally applied currents and is nearly

absent at low currents. Thus j_{tip} decreases faster at high externally applied currents than at low. Consequently j_{min} is reached after a shorter period of time.

The observed architecture of pores offers new insights into the mechanism of pore formation in GaAs, and also represents an interesting variety of possible pore structures for applications. The pores obtained at high current densities after the voltage jump look like asymmetrically-modulated microchannels, and according to the new concept of drift ratchet [13], could be suitable for designing micropumps to separate micrometer-size particles dissolved in liquids.

5.5   Summary and Conclusions to Chapter 5

The most common type of pores in III-V compounds are the crystallographically oriented pores which grow along $\langle 111 \rangle B$ directions. Such kind of pores have been observed in GaAs, InP as well as in GaP. The crystallographically oriented pores have two anisotropic features: their direction of growth and their triangular shape. This fact demonstrates that direct dissolution is dominant during the growth process of such kind of pores.

However, depending on the etching conditions other types of porous morphologies can be obtained: catacomb-like pores in GaP (see Chapter 8), tetrahedron-like pores and domains of crystallographically oriented pores in GaAs, current-line oriented pores InP and GaP.

The current-line oriented pores grow perpendicularly to the equipotential lines of the electric field in the sample and do not expose strong anisotropic features characteristic to crysto pores. Therefore, it is assumed that dissolution via oxide formation is the dominant dissolution mechanism in this case.

The most determinant parameter is the applied current density. At low current densities the crystallographically oriented pores dominate, whereas at high current density other types of pores develop. Nevertheless, other parameters like electrolyte type and concentration, temperature, pH value prove to influence the characteristic of the pore morphology. For example the concentration of the electrolyte and passivation effects determine when the tetrahedron-like pores will start to grow. We will see that some other effects like self-induced voltage oscillations or the nucleation layer of the current-line oriented pores are temperature, current density and electrolyte concentration dependent.

Chapter 6

Voltage Oscillations - a Self-Organized Process during Pore Formation

6.1 Voltage Oscillations at Semiconductor Electrodes

Oscillations in chemical as well as in electrochemical systems are well known [69]. For semiconductor electrodes the most well known oscillations are the current oscillations in time during the electropolishing of Si [70]. The investigation of oscillations at different etching conditions supplied a lot of information about the mechanism of Si dissolution. Now it is well accepted by the scientific community that oscillations at Si electrodes are related to a periodic process of oxide formation followed by dissolution. However, how does this periodic process occur in reality is still under discussion.

According to the current burst model (see section 3.6) the macroscopic oscillations in the electropolishing regime can be treated as a self-organized process of some local oscillators, *i.e.* current bursts. The essence of self-organization is that the structure/behavior of the system develops without explicit pressure or constrain from the outside world. Self-organized processes have been observed also in the pore formation regime, *e.g.* in Al_2O_3 [71]. Illustrative for III-V compounds in this regard are the already discussed tetrahedron-like pores in GaAs, which begin to grow without any special constrains from exterior [72], or the domains of crystallographically oriented pores (see Chapter 5).

Taking into account that pore formation can be considered as a particular case of electropolishing, *i.e.* electropolishing at pore tips, the current burst model predicts that material dissolution at pore tips also occurs in an oscillating fashion. However, even if there is an oscillation at the pore tip, it does not mean that these oscillations will be observed externally. Additional "ingredients" are required for this purpose. InP was the first semiconductor where *oscillations in the pore formation regime* were reported [56]. As in the case of electropolishing, the investigation of oscillations during pore formation can provide important information about the mechanism of pore formation.

6.2 Voltage Oscillations: Experiment and Observations

6.2.1 Experimental Conditions

Investigation of voltage oscillations has been performed at high constant current densities (galvanostatic regime), *i.e.* $j > 10\ mA/cm^2$, in aqueous HCl electrolytes at different temperatures and concentrations. The material was (100) and (111), S-doped n- InP. However, from the oscillation point of view no difference between the two orientations was observed, mainly due to the current-line nature of the pores at which the oscillations are observed. The doping level of the samples were between $10^{16} - 10^{18}\ cm^{-3}$. For description of the set up see Chapter 4. The anodized samples have been rinsed in acetone and deionized water and consequently investigated by a Philips XL series Scanning Electron Microscope working at an accelerating voltage of 10 kV.

6.2.2 Morphology and Voltage Oscillation Observation

By anodizing InP samples under galvanostatic conditions at current densities higher than $j = 10\ mA/cm^2$ an interesting behavior of the voltage measured between the sample and the Pt electrode in the electrolyte (RES and REE) was observed for the first time. For low doped samples, *i.e.* $n = 1.5 \cdot 10^{16}\ cm^{-3}$, at the beginning of anodization the voltage usually increases monotonically from 0 to about 60 V. If the current density is high enough, stable voltage oscillations can be observed as illustrated in Figure 6.1a. The cross sectional SEM image of a porous sample obtained under these etching conditions is shown in Figure 6.1b.

The first conclusion we can make is that the pores are current line oriented, *i.e.* they grow mainly perpendicular to the surface and not along $\langle 111B \rangle$ directions as the crystallographically oriented pores do (see section 5.1). An additional feature which was not observed at current-line oriented pores anodized at constant voltages (see section 5.2 and Chapter 7) is the strong modulation of pore diameters. The local increase of the pore diameter will be called 'a pore node'.

Comparing Figures 6.1a and b shows that each horizontal set of nodes is directly coupled to one voltage peak. The voltage maxima and the corresponding pore nodes are marked in Figure 6.1a and b as P1 to P22 (note that Figure 6.1b shows only the nodes from P4 to P22). Thus, a second short conclusion is that the macroscopic oscillations occurred as a result of a synergetic behavior of the pores, *i.e.* the pores interact somehow with each other (see later in this chapter) and together "force" the voltage to oscillate.

Figure 6.1 shows that during 10 min of etching a porous layer with a depth of nearly 60 μm was obtained. Thus, the growth velocity for the current-line oriented pores is much higher than the usual growth rate of the crystallographically oriented pores or the macropores in Si (in the range of 1 $\mu m/min$). The main reason for the high growth rate of the current-line oriented pores is the high current density and the easy dissolution of InP oxides in acidic solutions. The direct correlation between the voltage maxima and pore nodes offers the possibility to calculate the rate of the pore growth. Figure 6.1a allows to calculate the time interval between two voltage maxima, whereas Figure 6.1b allows to estimate the growth depth during the corresponding period.

Combining both numbers, Figure 6.2 shows that the rate of pore growth decreases from nearly 10 $\mu m/min$ at the beginning to approximately 5 $\mu m/min$ at the end of the experiment (after 10 min). The retardation of pore growth, in spite of the fact that the electrolyte was continuously pumped through the cell, can be caused by the continuously decreasing diffusion flux (transport)
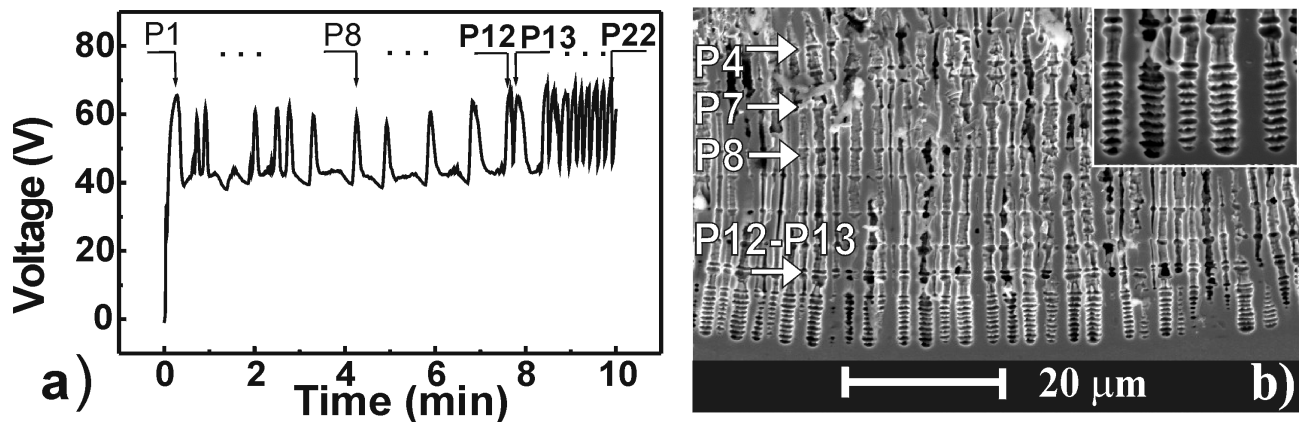
Figure 6.1: *Data taken from an (100) n- InP sample with $n = 1.5 \cdot 10^{16}$ cm^{-3} anodized at a current density of $j = 100$ mA/cm^2. a) The observed macroscopic voltage oscillations in time; b) Cross-sectional SEM of the sample. The inset shows the magnification of the nodes at the bottom of the porous layer;*

of chemical species from and to the pore tips. At the beginning of the experiment (etching in the vicinity of the initial surface) more oxide dissolving species were available for the dissolution while in depth the number of oxide dissolving species, provided by diffusion, decreases and consequently the growth rate goes significantly down.

However, in a galvanostatic experiment the amount of consumed charges per unit of time at the beginning as well as at the end of the experiment should be constant. Therefore, the pore growth rates should be constant in time as well, which is in contradiction to what was experimentally observed. These contradictory observations can be explained in two ways:

▸ The valence of dissolution increases strongly in time. Valence means the amount of charge which flows through the external circuit, necessary to dissolve one In-P couple (pair).

▸ Or, the diameter of the pores increases in time, *i.e.* an increased lateral growth occurs.

It is highly probable that the valence of dissolution can not increase so strongly as to decrease the pore growth rate by a factor of two. This follows because the pores with self-induced modulated diameters are current-line oriented pores and thus the dissolution at the tips of the pores proceeds

Figure 6.2: *The rate of pore growth during the anodization of InP at constant current densities. The rate decreases due the lack of oxide dissolving species at the tips of the pores (diffusion problems) and a consequent increase of pore diameters. (100) n-InP, $n = 1.5 \cdot 10^{16}$ cm^{-3} anodized at $j = 100$ mA/cm^2.*
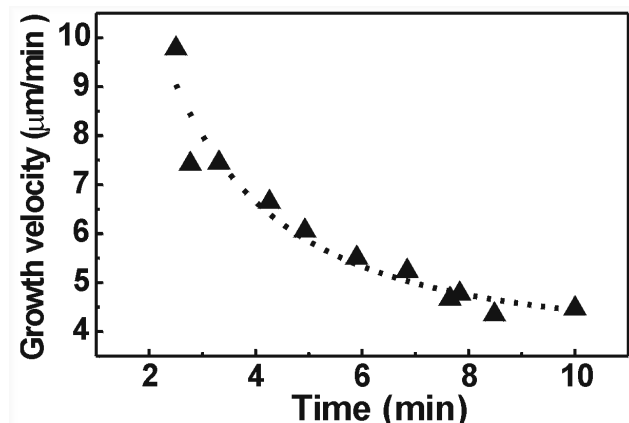
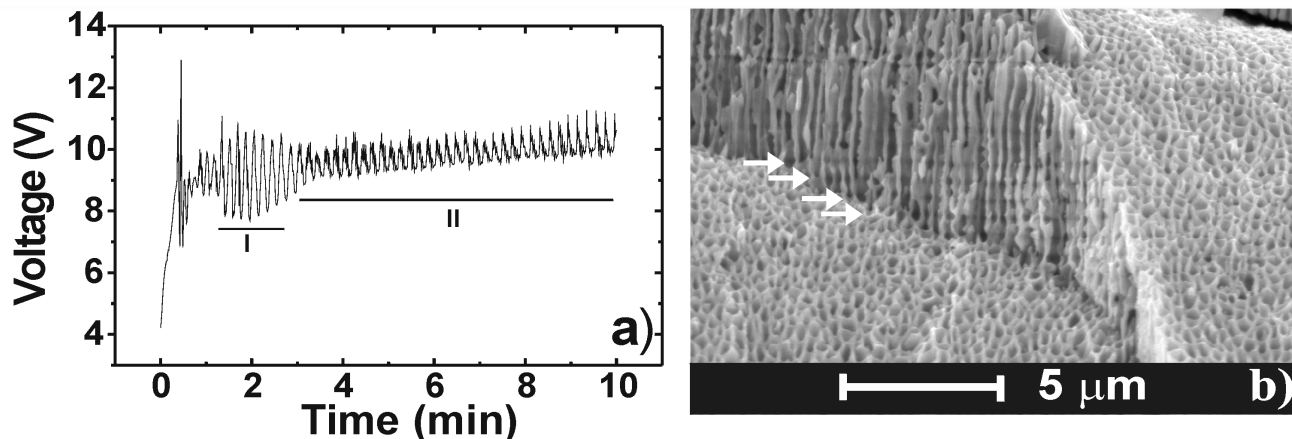Figure 6.3: *Data taken from a n- InP sample with $n_2 = 3 \cdot 10^{17}$ cm^{-3} anodized at a current density $j = 100$ mA/cm^2. a) Voltage oscillations; b) SEM image in cross section.*

mainly via oxide formation. Therefore the valence of dissolution should have its maximum value during the whole experiment, *i.e.* eight holes per In-P atom pair. On the other hand in Figure 6.1b it can be observed a general tendency of the diameters (between two consecutive nodes) to become bigger as the pores grow into the depth of the substrate. Therefore, it is more probable that the decrease in the pore growth rate is a result of the increase of pore diameters.

Voltage oscillations have been observed also for InP samples with a higher doping level $n_2 = 3 \cdot 10^{17}$ cm^{-3} (see Figure 6.3a). In these experiments the amplitude of the oscillation varies considerably during the time of anodization. Strong amplitude voltage oscillation (region *I* in Figure 6.3a) can be traced to a synchronous modulation of the pore diameters. In this case the SEM images in cross section show weaker horizontal trajectories (see Figure 6.3b) as compared with lower doped samples (see Figure 6.1b). However, both horizontal trajectories (marked by arrows) in cross section and the morphology of the porous layer as a function of depth are clearly visible. The correlation between pores, however, seems to be lost at larger depths. A main factor for the less stable oscillations at higher doping levels can be the difference in space charge region width, which is smaller than in the case of low doped samples. As we will see, the space charge region is supposed to induce the synchronization between the pores. Thus, less interaction between the pores will lead to less expressed external oscillations.

6.3 Temperature and Current Density Dependence of the Oscillating Frequency

As an indirect approach to gather additional information about the system can serve the detailed analysis of the observed external macroscopic oscillations. In what follows we will use the wavelet analysis, described in some more detail in Appendix C, to characterize the oscillations observed during the pore formation in n-InP. Such kind of analysis allows to investigate the changes in frequency of the oscillation at different stages of the pore formation.

The oscillation behavior of the etching system was investigated at different concentrations and temperatures of the electrolyte. Examples of voltage oscillations observed during the pore for-

mation process at two electrolyte concentrations and their corresponding Wavelet transformation maps are presented in Figure 6.4. The X and Y axis of the wavelet diagrams represent the (etching) time and frequency respectively. Please note that the frequency on the Y-axis is inverted, *i.e.* low frequency is up and high frequency is down on the axis. Each point (t, f) in the diagram has a definite color showing the value of the amplitude of the wavelet transformation taken between the investigated signal in the neighborhood of the moment t, with a "mother" function of frequency f. For a normalized amplitude between 0 and 1, the red color means amplitude 1, whereas the black color means zero amplitude. The amplitude will tend to its maximum if the frequency of the investigated signal in the neighborhood of the point t will match the frequency of the mother function.

In Figures 6.4b and d a continuous red region is easily observed. The red-color region represents the change in the dominant frequencies of the investigated signal along the time axis. From the diagrams it can be observed that in both cases the dominant frequency has a negative slope, or otherwise stated the dominant frequency is decreasing in time. Thus, at the beginning the frequency is higher than at the end of the signal, which are actually the beginning and the end of the experiment. The experiments show that the decreasing in time of the dominant frequency is always valid independent of the electrolyte concentration, temperature or doping level of the samples.

The frequency dependence on temperature and external current density is shown in Figure 6.5 on page 73. From Figures 6.5a, b, c and d it is obvious that the voltage oscillations are much more stable at low temperatures, and the amplitude as well as the stability of the signal is decreasing as the temperature is increased from $T = 5^o\ C$ to $T = 20^o\ C$. At $j = 26\ mA/cm^2$ and $T = 20^o\ C$, the oscillations nearly disappear.

In Figure 6.5e and f is shown the dependence of the average oscillations frequency on temperature and current density. As mentioned above, the dominant frequency is changing in time, therefore the average value in this case means $\frac{1}{2} \cdot (f_{begin} + f_{end})$, where f_{begin} and f_{end} are the oscillation frequencies at the beginning and at the end of the experiment respectively. The mean oscillation frequency increases both by increasing the current density and by increasing the temperature of the electrolyte. In addition, the frequency increases linearly with the current density. This means that the charge consumed per oscillation cycle (see the slope of the curves in Figure 6.5f on page 73) is constant and does not depend on the current density.

It is important to note that the observed data agree completely with qualitative predictions of the current burst model. As mentioned in Chapter 3.6, the dominant time constants of a current burst are the oxide formation time, oxide dissolution time and passivation time. Every parameter which will change the sum (t_{sum}, see Equation 6.1) of these time constants will consequently also affect the frequency of the external oscillations.

$$t_{sum} = t_{ch.-tr.} + t_{ox.-diss.} + t_{pass.} \tag{6.1}$$

For example, the decrease of the frequency as the pores grow into the substrate can be directly related to oxide dissolution time constant. As the pores grow into the substrate the oxide is less effectively dissolved due to diffusion losses, as a consequence t_{sum} increases, thus the frequency of the external oscillations decreases. On the other hand, for higher temperatures the oxide dissolution time constant decreases (t_{sum} decreases), the oxide is faster dissolved and thus the frequency should increase.
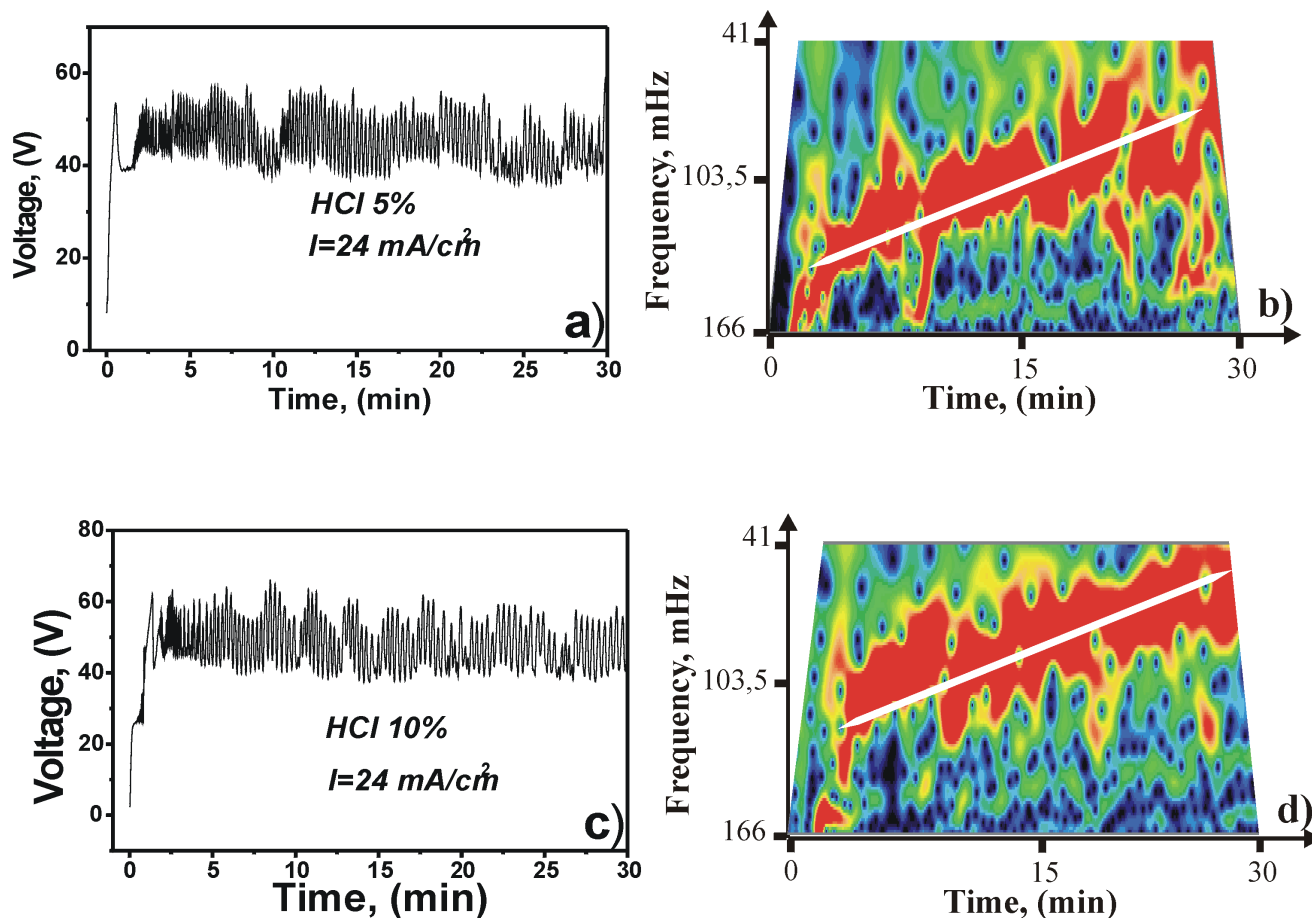
Figure 6.4: *Wavelet transformation used to analyze the external voltage oscillations observed during the formation of porous n- InP. a,b) the oscillation in time at $j = 24$ mA/cm^2 in 5% HCl aqueous electrolyte solution and the corresponding wavelet map; c,d) the oscillation in time at $j = 24$ mA/cm^2 in 10% HCl aqueous electrolyte solution and the corresponding wavelet map. The red regions (see the white lines) represent the dominant frequency in the spectra.*

Concerning the frequency increase as the current density increases, it is most probable that the passivation time constants is decreased in this case. Therefore t_{sum} decreases, resulting in an increased frequency. However this can be true only if the passivation time constant has the same order of magnitude as the oxide dissolving time constant. This is not the case in Si, where the time for oxide dissolution is much higher than the time for passivation. In InP however all three constants can be expected to be in the same order of magnitude, because of the instability of InP-oxides in acidic solutions.

6.4   Current Burst Model and Voltage Oscillations

The current burst model was the only model that predicted the oscillation behavior during the pore formation. In what follows a simplified model, based on the CBM, explaining the macroscopic oscillations in InP will be discussed.
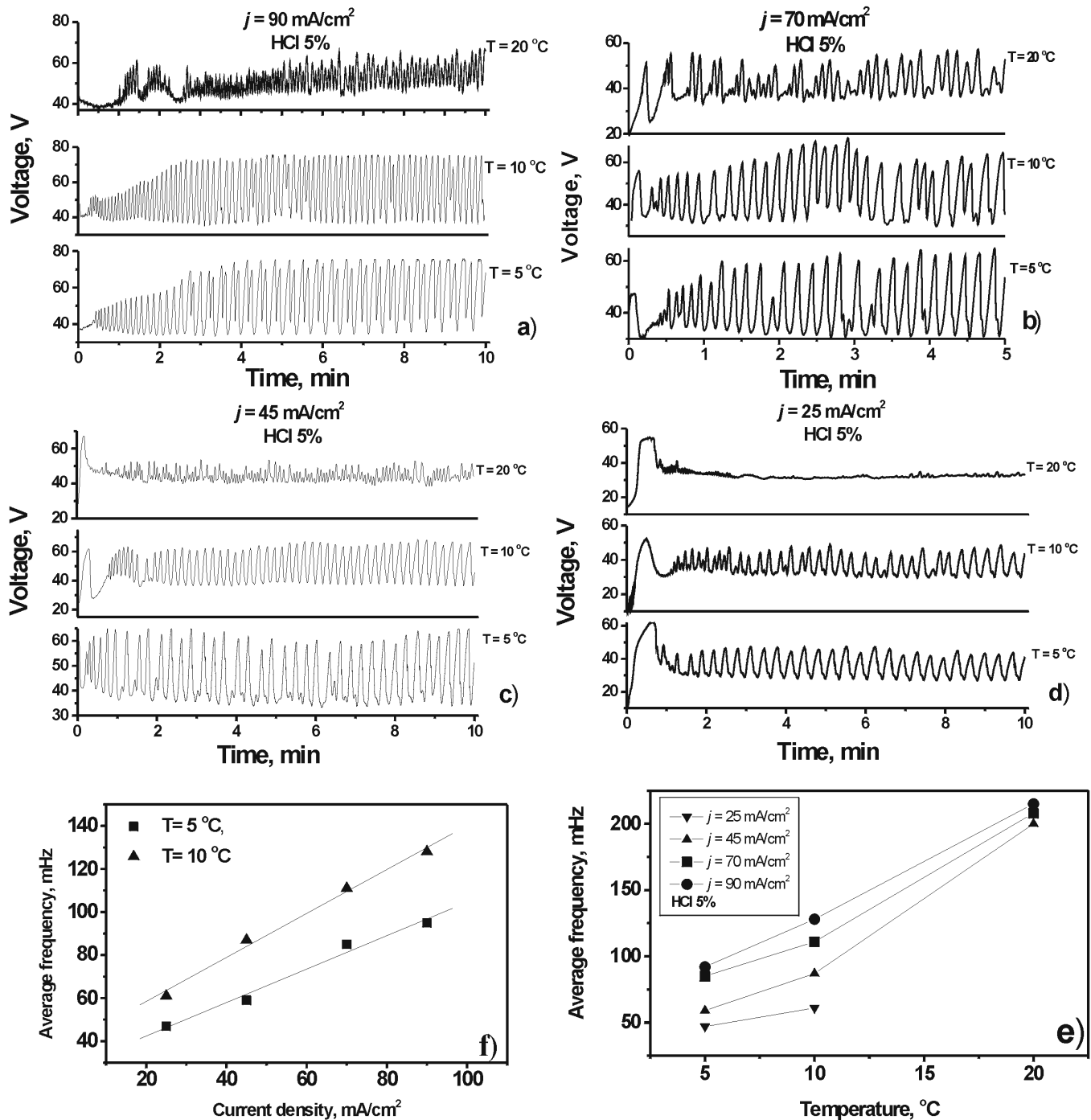
Figure 6.5: *Temperature and current dependence of voltage oscillations. a,b,c,d) The voltage oscillations observed at different current densities and three different temperatures. The oscillations are more stable at low temperatures. e,f) Dependence of the average frequency on the current density and temperature.*
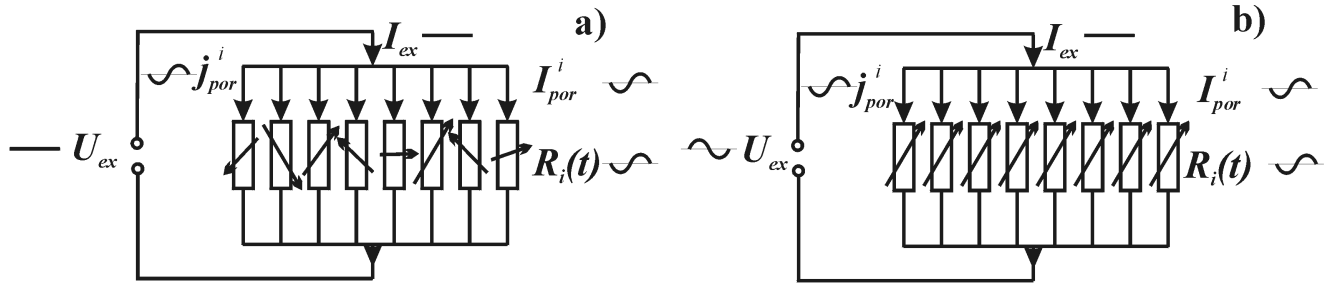
Figure 6.6: *A schematic representation of pores as oscillating resistors, where $R_i(t)$, I_{por}^i, j_{por}^i- are resistance, current and current density respectively of a pore; U_{ex}, I_{ex} - are externally implied current (constant) and measured voltage respectively. a) uncorrelated pores, j_{por}^i, I_{por}^i, $R_i(t)$ - oscillate, U_{ex} constant; b) synchronized pores, j_{por}^i, I_{por}^i, $R_i(t)$ - oscillate, U_{ex} and pore diameter are oscillating;*

In contrast to current oscillations which may occur locally under constant voltage conditions at pore tips (or, more generally, in arbitrarily large domains) but add up to a constant external current if the phases are distributed randomly, local voltage oscillations are not possible - the voltage along any path between the electrodes must be the same. Therefore, the voltage oscillation under constant external current conditions may be understood if we assume that the current at the pore tip generally oscillates while the diameter stays nearly constant, *i.e.* the current density oscillates, too. Both assumptions which we adopt, in general, without knowing the exact current oscillation mechanism at this point [54] are general properties of the current burst model. In terms of an equivalent circuit each pore may then be described by an oscillating resistor $R(t)$ with the average value $\langle R \rangle$ (Figure 6.6). The total current is given by switching all resistors, *i.e.* pores, parallel to the voltage/current source. As long as the phases of the oscillating resistors are uncorrelated, *i.e.* random, the total current will have some constant average value given by $\langle I \rangle = U / \langle R \rangle$, $U =$ voltage (see Figure 6.6a).

We consider each pore as a resistor defined as

$$R_{pore} = \rho \frac{L}{A} \tag{6.2}$$

where ρ is the resistivity of the oxide layer formed at the tip, L is the thickness of the oxide layer, and A is the surface of one pore tip. In a general case at least one on these parameters should oscillate in order to obtain an oscillating "pore-resistor". However, we will consider only the most evident case. Namely, A oscillates and L and ρ are constant. The oscillation of A is proved by the observed modulated pores (see Figure 6.1 and 6.3).

The system is varying this parameter in time aiming to minimize the resistance of the entire sample. The pores are closed packed and begin to interact via their space charge regions. The interaction between pores may influence the whole system, and a correlation (synchronization) between a certain number of pores can be achieved. Synchronization of pores in some parts of the sample (domains) or on the whole sample can only be achieved by correlating the phases of the oscillating resistors (see Figure 6.6b). The total current through a sample now will no longer average out to a constant value, but will also oscillate and the constant current condition enforced

by the external current source now can only be maintained if the voltage oscillates so that

$$\langle I \rangle = const = \frac{U_{oscilates}}{\langle R \rangle_{oscilates}} \tag{6.3}$$

This simple model can explain the observation. Of course, in a better approximation one would have to describe a pore by a more complex equivalent circuit containing capacitors. The displacement currents (Equation 6.4) have also to be compensated by the voltage adjustments, causing some degree of feedback in the system.

$$I_{cap} = C \cdot \frac{dU}{dt} \tag{6.4}$$

Nevertheless, the ultimate causes of the voltage oscillation are most probable intrinsic current oscillations together with some phase coupling or correlation between pores. This consideration, if turned around, gives a clue to the interaction mechanism between neighboring pores. If, by random fluctuation of pore diameters, pores come close enough to experience some kind of interaction, a feedback mechanism may start that leads to phase coupling of the pore growth states and by percolation to the formation of a synchronized domain.

This domain, however, may cover only a part of the specimen surface, *i.e.* regions with uncorrelated pores may also be found. Moreover, since percolation does not have to take place at every cycle of the oscillation - especially if the general conditions are just near the percolation point of the system - somewhat irregular voltage oscillations as shown in Figure 6.3a on page 70 are possible. The frequency of the voltage oscillation in this model can be determined by the frequency of the current oscillations inherent to the current burst model.

From the observation described above, it can be concluded that the voltage oscillation can be considered as an emergent property of strongly interacting pores, which means that the oscillation will immediately disappear if the pores stop interacting.

In case the pores do not interact, they have the freedom (more or less) to choose their own mode of growth: the frequency of current (not voltage) oscillation at the pore tip, diameter, velocity of growth etc. Actually, these parameters do not differ extremely from pore to pore, but nevertheless can be different and random. When the pores begin to interact, phase coupling can be one of the consequences. The interaction of pores restricts the available options to a small "volume" of its parameters space.

In essence the system moves to an "attractor" that covers only a small volume of the parameter space. An attractor is a stable state for the system and if the system starts from another state it will evolve until it arrives at the attractor, and will then stay fix in the absence of other effects. An attractor can be a point, a path, a complex series of states *etc.* All of them specify a restricted volume in parameter space. In our case the current-line oriented pores can be considered to be an attractor and the point at which the macroscopic voltage oscillations start can be considered as the evidence that the system has reached or is on the way to reach the attractor.

Actually, this point can be considered also to be a critical point of the system, where the system properties change suddenly, *e.g.* the pore matrix can go from a non-percolating to a percolating state and vice versa. The two states of the system on both sides of the critical point are usually defined as two different phases, pretty much in the same way as the 0^oC is considered the critical point between the solid and liquid state of water. Percolation in our system can be regarded as the arrangement of pores in such a way that a property, in our system the phase of

current oscillation, connects the opposite sides of the structure. This can be regarded as making a path in a disconnected pore array. The boundary at which the system goes from disconnected to connected is a sudden one and the main feature is that at this boundary the system has a correlation length that just spans the entire system.

In general terms for self-organization to occur, the system must be neither too sparsely connected (so most of units are independent) nor too richly connected (so that every unit affects every other). An autocorrelation-analysis of the pore positions shows an interaction between the pores of up to the sixth neighbor. This actually means that one pore can 'feel' or is connected up to six neighbors aligned along one straight line.

Thus, it can be concluded that in order to see voltage oscillations it is not necessary that each pore in the sample should interact directly with the rest of the growing pores. It is sufficient that each pore will interact directly with a limited number of its neighbors - making a domain. The domains will interact at their turn between them making bigger domains and so on until self-organization will appear on the whole sample.

6.5 Voltage and Diameter Oscillation: III-Vs vs. Si

Porous silicon has been studied in numerous papers [73], mainly due to the photoluminescence of micro porous silicon. Its preparation, generally based on electrochemical etching in a hydrofluoric acid containing electrolyte, is now controlled up to a remarkable level of reproduction. Another growing area of interest are macropores, first described 1990 by Lehmann and Foell, obtained using back side illumination for n-type silicon in an aqueous hydrofluoric electrolyte [74]. The first macropores in p-type Si were found by Propst and Kohl in 1994 using an organic electrolyte [75]. In the last few years many kinds of meso- and macropore morphologies have been obtained in n-type and p-type Si under varying, sometimes quite different, etching conditions.

There are few papers which compare pore formation mechanisms or the morphologies of pores in Si with pores in . Ross *et al.* compared the morphologies of pores in GaAs and Si, while Chazalviel et al. claim applicability of their diffusion instability model, originally introduced for silicon, also to pores in III-V compounds [76]. Two new papers on the comparison between porous morphologies in Si and III-Vs have been published recently by our group [77, 78].

A natural question is why external voltage oscillations have been observed up to now only in InP and GaP (see Chapter 8 for GaP)? As it was already been discussed the reason is that in these materials the pore density is normally very high and the pores can interact strongly via the space charge regions surrounding the pores. This leads to a synchronization of the oscillation currents inside the pores and consequently under galvanostatic conditions the voltage and diameter oscillations emerge. If this is true such kind of self induced voltage and diameter oscillations will be possible to observe also in Si, if a sufficiently high pore density will be possible to achieve.

6.5.1 Experimental Results and Discussions

By choosing special anodization conditions it was possible to observe voltage and diameter oscillations in Si as well (see Figure 6.7)[1]. Special anodization conditions in this context mean conditions for high pore density, *i.e.* Si samples (n-type, (2 - 6) $\Omega \cdot cm$, (100); p-type, (1-16) $\Omega \cdot cm$, (100))

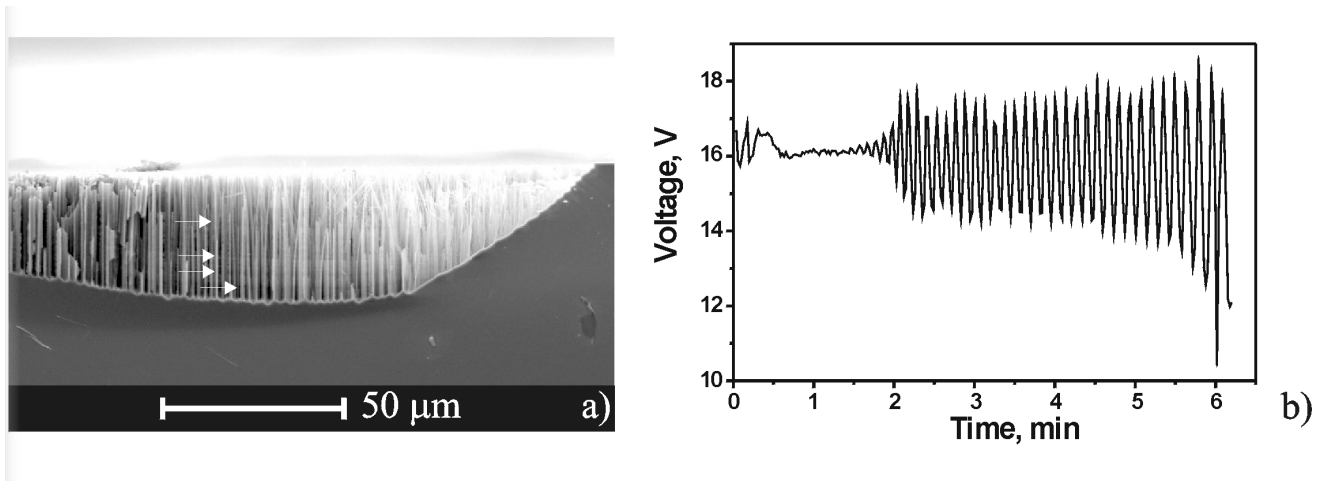[1]These experiments have been done in collaboration with Dr.-Ing. M. Christophersen

Figure 6.7: *Voltage and diameter oscillations observed in Si. The anodized area is 500 μm in diameter and is defined by a window in a nitride mask. The current which is flowing through this area was 0.2 mA; a) SEM picture in cross section taken from a p-type Si sample anodized at high pore density conditions. The arrows show the diameter modulations due to the interactions between the pores. The modulations are not so evident as in InP, mainly due to the fact that the quality of Si oxide is much higher and therefore is difficult to obtain a high self-induced amplitude of pore modulations; b) The corresponding external voltage oscillations observed during the anodization of the sample presented in a. Thus, as in the case of InP and GaP, also in Si is possible to observe self-induced voltage and diameter oscillations at high pore densities. This is a prediction of the current burst model which assumes that the current inside the pores always oscillates.*

were etched under the following conditions: 4 Volt etch bias, and galvanostatic current densities between $4-10\ mA/cm^2$. Front side illumination of n-type samples was used. The illumination was computer controlled to maintain a constant current density. For the generation of break through pores no illumination of the sample was used. The electrolyte was 4 wt.-% to 10 wt.-% HF in aqueous electrolytes (always with the addition of a tenside). The temperature of the electrolyte was fixed at 20^oC, and the etch time was 60 min for all experiments. For some experiments instead of water, dimethylformamide (DMF) as an organic solvent was used.

It was observed that when a nitride mask is used to delimit the anodized area of Si, the nucleation density as well as the etch rate near the edges of the mask is much higher compared to the case of a simple rubber O-ring. Therefore, small areas (500 $μm$ in diameter) defined by a nitride window were chosen for these special experiments.

In this way the area where the pore density is very high (near the edges of the mask) is higher or at least comparable with the area of low pore density (middle of the window). Taking into account that the nucleation in the middle of the window is slower as near the mask edge, it can be concluded that during the first few minutes of the experiment only the pores near the edges will grow and they will try to synchronize (having a high density), thus resulting in external voltage oscillations as was explained for InP. As the time goes on the synchronization will be lost because in the middle of the sample additional pores will start to nucleate, which do not have a high density. Consequently the pores nucleated in the middle of the window will be a source of desynchronization over the entire anodized area. Please note that in Figure 6.7b only the first stage of the voltage oscillations is presented, *i.e.* at the beginning of the experiment.

6.6   Summary and Conclusions to Chapter 6

Self-induced diameter and voltage oscillation show self-organizing features. The current burst model explains them assuming that the current inside one pore always oscillates and the interaction between the pores is so strong that current phases from different pores synchronize on the whole surface of the sample.

The frequency of the oscillation decreases in time, *i.e.* at the beginning the frequency is higher than at the end of the experiment. This is easily proved by the Wavelet transformation. The frequency also increases by increasing the current density, temperature and concentration of the electrolyte. At low temperatures the oscillations are much more stable. At relatively high temperatures and low current densities the oscillations can even disappear.

In spite of the fact that Si and III-V compounds are quite different, similar morphologies and growth mechanisms have been found for the pore formation. The most important similarities are the octahedron/tetrahedron structures and the self-induced voltage and diameter oscillations. Both can be explained by means of the current burst model. This demonstrates that some general principles can be applied in order to explain the pore formation in different semiconductors.

The main advantage of the studies comparing different porous semiconductors is the possibility to find new features which have not been observed before. A prominent example is the voltage oscillation in the pore formation regime observed in Si after the guiding rules from InP and GaP.

Chapter 7

Quasi-uniform and Uniform Porous Structures in III-V Compounds

The uniformity of porous semiconductor structure is a requirement if these structures are intended to be used *e.g.* as photonic band gap materials. The standard way for obtaining highly ordered porous structures in semiconductors is lithography, *i.e.* defining a pre-patterned surface. As already mentioned, on a clean surface the pores start to nucleate randomly, predominantly on bad passivated surfaces, *e.g.* at defects. Standard lithography allows to pre-pattern a whole wafer with windows in a thin layer of resists where the pores are intended to grow. Sometimes, in a second purely chemical step, shallow holes can be etched into the semiconductor through the windows. These holes serve after that as nucleation sites for the electrochemically etched pores.

If the characteristic dimensions of the mask, *i.e.* window diameter, distance between windows *etc.*, correspond to the 'internal dimensions' of the *semiconductor-electrolyte* system the pores will start growing at the artificial defects within the resist windows. Thus, it is possible to define *a priori* the exact arrangement of pores. In Si this method is extensively used for obtaining ordered 2D porous structures, *e.g.* for the fabrication of 2D photonic crystals [13].

In this chapter the possibility to obtain uniform porous structures in III-V compounds will be discussed, mainly by self-organization. Taking into account that self-organization does not result in ideally periodic structures, a tool is necessary to measure the degree of ordering in a self-arranged porous structure.

It is well known that diffraction patterns (DP), *e.g.* X-ray, TEM *etc.*, from classical crystals provide a way for studying the structure and uniformity of atomic crystals. Investigating the DP of different materials it is possible to distinguish between perfect, amorphous, textured *etc.* structures. In fact, diffraction patterns are nothing else but the image of the crystal in the reciprocal space, *i.e.* the Direct Fourier Transform (DFT) of the crystal. Using the Inverse Fourier Transform (IFT) it is possible to reconstruct the image of the crystal from its DP.

However, we are not going to use hardware methods like TEM or X-ray in order to generate DPs. We will numerically generate the DP of the porous structure (2D crystal), *i.e.* by taking DFTs from SEM images. Thus, a DP will be obtained calculating the direct 2D Fourier Transform from the pixel-array of SEM pictures. The structure of a DP, *i.e.* rings, spots *etc.*, will be the main characteristic for the arrangement of the pores. More details about the 2D Fourier Transform are discussed in Appendix D.
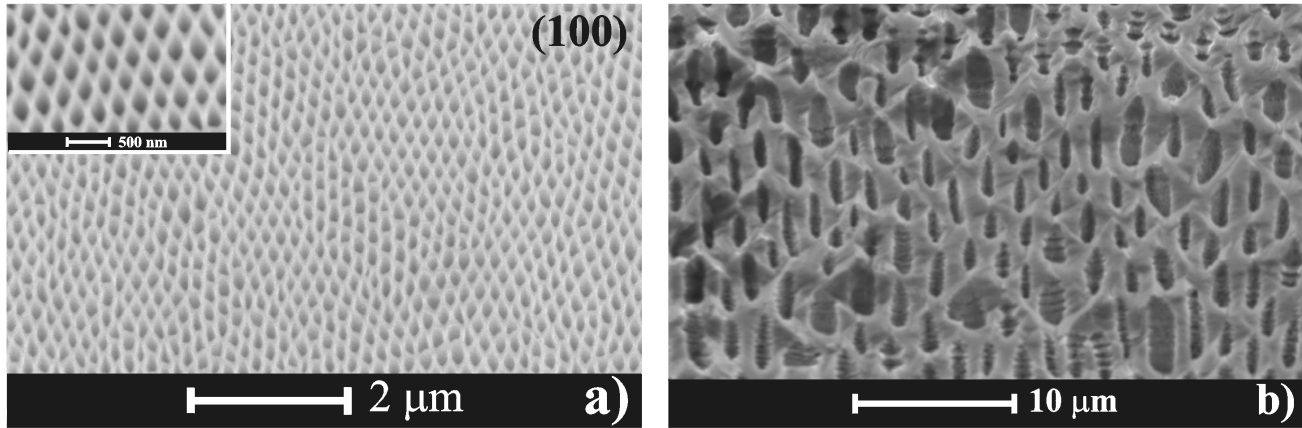
Figure 7.1: *Hexagonal arrangement of current-line oriented pores after the nucleation layer has been removed. a) Potentiostatic control. The inset shows a nearly perfect pore domain. b) galvanostatic control. The difference in pore diameters in a and b is caused by the doping level: $n = 10^{18}$ cm^{-3} and $n = 10^{16}$ cm^{-3} respectively. Please note in b the modulation of the diameters of the pores (galvanostatic control).*

7.1 Long Range Ordering of Pores Obtained by Self Organization in InP

7.1.1 Experimental Results

As already emphasized, in III-V compounds the only mechanism for hole generation, required for electrochemical dissolution during the pore formation, is junction breakdown or 'break through'. Two types of break through pores have been observed in n- InP up to now: crystallographically oriented pores and current-line oriented pores (see Chapter 5). In order to understand the self-organization mechanism of pores on large areas, we will mention once again the conditions of growth for the two types of pores.

Crystallographically oriented pores are usually obtained at low voltage/current densities, and like most break through pores in Si expose a high level of anisotropy. As indicated by the name, crystallographically oriented pores grow along a definite crystallographic direction, *i.e.* $\langle 111 \rangle B$. They have triangular shapes exposing three {112} planes [56, 67].

The second type of breakthrough pores, the current-line oriented pores, grow only at relatively high current densities and do not have preferential crystallographic directions of growth, *i.e.* they grow always perpendicularly to the equipotential lines of the electric field inside the sample, independent of the sample orientation. Depending on the etching conditions they also can still have slightly triangular shapes (see Figure 7.3b), but normally the shape tends to be round.

The most interesting properties are exposed by the curro pores, however not without the help of the crysto pores. An important feature of the curro pores is that they self arrange locally in a hexagonal closed packed lattice. Local self arrangement means that domains of nearly perfectly arranged pores can easily be distinguished. Such kind of domains with a hexagonal arrangement of pores are presented in Figure 7.1a, where the inset shows a higher magnification of a nearly perfect domain.

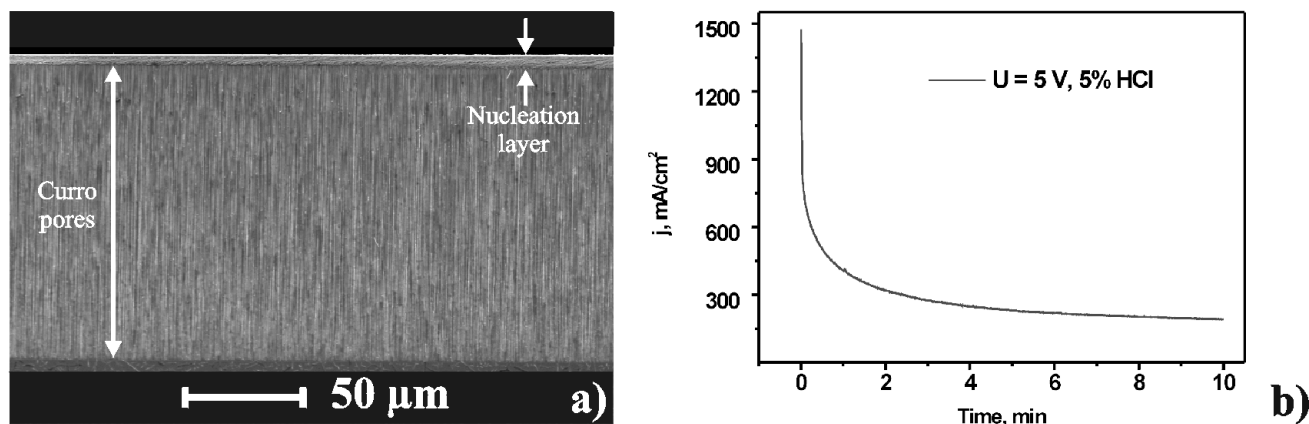Please note, that the current-line oriented pores obtained at high constant current densities

Figure 7.2: *a) The nucleation layer, i.e. crystallographically oriented pores, is followed by the layer of stable pore growth, i.e. current-line oriented pores; b) In a potentiostatic experiment the externally measured current decreases exponentially and not oscillations are observed. The exponential current decrease is due to diffusion limitations.*

(galvanostatic experiments) differ from those obtained at potentiostatic conditions. As it has already been discussed in Chapter 6 the pores obtained galvanostatically show strongly modulated diameters and external voltage oscillations due to synchronization between neighboring pores [56]. On the other hand, potentiostatically grown pores, at optimized etching conditions, expose smooth pore walls and no sudden change in pore diameters (Figure 7.2a) or externally measured current oscillations (Figure 7.2b) can be observed. As it can be observed from Figure 7.2b the current in a potentiostatic experiment decreases exponentially in time in a nearly perfect way. In spite of these differences, in potentiostatic as well as in galvanostatic experiments the pores arrange themselves locally in a hexagonal lattice (see Figure 7.1a and b).

However, the curro pores do not start growing in a hexagonal lattice immediately on the surface of the sample. The hexagonal arrangement will be always preceded (at least in HCl aqueous electrolytes) by a nucleation layer (NL). The NL layer is also porous and is made of crysto pores. A SEM micrograph illustrating the NL layer followed by a stable curro pore growth layer is presented in Figure 7.2a. The width of the nucleation layer is normally up to several microns and depends on the electrolyte concentration and voltage/current applied to the sample. It increases slightly by increasing the electrolyte concentration and by decreasing the voltage/current.

In order to see the current-line oriented pores and their arrangement into the depth of the sample, the NL must be removed. The NL layer can be removed purely chemically or mechanically. For example the NL in Figure 7.1 was mechanically removed. In this example the domains of current-line oriented pores are totally uncorelated *i.e.* each domain is more or less arbitrarily oriented with respect to its neighbors. Thus, if a notion from the classical atomic crystals is used, it can be intuitively assumed that the entire porous array can be regarded as a polycrystalline structure. As it has already been mentioned, a suitable method for proving this assumption is the 2D DFT using Fast Fourier Transform (FFT) analysis.

By means of FFT mainly two kinds of SEM micrographs have been analyzed:

� a) Micrographs taken from the surface of the sample, and

▶ b) Micrographs taken from the current-line oriented layer after the nucleation layer has

been mechanically removed.

For FFT analysis a large area of the porous array should be chosen. Figure 7.3a on page 83 presents a SEM picture taken immediately from the surface of the anodized sample, whereas the inset shows the frequency domain pattern, *i.e.* the diffraction pattern, generated by 2D FFT analysis. It is evident that the frequency domain pattern is a highly diffuse spot, which undoubtedly is a characteristic of a highly random arrangement of nucleated pores.

However, the DP changes if the FFT is taken from the top of a current-line oriented layer (see for example Figure 7.3b) after the nucleation layer has been removed. In this case the frequency domain pattern transforms into a diffuse ring. Interestingly, the ring exposes slight variations in intensity along its perimeter. Namely, six regions with a slightly higher intensity can be distinguished. This means that there are six directions along which the pores are arranged more preferentially, *i.e.* the pores tend to expose a long-range six fold symmetry.

Thus, from Figure 7.3b follows that the current-line oriented pores have a significant improvement in their arrangement as compared to the crystallographically oriented pores nucleated immediately on the surface of the sample. The self-arrangement of the current-line oriented pores can be further improved by optimizing the etching conditions. Figure 7.3c shows a top view SEM picture taken from a sample anodized under optimized conditions. The FFT pattern, taken from a larger area of the presented picture, shows evident spots exhibiting clearly a six fold symmetry of a closed packed structure. The presence of spots instead of rings in the frequency domain pattern is undoubtedly a prove for a long-range order, or in other words the structure is monocrystalline. In spite of the fact that the monocrystalline porous structure is still not perfect, *i.e.* it has a high number of defects which make the spots to be more or less diffuse, this is the first self-arranged long-range ordered 2D porous structure ever reported (see Figure 7.3 d and Figure 7.4 for larger views).

The anodization conditions must be carefully optimized in order to obtain the long-range order. The optimized conditions mainly depend on the electrolyte concentration, substrate doping level and the anodization voltage. For example, for (100) InP, $n = 10^{18}\ cm^{-3}$ and 5% HCl aqueous electrolytes the long-range order is obtained at approximately $U = 6\ V$. Amazingly, at anodization voltages higher that the optimum, the long-range order disappears. More than that, the intensity of the ring in the DP is uniform distributed along its perimeter. Thus, at voltages higher than the optimum the tendency to long-range order disappears completely.

The arrangement of the pores in a long range order is a self organized process, therefore it is obvious that there are internal 'forces', which guide the system to this state. In order to find a hint concerning the internal 'forces' responsible for the long-range order it is important to compare in more detail the samples with and without a long-range ordering of pores.

Figure 7.5 shows SEM pictures in cross section taken from samples with a long range order (Figure 7.5a) and without (Figure 7.5b). The most evident difference between Figure 7.5a and b is that in Figure 7.5a the nucleation layer is quite thick whereas in Figure 7.5b the nucleation layer is practically absent. Thus, one of the 'forces' leading to a monocrystalline self-arrangement of pores could be the nucleation layer.

Indeed, the nucleation layer can have a strong influence on the whole porous structure if is taken into account that the nucleation layer is formed of crystallographically oriented pores, *i.e.* the crystallographic nature of the NL can determine somehow the global ordering of curro pores.
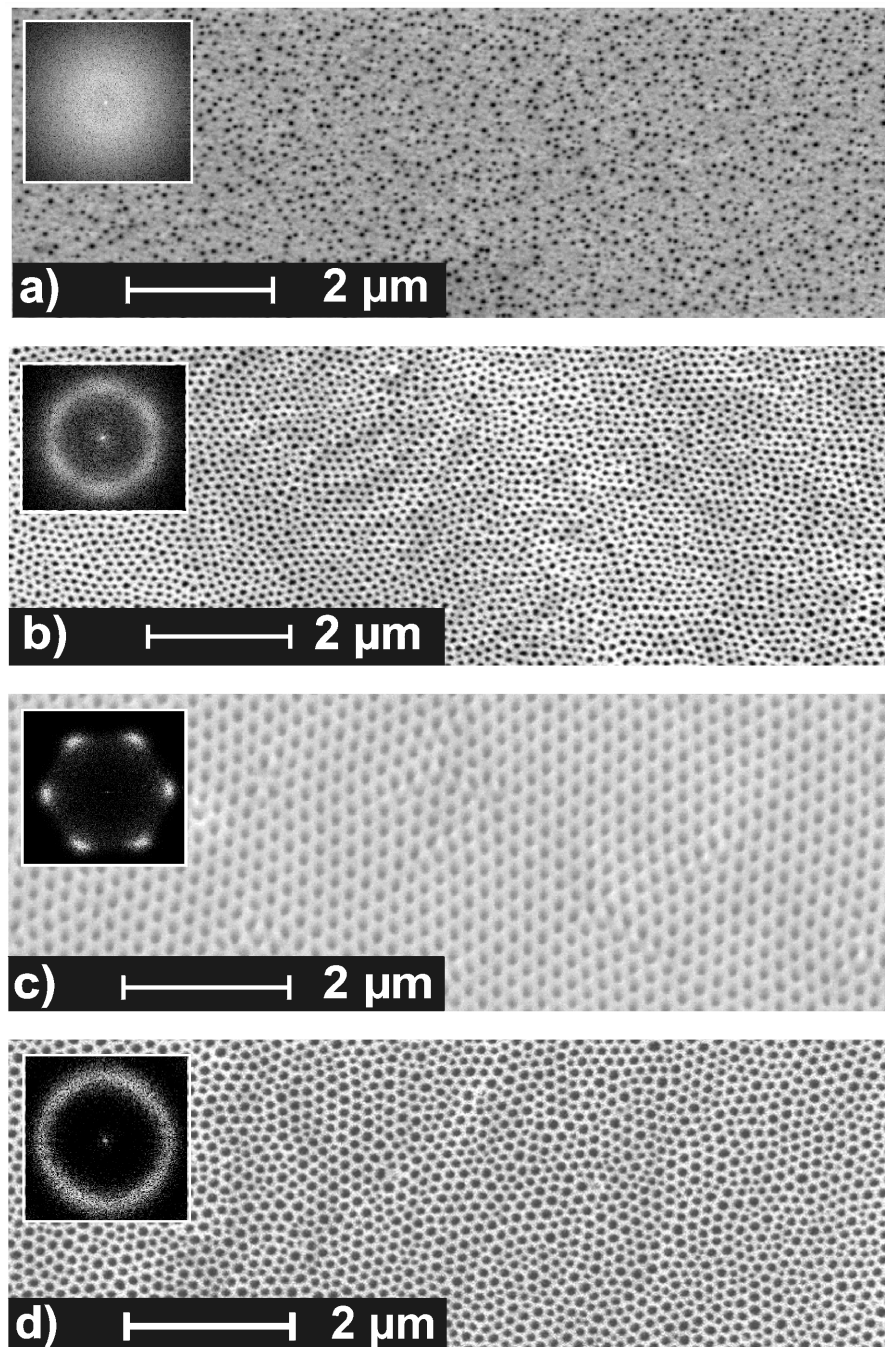
Figure 7.3: *(100) n- InP, n = 10^{18} cm^{-3} anodized in 5% HCl at different voltages. SEM picture taken from: a) the surface of the anodized sample and the corresponding 2D FFT image (inset). The FFT image is a highly diffuse spot, i.e. the nucleated pores are randomly distributed. b) a sample anodized at U = 5 V, i.e. lower than the optimized voltage. The corresponding 2D FFT image which is composed of a diffuse ring exposing six slightly higher in intensity spots, i.e. a tendency to a long-range six fold symmetry. c) a sample anodized at an optimized voltage of U = 7 V. The six fold symmetry is easily visible in the FFT image (inset), i.e. instead of diffuse rings this time spots along definite directions are present. This is a clear indication that the structure has a long range order, i.e. is a monocrystalline structure but with a high density of defects. d) a sample anodized at U = 8 V, i.e. above the optimized voltage U = 7 V. The long range order is destroyed again, i.e. the FFT image is a diffuse ring which is a characteristic of amorphous structures.*
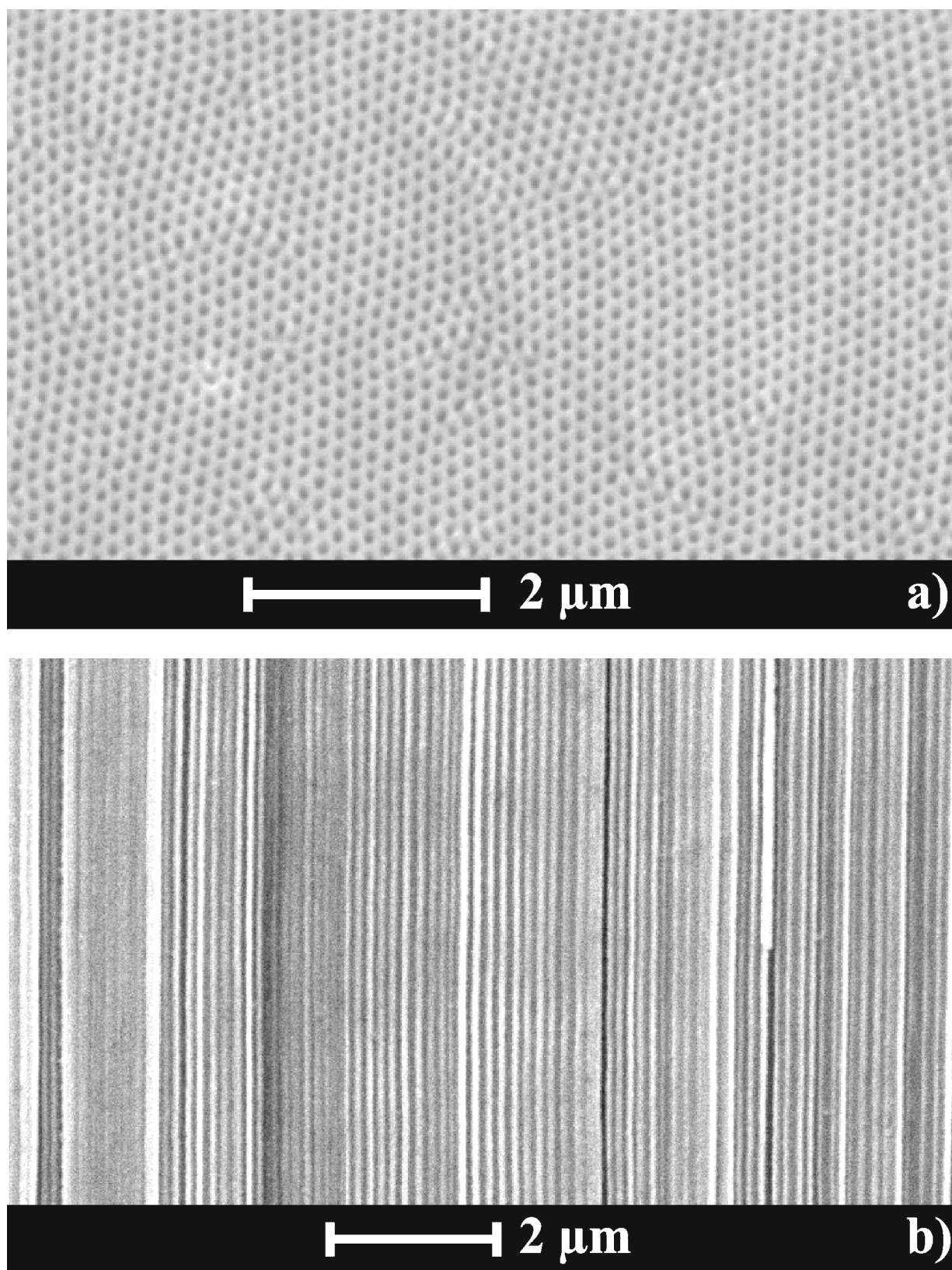
Figure 7.4: *Large area a) top and b) cross section view taken from a self-arranged monocrystalline porous array.*
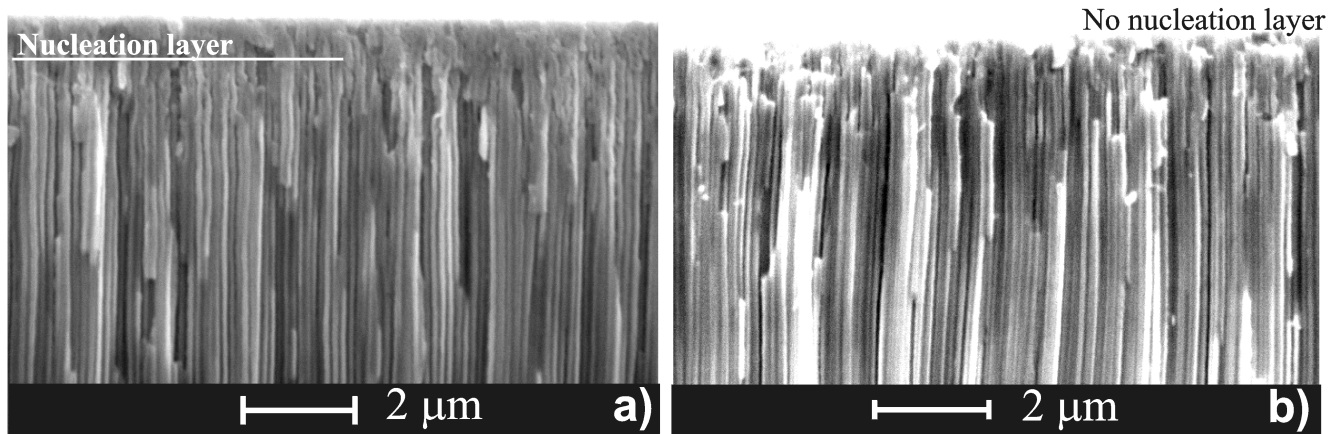
Figure 7.5: *(100) oriented n- InP, $n = 10^{18}$ cm^{-3}, 5% HCl solutions a) at U = 6V the nucleation layer is prominent; b) at U = 9V no significant nucleation layer is present;*

7.1.2   A Model for Long Range Order

As was mentioned earlier (see Chapter 5), crystallographically oriented pores have a very high tendency to branch [67, 61]. They can also branch and grow upwards towards the surface of the sample, forming the so-called domains of crystallographically oriented pores. Such kind of domains were discussed for GaAs in Chapter 5 and were observed in InP as well in a mixture of HCl and HF solution. An example of crysto domains obtained in InP is presented in Figure 7.6. The similarity between the crysto domains shown for (100) InP in Figure 7.6 and those shown for (100) GaAs in Figure 5.12 on page 59 is more than evident.

It should be noted that the surface of InP samples anodized in 5% HCl (without HF) aqueous electrolyte is not covered by domains like those presented in Figure 7.6. However, if such domains exist in a solution of HCl with a little addition of HF, it is hard to believe that the absence of HF could suppress totally the formation of domains. It is more probable that HF only 'helps' the upward growing branches to reach the surface of the sample, *i.e.* increases the number of upward growing branches and thus the probability that more of them will succeed to reach the surface. The number of upward growing branches can be increased by increasing the degree of passivation at downward growing pore tips, thus forcing the system to use all the possibilities to carry the current, *i.e.* generate more upwards growing pores. Thus, it is highly probable that crysto domains can form also in 5% HCl aqueous solutions without HF, but the upward growing pores of the domain do not succeed to reach the surface of the sample. Thus, the nucleation layer is formed of such 'invisible' crysto domains aligned along certain crystallographic planes, *i.e.* {011} planes. A schematic representation of a domain for (100) and (111) oriented samples, is presented in Figure 7.7.

Consequently, the current-line oriented pores, which start growing as a prolongation of the crystallographically oriented pores, will also form a domain whose orientation will be determined by the *a priori* developed crysto domain. It is evident that the size of crysto and thus also of curro domain will depend on the thickness of the nucleation layer. The thicker the nucleation layer, the larger will be the domains and vice versa.

Now it is clear how the long-range order appears. Due to the high number of nucleation
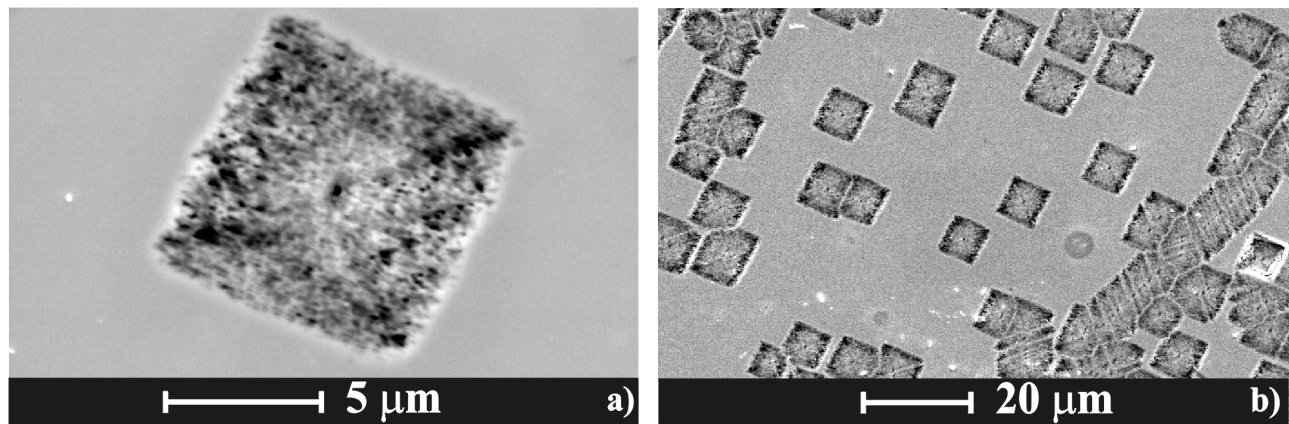
Figure 7.6: *(100) oriented n- InP, $n = 10^{18}$ cm^{-3}, 5% HCl+HF solutions a) a high magnification of a crysto domain in InP; b) An overview of crysto domains in InP; The similarity between the crysto domains in InP and GaAs (see Chapter 5, page 57) is more than evident.*

points at the surface of the sample, a corresponding number of crysto domains and thus curro domains will be formed. All these domains will have one and the same orientation determined by the crystallographic orientation of the sample. However, as it was already mentioned there is an optimum voltage at which the long-range order appears. An inborn question is why at lower or higher voltages than the optimum one, the long-range order disappears (see Figure 7.3)?

The answer is rather simple if taking into account both factors responsible for the long-range order, *i.e.* local closed packed arrangement within the curro domains and the nucleation layer as a global 'aligner'. If one of the two is not sufficiently strong, then no long-range order can be obtained. For example, if the anodization voltage is lower than the optimum one, the space charge region of the pores is also smaller, *i.e.* the pores do not interact sufficiently strong with each other in order for the local closed packed order to appear. This insufficient interaction is also proved by triangular shapes of the curro pores at lower voltages (see Figure 7.3b). On the other hand, at higher voltages (than the optimum) the thickness of the nucleation layer decreases, *i.e.* the domain size decreases, and as a result the disorder in the structure increases (see Figure 7.3d).

Thus, the 2D long-range ordering of current-line oriented pores in InP results from an interplay of two independent phenomena:

▮ The overlap of the space charge regions of neighboring pores induces a next neighbor repulsing force, leading to a medium range ordering and locally closed packed pore array.

▮ The nucleation layer of crystallographically oriented pores induces a global orientation for all domains of current-line oriented pores;

7.1.3   Inducing Periodicity in the Z Direction

As discussed above the current-line oriented pores can form a two dimensional (*X, Y* directions) periodical structure, whereas in the *Z* direction a continuous medium is found. However, the self-induced diameter and voltage oscillations observed in InP (see Figure 7.9b and c on page 88) as well as the sharp transition from current-line oriented pores to crystallographically oriented pores,
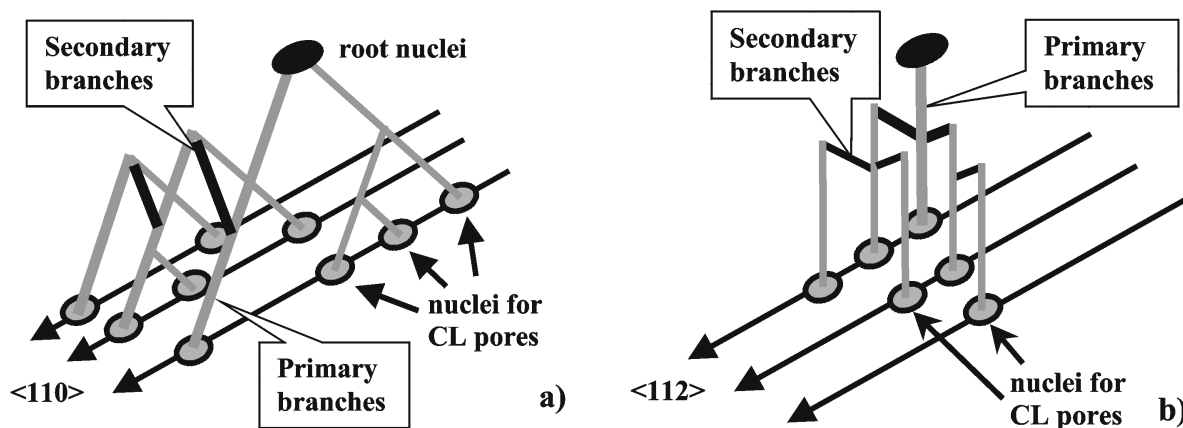
Figure 7.7: *Schematic representation of the nucleation layer in (100) and (111) oriented samples. a) (100) samples. From one nuclei two pores begin to grow. These primary pores begin to branch. The branches can be oriented into the substrate towards the surface of the sample. The entire set of branches form a domain with one and the same nucleation ancestor on the surface. These crysto pores are aligned within {011} planes. Consequently, the curro pores which nucleate at the tips of the crysto pores from one and the same crysto domain will also form a domain with the same characteristic, i.e. the curro pores will be situated within {011} planes. Thereby, all curro pore domains will be oriented along ⟨011⟩ directions leading to a long-range order. b) The same schematic representation for (111)B oriented samples. In this case only one primary pore is found (perpendicular to the surface). Therefore, the domains are smaller if compared with (100) samples. As a result the long-range ordering will be more difficult to achieve.*

when decreasing the current density, can be used to induce periodicity in the third dimension as well (see Figure 7.9a).

In order to change the degree of porosity as a function of depth (Z-direction), the anodic etching was periodically switched on and off, *e.g.* from $I = 600 \ mA/cm^2$ (duration $t_1 = 0.1 \ min$) to $I = 0 \ mA/cm^2$ (duration $t_2 = 0.5 \ min$) and vice-versa. It is obvious that etching occurs only during the first 0.1 min of the cycle, while in the last 0.5 min no dissolution is possible since no current is flowing.

The general finding is that an interruption of the etching process for 0.5 min is enough for the system 'to loose its memory', *i.e.* to start the pore etching with a new nucleation layer. When the current is switched on again, a new nucleation phase is required, *i.e.* a new nucleation layer with crysto pores emerges before the formation of curro pores. Note that this fact is not understandable in any static pore formation model where the equilibrium structure, once reached, should be maintained under all conditions. This observation, however, fits exactly into the general scheme of the current burst model (see Section 3.6) because in the current-free phase the pore tips become passivated and the self-ordering process of current bursts has to be started again.

Thus, periodically pulsing, the current leads to concomitant switches from crysto pores to curro pores and vice versa. The result is a stack of porous layers with different porosities and consequently different effective refractive indexes. Such structures are called Bragg-like structures (Figure 7.8).

The difference in the porosity between the layers of the structure is also confirmed by cathodo-luminescence (CL) measurements (see Chapter 8, Figure 8.10 on page 110). SEM and CL images have been taken from the same cleavage of a Bragg-like structure. As we will see from Figure

Figure 7.8: *Cross-sectional SEM micrograph of a porous n- InP Bragg-like structure with spatially modulated porosity. The current was periodically switched from $I = 600$ mA/cm^2 (duration $t_1 = 0.1$ min) to $I = 0$ mA/cm^2 (duration $t_2 = 0.5$ min).*
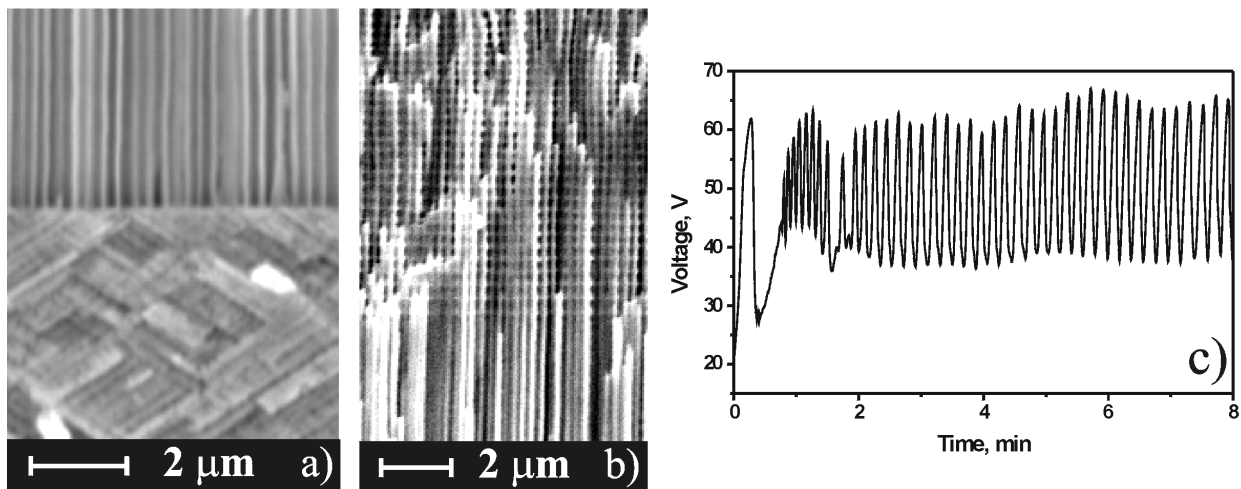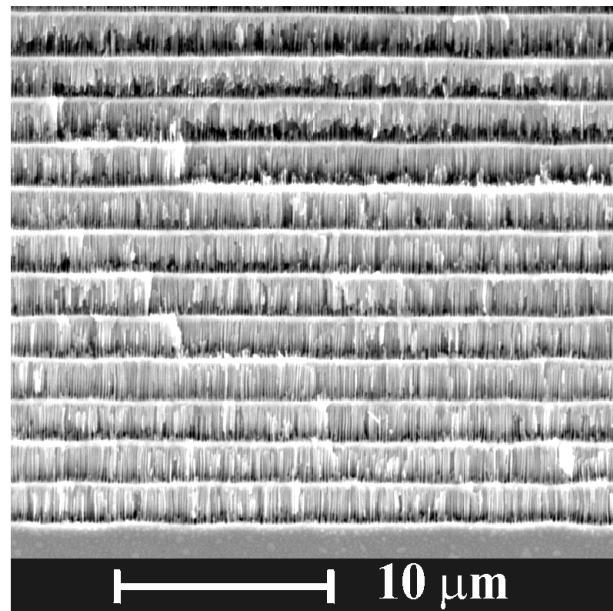

Figure 7.9: *a) Current line oriented pores in a (100) sample in the upper part, and crystallographically oriented pores branched in two $\langle 111 \rangle B$ directions in the lower part. b) Self- induced synchronized diameter oscillations of current-line oriented pores in a InP sample. c) Example of well developed voltage oscillations always observed together with synchronized diameter oscillation.*
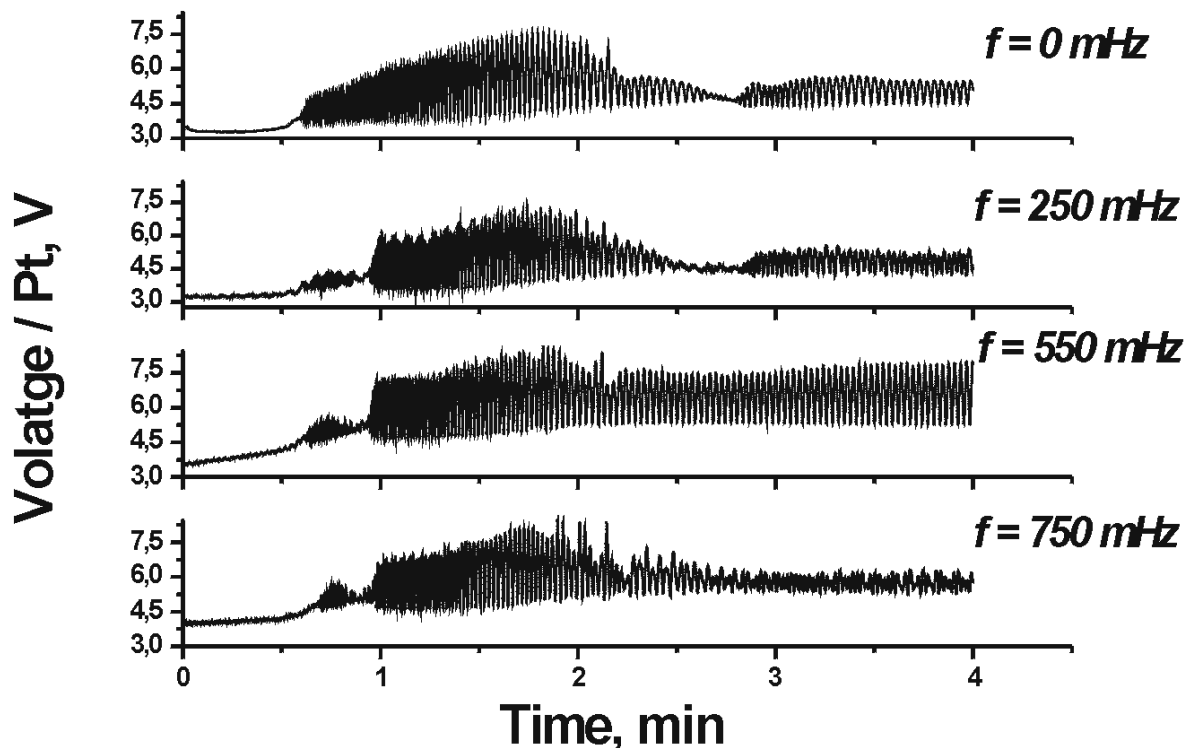
Figure 7.10: *Voltage oscillations obtained during the anodization of (100) n- InP, $n = 10^{18}$ cm^{-3}, in 5% HCl at different external modulation frequencies of the current density. The current density was modulated around $j = 100$ mA/cm^2 with an amplitude of 5 mA/cm^2. The resulting voltage oscillations are as follows: a) without external modulations of the current (f = 0 Hz). b) obtained at f = 250 mHz. c) obtained at f = 550 mHz. d) obtained at f = 750 mHz.*

8.10b on page 110b, the CL proves to be spatially modulated. The CL intensity from nucleation layers is higher than that from the curro pores layers. Taking into account that the CL intensity from bulk InP is higher than that from a porous layer, it can be concluded that a porous layer with a higher CL has a lower porosity (more similar to the bulk) than the one with a lower CL. Different porosity means also different refractive indexes. Thus, porous layers with crysto pores have a higher refractive index than those formed by curro pores.

A second variant of 2D pore crystal with some overlap to 3D crystals are 2D crystals with periodically modulated pore diameters. They may be obtained in several ways. Most directly by external modulation of the pore diameter during the growth of a 2D pore crystal [79]. In Si this has been tried and found to be quite difficult mainly because the system often reacts in a strongly nonlinear fashion to changes in the etching current I. In other words, the $I(t)$ profile is not necessarily found in the variation of the pore diameter d with depth Z. This is not surprising, considering that in all materials investigated so far it has been found that pore growing systems have intrinsic time constants.

Figure 7.10 shows the behaviour of voltage oscillations at different externally induced frequencies, *i.e.* the voltage is measured while the current density is modulated externally around a certain value with a certain amplitude, at a certain frequency. As it can be observed the amplitude
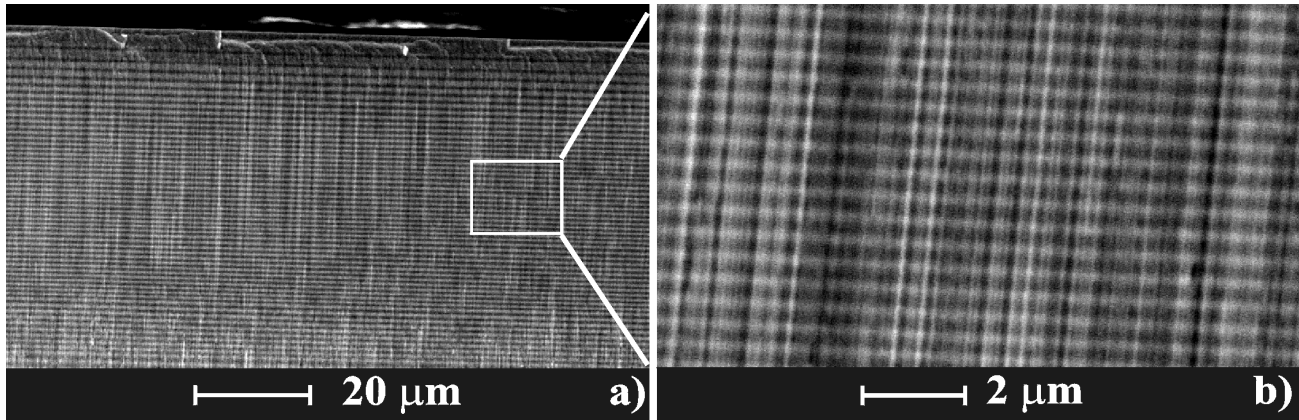
Figure 7.11: *(100) n- InP, $n = 10^{18}$ cm^{-3}, in 5% HCl, $j = 100$ mA/cm^2 with an amplitude of 5 mA/cm^2, $f = 550$ mHz. a) The pore diameter modulation is not uniform, i.e. the distance between two modulations decreases as the pores grow into the substrate; b) A higher magnification taken from a.*

of oscillations is maximal at approximately 550 mHz (Figure 7.10c), whereas at lower or higher external frequencies (Figure 7.10b and d) the amplitude decreases compared with Figure 7.10a where no induced oscillations were applied. Thus, the frequency of 550 mHz is directly related with the intrinsic time constant of the system. It should be noted that due to diffusion effects the intrinsic constant of the system changes in time while the pores grow into the substrate, *i.e.* internal oscillation frequency decreases (see section 6.2). As a result, by modulating externally the current with a constant frequency will result in a non uniformly modulated structure in the Z direction, see Figure 7.11.

Therefore, it is reasonable to let the system choose its own modulation periodicity (see Figure Figure 7.9b and c) or to change the external modulation accordingly while the pores are growing into the substrate. With a strong degree of self-organisation present in InP, it was possible to obtain for the first time a completely self-organized 2D crystal with modulated pores in the *Z* direction (2.5D) as shown in a collage giving some perspective in Figure 7.12.

Considering that the pores are arranged as a single (but defective) crystal in the XY-plane with a lattice constant between 50 nm and 1 μm, this is the best approach to a large 2D photonic pore crystal far below the 1 μm range obtained so far. With proper external stabilization of the pore arrangement and tight control of the growth conditions including external current modulations, perfect 2D crystals with a periodicity in the *Z* direction appear to be possible.

7.2   Integrated Waveguide Structures Based on Porous InP

There are many key elements on which the broadband information networks must rely on. Wavelength Division Multiplexing (WDM) technology is one of the most important ones. The choice of material and technological solutions for WDM depends on many factors: performance, costs, reliability etc. InP is the most promising material because of its integrability with other optoelectronic devices. In what follows we will discuss the possibility to obtain wave-guide-like structures using porous InP.
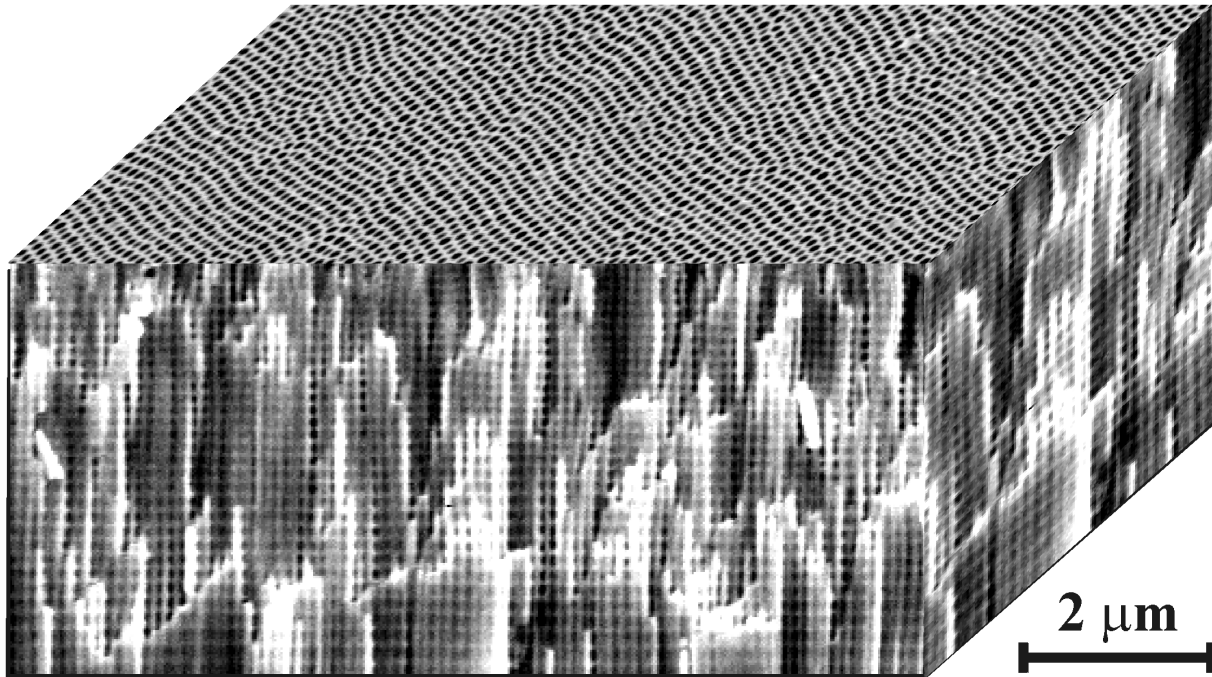
Figure 7.12: *A collage of the first 2.5D single pore crystal obtained by self-organization.*

7.2.1 Experimental Conditions

(100) and (111) oriented S-doped, n- InP, $n = 10^{18}$ cm^{-3} wafers have been used. The samples were covered with a layer of photoresist in which by standard lithography parallel 10 μm broad stripes have been opened (Figure 7.13a)[1]. Consequently, the samples were anodized in 5% HCl aqueous solutions at potentiostatic conditions ($U = const.$). The etching conditions were specially chosen in order to obtain current-line oriented pores, *i.e.* $U = 3 - 9$ V. The etching time was between 0.1 and 1 min. After the etching the samples have been investigated in cross section and top view using a Philips XL series Scanning Electron Microscope working at 10 and 15 kV. Please note that the polymer mask was intentionally not removed from the sample after the etching, in order not to affect the structure.

7.2.2 Results and discussion

Figure 7.13 shows the results of the experiments done with samples patterned with a polymer photoresist ($U = 6$ V for $t = 0.2$ min). Figure 7.13a and b show a general top overview and a magnified top view under the photo-resist respectively. In order to see the structure under the photo resist the accelerating voltage of the SEM was increased from 10 to 15 kV. Figure 7.13c and d show the cross section general overview (c) and a magnified cross section situated directly under the photoresist (d). Figure 7.13e shows the cross section view of a region between two stripes of

---

[1]The lithographic patterning has been done in collaboration with M. Hermann from the Walter Schottky Institute, Technical University of Munich, Germany

photoresist.

From Figure 7.13e can be observed that the pores nucleate only on the surfaces not covered by photo resist, *i.e.* between two stripes, and grow radially, also under the photo resist, away from the nucleation region. It is evident that the pores do not expose any crystallographic characteristic of the single crystalline substrate. The direction of pores changes gradually from perpendicular to the substrate surface (in the center of the nucleation region), to parallel to the surface (at the edges of the nucleation region, *i.e.* near the photo resist).

The pores growing parallel to the surface are clearly visible in Figure 7.13b and d. The radial growth of current-line pores is an additional prove of the fact that such pores grow perpendicular to the equipotential lines of the electric field in the anodized substrate. Making an analogy between a light wave passing thought a small aperture and the current flow through a region of uncovered InP surface surrounded by two stripes of photoresist, the equipotential lines of the electric field will behave similar to the wave front of the light passing thought the aperture, *i.e.* will move radially outward of the slit, exposing a semispherical shape. The bulk wall visible between the two porous regions is a hint that the current-line oriented pores can not intersect, therefore they will stop to grow or will change their direction of growth when the pore wall becomes equal to the double width of the space charge region. This is in contrast to the crystallographically oriented pores which can intersect without changing their direction of growth (see also section 5.1) [56].

A careful investigation of Figure 7.13d and e reveals that the diameter of the pores increases slightly as the pores grow deeper into the substrate (or under the photo resist). In this way the porosity of the porous layer increases as well. Considering the porous layer as an effective medium with a porosity dependent refractive index, it is straightforward that the (effective) refractive index of the porous structure will decrease as the porosity increases. As a result, a gradient in the refractive index in the depth of the structure is obtained. Recently, layers exposing a porous gradient have been proposed as wave guide-like-structures in Si [80]. In InP such structures are of interest as well, taking into account the integration possibility of passive (*e.g.* wave guides) and active elements (*e.g.* LEDs) on the same chip. The main idea for waveguiding as well as for optical fibers is based on the reflections occurring at the interface between a high refractive index core and a low index cladding. The light is kept inside the core as a result of the total internal reflection (TIR) effect, a consequence of Snell's law, which occurs for angles larger than a critical angle when the light passes from a high to a low refractive index material.

A more evident difference in the porosity and thus in refractive index is shown in Figure 7.14. In this case a layer of crystallographically oriented pores is first formed with a low porosity and then the radial growth of the current-line oriented pores is allowed (higher porosity). The low porosity layer can be considered to be the core whereas the current-line oriented pores supply the cladding layer of a wave-guide-like structure. Taking into account that the porosity of porous layer made of crystallographically oriented pores is not higher than 15 %, and the current-line oriented layers are at least two time as porous, as a very rough approximation the refractive index of the core and cladding layers shown in Figure 7.14 differ with 15 % and 30 % respectively, from the refractive index of bulk InP ($n = 3.1$). The simulations [2] made on the structures shown in Figure 7.14 show that such a wave guide will be multimode, and in order to make it monomode it is necessary to decrease the dimensions of the core to nearly 1 μm

However, guiding of light can be realized also using other principles than TIR. Recently optical

---

[2]The simulations have been done in collaboration with G. Boettger from the University of Hamburg-Harburg, Germany
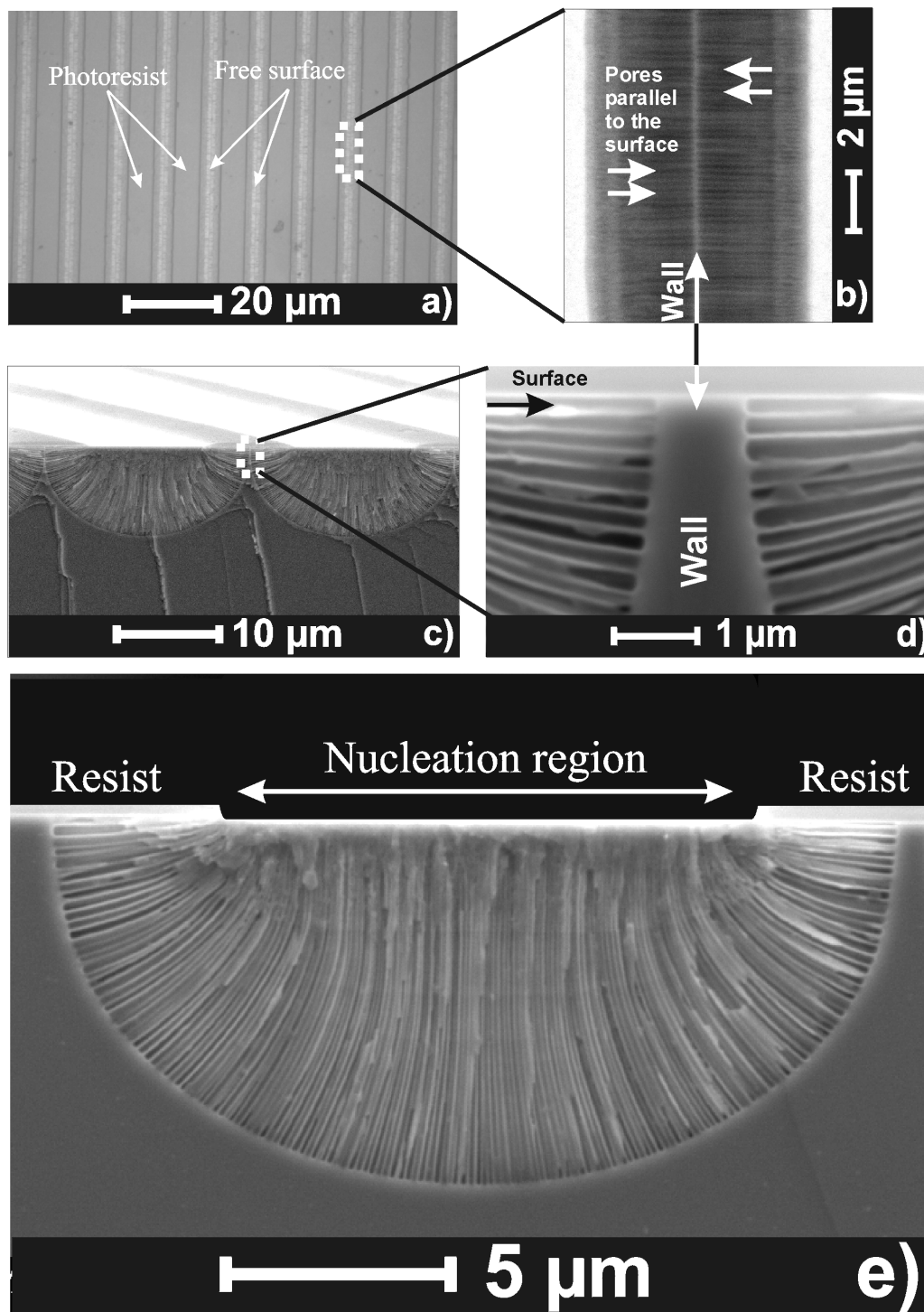
Figure 7.13: *Curro pores suitable for integrated wave guide structures. U = 5 V, t = 10 sec, 5% HCl; a) Top view showing the overview of the patterning; b) High magnification top view between two waveguide structures; The pores growing parallel to the surface of the sample as well as the wall between the neighboring waveguides are indicated by arrows; c) Cross section view of two neighboring wave-guide-like structures; d) Cross section view; Higher magnification between two waveguide structures; The pores growing parallel to the surface are also easily visible; e) Cross section view; An overview showing clearly the radial distribution of the pores;*
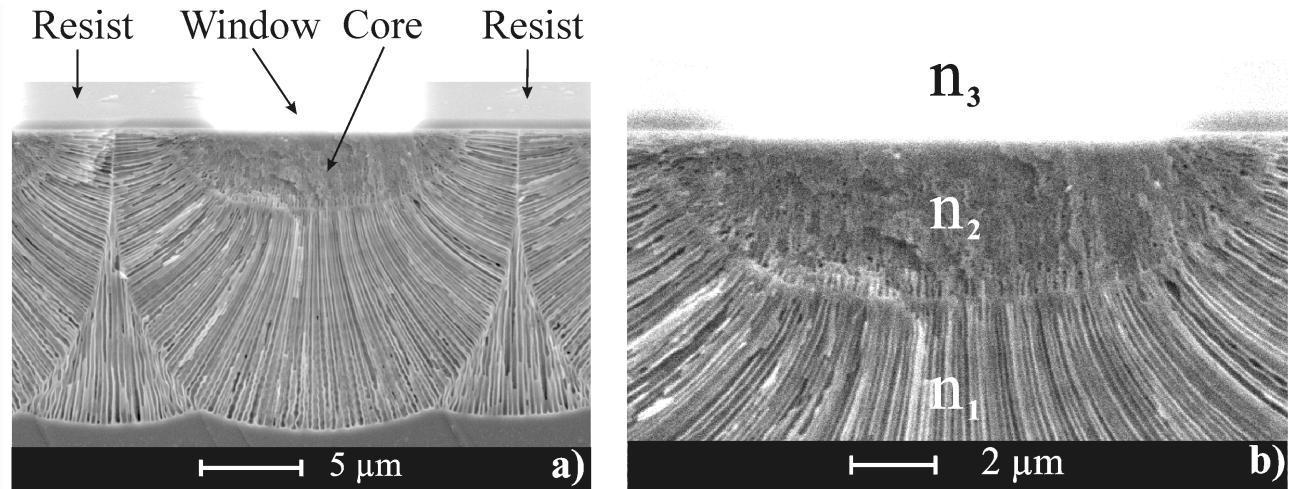
Figure 7.14: *Curro pores suitable for integrated wave guide structures: higher core-shell contrast. U = 4 V, t = 1 min, 5% HCl; a) Cross section view; b) Cross section - higher magnification. $n_3 < n_1 < n_2$.*

fibers with a cladding based on photonic crystals (PC) have been reported. Taking into account that PCs are Bragg-reflectors in three dimensions it is probably possible to use the porous Bragg-like structures (see section 7.1.3) for wave guiding purposes as well. An example of a wave-guide-like structure with a Bragg-like cladding is presented in Figure 7.15a. However, the periodicity of the Bragg structure changes by moving from the center to the sides of the structure. Nevertheless, we think that by a proper design it will be possible to improve the light confinement within the core of the wave guide structure using such kind of Bragg-like cladding. In order to make it easier to imagine a porous InP wave guide structure in space, a 3D collage picture of the waveguide structure is presented in Figure 7.15b.

In this work we showed that such structures are possible to be realized in InP. However, the exact design and the wave guiding properties of these structures still have to be tested. In what follows we will give some general notions about Wavelength Division Multiplexing, which is a possible application for wave-guide-like structures in InP.

7.2.3 General Notions About WDM

The amount of information transmitted in a unit of time through an optical fiber can be increased in 2 modes: by increasing the speed of the signal and/or by increasing the wave length channel number on optical fibers. A WDM system takes the second approach: the signal emitter sends the information to the receiver by combining a large number of channels (wavelengths) into a single fiber. The receiver at its turn separates the wavelengths again and uses them for its purposes. Thus, it is possible to send a huge amount of information through a single optical fiber. The main challenge in this approach is combining and separating the wavelengths. The combining process is normally called multiplexing, whereas the separation one is called demultiplexing. Therefore, the whole process is called Wavelength Division Multiplexing.

There are several ideas how the multiplexing/demultiplexing process should be performed, *e.g.* using etched grating- waveguide demultiplexers or arrayed waveguide gratings (AWG). In both
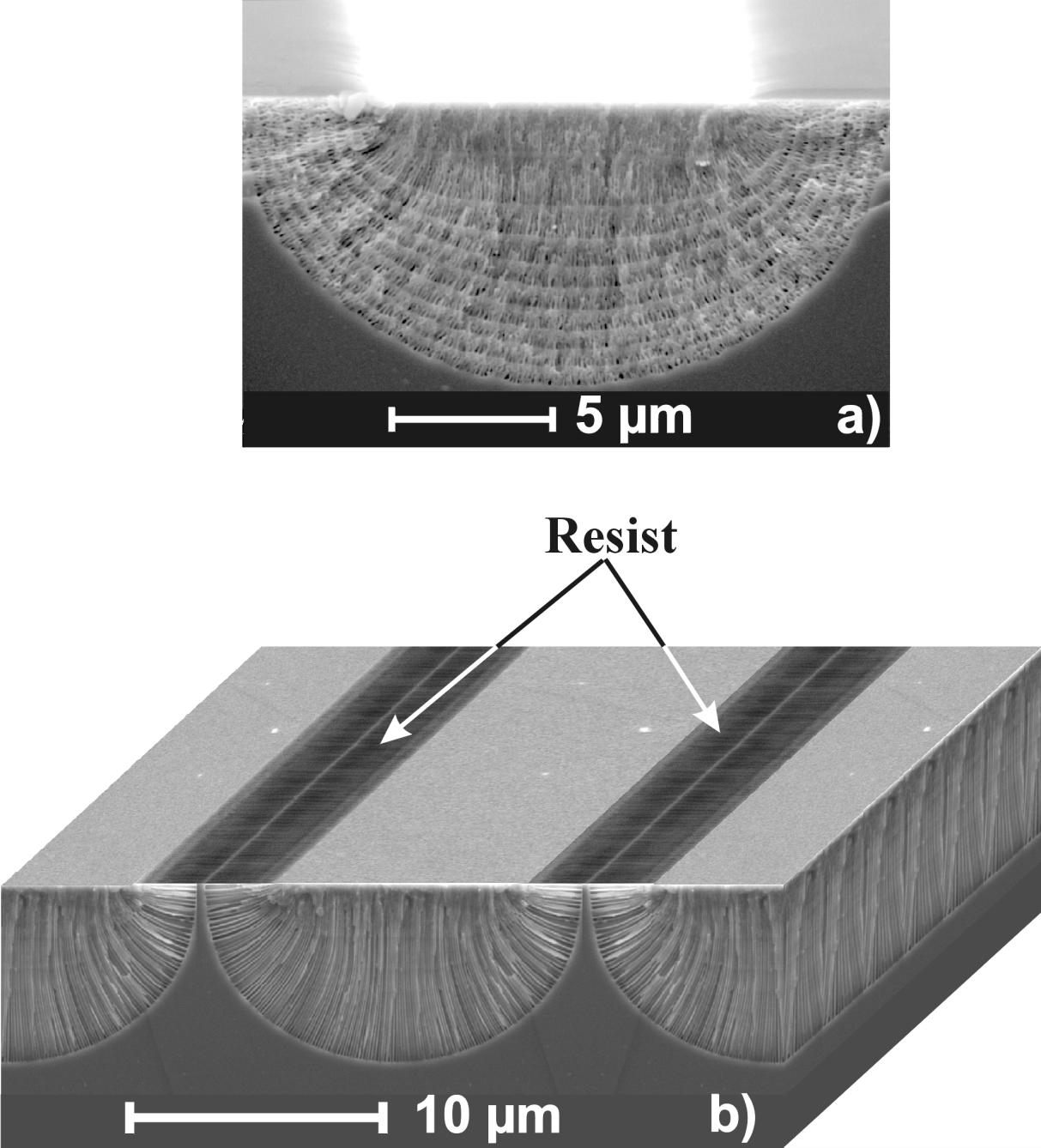
Figure 7.15: *a) Bragg structure around the core was obtained by modulating periodically the current density; b) A 3D collage picture of waveguide-structure in InP;*
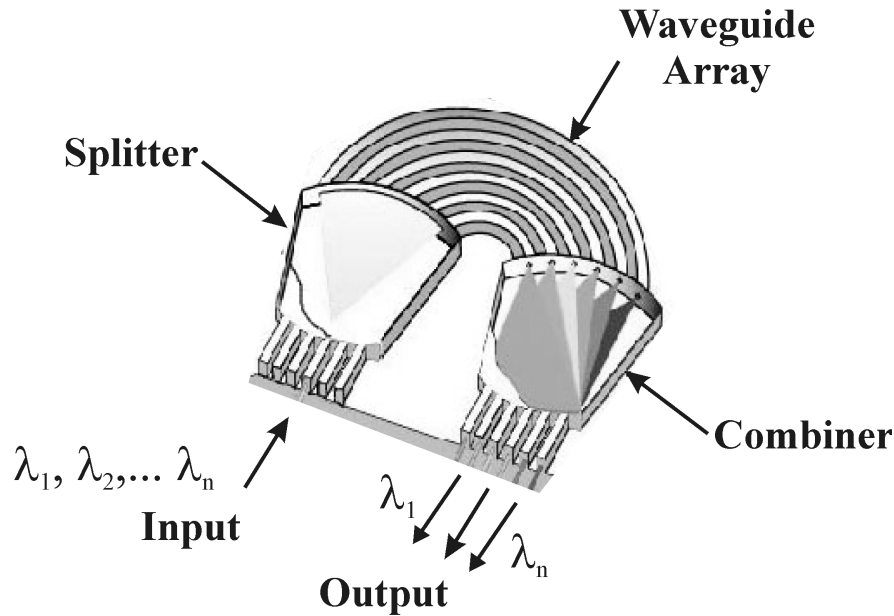
Figure 7.16: *A schematic representation of an AWG structure.*

these approaches the main elements are the integrated waveguides. Thus, if we will be able to design high quality integrated wave guides we will be able to design also multiplexing/demultiplexing components like AWGs.

A typical AWG is represented in Figure 7.16. The structure is made up of three parts, a separator/splitter, a waveguide array, and a combiner. An input signal is coupled by the splitter into the waveguides. The wave guides have different lengths, this way they introduce different phase shifts in the signals. Finally, the array waveguide outputs are recombined so that constructive interference will occur at one unique output for each wavelength in the system. In this way the AWG acts as a wavelength demultiplexer. The device is symmetric, so it can also serve as a multiplexer when used in the reverse configuration.

7.3   Towards Uniform 3D Structures in GaAs.

As mentioned above the dissolution (nucleation) usually starts at badly passivated surfaces, *i.e.* at defects. In order to obtain a uniform porous structure suitable as photonic material, it should therefore be possible to use a predefined uniform network of defects (etch pits) as starting points for the pores.

A uniform structure could be obtained if the pores would nucleate easily on predefined defects and grow stable along definite directions. The stable directions of growth are normally defined by the etching anisotropy, and in GaAs these crystallographic directions are $\langle 111 \rangle B$ (see section 5.1).

As it was noted in section 5.1 pore growth along $\langle 111 \rangle B$ directions may lead to the formation of a 3D structure. Note that $\langle 111 \rangle B$ oriented pores intersect each other without changing their direction of growth or shape. This is essential for producing 3D periodic structures by intersection
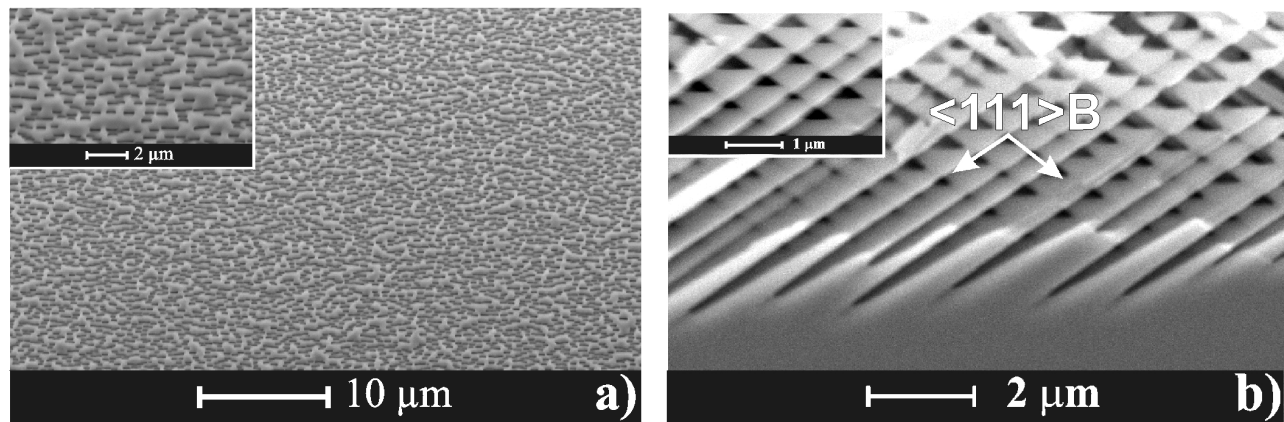
Figure 7.17: *(100)-oriented n- GaAs, cross section; a) Top view. Random nucleation of pores on the surface of a (100) n- GaAs sample after the first anodization step. b) A quasi-uniform 3D structure obtained after the second anodization step was applied.*

of pores starting from a common nucleus in analogy to the pores in Si forming the 'Kielovite' structure [81]. However, experimentally it is not simple to fabricate such 3D structures. This is because the $\langle 111 \rangle B$ directions have a high tendency to branch and thus the uniformity will be destroyed as more and more branches appear.

The experiments show that branching will be avoided only when the density of nucleated pores will be very high, thus the branches will simply have no 'space' for growth and only the pores nucleated on the surface will grow. For a dense pore nucleation the current density is critical, taking into account that by increasing the current density branching 'power' of pores increase as well. Thus, a compromising value for the current density should be chosen. Other parameters, which should be subjected to optimization are concentration and flow of the electrolyte, both of them being important for uniform nucleation. An example of a 3D structure obtained at optimized conditions is shown in Figure 7.17.

The special approach used by us in order to obtain a uniform nucleation in GaAs consisted of a two-step anodization process:

▸ The first step employs a set of rectangular periodic current pulses.

▸ The second step employs usual galvanostatic/potentiostatic conditions.

The goal of the first step is to create a high density of surface defects, which will serve as nucleation points for pores in the second step. The amplitude and duration of pulses, *i.e.* the amount of charge per pulse per unit area, is critical and should be optimized for an efficient generation of dense nucleation points.

If the first step is not optimized, domains of crystallographically oriented pores will develop at this stage. Consequently, during the second step no new pores will nucleate between the domains, but branches inside the already existing porous domains (created during the first anodization step) will be nucleated, increasing the already existing domains.

For the optimization of the first step it should be taken into account that two types of pulses with equal amount of charge per pulse per unit area can be distinguished: a) low current and long time; b) high current and short time. These two cases are presented schematically in Figure 7.18.
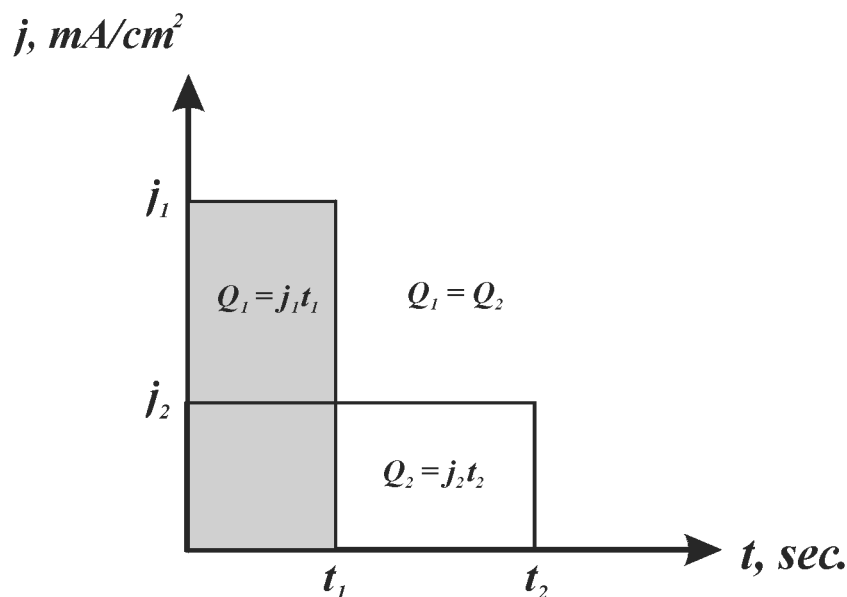
Figure 7.18: *Two types of pulses with the same amount of charge per pulse per unit area.*

It was found that for the case a), the domains formed tend to be of large size and low density (number of domains per unit area). On the other hand, for the case b), the domain size decreases while their density increases significantly. Thus, in order to obtain uniform nucleation, *i.e.* to avoid domain formation altogether, high-current/short-time pulses should be considered. The interval of currents and pulse widths investigated by us was between $j = 50 - 350 \ mA/cm^2$ and $t = 0.3 - 12 \ sec.$ respectively. The most uniform nucleation achieved in our experiments was at $j = 300 \ mA/cm^2$ and $t = 2.8 \ sec..$

The second anodization step should provide necessary etching conditions for the pores (nucleated in the first step) to grow into the substrate as deeply as required. We performed the second step at constant current density $j = 30 \ mA/cm^2$. It has to be noted, that special care should be taken for the second step as well. Too low current densities could result in fewer pores growing into the substrate than initially nucleated, whereas too high current densities could result again in domain formation.

In spite of the fact that the structure in Figure 7.17 seems to be quite uniform - it is not, because the initially nucleated pores are randomly distributed on the surface of the sample. In order to nucleate pores in a highly ordered manner, lithography is required. Electron beam lithography has been used to pattern (100) oriented GaAs wafers with arrays of windows in the resist with diameters of 300 nm. Patterns with triangular and square lattices have been used. The lattice constant varied from 300 nm to 2 μm.

A top and cross sectional view of the first attempts to anodize pre-patterned samples is presented in Figure 7.19 on page 99. One can see (Figure 7.19a, b and c) that the pores indeed nucleate in the windows defined by the electron beam lithography. In each window two small black spots can be observed separated by a white band. The black spots are the nucleated $\langle 111 \rangle \, B$ pores. In spite of the fact that nucleation in predefined windows seems to work, some other problems can appear during the etching process. For example, in addition to the pores nucleated in predefined
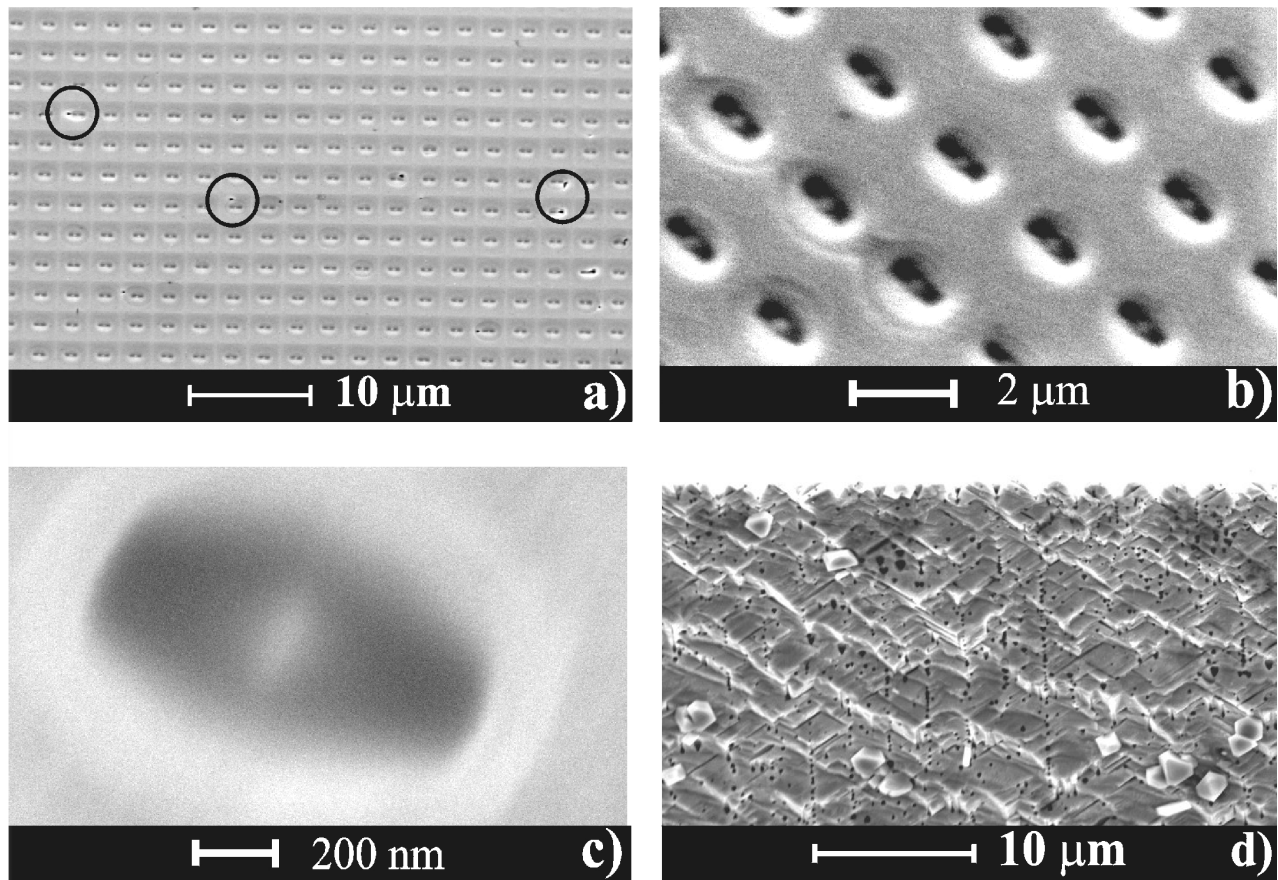
Figure 7.19: *a, b) Top view at two magnifications of the nucleated pores in photolithographycally defined windows; c) high magnification of the nucleated pores. The two ⟨111⟩ B directions can be observed; d) Cross section view of the nucleated pores. As can be observed due to branching the uniformity defined by lithography is lost into the depth of the structure.*

windows some random pores nucleate, too. Such randomly nucleated pores are marked in Figure 7.19a by black circles. It is likely that random pores nucleate at defects with a lower breakdown voltage, leading to faster nucleation, faster growth, high current densities and successive branching, diminishing the necessity to nucleate or sustain pores in the predefined windows in order to carry the external current. Therefore, even the pores which have started to nucleate in predefined windows can stop growing in favor of the randomly nucleated pores.

In Figure 7.19d is presented the cross section taken from an anodized pre-structured sample. As easily observed, the uniformity of the porous layer is not following the predefined structure on the surface. The main obstacle here is the branching of pores from the already nucleated pores. A further optimization of the mask as well as of the etching conditions is required in order to obtain uniform 3D structures in GaAs by means of anodization.

7.4   Summary and Conclusions to Chapter 7

Uniform 2D and 3D porous structures are important from the point of view of photonic crystals. In order to define the uniformity of the structure the so-called prestructuring is extensively used in Si.

In InP it is possible to obtain single crystalline 2D porous structures by means of self-organisation. Two ingredients are responsible for the observed long-range order: interaction between the neighbors via the space charge region, which leads only to a short-range order, and the nucleation layer which extends the local order to a long-range order. This finding allowed for the first time to obtain a 2D monocrystalline porous structure by no means of lithography. The periodicity in the third direction can be obtained by modulating the pore diameters or by switching ON/OFF the current through the sample.

By using optical lithography and anodization technique it is possible to obtain wave guide structures: high index surrounded by low index porous structures. Taking into account that InP is an important material in optical communications, such wave guide structures could be used for designing integrated wavelength division multiplexing systems for modern optical telecommunications.

Uniform 2D and 3D porous arrays in GaAs are also interesting. However, in this case the self-organisation does not work and prestructured samples should be used. In order to obtain real 2D and in GaAs more work is required for optimizing the nucleation and avoiding branching of the already nucleated pores.

Chapter 8

Cathodoluminescence of Porous III-V Layers

Optical properties of porous III-V materials are always interesting for the scientific community. Their suitability for optical applications makes them the main materials used in modern opto-electronics. Interestingly, porous semiconductors expose new optical properties not observed in bulk materials. It is noteworthy to mention that the huge interest for porous semiconductors has been increased due to an optical effect observed in porous Si. Si is an indirect semiconductor, therefore the quantum efficiency of radiative recombination in bulk Si is very low. Surprisingly, nano porous Si proved to behave differently as compared to the bulk material. Simultaneously but independently, Canham and Lehmann observed visible photoluminescence from nano porous Si [82, 83]. This discovery gave a great impulse for the investigation of optical properties of porous semiconductor materials other than Si.

So far, most experiments investigating emission characteristics of porous III-V materials have been restricted to photoluminescence (PL). PL of porous GaP, GaAs and InP at energies above the band gap of the bulk material has been attributed to quantum size effects [47, 51, 84, 63]. Furthermore, a porosity-induced increase of the near-band-edge emission was observed in gallium phosphide [14]. Nevertheless, no correlation between luminescence properties and morphology features of porous III-V material has been reported yet. In what follows the morphology and cathodoluminescence (CL) characteristics of porous layers obtained by electrochemical dissolution of n- GaP substrates in H_2SO_4 aqueous based electrolytes will be discussed in more detail . Additional details concerning CL basics are presented in Appendix B.

8.1   CL Experimental Details

The CL experiments were performed in a Scanning Electron Microscope (SEM) equipped with an Oxford Instruments MonoCL2 cathodoluminescence imaging and spectral analysis system, and a cryogenic specimen stages. CL[1] and SEM images were taken from the same sample areas for comparison. The CL was excited with a continuous electron beam at normal incidence, and measured using a retractable parabolic mirror collector. CL spectra were collected over the wave-

---

[1]These experiments have been done in collaboration with Dr. M. Stevens-Kalceff, from the Department of Applied Physics, University of Technology, Sydney, Australia

length range 250-900 nm using a Hamamatsu R943-02 high sensitivity photomultiplier with a 1200 $line/mm$ grating, blazed at 550 nm. The CL spectra were collected over a range of beam energies ($E_b = 15 - 30\ keV$) and beam currents ($I_b = 0.25 - 100\ nA$) and from $\sim 7000\ \mu m^2$ regions to reduce electron beam induced effects. The spectra were converted from wavelength to energy space, and corrected for monochromator dispersion and total instrument response.

The MonoCl2 has two operating modes: panchromatic and monochromatic. Mono CL2 employs high performance mirrors to direct the emission along different light paths. In panchromatic mode, all the light is directed at the detector. This allows the combined intensity of all CL wavelengths within the response of the detector to be imaged. The monochromatic mode is used for recorded photon counting spectra in serial mode, for imaging with just one wavelength bandpass.

8.2   Correlation between Morphology and Cathodoluminescence in Porous GaP

In this section SEM and CL data will be compared in more detail. The SEM images presented in Figure 8.1 on page 102 and Figure 8.2a on page 103 show the development of porous regions in n- GaP samples subjected to anodic etching under potentiostatic conditions for 10 and 120 min respectively. In both cases a constant voltage of 10 V was applied to the sample. At the beginning of the process the etching starts at surface imperfections forming the so-called catacomb-like pores [17]. After initial pitting of the surface, further dissolution proceeds in directions both perpendicular and parallel to the surface. A pore starting at a surface imperfection and growing along a current-line, *i.e.* mainly perpendicular to the initial surface, is called a primary pore. Pores originating at the surface of a primary pore and propagating away from it are called secondary pores. The development of secondary pores occurs underneath the initial surface. As it can be seen from Figure 8.1a, the secondary pores in n- GaP propagate radially away from the primary
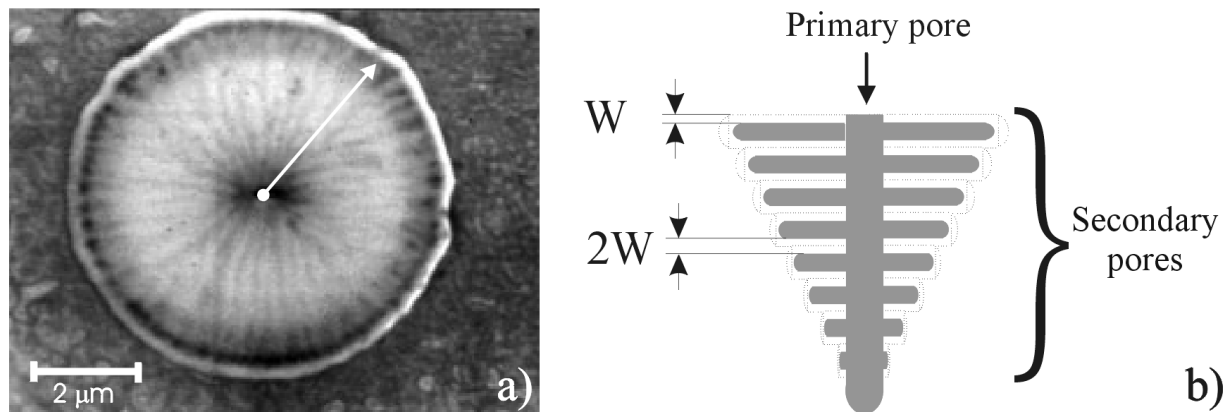

Figure 8.1: *a) SEM micrograph of the top surface of a GaP sample anodically etched for 10 min at a constant voltage of 10 V. It shows the so-called catacomb-like porous structures. b)A schematic representation of the catacomb-like pores obtained in n- GaP during the anodization process at constant voltages. The primary pore is growing perpendicularly to the surface, whereas the secondary pores grow radial from the primary pore. The distance between secondary pores is 2W, where W is the width of the space charge region in the semiconductor.*
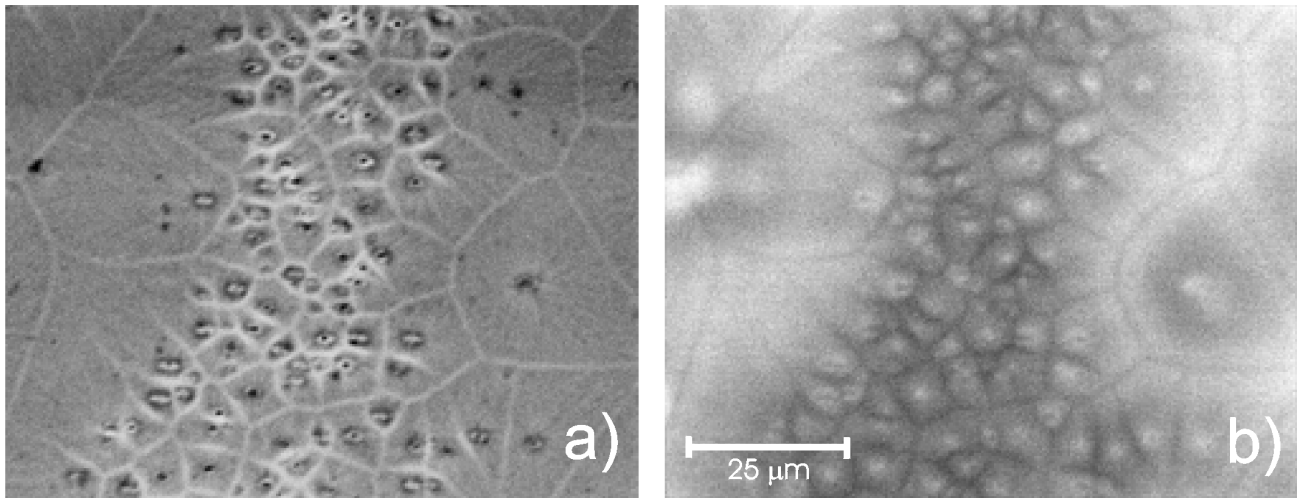
Figure 8.2: *SEM and CL micrographs taken from the top surface of a n- GaP ($n = 3 \cdot 10^{17} cm^{-3}$) sample anodically etched for 120 min at a constant voltage of V = 10 V. For CL images the beam energy was 15 keV, and the beam current was 0.025 nA a) SEM micrograph; The white borders of the domains are twice the width of the space charge region. The domains are not round anymore as in Figure 8.1 because the etching stops when two domains meet each other. Therefore, the round shape is destroyed. b) CL panchromatic images, i.e. all wavelengths are used for imaging. The domains again can be easily observed on the CL micrographs and the similarity to the SEM is evident. In this case the borders between the domains are dark, which means that the CL efficiency is lower.*

pore, forming a symmetric set of 'catacombs'. Since the etching proceeds at the same rate in all directions, the boundary of the porous region, or in other words the porous domain, is circular. In comparison to the domains observed in n- GaAs and InP, where the domains can be rectangular and the pores are strictly oriented along $\langle 111 \rangle B$ directions, the catacomb-like pores in GaP expose no specific crystallographic features.

A schematic representation of the catacomb-like pores in n- GaP is presented in Figure 8.1b. As already mentioned, the primary pore starts at a defect at the surface, whereas the secondary pores grow radially from the primary pore. The distance between the secondary pores is twice the width of the space charge region. The first set of radial pores begin growing underneath the initial surface. The thickness of the walls that separate the surface and the secondary pores is W - the width of the space charge region. This is the reason why when looking with the naked eyes at such samples one gets the impression that the surface is intact.

Following etching for an extended period, the secondary pores from different domains eventually meet, leaving nearly straight walls between neighboring porous domains (Figure 8.2a). The thickness of these walls is also defined as by twice the thickness of the surface depletion layer during anodization [17]. As it can be seen in Figure 8.2a, the lateral dimensions of porous domains depend upon the local density of surface imperfections (*e.g.* dislocations, scratches *etc.*) initiating the formation of primary pores.

Figure 8.2b shows a panchromatic CL image taken from the same region of the as-anodized n- GaP sample from Figure 8.2a. It clearly shows a porosity-induced increase of the emission efficiency of gallium phosphide. The light areas in the panchromatic CL image result from enhanced luminescence collected for wavelengths between 250 and 900 nm, with response maximum at ~ 550 nm (2.25 eV). It is evident that there is a good correlation between the enhanced CL

Figure 8.3: *Panchromatic CL image taken from the top surface of a GaP sample anodized under temporary variations of the applied voltage from 5 to 15 V. The beam energy is 15 keV, the beam current is 1 nA. The variation of the voltage is accompanied by the change in porosity and by the modulation of the CL intensity (see the rings). Quite obviously the CL depends on the porosity.*
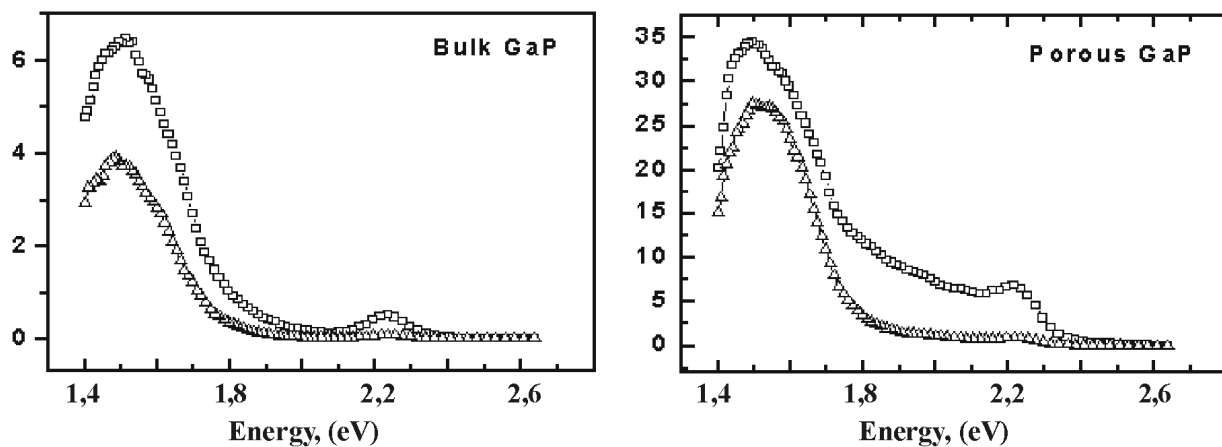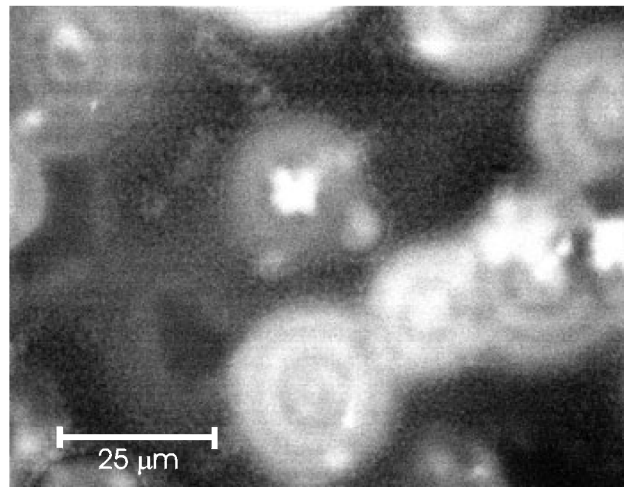

Figure 8.4: *CL spectra of bulk and porous GaP measured at accelerating voltage of 25 keV and current intensities 10 nA (triangles) and 50 nA (squares). The CL intensity from the bulk material is lower than from the porous one. The band catered at ~ 2.25 eV is more pronounced when increasing the intensity of the incident electron beam.*

emission (lighter areas) in the panchromatic CL image and porous domains in the SEM image. The walls between porous domains are less luminescent and therefore are easily distinguishable in Figure 8.2b as dark lines.

To demonstrate the dependence of the emission efficiency upon the degree of porosity, a panchromatic CL image was taken from a sample rendered porous under etching conditions, when the applied voltage was temporarily varied between 5 and 15 V. The modulation of the applied voltage is accompanied by an increase and decrease of the anodic current density that causes synchronous modulation of the degree of porosity. As one can see from Figure 8.3, successions of high and low voltages lead to the observation of annular bright and dark traceries around most of the observed etch pits. Note that the dark areas in Figure 8.3 correspond to regions unaffected by anodization.

In Figure 8.4 the CL spectra from bulk and porous GaP fabricated at a constant voltage of 10 V are shown. The spectra are dominated by a broad band at ~ 1.5 eV and a lower intensity band at ~ 2.25 eV. It was found that increasing the beam power, *i.e.* $E_b \cdot I_b$, increased the

intensity of the emission at 2.25 eV in absolute terms and relative to the ~ 1.5 eV emission in both bulk and porous GaP. These two broad emission bands may be attributed to sulfur and some residual impurities including C, O, Zn and Cd [85]. The emission observed at ~ 2.25 eV has been investigated by a number of groups [86, 87, 88] and was associated with the radiative recombination at sulfur and carbon atoms on phosphorus sites. Note that, according to the earlier published data on luminescence, deep level transient spectroscopy and optically detected magnetic resonance in n- GaP [89, 90] the 1.5 eV band has been attributed to the radiative recombination of non-equilibrium carriers via donor-acceptor pairs, the donor being a shallow centre.

Further evidence of the impact of porosity upon the luminescence efficiency was obtained when studying samples prepared under galvanostatic etching conditions at different anodic current densities. Figure 8.5 shows SEM and CL images in cross-section taken from a sample subjected to successive anodization steps at two current densities: $j_1 = 80 \ mA/cm^2$ for 60 min and $j_2 = 1 \ mA/cm^2$ for 240 min. As discussed in Chapter 5 etching at high anodic current density leads to the formation of the so-called current-line oriented pores (Figure 8.5a). Under these conditions the high density of etching pits at the initial surface excludes the formation of porous domains. When the current density is switched down to $j_2 = 1 \ mA/cm^2$, the rate of dissolution and the degree of porosity sharply decreases. As discussed in Chapter 5, the pores in this case grow along specific crystallographic directions, namely along $\langle 111 \rangle B$ directions (see Figure 5.6 on page 51).

In perfect agreement with the data obtained on potentiostatically anodized samples a strong correlation between a high porosity and a high CL intensity is found. As it can be seen from Figure 8.5, the top layer fabricated at the current density j_1 is more luminescent than the second layer produced at current density j_2. Even non-uniformities in the thickness of the top porous layer and small particles related to the cleavage process are clearly distinguished in the CL image. The CL
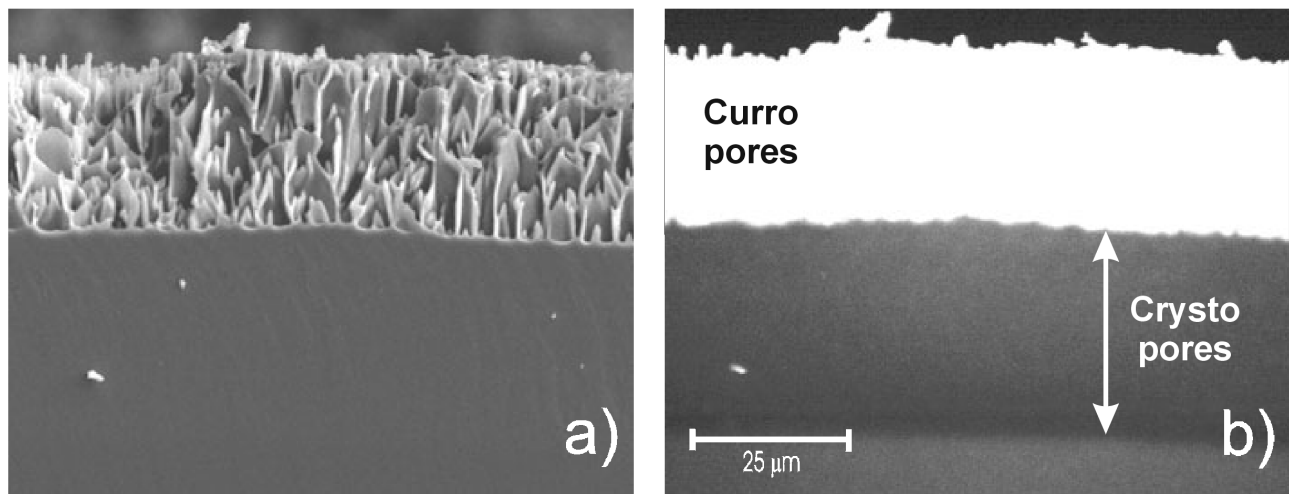

Figure 8.5: *a) SEM and b) panchromatic CL images in cross-section taken from a sample anodized galvanostatically at two current densities: $j_1 = 80 \ mA/cm^2$ for 60 min and $j_2 = 1 \ mA/cm^2$ for 240 min. Due to the differences in size of the pores at the two current densities, it is not possible to see explicitly the second layer (with crystallographically oriented pores). However, a great difference in CL intensity is observed between bulk and the porous layer with current-line oriented pores. More than that, in the CL image it can be observed that there is a difference in CL intensity between the bulk and the porous layer obtained at low current densities (crystallographically oriented pores): $CL (bulk) > CL (crystallographic pores)$.*
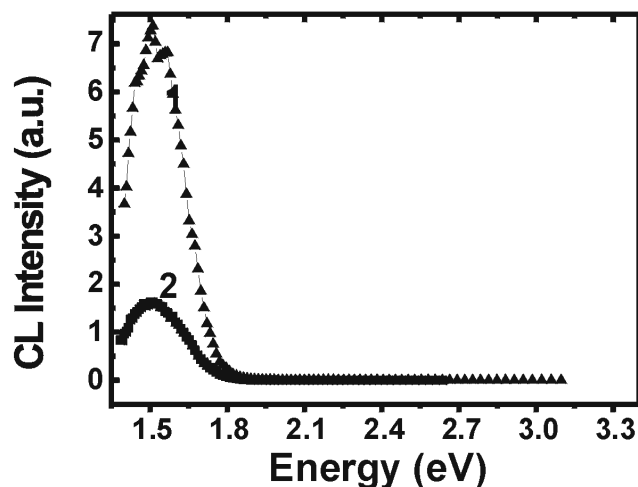
Figure 8.6: *CL spectra of porous layers pro-duced at current densities $j_1 = 80\ mA/cm^2$ (curve 1) and $j_2 = 1\ mA/cm^2$ (curve 2). The beam energy is 15 keV, the beam current is 0.025 nA.*

spectra from both layers show luminescence in the near infra-red region with the band maximum at ∼ 1.5 eV when excited by a low-current electron beam (Figure 8.6). The near-band-edge CL at ∼ 2.25 eV was observed at high beam currents. Under intense excitation however, the CL from the porous layers was considerably attenuated by the electron beam. The dynamic of CL attenuation with the time is illustrated in Figure 8.7 on page 106.

Another interesting feature of the anodization process at high constant current densities is the oscillation of voltage in time, similarly to the oscillations observed in n-InP, see Chapter 6. Figure 8.8 illustrates the time dependence of the voltage measured on the sample during anodization. Under constant galvanostatic etching conditions, the measured voltage oscillates. Although it is difficult to find a direct relation between peaks visible in the voltage/time diagram and horizontal trajectories in the SEM image, it is highly probable that the self-induced voltage oscillations are responsible for the synchronous modulation of the pore diameters as in the case of InP.

A subject of particular interest is the difference in CL intensities between the bulk and the porous layer with crystallographically oriented pores. Although, neither in Figure 8.5b nor in Figure 8.8c the difference in CL intensity between the bulk and crystallographically oriented pores is evident, it exists, and can be confirmed by the CL spectra. This is shown in Figure
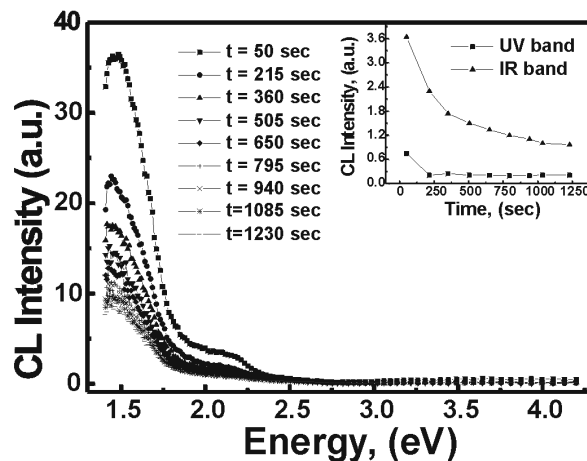

Figure 8.7: *The time evolution of the CL at-tenuation. The insert shows the time depen-dence of the intensities of the near infrared (1.5 eV) band and UV emission (integrated from 2.75 to 4.2 eV). The beam energy is 25 keV, the beam current is 50 nA.*
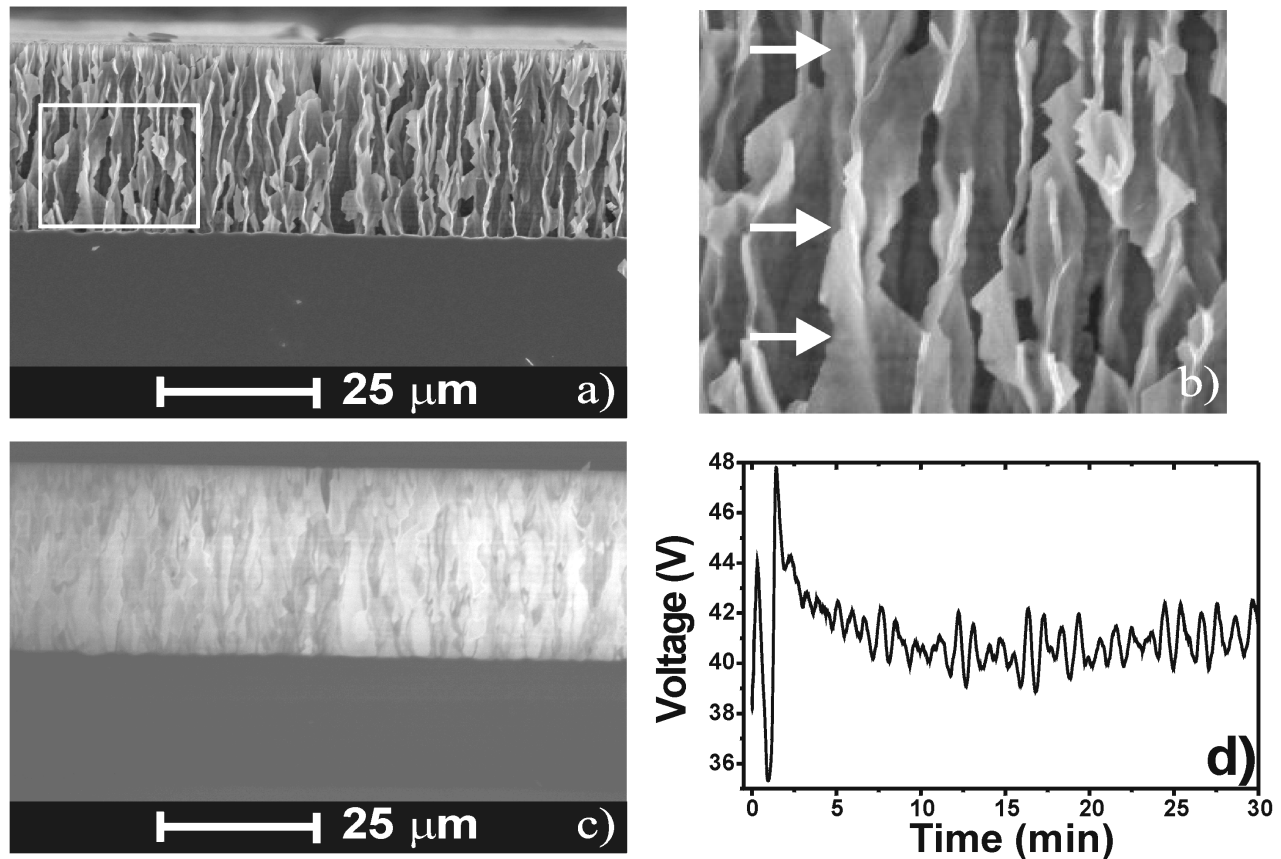
Figure 8.8: *a, b) SEM and c) panchromatic the CL images in cross-section taken from a sample anodized galvanostatically at two current densities: $j_1 = 100 \ mA/cm^2$ for 30 min and $j_2 = 1 \ mA/cm^2$ for 240 min. d) As in the case of n- InP at high current densities self-induced voltage oscillations are observed. Voltage oscillations induce the pore diameter oscillations (see b an c), although the correlation between the diameter and voltage oscillations is not so evident as in the case of n- InP.*

8.9, where the CL spectra of bulk GaP and porous layers produced at high and low current densities are illustrated. Although all the spectra are dominated by a band with the maximum at approximately 1.5 eV, they give further evidence that the top porous layer exhibits the most intense luminescence. As to the second layer produced at the current density $1 \ mA/cm^2$, it shows less luminescence in comparison to both the top porous layer and bulk GaP.

Taking into account the effect of H- passivation of pore walls in Si, one may expect the {112} planes (forming the triangular shape of the crystallographically oriented pores) in III-V compounds to have a high stability against dissolution, *i.e.* they are an easily passivated set of planes enveloping ⟨111⟩ directions. We suggest that in this case, as in the case of GaAs and InP the crystallographically oriented pores obtained at the current density $1 \ mA/cm^2$ expose {112} planes which are efficiently passivated in the electrolyte. On the other hand, under ambient conditions these planes seem to be characterized by bad passivation. As a result, the non-radiative recombination of the free carriers via surface states becomes as strong as to compete with the radiative recombination processes. This explains qualitatively the decrease in the luminescence intensity caused by anodic etching at the current density $1 \ mA/cm^2$ (Figure 8.9, curve 3).

Figure 8.9: *CL spectra of bulk GaP (curve 1) and porous layers produced at current densities $j_1 = 100$ mA/cm^2 (curve 2) and $j_2 = 1$ mA/cm^2 (curve 3). The beam energy is 25 keV, the beam current is 50 nA. This spectra demonstrate clearly that the porous layers obtained at very low anodization current densities are less luminescent than the bulk (curve 3).*
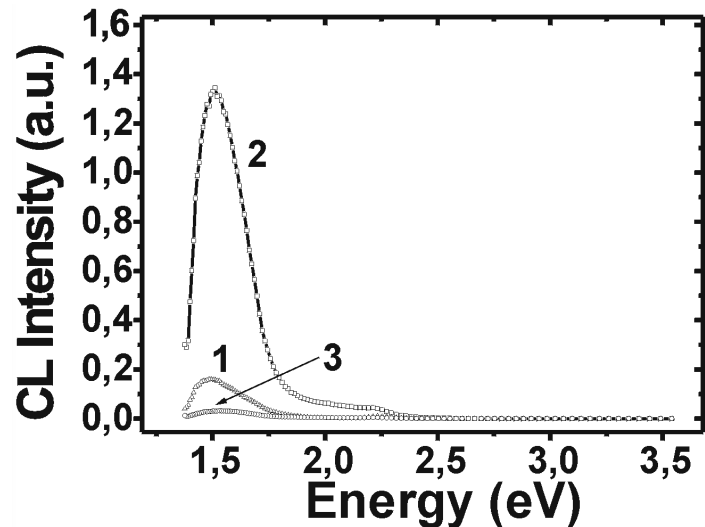
In contrast, the pore walls at high anodic current densities exhibit weak passivation in the solution and efficient passivation under ambient conditions. The saturation of the dangling bonds, however, does not explain the strong increase (relative to the bulk material) in the luminescence intensity induced by the porosity. It is well known that electrochemical dissolution of n-type semiconductor materials removes preferentially the dislocations and other lattice imperfections that may play the role of non-radiative recombination centers. The decrease in the density of non-radiative recombination centers accompanied by in-situ surface passivation can explain qualitatively the observed increase in CL intensity induced by porosity. One should also take into account that GaP, being an indirect gap semiconductor, in the porous form exhibits surface related vibrations [91]. Porous structures expose more surface, thus more surface vibrational modes can be excited and participate in the process of free-carrier radiative recombination and, consequently, increase its probability considerably.

The degradation of luminescence in bulk GaP and GaP-based light emitting diodes under neutron irradiation, intense laser excitation, etc., has been studied extensively for many years [92, 93, 94]. Particle irradiation usually introduces non-radiative recombination centers, attenuating the luminescence. However, for beam currents I_b larger than 50 nA, the emission in the porous specimens is much more susceptible to beam damage than in as-grown GaP. It is therefore possible that the pronounced CL attenuation in porous GaP is due to irradiation-stimulated out-diffusion of radiative centers. In porous layers possessing a high surface-to-volume ratio stimulated out-diffusion of impurities should obviously be much more significant than in bulk material.

Ultraviolet luminescence from porous GaP has been reported in the literature previously [16, 15]. Broad, very low intensity emission at energies higher than 2.75 eV was occasionally observed in the porous samples presented in Figure 8.7 on page 106. This emission is sensitive to irradiation, *i.e.* and is very rapidly attenuated by radiation (see the insert in Figure 8.7). Currently, there are two possible reasons for the occurrence of UV emission. According to the SEM analysis, the dimensions of the main structural entities of the porous layers are of the order of 100 nm or higher, and therefore they cannot provide conditions for quantum confinement of free carriers. However it is feasible that the micro-porous skeleton may be covered by a thin nano-porous film in which the occurrence of quantum size effects is possible. For example in GaAs electrochemical etching processes have been shown to result in a wide distribution of porosity, varying from micrometer to

nanometer range features [95]. If this is the case for these porous GaP samples, then the relatively rapid attenuation of the UV emission under the action of the electron beam (see the insert in Figure 8.7) can be attributed to local heating due to the reduced thermal conductivity of the film. The second possible reason for the observation of UV luminescence is the formation of a thin oxide film covering the surface of the pores during [96]. Electron beam induced dissociation/damage of the oxide would account for the attenuation of the emission during irradiation. Further studies are necessary to elucidate the origin of UV emission in porous gallium phosphide.

8.3 Porosity-Induced Spatial Modulation of the Cathodoluminescence in InP

The optical properties of porous InP are interesting both from a fundamental as well as from a practical point of view. The most intensive studied optical property of porous InP is the photoluminescence (PL). These investigations were motivated by several reasons.

� As in the case of GaP there are no SEM - CL comparison studies for porous InP.

▸ Cathodoluminescence can provide additional information about the optical properties of the porous structure.

▸ It is interesting to see the difference and similarities between the CL properties of porous GaP and InP.

Therefore, in this chapter the CL particularities of crystallographically or current-line oriented pores and bulk n- InP will be discussed. It will be shown that a synchronous spatial modulation of the degree of porosity and CL intensity can be reached in InP by periodically switching the dissolution current.

The samples used for these experiments were (100)-oriented S-doped n- InP with a free carrier concentration $n = 10^{18}$ cm^{-3}. The CL was excited with a continuous 15 keV, 0.25 nA electron beam at normal incidence and was collected from 125 μm^2 regions to reduce electron beam induced effects.

Figure 8.10a shows the SEM image in cross-section taken from a sample subjected to anodization in 5% HCl electrolyte. In order to modulate the degree of porosity as a function of depth, the anodic etching current was periodically switched on and off, *i.e.* the anodic current changed from 80 mA to zero and vice versa with a period of 0.2 min. The etching takes place only during the first 0.1 min of the cycle, while in the second 0.1 min no dissolution occurs (no current flows). However, the process interruption for 0.1 min proves to be very important because in the meanwhile the pore tips become passivated. When the current is switched on again, a new nucleation phase is required, *i.e.* a new nucleation layer (NL) emerges similar to the NL related to the first stage of the dissolution starting at the initial surface of the sample. Applying this procedure, a structure was obtained with a spatially modulated porosity consisting of 14 alternating layers of high and low porosities (Figure 8.10a). Although neighboring layers exhibit quite different morphologies and degrees of porosity, the interfaces prove to be rather sharp, see the insert in Figure 8.10a. The degree of porosity in the NL is less than 10 %, the pores being oriented along
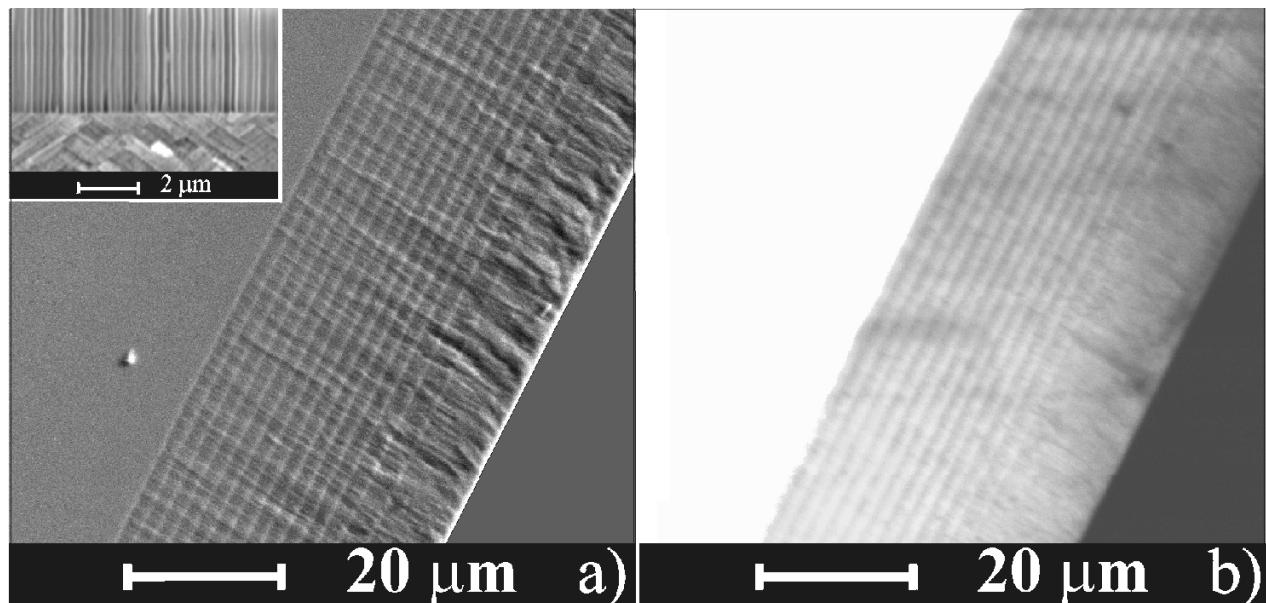
Figure 8.10: *a) SEM and b) panchromatic CL images in a cross section taken from a porous InP structure with spatially modulated degree of porosity. The insert shows the interface between two neighboring porous layers. In contrast to n- GaP, here the bulk material is much stronger luminescent than the porous layers. Also the porous layers with crystallographically oriented pores have a higher CL intensity than the porous layers with current-line oriented pores (the white thin lines on the SEM and CL images are porous layers with crystallographically oriented pores).*

{111}B crystallographic directions. As to the high porosity layers, they exhibit pores oriented perpendicularly to the initial surface - (Figure 8.10a, the upper part of the insert).

The porosity relief caused by periodical switching of the dissolution current on and off was found to give rise to spatial modulation of the CL intensity (Figure 8.10b). Note that the higher the degree of porosity the lower the CL efficiency. The spectra presented in Figure 8.11 on page 111 also show that the CL intensity from the current-line oriented pores is nearly 3 orders of magnitude lower than from the bulk n- InP and 2 orders lower that the crystallographically oriented pores. This decrease in CL intensity with porosity can be understood if it is supposed that the non-radiative recombination centers (mainly at the surface) in porous n- InP are not passivated by the species in solution during the electrochemical etching and they also can not be passivated in air, *e.g.* by formation of an oxide. Therefore the rate of non-radiative recombination of free carriers increases with porosity (surface exposed to the air), *i.e.* the number of surface defects increases.

Both the degree of porosity and the transverse dimensions of pores and skeleton walls can be effectively modified by changing the electrolyte composition. In particular, in 5% HCl electrolyte the transverse sizes of pores and InP wall thickness is equal to 200 and 120 nm respectively, leading to a degree of porosity of about 55%. The SEM top view of sample taken after removal of the NL show the spatial distribution of pores to be uniform (Figure 8.12).

According to the inserts a) and b) presented in Figure 8.12, doubling the electrolyte concentration results in a nearly 3-fold reduction of the skeleton wall thickness. This in turn further reduces the intensity of luminescence. As seen from Figure 8.13, the intensity of the near-band-edge CL decreases 100 and 4000 times after sample anodization in 5 % and 10 % HCl electrolytes

Figure 8.11: *CL spectra of bulk InP (squares) and porous layers produced at low - crystallographically oriented pores (spheres) and high current densities - current-line oriented pores (triangles) in 5 % HCl electrolytes, T = 80 K.*
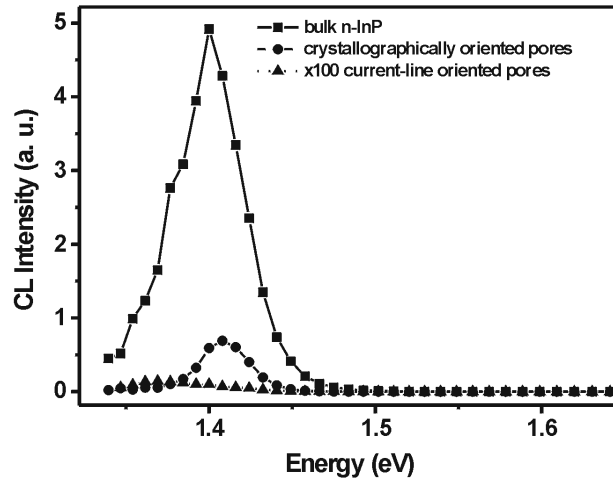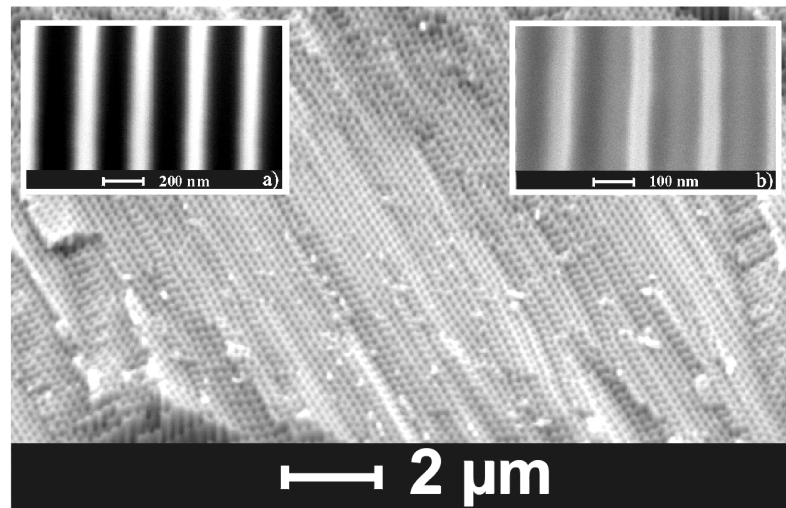

Figure 8.12: *SEM micrograph of the top surface of an InP sample after anodization in 5% HCl electrolyte with subsequent removal of the NL. The inserts show cross-sectional SEM images taken from samples anodized at (a) 5% and (b) 10% electrolytes respectively. The pore walls as well as the pore diameter can be reduced if the concentration of the electrolyte is increased.*

respectively. Please note that at 10 % HCl the pore walls are in the range of 50 nm. In this range the quantum size effects can already be expected. Indeed, a small upward shift of the frequency ($\sim 5\ meV$) of the CL band maximum in the sample anodized at 10 % electrolyte in comparison to that of the as-grown specimen is found. One should be careful if intending to increase the concentration of the electrolyte in order to decrease the thickness of the pore walls. This is caused by the fact that by increasing the concentration we also increase the number of undissociated HCl molecules, which can etch chemically (and uncontrollably) the pore walls and thus destroy the porous structure.

8.4   Summary and Conclusions to Chapter 8

In GaP three different types of porous morphologies have been observed. The 'catacomb-like' porosity is introduced under 'soft' anodic etching of the as-grown samples. In this case the etching starts at surface defects such as emergent dislocation loops and occurs at relatively low current densities not exceeding a few mA/cm^2 under constant voltage within 5 to 15 V. The symmetric distribution of secondary pores propagating radially away from the primary pore probably reflects
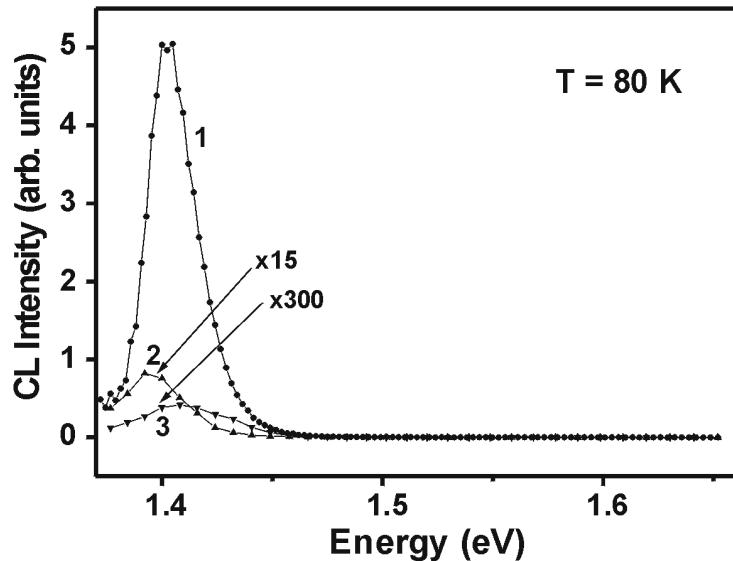
Figure 8.13: *CL spectra of bulk InP (curve 1) and porous layers produced by anodization in 5 % (curve 2) and 10 % (curve 3) HCl electrolytes. T = 80 K. The CL decreases as the porosity is increased. A frequency shift at high porosity is observed (curve 3) which can be attributed to quantum size effects.*

the distribution of lattice strain around the dislocations.

The electrochemical dissolution at high current densities is called 'shock' type anodization. A high anodic current is supplied by a high voltage which in turn, provides conditions for a large band bending. The holes necessary for material dissolution can then be generated by tunneling or thermal activation of the electrons from the surface states to the conduction band [61]. The pores grow along the current-lines and the crystallographic orientation of the sample has no influence upon the porous layer morphology. The degree of porosity is entirely defined by the anodic current density and the substrate conductivity.

The switch from dissolution at high current density to anodization under 'soft' conditions (*e.g.* at the current density of about $1 \ mA/cm^2$), gives rise to a new type of morphology where the pores are oriented preferentially along crystallographic $\langle 111 \rangle B$ directions, as can be seen in Figure 5.6 on page 51. This kind of morphology can also be obtained at depth in porous layers under etching conditions which result in the formation of catacomb-like porosity in the vicinity of the initial surface. We found that a decrease in the anodic current density up to $1 \ mA/cm^2$, after the porous domains meet, favors further growth of pores along $\langle 111 \rangle B$ crystallographic directions.

The observation of intense luminescence, in spite of the high surface-to-volume ratio, implies that the pore surfaces are passivated. Taking into account the composition of the electrolyte, sulfur may be considered as a possible candidate for in-situ passivation of the porous GaP layers. Sulfur was recently identified as one of the most important surface passivators in III-V compounds [97]. Further, electrochemical dissolution of n-type semiconductor materials is known to preferentially remove the dislocations and other lattice imperfections [17, 98] which may play the role of non-radiative recombination centers. Reducing the density of non-radiative recombination centers accompanied by in-situ surface passivation may explain qualitatively the observed increase in the CL intensity induced by porosity.

On the other hand in InP CL intensity from crysto pores proved to be higher than from curro pores, just the opposite effect as for GaP. Nevertheless, the intensity of CL in InP can be also spatially modulated by varying the anodization conditions. More than that, CL can be used as a porosity indicator for two porous layers in InP: high CL - low porosity, low CL - high porosity.

This demonstrates the ability to fabricate multilayer structures with controlled porosity that may provide opportunities for manufacturing Bragg mirrors, Fabry-Pérot filters and waveguides ready to be integrated in optoelectronic circuits.

Chapter 9

Conclusion

9.1 Summary

Pore formation in III-V semiconductors provides for fascinating cross-disciplinary research, combining semiconductor physics, electrochemistry, and stochastic physics. Even at the presently very early stage of investigation, porous layers in III-V materials show a wealth of new properties. Applications of porous III-V semiconductors have to wait for more work in this general area of research, but are certainly feasible based on the findings obtained so far.

This work showed that the systems are intrinsically dynamic. This is expressed mostly by the strong tendency for current oscillations in growing pores. A remarkable degree of self-organisation and pattern formation can result from the system dynamics, and it is safe to say that many features are still awaiting discovery, not to mention explanation. It is hoped that the results presented in this work have enlarged the data base about porous semiconductors and also triggered new discoveries concerning pores in Si, like current-line oriented pores. While the results demonstrate that differences in basic chemistry and electrochemistry are certainly important, they also demonstrate that there is much common ground resulting from general semiconductor properties and features.

The main findings from the present work can be enumerated as follows:

▰ **Current line oriented pores**, never seen or described before, can be formed in InP, GaP, and, after their dicovery in III-Vs, in Si, too. These pores always grow perpendicular to the equipotential lines of the electric field in the sample.

▰ **Crystallographically oriented pores** grow only along one of the two possible $\langle 111 \rangle$ direction, i.e. along $\langle 111B \rangle$. This was not realized before.

▰ Crystallographic pores, upon branching, may also grow upwards, promoting the formation of unique **pore domains** in InP and GaP that have not been observed before.

▰ In InP, **a self-organized single crystalline pore array** with hexagonal symmetry on (100) substrates was obtained for the first time. It results from an involved nucleation and self-organization mechanism which was investigated in detail.

▰ Well-defined **Bragg mirrors** (1D photonic crystals) could be obtained by simply switching from one type of pores to another, *i.e.* from crysto to curro and vice versa.

▗ **Voltage oscillations** under galvanostatic conditions in InP and GaP were observed for the first time and shown to be correlated to spatially synchronized pore diameter oscillations. A model explaining this self-organisation feature was established.

▗ It was demonstrated for the first time, that contrary to general belief, **crystallographic pores can easily intersect** each other. This is an important condition for the formation of 3D photonic crystals.

▗ It was shown that **self organized 3D photonic crystal** structures can be obtained by using the self-induced diameter and voltage oscillations or by using the ability of crysto pores to intersect.

▗ **Tetrahedron-like pores in GaAs** have been observed for the first time. This self-induced oscillation in space of pore diameters can be explained by the aging concept introduced by the the Current Burst Model.

▗ It was demonstrated that the current line nature of pores can be used for manufacturing **integrated waveguide structures on InP**.

▗ The first **cathodoluminescence comparison between porous GaP and InP** was made. It was observed that CL intensity from a curro porous layer in GaP is much higher than from bulk material, whereas in InP it is the other way around.

▗ It was shown that **self-organization plays a major role** during pore formation not only in III-Vs but also in Si (e.g. for tetrahedron like pores, domains of crystallographically oriented pores, self induced diameter and voltage oscillations, single crystalline pore crystal etc

▗ **Uniform nucleation** on not lithographically patterned samples of GaAs have been obtained by using a two step anodization method. These process leads to a quasi-uniform 3D porous structure.

▗ **Nucleation on lithographically patterned (100) GaAs** was tried for the first time. In spite of the fact that the pores start to nucleate within the defined windows the uniformity of the structure is destroyed in time due to branching of the pores and pores nucleated at severe defects in the substrate. Additional etching optimization it is required in this regard.

For an overview of different types of pores observed in III-Vs and the corresponding etching conditions see Appendix F. These findings allowed to conclude that pore etching in general and in III-V compounds in particular is dominated by a series of non linear interactions in time and space. These interactions in space and time can explain many of the observed features, for example:

▗ The formation of a nearly closed packed 2D array of pores in InP.

▗ Self-induced simultaneous diameter oscillations of all pores in InP, GaP and Si.

▗ Intersection of crystallographically oriented pores.

▗ Formation of tetrahedron like pores in GaAs *etc.*

Due to this high complexity of non-linear interactions, different pore morphologies can be found in one and the same system, just by changing one parameter, *e.g.* the current density. More than that, critical points exist for the switch from one growing phase to another, indicated *e.g.* by a voltage jump in the case of tetrahedron-like pores.

The current burst model was extended also to III-V compounds. According to the current burst model the current always flows in local bursts consuming a defined amount of charge. This model in principle can be applied to pore formation in all semiconductors. The differences in the pore morphologies for different III-V compounds depend on the stability of the generated oxide and the passivation properties of the semiconductor electrolyte interface. Also, due to the 'chaotic' behavior of the pore formation, moderate differences in the reaction's kinetic may lead to extreme differences in the resulting pore morphologies.

Since the electrochemically etched pores in III-V compounds show a great potential for application (*e.g.* highly ordered 2D and 3D pore arrays for photonic application), a fundamental understanding of the underlying basic electrochemistry as well as the interactions between pores is very important. The results presented in this work show that pore formation is an interplay of electrochemistry, semiconductor and statistical physics. Controlled pore formation is therefore a big challenge and will need some more years of research, although promising results already exist.

9.2 Outlook and Future Research

There is still a lot of work to do related to pore formation in III-V compounds. In my opinion, in the near future the primary attention should be still paid to electrochemical aspects. The most important are:

▰ To find conditions for pore formation in p-type III-V materials. This will allow to have a more complete picture of the pore formation mechanism in general, comparing them with the pores in p-type Si.

▰ To test new electrolytes in order to find conditions for current-line oriented pores for other semiconductors like GaAs and Ge. This will probably allow to obtain ordered structures similarly to those in InP.

▰ To optimize the etching conditions for pre-patterned samples in GaAs as well as to repeat such experiments in InP and GaP.

▰ To perform impendance spectroscopy measurements in the pore formation regime. This will give new information about the oscillations which take place inside the pores.

▰ To develop some *in situ* measurement techniques for pore growth control, *e.g.* fast IV measurements or impendance spectroscopy.

Also the optical properties of the porous structures should be investigated in more detail:

▰ To measure the transmission and reflection spectra for different light polarization and wavelengths of the self-organized 2D porous structures obtained in InP.

� To find a more ample answer why the CL intensity in porous and bulk InP is inverted as compared to porous and bulk GaP. To test if passivation or some other reasons are responsible for this effect.

▷ To measure the optical properties of the wave-guide structures obtained in InP, *etc.*.

Last but not least, for a better understanding of pore formation in semiconductors some other compound materials interesting for the modern electronics should be investigated from the 'pore' formation point of view, *e.g.* GaN, SiC, InAs etc. The first experiments on n-type GaN [99] and Ge [100] have been already started by us. See the first results on macropores in Ge in Appendix E.

Appendix A

Introduction to Photonic Crystals

How a periodic structure can control and manipulate the light is not evident. The easiest way to understand the behavior of light in a photonic crystal is to compare it to the movement of electrons in a semiconductor. In a semiconductor the electrons do not move freely, but experience potential interactions with the atom nuclei via the Coulomb force. Due to the fact that the atoms in semiconductors (crystals) are arranged periodically the potential interaction will be periodic as well. It is well known that namely this potential interaction results in the formation of a forbidden energy gap in semiconductors. The formation of the band gap makes the semiconductors so special in the modern electronics.

In the case of light the photons can not interact with the atoms via the Coulomb force, nevertheless they can 'feel' the surrounding medium in which they are propagating. This is evident when the light passes from a more to a less dense environment or vice versa. A part of the light is reflected and another part is refracted. The reflection and refraction is nothing else but the accommodation of the light to the new environment. In order to account for this effect each medium is characterized by a refractive index n.

If photons are moving through a transparent dielectric material that contains a number of air holes arranged in a periodic manner, they will pass through both regions: dielectric and air. The periodicity in the refractive index can be treated mathematically like the periodic potential that an electron experiences when traveling through a semiconductor. However, depending on the wavelength, the light will be confined either within the dielectric material or the air holes. This confinement results in the formation of allowed energy regions separated by a forbidden region - the so-called photonic band gap, similarly to the electronic band gap in semiconductors. Thus, the patterned dielectric material will have the ability to pass freely only the light which is not within this band gap, whereas will reflect or block the light with the energy in the photonic band gap.

The potential of photonic-crystal structures was first realized in 1987 by Eli Yablonovitch [62]. In 1991, Yablonovitch *et al.* produced the first photonic crystal by mechanically drilling holes a millimeter in diameter into a block of material with a refractive index of 3.6. This structure became known as 'Yablonovite' exhibited a 3-D photonic band gap, *i.e.* prevented propagation of microwaves (in the photonic band gap of this structure) in any direction.

However, in order to make photonic devices compatible with the already existing optoelectronic ones, it is necessary to go to *shorter* wave lengths, *i.e.* towards the visible spectrum. This means that the size of dielectric particles constituting a *PC* should be in the micrometer or even

sub-micrometer range. Roughly, the dielectric 'particles' should have dimensions equal to the wavelength of the light, for which the *PC* is designed, divided by the refractive index of the medium. This means that the bigger the refractive index of the material is, the smaller the constituent dielectric blocks should be. Taking into account that a photonic band gap is easier to obtain in dielectrics with high refractive indexes it is evident that challenging technological problems are to be expected.

It took more than a decade to fabricate photonic crystals that work in the near-infrared (780-3000 nm) and visible (450-750 nm) regions of the spectrum. The main challenge has been to find suitable materials and processing techniques to fabricate structures that are made of dielectric regions in the nanometer scale.

For example, when creating a photonic crystal that could trap near-infrared light with a wavelength of 1 μm in a material with a refractive index of 3.0, one would have to create a structure in which the dielectric regions and air holes are separated by about 300 nm - a relatively difficult task.

Such small dimensions are nearly impossible to be obtained using standard mechanical drilling technique. A couple of other techniques have been developed for producing *2D* and *3D* photonic crystals, like:

� The stacking technique [101].

▶ Very Large Scale Integration (VLSI) tools [102].

▶ Holographic lithography [103],

▶ Dry etching [104].

▶ Last but not least electrochemical etching [105].

Most of them are quite expensive and are partially incompatible with the existing *IC* technology. Electrochemical etching does dot suffer from these disadvantages. First, because electrochemical etching is compatible with the modern technological processes and secondly, it does not require sophisticated equipment.

Why photonic crystals? The semiconductors in tandem with the metal wiring offer the possibility to control efficiently the flow of electrons on very small scales. This is the reason why they are the main materials in the modern integrated circuit technology. In addition, photonic crystals show a great potential for controlling the flow of light, therefore they are treated as the future technology. In what follows some examples will demonstrate how photonic crystals could be used.

In order to increase the amount of information transmitted through an optical fiber two main solutions are possible:

▶ to increase the sped of operation of the source and of the receiver,

▶ to use more independent wavelength along one and the same fiber.

However the speed of electronic devices can not be increased at infinity. Current optical systems have achieved rates in excess of 40 gigabits per second. If more that one wavelength is used then the amount of information can be further doubled, tripled etc.

Due to the fact that the optical fibers usually are transparent only for a very short range of wavelengths, the wavelengths for transmitting information through one fiber should be very near to each other. Unfortunately, typically the widely used sources of lights, the light-emitting diodes, emit photons in randomly oriented directions and have a large range of wavelengths. To solve this problem a mirror can be used in order to direct the light along the desired direction. Photonic crystals could be used to design a mirror that reflects a selected wavelength of light from any angle with high efficiency. They also could be integrated within the photoemissive layer to create a LED that emits light at a specific wavelength and direction. This allows to fabricate light sources with slightly differing wavelengths.

Ideally, to gain complete control of the light in all three dimensions one would need a structure which is periodic in all three directions. This is a very difficult technological problem and only some ingenious ways to produce these so-called 3D photonic crystals have recently been reported in addition to Yablonovitch's method. However, the structures produced this way are usually difficult to integrate with the already existing technology. Fortunately 2D periodic lattices exhibit some of the useful properties of a truly 3D photonic crystal, and are far simpler to make. These structures can block certain wavelengths of light at any angle in the plane of the device, and can even prevent light entering from certain angles in the third dimension (i.e. perpendicular to the surface). Thus 2-D photonic crystals are a good compromise for many applications and are easily incorporated within planar waveguides.

Appendix B

Electron Microscopy and Cathodoluminescence

Electron Microscopes (EMs) use a focused beam of electrons to 'bombard' the sample and gain information about its structure and composition. The basic ideas of an *EM* are:

� A beam of electrons is generated by the electron source and accelerated towards the specimen by means of a positive electrical potential.

▲ The beam is focused into a thin monochromatic beam using metal apertures and magnetic lenses.

▲ Then the beam is focused onto the sample using again a magnetic lens.

▲ The beam interacts strongly with the specimen.

The 'products' resulting from the interaction of the electron beam with the sample, like X-rays, back-scattered, Auger, and secondary electrons, cathodoluminescence (see Figure B.1 on page 124), are detected and transformed into an image. In what follows we will discuss in more detail secondary electrons and CL.

Secondary electrons generation depend strongly on the topography. Due to their low energy of 5 eV only the secondary electrons that are created near to the surface (10 nm) can leave the sample and be collected. Any change in topography in the sample that is larger than this sampling depth will change the yield of secondary electrons due to the collection efficiency. Collection of these electrons is made by a collector in combination with a secondary electron detector. The collector is a mesh with a +100V potential applied to it which is placed in front of the detector, attracting the negatively charged secondary electrons. The electrons then pass through the grid-holes into the detector to be counted.

For each point on the studied area the microscope counts the number of secondary electrons reaching the detector and displays it as a pixel on a picture/display. The pixel intensity is determined by the number of the counted electrons. This process can be repeated in a scanning mode, *e.g.* 30 times per second, thus obtaining a Scanning/Secondary Electron Microscope (SEM) picture of the investigated area. Due to its high resolution compared to optical microscopes, electron microscopes are fascinating tools for investigating porous semiconductors.
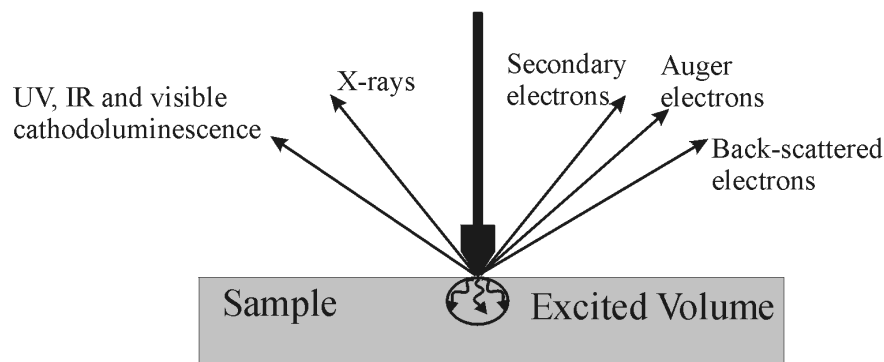
Figure B.1: *Schematic representation of the energies produced from electron beam interaction with solid matter; The sample is bombarded by an electron beam. Due to the interaction of the beam with the sample different light and electrons are generated: UV, IR, Visible, X-rays, secondary, Auger and back-catered electrons. For CL measurements are important only UV, IR and visible light. X-rays, secondary, Auger and back-scattered electrons are used in other types of investigation techniques. Also, a part of the energy of the incident electrons is absorbed by the sample rising its temperature. Scanning the sample with the incident beam will allow us to collect CL spectra from different regions of the sample, and thus 2D CL photographs can be obtained. More tan that, the penetration depth of the incident beam and thus the excited volume in the sample depends on the energy of the incident electrons. Thus, a 3D image of the sample is possible to be obtained if the scanning mode and wavelength changing are combined.*

Similarly, all the other interaction products can be used (see Figure B.1) to characterize the samples, *e.g.* cathodoluminescence. In what follows some more detailed notion about cathodoluminescence and luminescence in general will be presented.

Luminescence is the emission of light from a solid, which is stimulated by some form of external energy. Luminescence also includes the commonly-used categories of fluorescence and phosphorescence. Fluorescence is said to occur when the emission disappears almost immediately after the exciting source was switched off and where there is no thermal cause, whereas in phosphorescence the emission decays slowly after removal of the excitation. The distinction between these classical types of luminescence is somewhat arbitrary and confusing. Confusion is avoided by using the term luminescence, and specifying the activating energy as a descriptive prefix. Thus Roentgenoluminescence is produced by X-rays, photoluminescence by light (e.g. ultra-violet), thermoluminescence results from heating and cathodoluminescence (CL) results from excitation by electrons.

Cathodoluminescence is the light emitted by specimens as a result of electron bombardment with wavelengths of about 160-2000 nm. The visible regime is between 400 and 800 nm. Shorter wavelengths are ultraviolet (UV), and longer are infra red (IR). A CL system is designed to detect only the wavelengths characteristic to CL (160-2000 nm).

X-rays have a higher energy than UV. Therefore they provide a finger print characteristic of the elements present in the sample. CL is associated with much lower energy transitions. For this reason, CL is not exclusively governed by chemical elements and is not used as an elemental analysis technique. On the other hand, CL is governed by factors such as physical chemistry, opto-electronic properties, temperature, crystal structure, strains *etc.*.

Photoluminescence and cathodoluminescence are said to be complementary. For example a scanning electron microscope configured with cathodoluminescence can yield information on the spatial distribution of the luminescence. Non-scanning PL methods can provide high quality macroscopic data. However, translating PL features in a CL system is not straightforward since matching experimental parameters, like temperature is difficult.

This becomes even more complicated by inherent differences in the nature of the excitation (electrons for CL and photons in PL) and the definition of excitation densities. It is believed that in general CL is more sensitive to excitation circumstance than PL. Sample charging and contamination related phenomena can have dramatic effects on CL. Also changes in surface conditions by passivation are observed to affect PL and CL signals differently.

Quite often the CL systems are supplied with cryogenic cooling. However, this really depends on the application. Specimen cooling increases the spectral discrimination and provides more insight about the physics of the light emission processes. Some direct band gap semiconductors give adequate CL at room temperature. However, the information contained in the CL emission may be blurred by thermal processes. Also, certain transitions may not be activated at low injection conditions unless the specimen is cold. This can be critical in achieving the mix of spatial resolution and spectral resolution from a sample. For most specimens, Helium cooling is preferable, but nitrogen can be adequate. For indirect band gap semiconductors, helium cooling is usually essential.

Appendix C

Wavelets Transformation

The basis set for Fourier analysis consists of harmonic (i.e. perfectly monochromatic) waves which extend to infinity. If we consider the 1D case, where the function being analyzed is a time signal, this is a process of decomposing the function $f(t)$ into its frequency components. Many physical problems involve waves and can be analyzed in this way. However, although we have gained information about the frequency content of $f(t)$ we have lost all temporal information. Alternatively we can consider the function $f(t)$ to be an expansion in terms of a basis set of Dirac functions - in other words the basis set (and hence the information gained) is localized in time but not in frequency.

In many cases we would wish to examine both time and frequency information simultaneously. This can be accomplished by expanding $f(t)$ in terms of functions that are both oscillatory and localized in time. These functions are known as wavelets, and this leads to wavelet transformation.

Let's consider the continuous wavelet transform first. A function is called a mother wavelet if it has certain properties: in particular, its integral equals zero. This implies that the function has some oscillatory characteristics. From the mother function a family of daughter wavelets, the so-called basis set, by scaling and shifting can be obtained. The scaling is performed in a self-similar manner. From this basis set one can construct an integral wavelet transform by taking the inner product between $f(t)$ and the various daughter wavelets.

In oder to calculate the inner product a special procedure was included in the SiPor program for pore etching. The wavelet procedure uses the so-called Morlet function as a 'mother' function. In practice, the Morlet wavelet is defined as the product of a complex exponential wave and a Gaussian envelope:

$$\Psi_o\left(\eta\right) = \pi^{-\frac{1}{4}} \cdot e^{i\omega_o\eta} \cdot e^{-\frac{\eta^2}{2}} \tag{C.1}$$

where Ψ_o is the wavelet value at non-dimensional time η , ω_o and is the wave number. This is the basic wavelet function, but now one needs some way to change the overall size as well as to slide the entire wavelet along the time axe. Thus the 'scaled wavelet' is defined as:

$$\Psi\left(\frac{n^{'}-n}{s}\right) = \left(\frac{\partial t}{s}\right)^{\frac{1}{2}} \cdot \Psi_o\left(\frac{n^{'}-n}{s}\right) \tag{C.2}$$

where s is the 'dilatation' parameter used to change the scale, and n is the translation parameter used to slide the function in time. $s^{-\frac{1}{2}}$ is a normalization factor, in order to keep the total "area" of the scaled wavelet constant.

For a time series X, with values of x_n, at time index n (each value is separated in time by a constant time interval dt) the wavelet transform $W_n(s)$ is just the inner product (or convolution) of the wavelet function with this time-series:

$$W_n(s) = \sum_{n'=0}^{N-1} x_{n'} \cdot \Psi^* \left(\frac{n'-n}{s} \cdot \partial t \right) \tag{C.3}$$

where the asterisk (*) denotes complex conjugate. The above sum can be evaluated for various values of the scale s, usually taken to be multiples of the lowest possible frequency, as well as for all values of n between the start and end data. Then, a two-dimensional picture can be obtained by plotting the wavelet amplitude, *i.e.* equation C.3, for different (n, s) pairs. Different colors can be used in the map in order to distinguish between different amplitudes.

The main information which one can get by analyzing such kind of two dimensional maps is the change in time of the dominant frequencies, *e.g.* the one with the highest amplitude of the wavelet. Therefore, this is an ideal tool to investigate the frequency change with time of the self-induced voltage oscillations observed during pore formation in InP.

Appendix D

Two Dimensional Fast Fourier Transformation

2D Fourier transforms simply involve a number of one dimensional Fourier transforms. More precisely, a 2D transform is achieved by first transforming each row, *i.e.* replacing each row with its 1D Fourier transform. This first step yelled an intermediary 'picture' in which the horizontal axis is frequency f and the vertical axis is space y . The second step is to apply 1D Fourier transform individually to the vertical line of the intermediate image. This new image will be the 2D Fourier transformation of the initial image.

A schematic representation how the 2D Fourier transform is performed is presented in Figure D.1. From the figure it is evident that a 2D Fourier transform from an image with $n \times n$ pixels consists of 2n one dimensional transforms. The formulas used for 2D Fourier transform (see D.1 and D.2) follow directly from the definition of the Fourier transform of a continuous variable or the discrete Fourier transform of a discrete system.

In the most general situation a 2D Fourier transform takes a complex array. But, the most common application is for image processing where each value in the array represents one pixel, therefore the real value is the pixel value and the imaginary value is 0.

$$F\left(u,v\right) = \frac{1}{M \cdot N} \sum_{x=0}^{M} \sum_{y=0}^{N} f\left(x,y\right) e^{-j \cdot 2\pi\left(\frac{ux}{M} + \frac{vy}{N}\right)} \tag{D.1}$$

$$f\left(x,y\right) = \sum_{u=0}^{M} \sum_{v=0}^{N} F\left(u,v\right) e^{j \cdot 2\pi\left(\frac{ux}{M} + \frac{vy}{N}\right)} \tag{D.2}$$

where $f\left(x,y\right)$ is the initial pixel array of the image; $F\left(u,v\right)$ is the direct Fourier transform of the image; N, M are the width and height of the image respectively. The Equation D.1 and Equation D.2 are usually called 2D Discrete direct and indirect Fourier Transform.

Also, although the spatial image is a set of integers, its transform is both complex (*i.e.*, consisting of a real and an imaginary part) and non-integer. To display the transform as a frequency image, an output form must be selected from among real R, imaginary I , module $\sqrt{R^2 + I^2}$, or phase. The values are then normalized (generally between 0-255) and truncated to integers for display.

As with the one dimensional Fourier transform for computation is preferred the so-called Fast Fourier Transform (FFT) which saves a huge amount of computation time. The number of
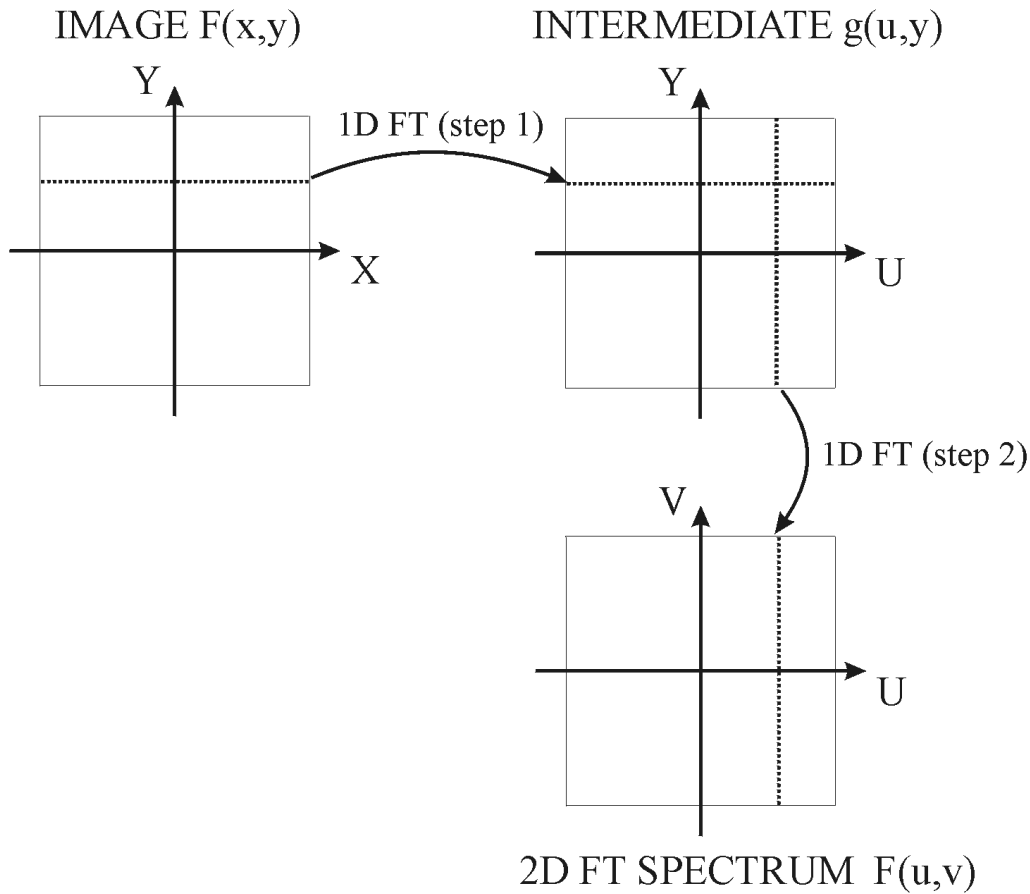
Figure D.1: *The schematic principle of 2D Fourier Transform (FT). 1D FT is taken first from the rows of the initial picture, thus an intermediate function $g(u, y)$ is obtained. Then, the resulting 2D FT spectrum $F(u, v)$ is obtained by taking once again the 1D FT from the of the intermediate function $g(u, y)$.*

operation used for FT is proportional to N^2, whereas for FFT is proportional to $nln(n)$. In order to perform a 2D FFT instead of the much slower 2D FT the image must be transformed so that the width and height are integer powers of 2. This can be achieved in one of the two ways, scaling the image up to the nearest integer power of 2 or zero pad to the nearest integer power of 2.

Fourier filtering and reconstruction is a well known technique extensively used by High Resolution Transmission Electron Microscope (HRTEM) people. The main steps involved in filtering HRTEM pictures are the following:

� Fourier transform is taken from a region of HRTEM image. The result will be a diffraction pattern *(DP)* of that region, which is nothing else but the initial image in the reciprocal space, *i.e.* the frequency domain.

▮ The *DP* is filtered by removing the irrelevant frequencies.

▮ Finally, the inverse Fourier transformation is taken from the filtered *DP* in order to obtain the filtered HRTEM image in real space.

This technique allows to do microscopy on the computer, *i.e.* the image becomes the specimen. Analyzing the computer generated DP's is the same as analyzing TEM difractograms, *i.e.* analyzing them it is possible to find a lot of useful information about the crystal. For example it is possible to find if the crystal is mono, poly, amorphous *etc.*

Appendix E

Pore Formation in Germanium

E.1 Introduction

From the general point of view the main difference between Si and III-Vs is that Si is an elemental whereas III-Vs are compounds semiconductors. From the chemical point of view however, the difference is mainly caused by the quality of the oxides: very good in Si and bad in III-Vs. In this work it was already shown how the difference in oxide quality defines the porous structure. However, it is challenging to investigate what kind of porous structures will develop in a semiconductor which combines the properties of Si and III-Vs, *i.e.* an elemental semiconductor with a bad oxide. Germanium (Ge) is the prominent candidate: it is non-polar like Si but similar to III-V compounds it does not form a stable anodic oxide.

However, just 5-6 papers concerning pore etching in Ge [106, 107, 108, 109] and no macropores were found so far, except those reported by us [100], although there is a wealth of information concerning general electrochemistry of Ge in the older literature, cf. [110]. While Ge today plays only a marginal role in semiconductor technology, pore formation in Ge still could be of interest for application, *e.g.* in the context of photonic crystals [111] or for sensors and special filters.

E.2 Etching Conditions

Ge samples from various sources with a thickness of 1 mm, polished surface and areas of typically 0.2 cm^2 were etched in an electrochemical double cell as described in Chapter 4. The surface orientations were {111} and {100}, all samples were n-type and the doping level was between 10^{18} and 10^{15} cm^{-3}. In this case no back side illumination was used, however there are hints that back side illumination influences pore growth in Ge. The necessary hole supply therefore must rely on a breakdown mechanism. Most likely avalanche breakdown of the space charge region. The electrolytes were H_2SO_4 (5 %, diluted with water), $H_2SO_4 + CrO_3$ (5 %, diluted with water), and HCl (5 %, diluted with water); all experiments were performed at a temperature of 20^oC, and under potentiostatic or galvanostatic conditions. Etching times were between 15 - 120 min. As usually, the samples were investigated with a scanning electron microscope (SEM) in plain view and in cross-section (after cleaving).

E.3   Results and Discussion

The first (unexpected) result is the general presence of some electropolishing, even during the stable growth of pronounced macropores. The plain view micrographs thus do not show the original surface, but a cut through the structure at a depth that depends on the total etching time. This seems to be a unique feature that has neither been observed in Si nor in III-V semiconductors.

The second general observation is that homogeneous pore nucleation is quite difficult to achieve. While this effect is also observed in III-V compounds [56, 83, 61] and must be expected to some extent when working in avalanche breakdown conditions, its dependence on the etching parameters (in particular on the current density) is quite different from the other semiconductors.

Figures E.1 and E.2 show pore nucleation on polished and rough {100} surfaces, respectively. The homogeneity achieved is distinctly different. For a smooth surface the pore density decreases with increasing current, while for a rough surfaces the pore density increases. The reason for this seems to be the co-existence of pore etching and electropolishing. Since electropolishing does not need nucleation, it will be dominant on smooth surfaces where pore nucleation is difficult. Only by reducing the overall current density, electropolishing can be slowed down to a point were pore nuclei can 'survive' for the time needed to induce stable pore formation. Figure E.2d shows a cross section of the pore structure obtained at a current density of 7.5 mA/cm^2 it demonstrates that distinct macropores with clear features are obtained. This is a remarkable observation because in n- Si under avalanche breakdown conditions mesopores (diameters $< 50\ nm$) are obtained exclusively. Macropores have only been observed under special condition in n^+-type Si [81]. However, comparable structures are found in n-type III-V compounds etched under breakdown conditions [67].

The pores show a certain tendency to form side pores in $\langle 100 \rangle$ directions. However, since the density is low and the side pores are not visible in the cleavage plane, they are not easily seen in cross section. Figure E.3a shows an exception (the cleavage plane is not flat in this case).

Since electropolishing is continuously exposing areas formerly hidden in the bulk, side pores become visible on the sample surface. This is shown in Figures E.3 b) and c). These pictures also illustrate several new features of Ge pore etching: The pore walls are very well expressed {110} planes, only sometimes with small {100} facets left in the corners (Figure E.3d). This has never been observed before. Si macropores have a comparatively weak preference for {100} planes, while III-V compounds strongly favor {111}B planes [112].

Figure E.3a also demonstrates that new pores are continuously nucleated. Larger pores nucleated earlier and therefore had more time to grow laterally. The pore shape is generally conical because the electropolishing acts on the pore walls, too. This is demonstrated in Figure E.4a. Only if neighboring pores come too close, their lateral growth will stop. The thickness of the remaining pore walls correlates with twice the space charge region width. Figure E.4b shows an example.

The subsequent nucleation processes only stop if the density of pores is so large that there is no more space for new pores. The already existing pores then may still increase their diameters somewhat until the ultimate limit of twice the space charge region width is reached for the wall thickness between two pores (Figure 3d).

A particular conspicuous issue preferably found on polished surfaces etched at high current densities is the formation of pronounced pore domains, *i.e.* clearly expressed systems of secondary pores always centered around a central primary pore, as shown in Figure E.1c.
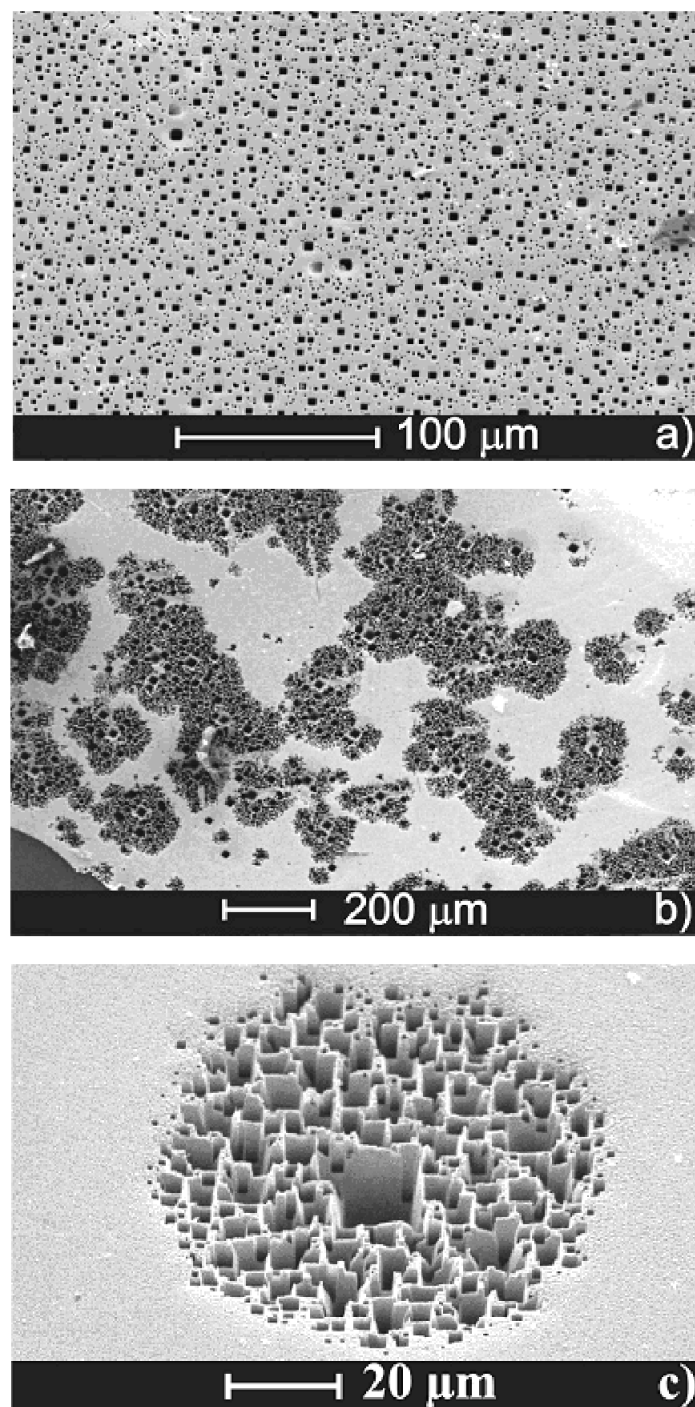
Figure E.1: *Smooth surface. 5% HCl, t = 120 min, T = 20ºC; a) j = 0.5 mA/cm^2; b) j = 2.5 mA/cm^2. b) Single domain.*
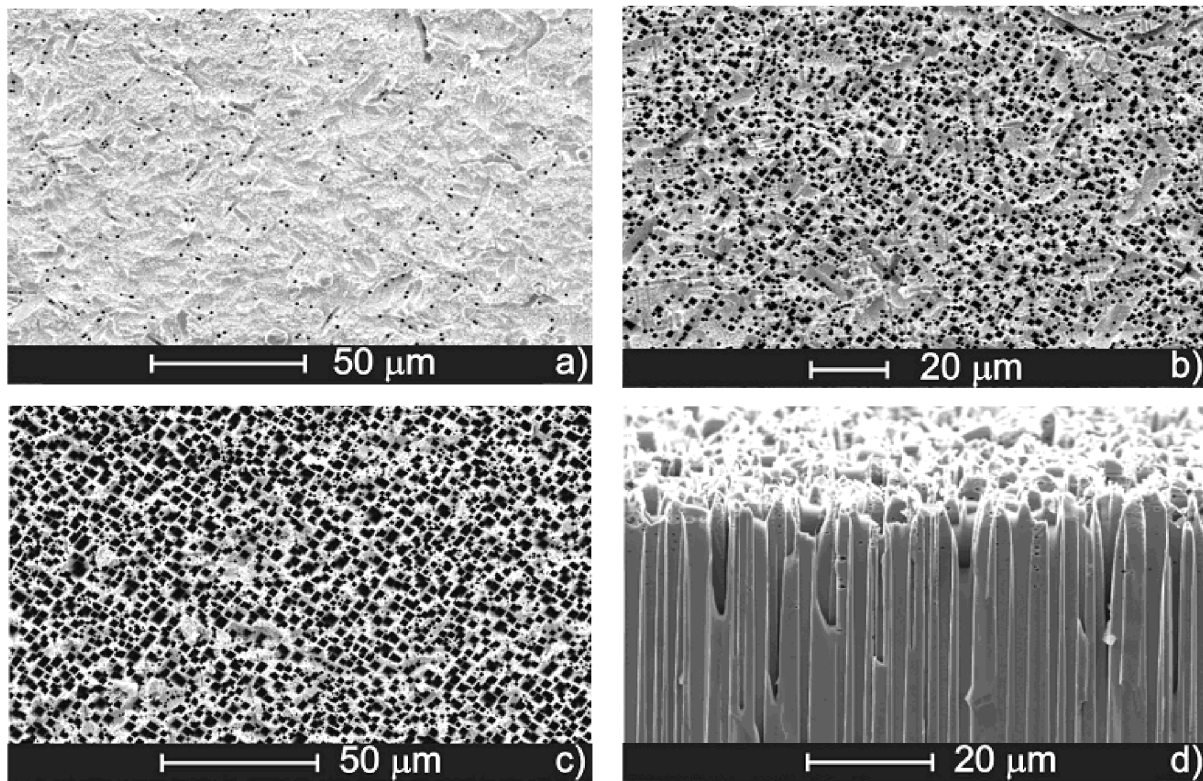
Figure E.2: *Rough surface. 5% HCl, t = 120 min, T = 20 °C; a) j = 2.5 mA/cm^2; b) j = 5 mA/cm^2; c) j = 7.5 mA/cm^2; d) cross section view of the pores.*

Bearing in mind that pore nucleation under those conditions is enhanced for reduced current densities, domain formation can be understood if the potential and thus the current is significantly reduced in an area around a primary macropore. This is precisely what will happen if there are ohmic losses, particularly in the electrolyte.

While it is too early to ponder on details of pore formation in Ge, it appears that two major points can be emphasized:

▼ All results are consistent with the assumption that the degree of passivation of Ge surfaces in the electrolytes used so far is smaller than in Si and while the relative differences between different crystal planes may be even more pronounced. Passivation in this context refers to the density of interface states in the band gap found after prolonged exposure to the electrolyte and with no current flowing [113].

▼ The necessary supply of holes is easily compared to other n-type semiconductors.

The first assumption is supported by the independent measurements of Chalzaviel *et al.* [114] who showed that the surface bond termination of Ge can be changed from H to OH (hydrophobic-hydrophilic) just by changing the applied potential, while in Si always H termination is found. This is a hint, that the binding energy of the hydrogen bonds in Si is larger than either the H or OH binding energy on Ge surfaces, since they can easily be broken by externally applying a
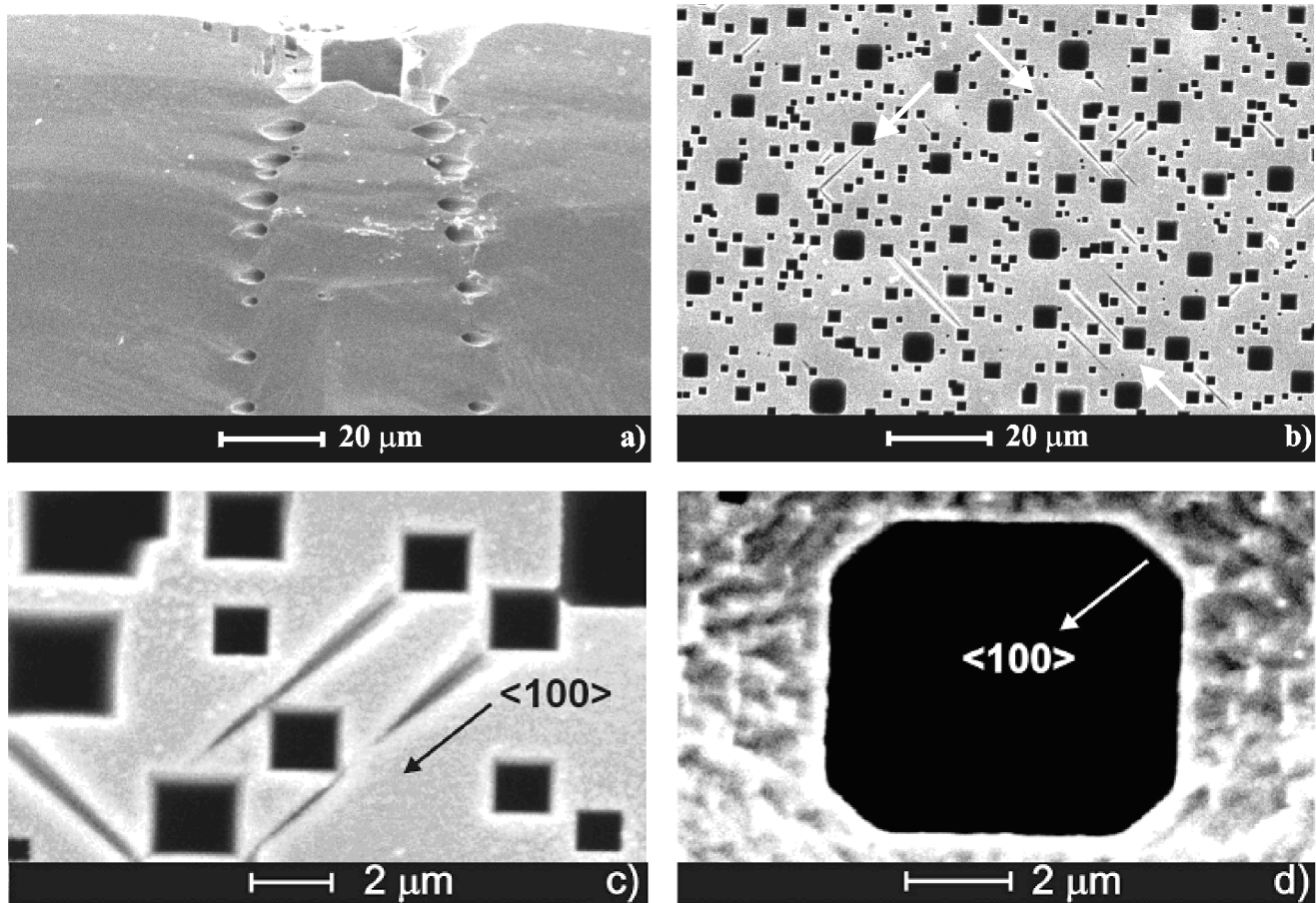
Figure E.3: *a) Side pores emerging from a central pore visible at the top, but obscured lower down by uneven cleavage; b) Side pores (marked by arrows) rendered visible by continuous electropolishing of the surface; c) enlarged view; d) top view of a pronounced main pore.*

voltage. The pores thus show pronounced crystallographic preferences, but the overall passivation is not strong enough to fully stabilize any surface including pore walls against electrochemical dissolution. Assuming that no perfect surface passivation exists, current flows through every point at the surface, even so the current density at pore tips is considerably larger than on flat surfaces. Constant current conditions coupled with pore formation and growth thus lead to a monotonically decreasing average current density since the total surface area increases monotonically.

As soon as the current density is significantly reduced, a new generation of macropores can nucleate and grow. This process can repeat several times and since the diameter of the pores reflects their 'age', a pore size distribution with pronounced peaks should be observed. This is indeed the case as shown in Figure E.3b.

The second assumption follows from the observation of continuously proceeding electropolishing, implying that there is a hole source in addition to avalanche breakdown at the pore tips. This might simply be the leakage current of the reverse biased Ge - semiconductor junction which is intrinsically larger than in Si owing to the smaller band gap, and contains an additional component due to the postulated unpassivated surface states.

In conclusion, it has been shown that pore etching in Ge holds promise not only for potential
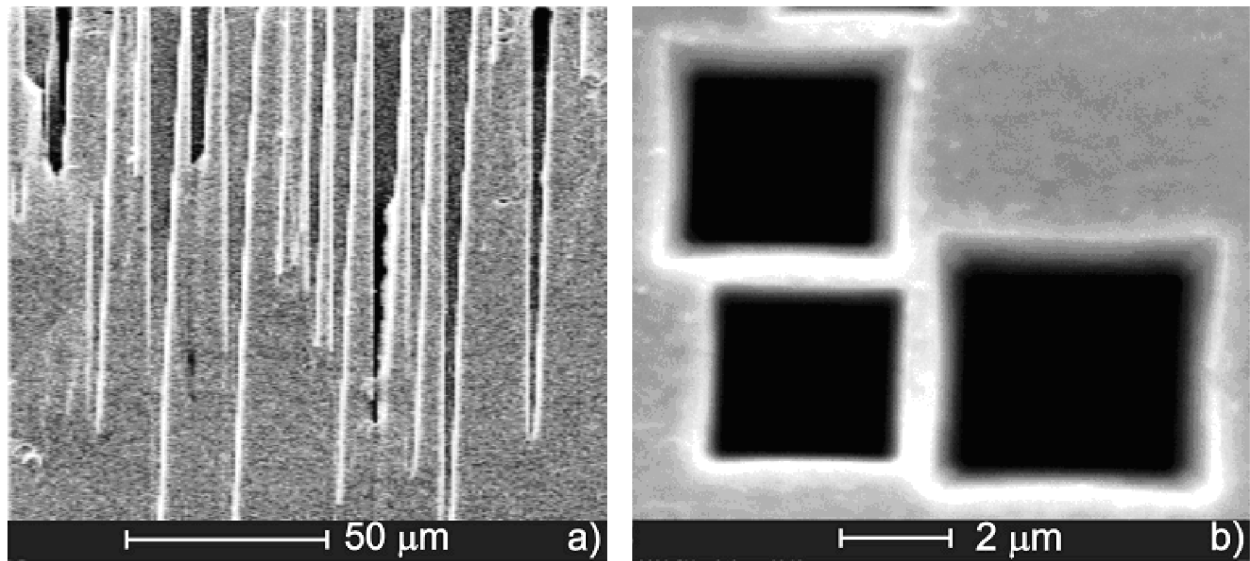
Figure E.4: *a) Conical pore shape (the picture has been shortened to enhance the effect; b) Pore walls between close pores.*

applications, but also for a better understanding of pore etching in semiconductors.

Appendix F

Salient Features of Pores in Si and III-Vs

Material	Si				GaAs	GaP	InP
Doping	n	p	n^+	p^+	n, n^+	n, n^+	n, n^+
Pore geometry	micro meso macro	micro meso macro	meso macro	meso	meso macro	meso macro	meso macro
Hole supply	Avalanche BSI FSI	Doping	Avalanche	Doping	Avalanche	Avalanche No definite effects of front side illumination	Avalanche
Growth direction (macro/meso)	100 113 Fractal	100 113	100 113	100 113	111B	111B curro pores	111B curro pores
Stopping planes	111	111	111	111	111A 112	111A 112	111A 112
	Chains of octahedrons		?	?	Chains of tetrahedrons		
Luminescence	micro	micro				macro meso	
Oscillations z = depth along pore	I(x,y) I(z) I(t) U(t)	I(x,y) I(t) U(t)	I(x,y) I(t) U(t)	I(x,y) I(t) U(t)	I(x,y) I(z)	I(x,y) I(z) U(t)	I(x,y) I(z) U(t)
Correlations between pores	S.D.O.	S.D.O.			(x,y)OD	S.D.O. z OD	S.D.O. z OD Pore crystal

Abbreviations and explanations: BSI or FSI = backside or front side illumination; (111)A or B refers to the polarity of the {111} planes; A = Ga or In layer, B = P or As layer; S.D.O = synchronized diameter oscillations; OD = ordered domains. "Stopping planes" means the crystallographic planes often (but not always) encountered as pore walls. Luminescence refers to above background intensity. I(x,y) or I(z) in "Oscillations" means that the current oscillates in space, i.e. that pores are formed, or in depth, respectively, implying pore diameter oscillations,

too. I(t) and U(t) denote oscillations in time observed without direct linkage to pore formation, e.g. during electropolishing (see the Table on the next page).

Appendix G

Partial Publications

G.1 Scientific Journals and Proceedings

1. S. Langa, I. M. Tiginyanu, J. Carstensen, M. Christophersen, H. Foell, *Formation of porous layers with different morphologies during anodic etching of n- InP*, J. Electrochem. Soc. Lett., 3 (11), 514 (2000).

2. S. Langa, J. Carstensen, I.M. Tiginyanu, M. Christophersen, H. Foell, *Self induced voltage oscillations during anodic etching of n- InP and possible applications for three-dimensional microstructures*, Electrochem. Solid-State Lett., 4, G50 (2001).

3. S. Langa, J. Carstensen, M. Christophersen, H. Foell, I. M.Tiginyanu, *Observation of crossing pores in anodically etched n- GaAs*, Appl. Phys. Lett., 78, 1074 (2001).

4. S. Langa, J. Carstensen, I.M. Tiginyanu, M. Christophersen, H. Foell, *Formation of tetrahedron-like pores during anodic etching of (100)-oriented n- GaAs*, Electrochem. Solid-State Lett., 5, C14-C17 (2002).

5. S. Langa M. Christophersen, J. Carstensen, I.M. Tiginyanu,H. Foell, *Single crystalline 2D porous arrays obtained by self-organization in n- InP*, Phys. Stat. Sol. (a), 197 (1,2), 77 (2003).

6. S. Langa J. Carstensen, M. Christophersen, I.M. Tiginyanu, H.Foell, *Voltage oscillations - an emergent property at high density pore growth*, Phys. Stat. Sol. (a), 197 (1,2), 186, (2002).

7. S. Langa, M. Christophersen, J. Carstensen, I.M. Tiginyanu and H. Foell, *Electrochemical pore etching in Ge*, Phys. Stat. Sol (a) 195(3), R4 (2003).

8. S. Langa, I.M. Tiginyanu J. Carstensen, M. Christophersen, and H. Foell, *Self-organized growth of single crystals of nanopores*, Appl. Phys. Lett. 82(2), 272 (2003).

9. H. Foell, S. Langa, J. Carstensen, M. Christophersen, I. M. Tiginyanu *Pores in III-V Semiconductors*, Adv. Mat., 15(3), 183 (2003).

10. H. Foell, J. Carstensen, S. Langa, M. Christophersen, and I.M. Tiginyanu, *Photonic Crystals: the Future of Optical Communications* , in Proceedings of the 3rd International Conference on Microelectronics and Computer Science, 1, Technical University of Moldova (2002).

11. H. Foell, J. Carstensen, S. Langa, M. Christophersen, and I.M. Tiginyanu, *Porous III-V compound semiconductors: formation,properties and comparison to silicon*, Phys. Stat. Sol. (a), 197 (1,2), 61, (2002).

12. H. Foell, S. Langa, J. Carstensen, M. Christophersen, I.M. Tiginyanu, K. Dichtel, *Pore Etching in Compound Semiconductors for the Production of Photonic Crystals*, MRS Spring Meeting, San Francisco (2002).

13. I.M. Tiginyanu, S. Langa, K. Hjort, J. Monecke, H. L.Hartnagel, "Nanotexturization of III-V compounds for THz-wave generation", Paper presented at the $8^t h$ Int. Conf. on Terahertz Electronics, Abstract Booklet, p. 275. Darmstadt, Germany, Sept. 28-29 (2000).

14. I.M. Tiginyanu, I.V. Kravetsky, S. Langa, G. Marowsky, J. Monecke, and H. Foell *Porous III-V Compounds as Nonlinear Optical Materials* , submitted to Phys. Stat. Sol. (a), 197 (1,2), 549,(2002).

15. I.M. Tiginyanu, S. Langa, M. Christophersen, J. Carstensen, V. Sergentu, E. Foca, O. Rios, and H. Foell, *Properties of 2D and 3D Dielectric Structures Fabricated by Electrochemical Dissolution of III-V Compounds* ,K2.7 MRS Proceedings Volume 692 (2002).

16. I.M. Tiginyanu, V.V. Ursaki, V.V. Zalamai, S. Langa, S. Hubbard and D. Pavlidis *Luminescence of GaN nanocolumns obtained by photon-assisted anodic etching* , in press Appl. Phys. Lett. (2003).

17. M.A. Stevens-Kalceff, I.M. Tiginyanu,S. Langa, and H. Foell, Correlation between morphology and Cathodoluminescence in porous GaP, Appl. Phys., 89(5), 2560-2565 (2001).

18. M.A. Stevens-Kalceff, S. Langa, I.M. Tiginyanu, J. Carstensen, M. Christophersen,and H. Foell, *Comparative SEM and Cathodoluminescence Microanalysis of Porous GaP Structures*, F5.31 MRS Proceedings Volume 638,(2001).

19. M. Christophersen, S. Langa, J. Carstensen, I. M. Tiginyanu, H.Foell, *A comparison of pores in silicon and pores in III-V compound materials*, submitted to Phys. Stat. Sol. (a),197 (1,2), 197 (2002).

20. M. Christophersen, S. Langa, J. Carstensen, P.M. Fauchet, and H. Foell, *Self-induced Voltage Oscillations and Diameter Modulations During Pore Formation in Si and InP*, in MRS Proceedings Spring Meeting:Invited Paper (2003).

21. S. Loelkes , M. Christophersen, S. Langa, J. Carstensen, and H. Foell, *Self-Organized formation of crystallographically oriented octahedral cavities during electrochemical pore etching*, E-MRS Spring Meeting, Strasbourg (2002).

22. J.C. Claussen, J. Carstensen, M. Christophersen, S. Langa, and H. Foell, *Open-Loop-Control of Pore Formation in Semiconductor Etching*, in Proceedings of Physics and Control, St. Petersburg, Russia (2003).

23. J.C. Claussen, J. Carstensen, M. Christophersen, S. Langa, H. Foell, *Self-organized pore formation and open-loop-control in semiconductor etching*, Chaos, 13, 217 (2003).

G.2   Books Contributions

1. S. Langa, J. Carstensen, I.M. Tiginyanu, M. Christophersen, H. Foell, *Selfordering in porous III-V compounds*, in Ordered Pore Systems, Ed. R. B.Wehrspohn - submitted to the Editor, 2001.

2. R.B. Wehrspohn, J. Schilling, J. Choi, Y. Luo, S. Matthias, S. Schweizer, U. Goesele, S. Loelkes, S. Langa, J. Carstensen, and H. Foell 4 *Electrochemically-prepared 2D and 3D photonic crystals*, in Photonic Crystals: Advances in Design, Fabrication and Characterization, Ed. K. Busch, S. Lölkes, R.B. Weherspohn, H. Föll, Wiley-VCH 2004.

G.3   Conference Oral Contributions

1. S. Langa, M. Christophersen, J. Carstensen, I.M. Tiginyanu,H. Foell, "Porous morphologies: New features in III-V compounds in comparison with those in Si", 8-9 October, Porous III-V materials, Kiel, Germany, 2001.

2. S. Langa, M. Christophersen, J. Carstensen, I.M. Tiginyanu, H. Foell, "Single crystalline 2D porous arrays obtained by self-organization in n- InP", 10-15 March,PSST, Tenerife, Spain, 2002.

3. J. Carstensen, S. Langa, S. Loelkes, I.M. Tiginyanu, H. Foell, "Fast IV measurements during the pore growth in Ge, InP and GaAs", 27 April -2 May, ECS Meeting, Paris, France, 2003.

G.4   Conference Posters

1. S. Langa J. Carstensen, M. Christophersen, I. M. Tiginyanu, H. Foell, *Voltage oscillations - an emergent property at high density pore growth* , Int. Conference of Porous Semiconductors - Science and Technology, 11-15 March 2002, Tenerife, Spain

2. S. Langa, M. Christophersen, J. Carstensen, I. Tiginyanu, H. Foell, *Self induced voltage oscillations during the process of pore formation in III-V materials*, DPG Spring Meeting, 16-30 March 2001, Hamburg, Germany

3. S. Langa, J. Carstensen, M. Christophersen, I. Tiginyanu, H. Foell, *Electrochemical etching of 2D and 3D photonic band gap structures in III-V materials*, Conference of Electromagnetic Crystals Structures, 9-14 June 2001, St. Andrews, Great Britain.

4. S. Langa J. Carstensen, S. Loelkes, I. M. Tiginyanu, H. Foell, *Particularities of Anodically Etched Pores in (100) Ge Substrates* , ECS Meeting, 27 April - 2 May 2003, Paris, France.

5. J. Carstensen, K. Steen, M. Christophersen, J. Bahr, G. Popkirov, S. Langa, S. Loelkes, H. Foell, *Large area etching of porous semiconductors*, ECS Meeting, 27 April - 2 May 2003, Paris, France.

6. I.M. Tiginyanu, V.V. Ursaki, I.V. Kravetsky, S. Langa, M.A. Bader, G. Marowsky, M.A. Stevens-Kalceff, H. Foell *Optical and Photoelectrical Properties of Electrochemically Nanostructured III-V Compounds*, ECS Meeting, 27 April - 2 May 2003, Paris, France.

7. I. M. Tiginyanu, S. Langa, J. Carstensen, M. Christophersen, H. Foell, *Self arrangement of submicron pores and modulations of their diameter in anodically etched n- InP*, MRS Meeting, 27. November - 1. December 2000, Boston, Massachusetts, USA

8. M. Christophersen, S. Langa, J. Carstensen, I. Tiginyanu, H. Foell, *Porous III-V materials for photonic crystal applications* , DPG Spring Meeting, 16-30 March 2001, Hamburg, Germany

9. M. Christophersen, S. Langa, J. Carstensen, I. Tiginyanu, H. Foell, *Porous Silicon vs. porous III-V compound semiconductors*, Int. Workshop ,,Porous III-V materials", 8-10 October 2001, Kiel, Germany

10. J. C. Claussen, J. Carstensen, M. Christophersen, S. Langa, H. Foell, *Oscillations, synchronization, and open-loop control in electrochemical semiconductor pore etching*, MPI for complex Systems, International Workshop and Seminar on ,,Control, Communication, and Synchronization in Chaotic Dynamical Systems", 14 October - 23 November, 2001, Dresden, Germany

11. M. Christophersen S. Langa, J. Carstensen, I. M.Tiginyanu, H. Foell, *A comparison of pores in silicon and pores in III-V compound materials*, Int. Conference of Porous Semiconductors - Science and Technology, 11-15 March 2002, Tenerife, Spain

12. J. C. Claussen, J. Carstensen, M. Christophersen, S. Langa, H. Foell, *Oscillations, synchronization, and open-loop control in electrochemical semiconductor pore etching*, DPG Spring meeting, 11-15 March, Regensburg, Germany

Bibliography

[1] *The Wall Street Journal*, 22, 1997.

[2] *IBM Research magazine*, 4:16, 1997.

[3] L. T. Romankiw, I. Croll, and M. Hatzakis. *IEEE Trans. Magn.*, 6:729, 1970.

[4] L. T. Romankiw. *Electrochim. Acta*, 42:2985, 1997.

[5] R.L. Smith, D.J. Fulmer, and S.D. Collins. In M. Datta, K. Sheppard, and D. Snyder, editors, *Electrochemical Microfabrication*, volume 203. Electrochem. Soc., 1992.

[6] N. F. de Rooij. In S.-C. Chang and S. W. Pang, editors, *Micromachining and Microfabrication Process Technology III*, volume 2-9. Society of Photo-Optical Instrumentation Engineers, Bellingham, WA,, 1997.

[7] P. J. McWhorter, A. B. Frazier, and P. Rai-Choudhury. In P. Rai-Choudhury, editor, *Handbook of Microlithography, Micromachining and Microfabrication*, volume 2. Society of Photo-Optical Instrumentation Engineers, Bellingham, WA,, 1997.

[8] Jr. F.W. Ostermayer, P.A. Kohl, and R.H. Burton. *Electrochim. Acta*, 43:642, 1983.

[9] R. Matz. *J. Lightwave Technol.*, 4:726, 1986.

[10] G. Heise, R. Matz, and U. Wolff. In R. T. Kersten, editor, *Integrated Optical Circuit Engineering III*, volume 651. Society of Photo-Optical Instrumentation Engineers, 1986.

[11] D. Xu, T. Enoki, T. Suemitsu, and Y. Ishii. *J. Appl. Phys*, 38:1182, 1999.

[12] J. N. Winn J. D. Joannopoulos, R. D. Meade. *Photonic crystals*. Princeton University Press, 1995.

[13] F. M"uller, A. Birner, U. Goesele, V. Lehmann, S. Ottow, and H. Foell. Structuring of macroporous silicon for applications as photonic crystals. *Journal of Porous Materials*, **7**:201, 2000.

[14] A.I. Belogorokhov, V.A. Karavanskii, A.N. Obraztsov, and V.Yu. Timoshenco. Intense photoluminescence in porous gallium phosphide. *JETP Lett.*, **60**:264, 1994.

[15] A. Anedda, A. Serpi, V.A. Karavanskii, I.M. Tiginyanu, and V.M. Ichizli. Time-resolved blue and ultraviolet photoluminescence in porous GaP. *Appl. Phys. Lett.*, **67**:3316, 1995.

[16] K. Kuriyama, K. Ushiyama, K. Ohbora, Y. Miyamoto, and S. Takeda. Characterization of porous GaP by photoacoustic spectroscopy: The relation between band gap widening and visible photoluminescence. *Phys. Rev. B*, **58**:1103, 1998.

[17] B.H. Erne, D. Vanmaekelbergh, and J.J. Kelly. Morphology and strongly enchanced photoresponce of GaP electrodes made porous by anodic etching. *J. Electrochem. Soc.*, **143**:305, 1996.

[18] F. Iranzo Marin, M.A. Hamstra, and D. Vanmaekelbergh. *J. Electrochem. Soc.*, 3:1137, 1996.

[19] E. Kukino, M. Amiotti, T. Takizawa, and S. Arai. Anisotropic refractive index of porous InP fabricated by anodization of (111) surface. *Jap. J. Appl. Phys.*, **34**:177, 1995.

[20] I.M. Tiginyanu, G. Irmer, J. Monecke, and H.L. Hartnagel. *Phys. Rev. B*, 55:6739, 1997.

[21] I.M. Tiginyanu, V.V. Ursaki, Y.S. Raptis, V. Stergiou, E. Anastassakis, H.L. Hartnagel, A. Vogt, B. Prevot, and C. Schwab. *Phys. Stat. Sol. b*, 211:281, 1999.

[22] C. Duan A. Liu. *Physica E*, 9:723, 2001.

[23] I.M. Tiginyanu, I.V. Kravetsky, G. Marowsky, and H.L. Hartnagel. Semiconductor sieves as nonlinear optical materials. *phys. stat. sol. (a)*, **175**:5, 1999.

[24] P.A. Kohl. Photoelectrochemical etching of semiconductors. *IBM J. Res. Dev.*, 42:629, 1998.

[25] N. W. Ashcroft and N. D. Mermin. *Solid State Phisics*. Saunders College Publishing, 1976.

[26] R. E. Hummel. *Electronic properties of materials*. Springer-Verlag, 1993.

[27] S. M. Sze. *Physics of Semiconductor devices*. John Wiley and Sons, 1981.

[28] K.J. Jackson. *Compound semiconductor devices*. Wiley-VCH, 1998.

[29] G. Wedler. *Lehrbuch der Physikalischen Chemie*. Wiley-VCH, 1985.

[30] J.-C. Vial and J. Derrien. *Porous silicon science and technology*. Springer-Verlag and Les Editions de Physique, 1995.

[31] S.R. Morrison. *Electrochemistry at semiconductors and oxidized metal electrodes*. Plenum Press, 1980.

[32] R.M. Noyes. *J. am. Chem. Soc.*, 84:513, 1962.

[33] F. Lohmann. *Z. Naturforsch.*, 22:843, 1967.

[34] S. Trasatti. *J. Electroanal. Chem.*, 52:313, 1974.

[35] R. M. Osgood, A. Sanchez-Rubio, D. J. Ehrlich, , and V. Daneu. *Appl. Phys. Lett.*, 40:391, 1982.

[36] D. V. Podlesnik, H. H. Gilgen, R. M. Osgood, A. Sanchez, and V. Daneu. In R. M. Osgood, S.R.J. Brueck, and H.R. Schlossberg, editors, *Laser Diagnostics and Photochemical Processing for Semiconductors.* North-Holland Press, New York, 1983.

[37] T. Takebe, T. Yamamato, M. Fujii, and K. Kobayashi. Sundamental selective etching characteristics of HF+H2O2+H2O mixtures for GaAs. *J. Electrochem. Soc.*, **140**:1169, 1993.

[38] N. J. Kadhim, S. H. Laurie, and D. Mukherjee. *Education*, 75:840, 1998.

[39] H. Gerischer and I. Wallem-Mattes. *Z. Phys. Chem.*, 64:187, 1969.

[40] H. Gerischer and W. Mindt. *Electrochim. Acta*, 13:1329, 1968.

[41] P.H.L. Notten, J.E.A.M. van den Meerakker, and J.J. Kelly. *Etching of III-V semiconductors: An electrochemical Approach.* Elsevier Science Publishers Ltd., Oxford, 1991.

[42] W. Plieth and S. Witzenstein. *Semiconductor Micromaschining: Fundamental Electrochemistry and Physics.* John WILEY and SONS, 1998.

[43] H. Foell, M. Christophersen, J. Carstensen, and G. Hasse. *Mat. Sci. Eng. R*, 39:93, 2002.

[44] C. Levy-Clement and M. Tomkiewicz A. Lagoubi. Morphology of porous n-type silicon obtained by photoelectrochemical etching. i. correlations with material and etching parameters. *J. Electrochem. Soc.*, 141:958, 1994.

[45] M.M. Carrabba, N.M. Nguyen, and R.D. Rauh. *J. Electrochem. Soc.*, 134:1855, 1987.

[46] H. Foell. Properties of silicon-electrolyte junctions and their application to silicon characterization. *Appl. Phys. A*, **53**:8, 1991.

[47] P. Schmuki, D.J. Lockwood, H.J. Labbe, and J.W. Fraser. *Appl. Phys. Lett.*, 69:1620, 1996.

[48] C. Kaneshiro, T. Sato, and H. Hasegawa. *Jpn. J. Appl. Phys.*, 38:1147, 1999.

[49] R.S. Muller and T.I. Kamins. *Device electronics for integrated circuits.* John Wiley and Sons, New York, 1977.

[50] X.G. Zhang. Mechanism of pore formation on n-type silicon. *J. Electrochem. Soc.*, **138**:3750, 1991.

[51] P. Schmuki, J. Fraser, C.M. Vitus, M.J. Graham, and H.S. Isaacs. *J. Electrochem. Soc.*, 143(10):3316, 1996.

[52] R.W. Tjerkstra, J. Gomesz-Rivas, D. Vanmaekelbergh, and J. J.Kelly. *Electrochem. Solid-State Lett.*, 5:32, 2002.

[53] J. Carstensen, M. Christophersen, G. Hasse, and H. Foell. Parameter dependence of pore formation in silicon within the model of local current bursts. *phys. stat. sol. (a)*, **182**(1):63, 2000.

[54] J. Carstensen, R. Prange, G.S. Popkirov, and H. Foell. A model for current oscillations in the Si-HF system based on a quantitative analysis of current transients. *Appl. Phys. A*, **67**:459, 1998.

[55] H. Foell, J. Carstensen, M. Christophersen, and G. Hasse. A new view of silicon electrochemistry. *phys. stat. sol. (a)*, **182**(1):7, 2000.

[56] S. Langa, J. Carstensen, M. Christophersen, H. Foell, and I.M. Tiginyanu. Observation of crossing pores in anodically etched n-GaAs. *Appl. Phys. Lett*, **78**:1074, 2001.

[57] S. Loelkes. *University of Kiel, Faculty of Engineering, Privat Communications*, 2003.

[58] M.C. de Santos and O. Teschke. *J. Vac. Sci. Technol. B*, 16:2105, 1998.

[59] K.W. Kolasinski. *Int. J. Mod. Phys.*, 9:2753, 1995.

[60] Z.H. Lu, F. Chatenoud, M.M. Dion, M.J.Graham, H.E. Ruda, I. Koutzarov, Q. Liu, C.E.J. Mitchell, I.G. Hil, and A.B. McLean. *Appl. Phys. Lett.*, 67:670, 1995.

[61] F.M. Ross, G. Oskam, P.C. Searson, J.M. Macaulay, and J.A. Liddle. Crystallographic aspects of pore formation in gallium arsenide and silicon. *Phil. Mag. A*, **75**:525, 1997.

[62] E. Yablonovitch, T.J. Gmitter, and K.M. Leung. Photonic band gap structure: The face-centered-cubic case employing nonspherical atoms. *Phys. Rev. Lett.*, 67:2295, 1991.

[63] I.M. Tiginyanu, C. Schwab, J.-J. Grob, B. Prevot, H.L. Hartnagel, A. Vogt, G. Irmer, and J. Monecke. Ion implantation as a tool for controlling the morphology og gallium phosphide. *Jpn. J. Appl. Phys.*, **71**:3829, 1997.

[64] P. Schmuki, L.E. Erickson, D.J. Lockwood, J.W. Fraser, G. Champion, and H.J. Labbe. Formation of visible light emitting porous gaas micropattern. *Appl. Phys. Lett.*, 72:1039, 1998.

[65] M. N. Ruberto, X. Zhang, R. Scarmozzino, A. E. Willner, D. V. Podlesnik, and R. M. Osgood. *J. Electrochem. Soc.*, 138:1174, 1991.

[66] G.S. Popkirov and R.N. Schindler. A new approach to the problem of good and bad impedance data in electrochemical impedance spectroscopy. *Electrochimica Acta*, 39:2025, 1994.

[67] S. Langa, I.M. Tiginyanu, J. Carstensen, M. Christophersen, and H. Foell. Formation of porous layers with different morphologies during anodic etching of n-inp. *J. Electrochem. Soc. Lett.*, **3**(11):14, 2000.

[68] C. Jaeger, B. Finkenberger, W. Jaeger, M. Christophersen, J. Carstensen, and H. Foell. Transmission electron microscopy investigations of the formation processes of macropres in n-si(001)/(111) and p-si(001)/(111). *Mat. Sci. Eng. B*, **69-70**:199, 2000.

[69] R.J. Field and M. Burger. Wiley, New York, 1995.

[70] D.R. Turner. *J. Electrochem. Soc.*, 105:402, 1998.

[71] H. Masuda and K. Fukuda. *Science*, 268:1466, 1995.

[72] S. Langa, J. Carstensen, I.M. Tiginyanu, M. Christophersen, and H. Foell. Formation of tetrahedron-like pores during anodic etching of (100)-oriented n-GaAs. *Electrochem. and Solid State Lett.*, **5**:14, 2002.

[73] R.L. Smith and S.D. Collins. *J. Appl. Phys.*, 71:1, 1992.

[74] V. Lehmann and H. Foell. *J. Electrochem. Soc.*, 137:653, 1990.

[75] E. K. Propst and P. A. Kohl. *J. Electrochem. Soc.*, 141:1006, 1994.

[76] J.-N. Chazalviel, R. B.Wehrspohn, and F. Ozanam. *Mater. Scien. and Eng.B*, 69:1, 2000.

[77] H. Foell, J. Carstensen, S. Langa, M. Christophersen, and I.M.Tiginyanu. *Phys. Stat. Sol. (a)*, 197:61, 2002.

[78] M. Christophersen, S. Langa, J. Carstensen, I. M. Tiginyanu, and H.Foell. *Phys. Stat. Sol. (a)*, 197:197, 2002.

[79] J. Schilling, F. Mueller, S. Matthias, R.B. Wehrspohn, U. Goesele, and K. Busch. *Appl. Phys. Lett.*, 78:1180, 2001.

[80] J. Charrier, E. Le Gorju, L Haji, and M. Guendouz. *J. Por. Mat.*, 7:243, 2000.

[81] M. Christophersen, J. Carstensen, A. Feuerhake, and H. Foell. *Mat. Sc. Eng. B*, 69:194, 2000.

[82] L.T. Canham. Silicon quantum wire array fabrication by electrochemical and chemical dissolution of wafers. *Appl. Phys. Lett.*, **57**:1046, 1990.

[83] V. Lehmann and U. Goesele. Porous silicon: a quantum wire effect. *Appl. Phys. Lett.*, **58**:856, 1991.

[84] T. Takizawa, S. Array, and M. Nakahara. Fabrication of vertical and Uniform-Size porous InP structures by electrochemical anodization. *Jpn. J. Appl. Phys.*, 33(5):643, 1994.

[85] A. E. Yunovich. *Radiative Recombination in Semiconductors*. Nauka, Moscow, 1972.

[86] P. J. Dean, C. J. Frosch, and C. H. Henry. *J. Appl. Phys.*, 39:5631, 1968.

[87] P. J. Dean, J. D. Cuthbert, and R. T. Lynch. *Phys. Rev.*, 179:754, 1969.

[88] A.T. Vink, A. J. Bosman, J. A. W. van der Does de Bye, and R. C. Peters. *Solid State Commun.*, 7:1475, 1969.

[89] Yu. Ishikawa, Yo. Hayashi, and N. Itoh. *J. Appl. Phys.*, 65:2035, 1989.

[90] O.O. Awadelkarim, M. Godlewski, and B. Monemar. *Mater. Sci. Forum*, 38:821, 1989.

[91] I.M. Tiginyanu, G. Irmer, J. Monecke, A. Vogt, and H.L. Hartnagel. *Semicond. Sci. and Technology*, 12:491, 1997.

[92] P. Daniel Dapkus and C. H. Henry. *J. Appl. Phys.*, 47:4061, 1976.

[93] C. E. Barnes. *J. Appl. Phys.*, 48:1921, 1977.

[94] K. Zdansky, J. Zavadil, D. Nohavica, and S. Kugler. *J. Appl. Phys.*, 83:7678, 1998.

[95] D.J. Lockwood, P. Schmuki, H. J. Labbe, and J. W. Fraser. *Physica E (Amsterdam)*, 4:102, 1999.

[96] A. Meijernik, A.A. Bol, and J.J. Kelly. *Appl. Phys. Lett.*, 69:2801, 1996.

[97] L. Yuan, X. M. Ding, B. Lai, X. Y. Hou, E. D. Lu, P.S. Xu, and X. Y. Zhang. *Appl. Phys. Lett.*, 73:2977, 1998.

[98] V. Lehmann. The physics of macropore formation in low doped n-type silicon. *J. Electrochem. Soc.*, **140**:2836, 1993.

[99] I.M. Tiginyanu, V.V. Ursaki, V.V. Zalamai, S. Langa, S. Hubbard, D. Pavlidis, and H. Foell. Luminescence of GaN nanocolumns obtained by photon-assisted anodic etching. *Appl. Phys. Lett.*, **83**:1551, 2003.

[100] S. Langa, M. Christophersen, J. Carstensen, I.M. Tiginyanu, and H. Foell. *Phys. Stat. Sol (a)*, 195:4, 2003.

[101] S. Noda, N. Yamamoto, and A. Sasaki. *Jpn. J. Appl. Phys*, 35:909, 1996.

[102] S.Y. Lin, J.G. Fleming, and E. Chow. *MRS Buletin*, 26:62, 2002.

[103] A.J. Turberfield. *MRS Buletin*, 26:632, 2002.

[104] B. DUrso, O. Painter, and A. Scherer. *J. Opt. Soc. Am. B*, 15:1155, 1998.

[105] R.B. Wehrspohn and J. Schilling. *MRS Buletin*, 26:623, 2002.

[106] J.M. Buriak. *Chem. Rev.*, 102:1271, 2002.

[107] H.C. Choi and J.M. Buriak. *Chen. Commun.*, 17:1669, 2000.

[108] S. Bayliss, Q. Zhang, and P. Harris. *Appl. Surf. Sci.*, 102:390, 1996.

[109] S. Miyazaki, K. Sakamoto, K. Shiba, and M. Hirose. *Thin Solid Films*, **255**:99, 1995.

[110] D.R. Turner. Experimental information on electrochemical reactions at ge and si surfaces. In P.J. Holmes, editor, *The Electrochemistry of Semiconductors*, page 155. Academic Press, 1962.

[111] L.K. van Vugt, A.F. van Driel, R.W. Tjerkstra, L. Bechger, W.L. Vos, D. Vanmaekelbergh, and J.J. Kelly. Macroporous germanium by electrochemical deposition. *Chem.Com.*, **62**:in press, 2002.

[112] B.D. Chase and D.B. Holt. *J. Electrochem. Soc.*, **119**:314, 1972.

[113] G. Hasse, J. Carstensen, G.S. Popkirov, and H. Foell. Current transient analysis of the oxidizing process in the complete anodic regime of the si-hf system. *Mat. Sci. Eng. B*, **69-70**:188, 2000.

[114] J.-N. Chazalviel, A. Belaidi, M. Safi, F. Maroun, B.H. Erne, and F. Ozanam. *Electrochem. Acta*, **45**:3205, 2000.

Curriculum Vitae

Name:	Sergiu Langa
Place of residence :	Bremerstr. 23, 24118 Kiel, Germany
Born:	10. October 1976 in Grozesti/Moldova
Marital status :	single
Citizenship	Moldova
Parents:	Iulia and Vasilie Langa

Schooling

1983 - 1991	General school in Grozesti/Moldova
1991 - 1994	Republican College of Informatics, Chisinau, Moldova
June 1994	Bachelor degree (Romanian version)
September 1994	Inmatriculated at the Technical University of Moldova

University Education

September 1994 - June 1999	Studies at the Chair of Microelectronics and Semiconductor Devices of the Technical University of Moldova,
June 1999	State examinations and Diploma thesis at the Chair of Microelectronics and Semiconductor Devices (TUM).
July 1999	Guest at the Technical University of Darmstadt, Germany (Chair of Prof. Dr. H.L. Hartnagel)
Since December 5th, 1999	Scientific collaborator at the Technical Faculty of the Christian-Albrechts University of Kiel, Germany (Chair of Materials Science, Prof. Dr. H. Foell)

List of Abbreviations

2D - Two dimensional.

3D - Three dimensional.

BSI - Back Side Illumination.

CBM - Current Burst Model.

Crysto pores - Crystallographically oriented pores.

Curro pores - Current line oriented pores.

CE - Counter electrode.

CL - Cathodoluminescence.

DP - Difraction pattern.

ECE - Electro-Chemical Etching.

EM - Electron Microscope.

FFT - Fast Fourier Transform.

FSI - Front Side Illumination.

GaAs - Gallium Arsenide.

GaP - Gallium Phosphide.

Ge - Germanium.

GL - Gouy layer.

HL - Helmholtz layer

HRTEM - High Resolution Transmission Electron Microscope

IC - Integrated Circuits.

IV - Current Voltage curve.

InP - Indium Phosphide.

MEMS - Microelectromechanical Systems.

NL - Nucleation Layer.

PC - Photonic Crystals.

PIC - Photonic Integrated Circuits.

PEC - Photo-Electrochemical Etching.

PFP - Pore Formation Potential

PL - Photoluminescence.

RE - Reference electrode.

SCR - Space Charge Region.

SHG - Second Harmonic Generation.

SE - Sense electrode.

Si - Silicon.

SEI/SEJ - Semiconductor Electrolyte Interface/Jounction.

SEM - Scanning Electron Microscope.

TEM - Transmitting Electron Microscope.

TIR - Total Internal Reflection.

WE - Working electrode.

WDM - Wavelength Division Multiplexing.

Acknowledgements

Eidesstattliche Erklärung

Ich erkläre hiermit, dass ich keine anderen als die von mir angegebenen Quellen und Hilfsmittel zur Erstellung meiner Dissertation verwendet habe. Den benutzten Werken wörtlich oder inhaltlich entnommene Stellen sind als solche gekennzeichnet.

Sergiu Langa
Kiel, in Januar 2004